FINAL REPORT

Wastewater Treatment Using Microbial Fuel Cells with Peroxide Production

SERDP Project ER-2239

JANUARY 2018

César Torres
Bruce E. Rittmann
Konstantinos Tsakalis
Patrick Evans
Arizona State University

Page Intentionally Left Blank

Page Intentionally Left Blank

REPORT DOCUMENTATION PAGE

Form Approved
OMB No. 0704-0188

1. REPORT DATE *(DD-MM-YYYY)*
01/28/2018

2. REPORT TYPE
SERDP Final Report

3. DATES COVERED *(From - To)*
9/28/2012 - 9/28/2017

4. TITLE AND SUBTITLE
Wastewater Treatment Using Microbial Fuel Cells with Peroxide Production

5a. CONTRACT NUMBER
Contract: 12-C-0047

5b. GRANT NUMBER

5c. PROGRAM ELEMENT NUMBER

6. AUTHOR(S)
César Torres

5d. PROJECT NUMBER
ER-2239

5e. TASK NUMBER

5f. WORK UNIT NUMBER

7. PERFORMING ORGANIZATION NAME(S) AND ADDRESS(ES)
Arizona State University
1001 S. McAllister Ave., PO Box 875701
Tempe, AZ 85287

8. PERFORMING ORGANIZATION REPORT NUMBER
ER-2239

9. SPONSORING/MONITORING AGENCY NAME(S) AND ADDRESS(ES)
Strategic Environmental Research and Development Program
4800 Mark Center Drive, Suite 17D03
Alexandria, VA 22350-3605

10. SPONSOR/MONITOR'S ACRONYM(S)
SERDP

11. SPONSOR/MONITOR'S REPORT NUMBER(S)
ER-2239

12. DISTRIBUTION/AVAILABILITY STATEMENT
Distribution A; unlimited public release

13. SUPPLEMENTARY NOTES

14. ABSTRACT

The overarching goal of our study is to develop a novel energy-neutral wastewater treatment technology that could aid in water reuse within a forward operation base, reducing water transport. To achieve this, we developed a microbial fuel cell capable of generating hydrogen peroxide as primary product. This technology takes advantage of the high-energy content of blackwater; the microbial fuel cell consumes and converts it into an electrical current that is used to generate significant amounts of hydrogen peroxide. The hydrogen peroxide can have several uses: (1) direct treatment of graywater towards reuse, (2) tertiary treatment of graywater and/or blackwater, (3) odor control for blackwater, and (4) treatment of blackwater itself for better effluent quality and solids destruction.

More specifically, our objectives were to (1) show the feasibility of hydrogen peroxide production from blackwater, (2) achieve hydrogen peroxide production at high efficiency, and (3) demonstrate the effective treatment of blackwater at near energy-neutral conditions using a microbial fuel cell.

15. SUBJECT TERMS
Microbial electrochemistry, Blackwater, Graywater, Wastewater treatment, Hydrogen peroxide, Cathode catalysts, Overpotentials, pH control, Potentiostat control, Hydraulic retention time (HRT), Volatile solids (VS), Primary sludge, Microbial peroxide producing cell (MPPC), microbial fuel cell (MFC), Anode-respiring bacteria (ARB), Life-cycle analysis

16. SECURITY CLASSIFICATION OF:			**17. LIMITATION OF ABSTRACT**	**18. NUMBER OF PAGES**	**19a. NAME OF RESPONSIBLE PERSON**
a. REPORT	**b. ABSTRACT**	**c. THIS PAGE**			César Torres
					19b. TELEPHONE NUMBER *(Include area code)*
UNCLASS	UNCLASS	UNCLASS	UNCLASS	236	480-727-9689

Page Intentionally Left Blank

TABLE OF CONTENTS

LIST OF TABLES

LIST OF FIGURES

LIST OF APPENDICES

LIST OF ABBREVIATIONS

1D	One-dimensional
A	Potentiostat's anode voltage
A/D	Analog to digital
AD	Anaerobic digestion
ADC	Analog to digital converter
ADM	Anaerobic Digestion Model
ADS	Anaerobic digested sludge
AEM	Anion exchange membrane
Ag/AgCl	Silver/silver chloride
AnS	Anode suspension
AO	Anthraquinone oxidation
AOB	Ammonium-oxidizing bacteria
ARB	Anode-respiring bacteria
ASM	Activated Sludge Model
ASU	Arizona State University
BAP	Biomass-associated products
BES	2–bromoethanesulfonic acid
BfC	Biofilm from the anode side facing the chamber
BfM	Biofilm from the anode side facing the membrane on the carbon fiber electrodes
BMP	Biochemical methane potential tests
BOD_5	Biological oxygen demand at 5 days
bp	Base pairs
BSCEB	Biodesign Swette Center for Environmental Biotechnology
BSM	Benchmark Simulation Model
BW	Blackwater
C	Controller
CASADM	Combined Activated Sludge-Anaerobic Digestion Model
CCBATCH	Co-Contaminants in a Batch reactor
CCE	Cathodic coulombic efficiency
CEM	Cation exchange membrane
CH_3COO^-	Acetate
CH_3COOH	Acetic acid
CH_4	Methane
Cl^-	Chloride ion
CO_2	Carbon dioxide
CO_3^{2-}	Carbonate
COD	Chemical oxygen demand
CSTR	Continuously stirred tank reactor
CT	Conventional treatment
CV	Cyclic voltammetry
D/A	Digital to analog

DAC	Digital to analog converter
DC	Direct current
DI	Deionized
e^-	Electrons
$E^{o'}$	Electrical potential at standard temperature, pressure, and pH
ED	Ecosystem diversity
EDTA	Ethylenediaminetetraacetic acid
EET	Extracellular electron transfer
EIS	Electrochemical impedance spectroscopy
E_{ka}	Anode potential at one-half of the maximum current density
EPS	Extracellular polymeric substances
ESTCP	Environmental Security Technology Certification Program
FE	Fermentation efficiency
FLS	Frequency loop shaping
FOB	Forward operating base
G	Plant
GDW	Gram of solids, dry-weight basis
GF	Glass fiber
GW	Graywater
GWRP	Greenfield Water Reclamation Plant
H^+	Protons
H_2	Hydrogen gas
H_2O	Water
H_2O_2	Hydrogen peroxide
H_2CO_3	Carbonic acid
HCO_3^-	Bicarbonate
HH	Human health
HNO_2	Nitrous acid
HO_2^-	Dioxidanide or hydroperoxyl anion
HPLC	High performance liquid chromatography
H_3PO_4	Phosphoric acid
$H_2PO_4^-$	Dihydrogen phosphate
HPO_4^{2-}	Hydrogen phosphate
HRT	Hydraulic retention time
IC	Integrated circuit
j	Current density
j-V	Current density-voltage
K	Controller gain
$k_{hyd\text{-}BMP}$	Hydrolysis constant based on biochemical methane potential tests' methane production
$k_{hyd\text{-}fermentation}$	Hydrolysis constant based on biochemical methane potential tests' volatile fatty acid production
L	Target loop
LCA	Life cycle assessment
LCI	Life cycle inventory
LCIA	Life cycle impact assessment

LSB	Least significant bit
LSV	Linear sweep voltammetry
MEC	Microbial electrochemical cell
MEC-H2O2	Microbial electrochemical cell for hydrogen peroxide production
MFC	Microbial fuel cell
MFC-E	Microbial fuel cell for electricity production
MNWWRP	Mesa Northwest Water Reclamation Plant
MPL	Microporous layer
MPPC	Microbial peroxide-producing cell
MPN	Most probable number
MPR	Methane production rate
MxC	Microbial electrochemical cell
MXR	Mixer
N_2	Nitrogen gas
Na^+	Sodium ion
$NaHCO_3$	Sodium bicarbonate
NH_3 or NH_3-N	Ammonia
NH_4^+	Ammonium
NO_2^-	Nitrite
NO_3^-	Nitrate
NOB	Nitrite-oxidizing bacteria
NPDES	U.S. EPA National Discharge Pollution Elimination System
O_2	Oxygen
ODE	Ordinary differential equations
OH^-	Hydroxide ions
OHRR	Oxygen reduction reaction to hydrogen peroxide
ORR	Oxygen reduction reaction
OTU	Operating taxonomic units
P&ID	Process and instrumentation diagram
PBS	Phosphate buffer solution
PC	Proton condition
PCB	Printed circuit board
PCBIOFILM	Proton Condition in Biofilm
PCOD	Particulate COD
PEF	Pulsed electric field
PEM	Proton exchange membrane
PFD	Process flow diagram
PI	Proportional intergral
PID	Proportional integral derivative
PMP	Pump
PO_4^{3-}	Phosphate
PPE	Hydrogen peroxide production efficiency
PRBS	Pseudo Random Binary sequence
PS	Primary sludge
PS_{in}	Primary sludge into the system

PS_{out}	Primary sludge leaving the system
R	Potentiontat’s reference electrode voltage
RA	Resource availability
RDP	Ribosomal Database Project
ROS	Reactive oxygen species
RRDE	Rotating-ring disk electron
RSC	Robust stability condition
S	Potentiostat’s set point
SCOD	Soluble COD
SERDP	Strategic Environmental Research and Development Program
SHE	Standard hydrogen electrode
SMP	Soluble microbial products
sMPPC	Single-chamber microbial peroxide-producing cell
SPF	Stitchbond polyester fabric
SPI	Serial Peripheral Interface
SRT	Solids retention time
SS	Semi-soluble
SSCOD	Semi-soluble chemical oxygen demand
STR	Self-cleaning strainer
TCOD	Total chemical oxygen demand
$TCOD_{in}$	Influent total chemical oxygen demand
TI	Treatment intensity
TNK	Tank
TOC	Total organic carbon
TSS	Total suspended solids
UAP	Utilization-associated products
UV	Ultraviolet
VFA	Volatile fatty acid
VSD	Volatile solids destruction
VSS	Volatile suspended solids
WAS	Wasted activated sludge
WW	Wastewater
WWT	Wastewater treatment
WWTP	Wastewater treatment plants
X_m	Methanogens concentration

LIST OF MATHEMATICAL VARIABLES

Symbol	Description	Units
α	Charge transfer coefficient	--
β_i^c	The formation constant of complex i adjusted for the solution's ionic strength	Varies
δ	The exponential weight	--
δ_{dzn}	A constant that represents a dead zone on the cost function in controls calculations	--
ε_{H2O2}	Efficiency of current conversion to H_2O_2	%
η_{act}	Activation overpotential	V
η_{an}	Anode overpotential	V
$\eta_{cathode}$	Cathode overpotential	V
η_{conc}	Concentration overpotential	V
η_{H2O2}	Concentration overpotential for O_2 reduction to H_2O_2	V
η_{OH-}	Concentration overpotential for H_2O_2 reduction to OH^-	V
η_{Ohmic}	Ohmic overpotential	V
η_{pH}	Overpotential due to increased cathode pH	V
λ	Settling parameter	1/t
λ_f	Forgetting factor	--
λ_{hg}	The stoichiometric coefficient of species h in reaction g	--
ν_{ij}	The stoichiometric coefficient giving the number of moles of component j in complex i	--
C	Controller transfer function	--
$\tilde{C}$	Non-adaptive part of PI controller	--
C^*	Local or actual concentration at the catalyst surface	M/L^3
C^{0*}	Standard concentration at the catalyst surface	M/L^3
C_{actual}	Actual H_2O_2 concentration	M/L^3
C^B	Actual bulk liquid concentration	M/L^3
CE	Coulombic efficiency	%
$C_k^{B,0}$	Influent bulk liquid concentration of component k	M/L^3
C_h	The concentration of the chemical or biological species h	M/L^3
c_{H^+}	Concentration of uncomplexed H^+	M/L^3
C_{H^+}	Total analytical concentration of H^+	M/L^3
C_{Hk}^*	Concentration of protonated form of species k	M/L^3
c_j	Concentration of component j	M/L^3
C_j	The total analytical concentration of component j	M/L^3
$\hat{C}_j$	Chemical formula for component j	--
C_{k-}^*	Concentration of deprotonated form of species k	M/L^3
C_{theory}	Theoretical concentration of H_2O_2	M/L^3

Symbol	**Description**	**Units**
COD_{final}	Final COD concentration	M/L^3
$COD_{influent}$	Influent COD concentration	M/L^3
$COD_{initial}$	Initial COD concentration	M/L^3
$COD_{unaccounted}$	Concentration of unaccounted for COD in the system	M/L^3
CR	Coulombic recovery	%
D	Diffusion coefficient	L^2/t
E	Fixed cell potential	V
E_{an}	Theoretical anode potential	V
E_{an}^0	Theoretical anode potential at standard temperature and pressure	V
$E_{an,observed}$	Observed anode potential	V
E_{ap}	Applied voltage	V
E^*	Apparent electric field	1/L
E_{ca}	Theoretical cathode potential	V
E_{ca}^0	Theoretical anode potential at standard temperature and pressure	V
Eff	Removal efficiency	%
Eff_{max}	Maximum removal efficiency	%
E_{KA}	The potential at which half of the maximum specific growth rate is achieve	V
E_{Th}	Theoretical voltage required for a given reaction	V
F	Faraday's constant	96485 C/mol
F_i	Filter bank	--
G	Plant transfer function	--
H	Henry's law constant	M/L^3
I	Current	A
I_{pH}	pH inhibition term	--
j	Current density	A/L^2
j_0	Exchange current density	A/L^2
J	Mass flux	M/L^2-t
J_{ion}	Total flux of an ion	M/L^2-t
J_{diff}	Diffusive flux of an ion	M/L^2-t
J_{mig}	Flux due to migration	M/L^2-t
$J_{membrane}$	Flux through the membrane	M/L^2-t
k	Time step in the controls sections	--
K^*	Controller gain	--
Ka_1	Acid dissociation constant of H_2CO_3 - HCO_3^-	--
Ka_2	Acid dissociation constant of HCO_3^- - CO_3^{2-}	--
Ka_3	Acid dissociation constant of H_3PO_4 - $H_2PO_4^-$	--
Ka_4	Acid dissociation constant of $H_2PO_4^-$ - HPO_4^{2-}	--
Ka_5	Acid dissociation constant of HPO_4^{2-} - PO_4^{3-}	--
K_{ARB}	Half maximum utilization rate of substrate for ARB	M/L^3
K_g	Plant gain	--

Symbol	**Description**	**Units**
$K_{h,inh}$	The inhibition factor (M/L^3) for species h	M/L^3
k_{hyd}	First-order hydrolysis-rate constant	t
K_{in}	Integral gain of the controller	--
K_La	Mass transfer coefficient	1/t
K_{pn}	Proportional gain of the controller	--
K_w	Acid dissociation constant of water	--
L	Length or thickness of the diffusion layer	L
L	Target loop transfer function (controls sections only)	--
L_f	Length or thickness of the biofilm	L
M	Mass	M
Me	Cumulative methane production from the BMP assay at time t	L^3
Me_{max}	Methane yield from BMP assay at the end of the incubation time	L^3
Mg	Constraint set of the controller gain	--
n	Number of electrons transferred as part of electrochemical reactions	--
N_c	Number of components in a system	--
N_{ca}	Number of negatively-charged components	--
N_p	The total number of complexes associated with component j	--
N_x	Number of complexes	--
$PCOD_{effluent}$	Effluent PCOD concentration	M/L^3
pH^*	Local pH	--
p_i	Concentration of complex i	M/L^3
$\widehat{P}_i$	Chemical formula for complex i	--
pH_{opt}	Optimal pH for bacteria	--
Q	Volumetric flow rate	L^3/T
q_1	Volumetric flow rate of HCl	L^3/T
q_2	Volumetric flow rate of H_2CO_3	L^3/T
q_3	Volumetric flow rate of H_3PO_4	L^3/T
q_4	Volumetric flow rate of NaOH	L^3/T
$\hat{q}X_f$	Maximum specific growth rate in the biofilm	M/L^3-t
R	Ideal gas constant	8.314 J/mol K
r_h	Reaction rate for component h	M/L^3-t
R_{Ohmic}	Cell Ohmic resistance	$\Omega\ L^2$
s	Laplace variable	--
S	Sensitivity of the target loop	--
$S_{h,inh}$	Substrate limitation function for component h	--
SA	Anode surface area	L^2
$SCOD_{effluent}$	Effluent COD concentration	M/L^3
t	Time	t
T	Temperature	T
$TCOD_{effluent}$	Effluent TCOD concentration	M/L^3

Symbol	**Description**	**Units**
Ts	Plant time constant	--
Tsen	Complementary sensitivity of the target loop	--
u	Plant input	--
V	Volume	L^3
Vol	Volume	L^3
W	Range of functional pHs for bacteria	--
W_a	Charge quantity to calculate charge balance	M/L^3
W_b	Concentration of carbonate ions	M/L^3
W_c	Concentration of phosphate ions	M/L^3
x	Spatial coordinate	L
y	Plant output	--
z_k	Charge of ion k	--

KEYWORDS

Microbial electrochemistry
Blackwater
Graywater
Wastewater treatment
Hydrogen peroxide
Cathode catalysts
Overpotentials
pH control
Potentiostat control
Hydraulic retention time (HRT)
Volatile solids (VS)
Primary sludge
Microbial peroxide producing cell (MPPC)
microbial fuel cell (MFC)
Anode-respiring bacteria (ARB)
Process control
Life-cycle analysis
Forward operating bases
Pilot-scale design

ACKNOWLEDGEMENTS

The lead investigators would like to acknowledge many people that contributed to this project and the body of knowledge that was generated. At Arizona State University, the main body of work was achieved through the efforts of three graduate students: Rakesh Joshi, Dr. Dongwon Ki, and Michelle Young. The leadership of research scientists Dr. Prathap Parameswaran and Dr. Sudeep Popat was also crucial to achieve the project goals. Through the 5 years of the project, the research scientists and graduate students mentored several other researchers, many of them volunteers, that provided significant contributions to the research presented. These include: Tabarak Abdelhabib, Nadrat Chowdhury, Francisco Brown-Muñoz, Emily Garver, Rick Kupferer III, Mikaela Links, Emily Garver, Scott Shearman, and Julia Thompson. A major part of the lead team's goals is to educate future engineers; we want to thank the SERDP team for providing the opportunity to impact many students at different levels.

We also acknowledge the work performed by the Honeywell team, particularly Bill Sheridan and Sachi Dash, who provided their expertise in various parts of the project. At CDM Smith, we acknowledge the work of Michaela Bogosh, Marco DeLiso, Brad Devins, Oscar Del Olmo, Ralph Frye, Josh Goldman, Engin Guven, Tung Nguyen, Eva Opitz, and Matt Schultz. This team provided their expertise to develop the final designs and life-cycle analyses for the project.

1. ABSTRACT

Objectives. The overarching goal of our study is to develop a novel energy-neutral wastewater treatment technology that could aid in water reuse within a forward operation base, reducing water transport. To achieve this, we developed a microbial fuel cell capable of generating hydrogen peroxide as primary product. This technology takes advantage of the high-energy content of blackwater; the microbial fuel cell consumes and converts it into an electrical current that is used to generate significant amounts of hydrogen peroxide. The hydrogen peroxide can have several uses: (1) direct treatment of graywater towards reuse, (2) tertiary treatment of graywater and/or blackwater, (3) odor control for blackwater, and (4) treatment of blackwater itself for better effluent quality and solids destruction.

More specifically, our objectives were to (1) show the feasibility of hydrogen peroxide production from blackwater, (2) achieve hydrogen peroxide production at high efficiency, and (3) demonstrate the effective treatment of blackwater at near energy-neutral conditions using a microbial fuel cell.

Technical Approach. We divided our approach into 8 Tasks aimed at achieving the objectives described. In **Task 1**, we studied the kinetics of microbial hydrolysis of organic solids and anode respiration in blackwater. This knowledge allowed us to define hydrolysis kinetic parameters, assess the efficiency of the microbial fuel cell treating blackwater, and develop mathematical models to predict treatment in **Task 2**. We developed a non-steady-state mathematical model, MYAnode, which integrates the chemical and biological processes in the bulk liquid of the microbial fuel cell with substrate utilization and current production in the anode biofilm.

The production of hydrogen peroxide at the cathode requires an optimization of materials that are suitable for this oxidant. In **Task 3**, we selected the best carbon-based materials for hydrogen peroxide at the cathode, anode materials with high surface area for current generation and blackwater treatment, and different membranes or separators between anode and cathode for their suitability when hydrogen peroxide is produced. In **Task 4**, we developed control strategies that will be useful for process optimization. Specifically, we focused on the development of anode or cathode potential control and the optimization of pH in the system. These strategies were implemented in microbial fuel cell prototypes in **Tasks 5 and 6**. We systematically characterized and reduced potential losses in microbial fuel cells through design optimization. We also optimized each part of the system by studying cathodic hydrogen peroxide production and blackwater treatment separately.

In **Task 7**, the microbial fuel cell prototypes were optimized to maximize effluent quality and hydrogen peroxide yields and rates of production. Two designs were tested, one in which hydrogen peroxide is collected for other uses and one in which the hydrogen peroxide is directly utilized to treat the blackwater. **Task 8** compiles the experimental results to develop an engineering design of a pilot-scale microbial fuel cell that produces hydrogen peroxide. The scope was expanded to include a life cycle assessment conducted in collaboration with SERDP project ER-2216.

Results. Comparisons on the operational conditions of microbial fuel cells fed with blackwater show that the hydraulic retention time (HRT) is an important parameter that controls its

performance. Semi-continuous operation achieved over 60% total chemical oxygen demand (TCOD) removal. The conversion of these solids to electrical current increased with shorter HRTs: 28%, 34%, and 32% for 12-, 9-, and 6-day HRTs, respectively, and methane fractions declined proportionally. A newly developed mathematical model, MYAnode, was able to predict similar behavior between methanogens and anode respiration, stressing the importance of pH and influent methanogens into the expected performance of the reactor. Based on these results, other studies focused largely on a 6-9 day HRT.

The study of cathode materials identified Vulcan carbon with a Nafion binder as the best catalyst for hydrogen peroxide production. Lower loadings of Vulcan carbon at ~0.45 mg/cm^2 were optimal to achieve the highest peroxide production over a wide range of cathode potentials. Membrane-stability tests identified AMI-7001as the most stable membrane in hydrogen peroxide conditions, making it ideal for further studies. Hydrogen peroxide stability in different buffers and pH values showed that high pH lead to a faster degradation rate, suggesting that operation at near neutral pH conditions at the cathode are desired. Based on this information, an adaptive pH controller was developed to control pH at the anode and cathode, taking into account the unpredictable variation of sludge alkalinity. Experimental results with the direct adaptive pH controller adapt reasonably well to the gain changes in the plant with the operating points and with the change in buffering capacity.

The development of an efficient microbial fuel cell prototype began with a characterization of potential losses and approaches to alleviate them. Cathodic pH was again responsible for 0.344 ± 0.019 V loss in the system, and the addition of CO_2 in the cathodic air removed most of this loss. Hydrogen peroxide production was tested as a function of air flow rate, cathodic HRT, buffer concentration, and the addition of EDTA as stabilizer using acetate as electron donor. The maximum concentration achieved was 3.1 ± 0.37 g H_2O_2 L^{-1} at a 4-h HRT and a 37% cathodic efficiency, while the highest rate of production was 57 g $L_{cathode}^{-1}$ d^{-1} at a 1-h HRT and a 78% cathodic efficiency. These efficiencies and concentrations are much higher than what is required for graywater tertiary treatment and other uses. However, upon using primary sludge as surrogate for blackwater, current densities were significantly lower and the same reactor design yielded a maximum of 0.23 g H_2O_2 L^{-1}. On the other hand, the use of hydrogen peroxide for the treatment of the sludge itself led to an effluent quality similar to that of class B biosolids, with a 55% volatile suspended solids removal and $1.2 \times 10^5 \pm 1.2 \times 10^4$ most probable number (MPN) fecal coliforms.

Through the kinetic and design parameters developed, we developed an engineering design specifically focused on a pilot-scale system that can be demonstrated under ESTCP that takes into account the materials selected and an adequate size for blackwater treatment.

Benefits. Our research not only demonstrates the feasibility to produce hydrogen peroxide from blackwater using a microbial fuel cell, it shows that high rates and production efficiencies are possible. The microbial fuel cell efficiently treats the blackwater with or without the aid of the hydrogen peroxide produced. However, higher quality and rates are achieved through the aid of hydrogen peroxide. The development of this technology can change approaches at forward operating bases and at municipal wastewater treatment plants by having an in situ chemical production of a strong oxidant for treatment.

2. OBJECTIVES

US forward operating bases (FOBs) are often burdened by water transport and wastewater treatment (WWT) and disposal. According to current estimates, approximately 80% of the delivery trucks for an FOB deliver water or haul wastewater away (Noblis, 2010). Thus, water and wastewater transport becomes a major burden to the military's budget due to the high cost of fuel in remote FOB locations. To avoid the costs and risks, the military must develop a reliable WWT that focuses on water reuse and is energy neutral or positive.

Traditional municipal WWT processes include a combination of aerobic and anaerobic process with dilute waste streams; however, microbial anaerobic treatment of wastewater can provide an energy efficient alternative for high strength wastes, such as blackwater (BW). Anaerobic treatment provides three major benefits: the electrons contained in the waste are consumed by microorganisms and converted into a form of energy that is readily used for human activities (e.g., hydrogen (H_2), methane (CH_4), electricity), but omits energy-intensive aeration processes used during traditional aerobic WWT (Rittmann and McCarty, 2001; Tchobanoglous et al., 2004). In addition, the anaerobic processes promote the solubilization of solids present in BW via the process of hydrolysis, reducing the amount of sludge for disposal. FOBs provide a perfectly concentrated BW stream for anaerobic processes: the average soldier produces ~0.5 pounds of chemical oxygen demand (COD) per day as BW (Barth et al., 1992) present in a low amount of water (6 gal/day; Noblis, 2010). Additionally, the BW is a slurry of ~1% solids that needs to be hydrolyzed and stabilized before disposal.

While several anaerobic treatment technologies exist, the microbial fuel cell (MFC) is one the most innovative and promising technologies (Rittmann et al., 2008; Torres, 2014). MFCs achieve a high degree of COD stabilization in wastewater because of the fast growth kinetics of anode-respiring bacteria (ARB) (Torres et al., 2008; Torres et al., 2010) due to the higher energy gain during anode respiration. This allows ARB to achieve treatment goals and reduce the reactor footprint in an FOB.

In our approach, we used the electrical current generated in an MFC to produce hydrogen peroxide (H_2O_2) at the cathode, which we termed a microbial peroxide producing cell (MPPC). A strong oxidant, H_2O_2 is a used in WWT with the Fenton process or combined with ultraviolet (UV) light to produce free radicals to achieve tertiary treatment and disinfection of graywater (GW; Snyder et al., 2008). H_2O_2 can also serve as a disinfectant or applied to accelerate or enhance oxidation of organics in BW. The conventional H_2O_2 production method, the anthraquinone oxidation (AO) process, is energy-intensive. Moreover, anthraquinone and its derivatives are potential carcinogens (Campos-Martin et al. 2006; Hart and Rudie 2014). Thus, an *in situ* production of H_2O_2 can reduce costs and provide sustainable WWT at FOBs moving towards a GW reuse scheme.

Our proposed MPPC system has BW treatment and H_2O_2 production as the primary objectives, with power generation as a secondary benefit. We developed two types of MFC focusing on hydrolyzing and stabilizing the solids contained in BW, while providing H_2O_2 production. The H_2O_2 was used to either treat the BW or collected to treat the GW stream. The advantages of this technology over current technologies used at FOBs (aerated lagoons, activated sludge, burn pits, off-site disposal, etc.) are:

- It decreases treatment costs and energy consumption due to minimizing aeration.
- It makes waste treatment energy neutral or positive.
- It has a compact design due to the use of a high-efficiency ARB-biofilm system.
- It provides on-site production of a water disinfectant/oxidant (H_2O_2) suitable for water reuse.

To further the development of MPPCs for BW treatment, we studied the kinetics of microbial oxidation of complex organic solutes and solids in MPPCs, found adequate materials for MPPC construction, and improved the MPPC design to meet FOB treatment requirements. The primary objective of this project is to conduct applications-driven research in order to design a practical MFC for the treatment of BW and concomitant production of H_2O_2. Specifically, our objective is to provide mechanistic understanding and design specifications needed to develop a field-scale MPPC for a follow-on Environmental Security Technology Certification Program (ESTCP) project; our research strategy is designed with this future transition in mind. The five specific objectives for our project are:

1. Study the kinetics of microbial hydrolysis of organic solids and anode respiration in BW - Our first objective is to develop scientific knowledge required to understand the kinetics of an MFC treating complex organics and solids found in BW. This knowledge allowed us to define hydrolysis kinetic parameters in an MFC, assess the efficiency of the MFC treating BW, and develop mathematical models to predict treatment.

2. Test various materials that are suitable for an MPPC producing H_2O_2 from BW - The production of H_2O_2 at the cathode requires an optimization of materials that are suitable for this oxidant. We tested carbon-based materials that will optimize H_2O_2 production at the cathode, anode materials with high surface area for ARB growth while treating BW, and different membranes or separators between anode and cathode for their suitability when H_2O_2 is produced. Our objective is to find the optimal materials for this application.

3. Design a process-automation system that will enhance the operation of MPPCs for field application - A process-automation system is crucial to the operation of the MPPC. FOBs must be able to maintain the excellent performance of the treatment facility without highly skilled labor. We studied key components of the control system to include dynamic simulation, sensing, data acquisition, monitoring, operator interface, controls, and optimization for the MPPC.

4. Design, build, and test lab-scale prototype MPPCs for H_2O_2 production - Our main research focused on the development of MPPC prototypes that will allow us to optimize its operation in a laboratory setting. We evaluated MPPC designs able to achieve a range of COD removals at the anode while producing H_2O_2 at the cathode. We evaluated two distinct types of MPPC configurations: (a) an MPPC in which H_2O_2 is produced at the cathode and collected for eventual use in GW treatment and MPPC-effluent polishing and (b) an MPPC in which H_2O_2 is produced at the cathode and fed to the BW to accelerate COD oxidation (Figure 1). These two configurations can be used separately or in concert in an FOB.

5. <u>Synthesize the knowledge into a preliminary design of a field-demonstration unit to be demonstrated under ESTCP</u> - Synthesizing the results from the above objectives, we developed design and operating criteria for an MPPC that is suitable for field demonstration. We also developed a life-cycle assessment tool to compare this MPPC to other MFC application and conventional WWT.

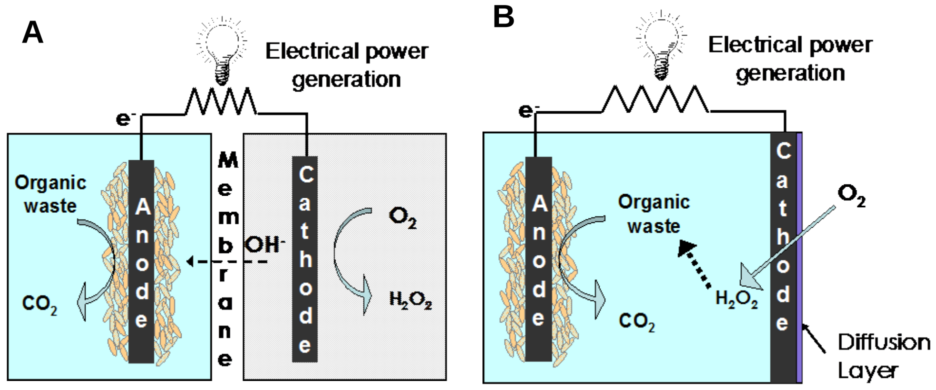

Figure 1. Schematics of MPPCs producing H_2O_2 from organic wastes. (a) Dual-chamber MPPC producing and collecting H_2O_2 in a cathode chamber. (b) Single-chamber MPPC directly oxidizing organic waste using H_2O_2 produced at the cathode.

3. BACKGROUND

Wastes containing high concentrations of organic solids, such as primary and waste activated sludge, BW, and livestock manure, offer high potential for energy recovery. These wastes can be stabilized using anaerobic digestion (AD) that produces CH_4, which is combusted to heat digesters and buildings or to generate electrical power (McCarty et al., 2011). MFCs, a new anaerobic biotechnology, convert organic compounds to electricity or other valuable products, e.g., hydrogen peroxide (Rittmann et al., 2008a; Rozendal et al., 2009; Torres et al., 2010; Young et al. 2016). Domestic and animal wastewaters and landfill leachate have been tested for MFC feasibility (Liu et al., 2004; You et al., 2006; Mahmoud et al., 2014).

Inside an MFC, ARB catalyze the conversion of organic matter directly into electrical current. ARB form a biofilm on the surface of an electrode (the anode) and transfer electrons to the anode produced during oxidation of a variety of organic materials, such as glucose, ethanol, acetic acid, wastewater, animal wastes, and others (Torres et al., 2007; Fornero et al., 2010; Pant et al., 2010). The removal of the electrons is what allows an MFC to stabilize the COD in the influent wastewater. The electrons must pass through a circuit, where energy is drawn, before they finally reach the cathode, where they reduce O_2. While the typical cathode product is H_2O to maximize electricity production, in order to reduce O_2 to H_2O effectively, a metal catalyst (usually platinum) is needed (Logan et al., 2006). These metal catalysts are expensive and can be irreversibly inactivated by compounds binding to the catalyst surface (U.S. DoE, 2004).

An alternative product at the cathode is reduction of O_2 to H_2O_2. Simple carbon cathodes, which are less expensive and less prone to inactivation, can efficiently carry out the 2-electron transfer in whom H_2O_2 is the final product: $O_2 + 2e^- + 2H^+ \rightarrow H_2O_2$. H_2O_2 production at the cathode provides is an alternate product with major advantages. A trade off to reduced cost and better cathode longevity is that the production of H_2O_2 at the cathode yields less energy than the complete O_2 reduction to H_2O: ~0.6 V for O_2 reduction to H_2O_2, versus ~1.1 V for O_2 reduction to H_2O.

H_2O_2 produced in an MPPC may turn out to be a more useful output in the wastewater-treatment setting than the more commonly studied outputs: electrical power in a microbial fuel cell (MFC) or H_2 gas in a microbial electrolysis cell (MEC). H_2O_2 is a useful chemical in WWT due to its strong oxidizing properties. H_2O_2 can be used in the Fenton process or be combined with UV for generation of free radicals to achieve tertiary treatment and disinfection of wastewater. The conventional method for H_2O_2 production, the AO process, is energy-intensive. Moreover, anthraquinone and its derivatives are potential carcinogens. Thus, an *in situ* approach using MPPCs can minimize energy and costs associated to the production and transport of this harmful chemical to an FOB. The H_2O_2 concentrations generated by an MPPC can also be well-suited for on-site use within a wastewater-treatment facility: e.g., cleaning membranes, tertiary treatment, reducing odors, pre-treating sludge or wastewater, and post-treating sludge.

Table 1. H_2O_2 production in MECs as reported in literature. All reactors were dual-chamber systems.

Authors	Cathode setup	Membrane type	Cathode HRT (h)	Anolyte/ Buffer	Catholyte	Maximum H_2O_2 concentration (g/L)	Maximum current and power/voltage applied	Power input required (W-h/g H_2O_2)
Arends et al. (2014)	Batch	AEM	4	Domestic and hospital wastewaters	50 mM NaCl	0.34	10 A/m^2 at 0.6 V	2.5
Chen et al. (2014)	Batch	3-D CEM	24	Domestic wastewater and 12 mM acetate media/50 mM PBS	50 mM $NaSO_4$	0.2	18.4 A/m^3 at 0.04V *produced*	0.09 *power output*
Fu et al. (2010)	Batch	CEM	3	Glucose media/50 mM PBS	50 mM $K_3Fe(CN)_6$ + PBS	0.08	0.2 A/m^2 at 0.4 V *produced*	0.06 *power output*
Li et al. (2016)	Continuous	CEM	0.023	12 mM acetate media/50 mM PBS	50 mM $NaSO_4$	8x10^{-5}	6.1 A/m^2 at 0.6 V	56
Modin & Fukushi (2012)	Batch	CEM	47	Acetate media	50 mM NaCl	5	2.5 A/m^2 at 3.8 V	2.3
Modin & Fukushi (2012)	Batch	CEM	21	Domestic wastewater	50 mM NaCl	0.08	0.4 A/m^2 at 0.9 V	1.8
Modin & Fukushi (2013)	Batch	CEM	21	6 mM acetate media/10 mM PBS	50 mM NaCl	9.7	1.7 A/m^2 at 11.8 V	3.0
Rozendal et al. (2009)	Batch	CEM	8	12 mM acetate media/190 mM PBS	50 mM NaCl	1.3	5.3 A/ m^2 at 0.5 V	0.93
Sim et al. (2015)	Batch	CEM	2-24	5 mM acetate media/50 mM PBS	Deionized water	1.4	7.7 A/m^2 at 1 V	2.6
Sim et al. (2015)	Batch	CEM	2-10	Raw domestic wastewater	Deionized water	0.15	0.56 A/m^2 at 6.3 V	28
Our study	**Continuous**	**AEM**	**4**	**Acetate media**	**200 mM NaCl**	**3.1**	**10.1 A/m^2 at 0.31V**	**1.1**

Given that water reuse is a major goal for operation of FOBs, the production of an on-site oxidant that can be used to improve the quality and utility of the water is an important ancillary benefit to the primary benefits of energy gain, cost, and longevity. According to our stoichiometric and efficiency calculations, an MFC producing H_2O_2 from BW can generate ~250 g H_2O_2/soldier-day. This generation is more than three times the H_2O_2 required to treat GW. We found 10 studies addressing H_2O_2 production in MPPCs, summarized in Table 1. Depending on the type of MPPC and its operation, the H_2O_2 concentration and production rate varied widely, from 8.5×10^{-5} to 9.7 g L^{-1} and from 7.9×10^{-4} to 18.6 g L^{-1} day^{-1}, respectively (Li et al. 2016; Modin and Fukushi 2013). Recent research on H_2O_2 production in MPPCs has focused on materials for cathodes and membranes as well as on improving oxygen diffusion to the cathode catalysts (Sim et al., 2015; Li et al., 2016). Most of these studies were carried out with synthetic medium (e.g., acetate or glucose) fed to the anode. H_2O_2 production with real wastewater has been reported in only four studies (Modin and Fukushi, 2012; Modin and Fukushi, 2013; Arends et al., 2014; Sim et al., 2015). Compared to synthetic medium (mostly acetate) as the substrate for the microbial electrochemical cell anode, H_2O_2 production with real wastewater was lower in terms of concentrations produced and the rates of production, and energy inputs were notably high (>2 kWh per kg H_2O_2). The deficiencies in performance reflect on the importance of reactor design and operation to improve voltage efficiency (Popat and Torres, 2016; Ki et al., 2016). Also, cathodic H_2O_2 production efficiency (PPE), which is the fraction of electrons used and measured as H_2O_2 generation to the electrons captured as Coulombs, was variable, ranging from 5% to 70% (Modin and Fukushi, 2012; Modin and Fukushi, 2013; Arends et al., 2014; Sim et al., 2015).

MPPC operation requires additional design considerations depending upon the final use of H_2O_2. Since H_2O_2 is a strong oxidant, the reactor materials need to demonstrate long term resistance to degradation from H_2O_2 exposure. Prior to this project, there was no investigation into the compatibility of common MFC materials with H_2O_2. To effectively capture H_2O_2, the anode and cathode are separated by a device capable of transferring protons (H^+) or hydroxide ions (OH^-) (Figure 1a); most MFC studies use a proton electrolyte membrane for this purpose (Logan et al., 2006). Although O_2 is required to run an MFC, its operation does not require pumping air into the wastewater. Instead, O_2 reaches the cathode through passive aeration from the air in contact with the cathode. Thus, aeration costs are greatly minimized, helping make WWT energy neutral or positive and more cost effective.

Our research team at ASU has worked extensively with the MFC technology, focusing on fundamental biofilm modeling (Marcus et al., 2007, 2010, 2011), managing microbial communities at the anode chamber of MFCs (Parameswaran et al., 2009, 2010, 2011; Miceli et al., 2012, 2014; Badalamenti et al., 2013), ARB kinetics and thermodynamics (Lee et al., 2008; Torres et al., 2007, 2008a, 2008b, 2010; Yoho et al. 2014, 2015; Lusk et al., 2015, 2016, 2017), and reactor design and process optimization (Lee et al., 2009, 2010; Ren et al., 2014; Ki et al., 2016). Similarly, our experiences allowed us to construct and design MFC reactors using comprehensive MFC models (Marcus et al., 2010; Popat et al., 2014) that optimize our design *in silico* before actual implementation.

We used this background knowledge to study, design, and optimize MPPCs as a novel technology for FOB applications. Our proposed work was organized into 8 Tasks, organized within the 5 objectives/aims discussed above. Figure 2 shows a schematic of our various Tasks and how they are integrated. Our report is organized based on these Tasks and we give a short background of their importance below.

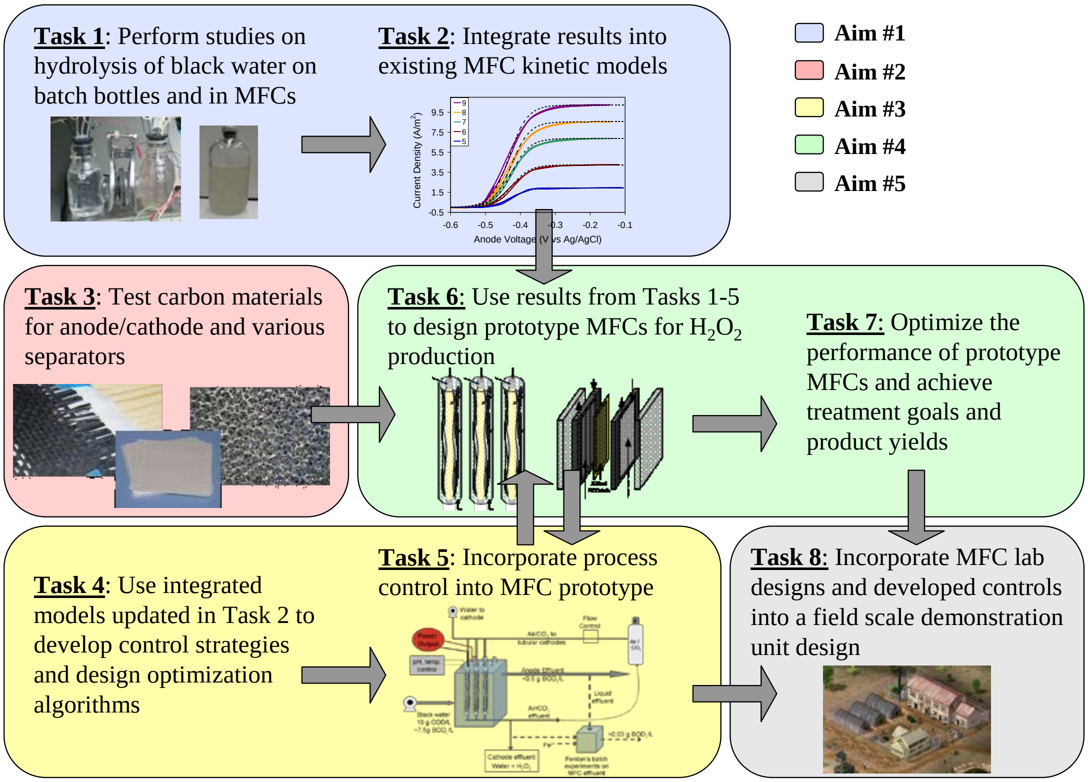

Figure 2. Schematic of Tasks in our research, their relationships within each other, and relevance within our Objectives/Aims.

Task 1 – Perform studies on hydrolysis of blackwater

While the BW generated is a readily accessible source of organic solids, a major bottleneck to use BW for energy recovery is the slow hydrolysis of particulate organics (Rittmann and McCarty, 2001; Ristow et al., 2006; Cokgor et al., 2009). Approaches such as two-stage AD – hydrolysis followed by methanogenesis (Ghosh, 1987; Bhattacharya et al., 1996; Ghosh et al., 1995) and various pretreatment methods (e.g., mechanical, thermal, alkaline, ultrasonication, and microwave) have been evaluated for several decades as a means to accelerate hydrolysis to improve CH_4 generation and solids destruction (Cho et al., 2012; Eskicioglu et al., 2006; Kim et al., 2003; Park et al., 2004; Pilli et al., 2011). In our studies in this Task, we used municipal primary sludge as a surrogate to BW, investigated the hydrolysis rates as a function of various pretreatments in batch methanogenic bottles and MFC reactors, and determined the minimum retention times in the MFCs that would allow effective solids destruction and sludge stabilization. Since ARB are significantly faster than methanogens at consuming volatile fatty acids (VFAs) (Torres et al. 2010), we hypothesized that hydrolysis rates will be the rate-limiting step in a well-designed MPPC.

Task 2 – Integrate results into MFC kinetic models

To date, few mathematical models have been developed to describe and predict MFC performance with complex substrates like wastewater (Sedaqatvand et al. 2013). When describing phenomena in the anode chamber, models must address a large range of scales, from micrometers to meters. For larger scale applications, the basic concepts applied in WWT plant models are applicable for bulk solutions at MFC anodes: The anode chamber of a MFC involves metabolic processes also present in AD and AD models, including hydrolysis and fermentation, as well as extracellular electron transfer (EET) mechanisms as part of ARB respiration to an anode.

Mediator-less EET as modeled by Marcus et al. (2007, 2010, 2011) has become the standard for describing high-performance biofilm anodes. Marcus et al. (2007) introduced the Nernst-Monod model, which represents ARB kinetics and EET using a unique form of steady-state, dual-limitation kinetics. While the Nernst-Monod model includes the normal Monod equation for the donor concentration, it exploits the Nernst equation to represent the acceptor "concentration" via the anode potential, and it explicitly allows for electrical conduction of electrons to the anode surface. The Nernst-Monod model was combined with mass balances and diffusive transport to describe current production in conductive biofilms, and experimental studies (Torres et al., 2009) confirmed the validity of the Nernst-Monod model for conductive biofilms dominated by *Geobacter sulfurreducens*.

Marcus et al. (2010, 2011) developed PCBIOFILM, a steady-state, one-dimensional (1D) model that couples the Nernst-Monod model and diffusion with pH calculations, electrical neutrality, and ionic migration. Within PCBIOFILM, Marcus et al. utilized CCBATCH, a modeling platform that incorporates kinetically controlled biological reactions with much faster pH and chemical speciation reactions using the proton condition (PC) (VanBriesen and Rittmann 1999). Utilizing the CCBATCH platform and the PC was especially important because of the large production rate of H^+ during the ARB's anode respiration.

Over the last five years, several models of the MFC anode chamber have expanded upon Marcus et al. (2007, 2010, 2011) to describe phenomena ranging from heat transfer due to EET to the molecular mechanisms of EET. Several researchers developed more detailed models of EET combined with biofilm formation, including mass balances on intracellular EET between redox mediators in ARB (Pinto et al. 2010, 2011), intracellular flux modeling of H^+ and electrons from the cell (Jayasinghe et al. 2014), and intra- and extracellular EET based on metallic-like conductivity through the biofilm (Korth et al. 2015). However, these models omit pH, which several works have demonstrated pH inhibition in ARB biofilms (Torres et al., 2008, Franks et al. 2009). Most models only include simple substrates like acetate or glucose, which are not realistic for real-world applications that involve complex organics. Furthermore, no model accounts for the formation of extracellular polymeric substances (EPS) and soluble microbial products (SMP), which can divert as much as 24% of the electron flow from cellular maintenance energy and synthesis (Noguera et al. 1994; Laspidou and Rittmann 2002a; Ni et al. 2010; Xie et al. 2012).

In this Task, we developed a non-steady-state mathematical model, MYAnode, which integrates the chemical and biological processes in the bulk liquid with substrate utilization and current production in the anode biofilm. MYAnode combines CASADM, a comprehensive WWT modeling software (Young et al. 2013b); CCBATCH, which combines rapid chemical speciation reactions with slower biological reactions (VanBriesen and Rittmann 1999); and PCBIOFILM, which describes the chemical, biological, and transport mechanisms within the ARB biofilm affecting current production (Marcus et al. 2010; Marcus et al. 2011). Using MYAnode, we explore the interactions between ARB and other anaerobic communities by varying operating parameters -- like hydraulic retention time (HRT) and oxygen intrusion -- to determine their effects on the MFC performance.

Task 3 – Test carbon materials for anode/cathode and various separators

The optimization of materials is a crucial part of the development of MPPCs. For the anode of these prototype MPPCs, carbon fibers with high specific surface area are used to grow ARB, as we have tested before (Ki et al., 2015; Ki et al., 2016).

Several abiotic studies (Otsuka and Yamanaka 1990; Yamanaka et al. 2003, Rabaey and Rozendal 2010) have demonstrated that H_2O_2 rapidly decomposes to H_2O when exposed to platinum-carbon catalysts via

$$H_2O_2 + 2e^- + 2H^+ \rightarrow 2H_2O \qquad (E = +1.778\ V_{SHE}) \qquad \text{(Eqn. 1)}$$

While carbon-based electrodes can achieve high H_2O_2 concentrations and current efficiencies (Otsuka and Yamanaka 1990; Foller and Bombard 1995; Yamada et al 1999; Li et al. 2016), they can also degrade the H_2O_2 to H_2O, particularly when the catalyst layer is thick.

The strong oxidant property of H_2O_2 further complicates MPPC design. H_2O_2 and its ions and radicals present chemical incompatibility problems with the materials typically used in MFCs, including catalysts, binders, and membranes, which concurrently results in H_2O_2 decomposition. Until now, research has not been performed to determine the compatibility of typical MFC materials with H_2O_2 and at high pH. Our work in Task 3 outlines a methodology for testing materials and designing MFCs for H_2O_2 production. We evaluated various membranes, cathode materials, and catholytes for H_2O_2 compatibility. We then apply our learnings to design and operate a continuous-flow cathode in a flat-plate MPPC to obtain a good balance of H_2O_2 concentration and a low power input.

Task 4 – Use integrated models to develop control strategies and design optimization algorithms

A process-automation system is important to the reliable operation of the MFC. In this Task, we developed control strategies that will be useful for process optimization. Specifically, we focused on the development of anode or cathode potential control and the optimization of pH in the system.

pH Control

pH can be an important source of overpotential in MPPCs. When the pH in the cathode chamber increases one unit at standard temperature and pressure, the MPPC incurs a ~60 mV drop in voltage based on the Nernst equation at standard temperature and pressure (Bard and Faulkner 2001). Because media for ARB is at their optimal pH of 7.0 (Lee et al. 2008), a pH 12 cathode incurs ~300 mV of concentration overpotential between the cathode and anode. Cathodic pH control is confounded by H^+ consumption during H_2O_2 synthesis via Eqn. 1, increasing cathodic pH and overpotential. Thus, strategies to reliably control pH in MPPCs are most crucial for their development.

pH control also plays an important role in various industrial processes, including WWT, biotechnology processes, and electrochemical cells. Because of its highly nonlinear nature and dependence on exogenous signals (e.g., time-varying buffer concentrations), pH control of a WWT process is a challenging process control problem. These characteristics also make it a benchmark problem to test nonlinear controllers (Alvarez et al., 2001). The nonlinear nature of the process implies that linear controllers are ineffective to control pH over a wide range and the time-varying nature of certain problems make it futile to control even around a given pH value (Joshi et al. 2014a, 2014b) While there are different versions of nonlinear controllers proposed (Al-Duwaish and Naeem, 2001; Henson et al., 1994), Henson et al. showed that nonlinear control algorithms fail to compensate the time-varying behavior due to changes in buffering capacity, making adaptive control as the best-suited solution.

Adaptive control is an extensively researched area with many control schemes reported in the literature; different versions of adaptive control schemes have been proposed for pH control (Gnoth et al, 2009; Peymani et al., 2008; Boling et al., 2007). Task 4 focuses on a new adaptive control strategy to address the problems that arise during practical implementations for WWT. A key instrument in the proposed solution is the usage of the normalized metrics that describe the gain of a suitable error operator, instead of the more customary signal errors often used in adaptive control that are prone to mis-adjustment under weak excitation conditions.

The experimental portion of this work was geared towards the development of an adaptive pH control algorithms that can be readily extended to pH control of an MPPC anode. The experimental setup with high retention time and variable buffer flow mimics the MPPC anode. In the MPPC problem, pH is only available measurement but the process gain depends also on the buffering capacity of the system. As a result, scheduling based only on the pH measurement is not sufficient to compensate for time-variations in the buffers.

Potential control

The anode potential plays an important role in the operation of an MPPC (Fu et al., 2010; Rozendal et al., 2009) and a potentiostat is a device that helps in controlling electrode potentials at their desired values. Commercially available analytical grade potentiostats are expensive with the cost of one unit around $6000. Analytical grade potentiostats are widely used in research labs, and offer excellent control performance, which is often an “overkill” for an industrial application. They are rarely used in the field because the practical limitations on performance (noise, disturbances) do not justify their high cost and large size. In the recent past, some researchers have proposed low-cost potentiostat alternatives (Friedman et al., 2012; Pandiaraj et al., 2014). These potentiostats use Op-amps to drive potentials of the cell and use analog to digital (A/D) and digital to analog (D/A) channels of an embedded micro controller to measure or to adjust set-points. Some drawbacks of these potentiostat designs are their low current rating and low measured signal accuracy. In this Task, we developed a low-cost potentiostat solution that can deliver high current and can read electrode potentials with higher accuracy as compared to other low-cost solutions. We tested our potentiostat and compared it against an analytical grade potentiostat (BioLogic Science Instruments-VMP3). It is shown the proposed potentiostat results in a performance comparable to BioLogic Science Instruments-VMP3 potentiostat.

Task 5 and 6 – Design prototype MFCs for H_2O_2 production and incorporate process control systems

Several different aspects of MFC processes have shown major progress in the last few years, including understanding EET in ARB (Malvankar et al., 2011; Bond et al., 2012; Pirbadian et al., 2012, Yoho et al., 2014), managing microbial communities to achieve high Coulombic efficiencies (Parameswaran et al., 2009; Kiley et al., 2011; Sun et al., 2012), and developing new, cheaper materials for electrodes and separators (Liu et al., 2014; Hoskins et al., 2014; Zhang et al., 2010). However, one of the major limitations still hindering the application of MFCs is their low voltage efficiency (Harnisch and Schroder, 2010; Rabaey and Rozendal, 2010). In the case of MFCs, a theoretical maximum of 1.1 V is available when coupling acetate oxidation at the anode to O_2 reduction at the cathode. Yet, at current densities of >5 A m^2, potential losses of as much as 0.8 V are observed (Sun et al., 2012; Hoskins et al., 2014; Torres, 2014). Such large potential losses are in stark contrast with most other fuel cells, where orders of magnitude higher current densities are possible (Wang et al., 2011; Ursúa et al., 2012). Thus, there is a need to consider design and operation tactics for MFCs that help reduce the overall potential losses in the system.

Potential losses in electrochemical systems are always classified into three major types: activation, Ohmic, and concentration overpotentials (Chen, 2013). Activation overpotential is related to the activation barrier for a given electrochemical reaction, and the properties of the catalysts in overcoming the activation barrier. Cathode activation overpotential relates to the energy loss at cathode during reduction of O_2 to water or H_2O_2 in MFCs. Ohmic overpotential is related to the transport of ions between the anode and the cathode, and depends on the conductivity of the electrolyte. MFCs generally employ low conductivity solutions in ARB growth media or wastewater solution, producing high Ohmic overpotential if the distance between the two electrodes is large. To reduce Ohmic overpotential, it is imperative to reduce the distances between the anode and the cathode, as previously suggested by many other studies (An and Lee, 2013; Pham et al. 2006; Liu and Logan, 2004). Concentration overpotential is related to Nernstian and activation losses resulting from not being able to maintain the concentrations of reactants on the electrode surface as well as not removing products from the electrode surface at a fast-enough rate. the most common form of concentration overpotential in MFCs is due to a pH imbalance that results between the two electrodes when using a membrane to separate the electrodes (Rozendal et al., 2006; Torres et al., 2008b). As mentioned earlier, for every pH unit the cathode pH is higher than the anode pH, a Nernstian concentration overpotential of ~60 mV results, significantly increasing system overpotential

In this Task, we systematically characterized and reduced overpotentials in MFCs through design optimization. We started with a logical design that reduced distance between the anode and the cathode and employed high surface area electrodes. Based on the characterized individual overpotentials, we systematically modified the materials and the operating conditions to reduce the overall overpotential. In this work, we also studied the importance of pH and potential control in order to maintain a better MFC performance.

Task 7 – Optimize MFC prototypes to achieve treatment goals and product yields
Using the MPPC designs developed in previous tasks, we focused on process optimization of various operating conditions to maximize effluent quality and H_2O_2 yields and rates of production.

From a cathodic perspective, most MPPC research has focused more on optimization of one or two variables, rather than a systematic investigation of factors affecting H_2O_2 production, net energy demand, and reactor design. Fu et al. (2010), Modin and Fukushi (2013), Arends et al. (2014), and Sim et al. (2015) focused on maximizing H_2O_2 production from different wastewater sources at different anode and cathode HRTs. Modin and Fukushi (2012) and Chen et al. (2014) focused on designing cathode catalysts for H_2O_2 production. Li et al. (2016) had a continuous-flow cathode, but focused primarily on optimizing abiotic catalyst performance. In Task 7, we combined our learnings from membranes, cathode materials, and catholytes testing to design and operate a continuous-flow cathode in a flat-plate MPPC to obtain a good balance of H_2O_2 concentration and a low power input. We optimized the reactor design to address the main operational parameters that influenced our goals: anodic HRT, cathodic HRT, cathodic potential and pH were the main operational parameters that influenced our goals. The two options discussed in Figure 1 (dual- and single-chamber MPPCs) are then evaluated in this Task using a similar prototype.

Task 8 – Engineering Design and Life Cycle Analysis
The original scope of Task 8 included engineering design of a pilot-scale MPPC based on laboratory results discussed in the preceding sections. The scope was expanded to include a life cycle assessment (LCA), which was conducted in collaboration with SERDP project ER-2216. Section 5.7.1 presents results of the engineering design specifically focused on a pilot-scale system that can be demonstrated under ESTCP. Section 5.7.2 presents the LCA approach for MEC systems at different FOB scales (company and battalion) as well as comparisons to conventional systems.

LCAs were conducted to quantify the environmental impacts over the useful life of different products, services, and activities. Combining LCA with economic analysis provides a holistic picture of both the environmental and cost burdens to facilitate effective FOB design. Results from the few LCAs that have been performed on MFCs indicate promising environmental benefit from their use over conventional technologies, such as anaerobic bioreactors (Foley 2010). Pant et. al. (2011) defined important factors to be included in a comparative LCA between MFC and conventional WWT technologies. Such benefits as electricity generation and use to operate the WWTP and chemical production are included in the boundary of the LCA so as to highlight benefits on these innovative technologies (Pant et al. 2011). We separated performance based on five critical design operational and design criteria for FOBs: chemical use, capital goods, energy use, sludge disposal, and transportation. The results of the LCA, when coupled cost and social impacts, provide a tiered approach to decision making.

4. MATERIALS AND METHODS

4.1. Studies on Hydrolysis of Blackwater (Task 1)

4.1.1. Batch methanogenic and fermentation reactors for hydrolysis on primary sludge

For Task 1 studies, we used primary sludge (PS) as surrogate of blackwaters in FOBs, and collected PS for this whole project from local WWT plants, Mesa Northwest Water Reclamation Plant (MNWWRP; Mesa, AZ) and Greenfield Water Reclamation Plant (GWRP; Gilbert, AZ). We also tested and compared pre-treatment technology (pulsed electric fields or PEF). We treated 30 liters of the PS in the PEF *alpha* unit (OpenCEL/Trojan Technologies, London, ON, Canada) located at the Biodesign Swette Center for Environmental Biotechnology (BSCEB) (Tempe, AZ). System and key process variables are described in previous studies (Lee et al., 2010; Salerno et al., 2009), and more details about PEF can be obtained at www.opencel.com. We maintained a sample conductivity of 0.175 mS/cm during PEF treatment. With a field-strength of 30kV, the treatment intensity (*TI*) was 33 kWh/m^3 (Salerno et al., 2009).

Reactor setup. Biochemical methane potential (BMP) tests were performed based on previous studies (Angelidaki et al., 2009; Owen et al., 1979). BMP reactors were set up with a 200-mL working volume in 250-mL serum bottles. Anaerobic digested sludge (ADS) from a well operating anaerobic digester in MNWWRP served as the inoculum after degassing in a 37°C shaker for four days. Triplicate control and PEF-treated PS samples were mixed with ADS in the volumetric ratio of 3:7 (ADS:sample), and buffer and nutrient supplements were added, as described in Angelidaki et al. (2009). Butyl rubber septa and aluminum caps were used for sealing the serum bottles after N_2-gas sparging for 10 minutes to establish anaerobic conditions. The bottles were incubated at 30°C on a shaker table (150 rpm). Negative controls contained the ADS and basal medium alone. CH_4 gas produced from the ADS inoculum was subtracted from the production from control and PEF-treated PS. The COD of the produced CH_4 was calculated from

$$1\ \text{mL CH}_4\ \frac{1\ \text{mmol CH4}}{24.86\ \text{mL}}\ \frac{8\ \text{meq e-}}{\text{mmol CH4}}\ \frac{8\ \text{mg COD}}{\text{meq e-}} = 2.57\ \text{mg COD at } 30\ °\text{C}$$

We performed three serial enrichments for PS fermentation with an ADS inoculum that was selectively inhibited for methanogenesis using 50 mM of 2–bromoethanesulfonic acid (BES) (Parameswaran et al., 2011). The first enrichment consisted of a 1:1 volume ratio of PS:ADS and was operated for 15 days, after which 10% of the reactor contents by volume were transferred to a subsequent serum bottle with PS for two more serial enrichments with batch operation times of 15-20 days. At the end of three serial enrichments for control or PEF-treated PS, we performed batch fermentation experiments with the enriched inoculum (10% v/v) for a period of 28 days and with 50 mM BES.

Determining the hydrolysis rate based on methane production. When hydrolysis is the rate-limiting step, the rate of CH_4 production in batch BMP tests can be used to estimate hydrolysis kinetics (Bolzonella et al, 2005; Pavlostathis and Giraldo-Gomez, 1991). First-order hydrolysis kinetics in terms of CH_4 production in a batch reaction is given by:

$$Me = Me_{max} [1 - \exp(-k_{hyd} t)] \qquad \text{(Eqn. 2)}$$

where Me= cumulative CH_4 production from the BMP assay at time t (mL)
Me_{max} = CH_4 yield from BMP assay at the end of the incubation time (mL)
k_{hyd} = first-order hydrolysis-rate constant (day^{-1})

Eqn. 2 provides an accurate representation of the BMP results when a) hydrolysis is the rate-limiting step, b) the maximum CH_4 production at the end of the batch tests (Me_{max}) represents the total concentration of hydrolysable COD at the beginning of the tests, and c) hydrolysis kinetics can be represented as first order in the concentration of hydrolysable COD.

Rearranging Eqn. 2 yields

$$\ln [1-\{Me/Me_{max}\}] = -k_{hyd} t \qquad \text{(Eqn. 3)}$$

which is a straight line with a slope whose magnitude is the hydrolysis rate constant (k_{hyd}). We obtained k_{hyd} by performing linear regression of $\ln [1-\{Me/Me_{max}\}]$ versus t.

Analytical methods. The amount of gas was measured with a frictionless glass syringe (PERFEKTUM, Popper and Son, NY) inserted into the septum until its pressure was equal to atmospheric. Gas composition was by sampling the gas phase using a 500-µL gas-tight syringe and performing gas chromatography and thermal conductivity detection (GC-TCD, GC 2010, Shimadzu) after separation on a packed column (Shincarbon ST 100/120, 2m, Restek, Bellefonte, PA). N_2 was the carrier gas with a constant pressure and flow rate of 5.4 atm and 10 mL/min, respectively. We employed temperatures of 120, 145, and 150 °C for injection port, column, and detector, respectively, and the current was 45 mA. Calibration was performed using an analytical grade gas standard (CH_4: CO_2: H_2 = 40%: 30%: 30%, Matheson Tri-Gas, Twinsburg, Ohio).
PS characteristics were assayed with total COD (TCOD), semi-soluble COD (SSCOD), total suspended solids (TSS), volatile suspended solids (VSS), NH_3-N, volatile fatty acids (VFAs), and soluble proteins. Semi-soluble (SS) means that COD analysis was performed on the permeate after filtration through a 1.2-µm glass-fiber filter (Whatman^{TM}, UK), as described in Lee et al. (2010). COD and NH_3-N were measured using HACH kits and spectrophotometer (DR2700, HACH, Loveland, CO). Soluble proteins were analyzed with the BCA method (Brown et al., 1989), using a BCA protein assay kit (Sigma-Aldrich, St. Louis, MO). Bovine serum albumin was used for the standard calibration curves of protein measurement. For VFAs analysis from the fermentation bottles, high pressure liquid chromatography (HPLC) was used for the separation of the acids, as described in Parameswaran et al (2009).

4.1.2. Continuous operations of fermentation reactors for microbial electrolysis cells

Fermentation set up and operation.

We started up fermentation reactors in batch mode and later switched them to semi-continuous mode for these experiments. Initially, we used a 3-day solids retention time (SRT = HRT) without any methanogen inhibitor. To improve hydrolysis of PS, we later increased the SRT to 15 days and operated with two different HRTs (6 and 3 days) by adding the appropriate amount of the concentrated solids back into the reactor after centrifugation. For example, we maintained a 15-day SRT and 6-day HRT by the following five steps: 1) remove 30 mL of mixed liquor from the 180-mL volume in the fermentation reactor (giving a 6-day HRT), 2) discard 18 mL, 3) centrifuge the remaining 12 mL (giving a 15-day SRT) at 3220 x g (Eppendorf Centrifuge 5810 R, USA), 4) mix the solids pellets with fresh PS to a total final volume of 30 mL, and 5) add the resultant PS mixture into the reactors.

MEC set up and operation. We used a flat-plate microbial electrolysis cell (MEC), the components of which are shown in Figure 3. The MEC had two anodes within a common anode chamber (0.3-0.35 L in volume) and two cathodes in two individual cathode chambers, 0.1-0.2 L each on either side of the anode chamber. The anodes were made of carbon fiber (24K Carbon Tow, Fibre Glast, OH, USA) woven into a titanium frame that was the current collector. The carbon fiber, already woven with the current collector before MEC assembly, was washed in the following order (An and Lee, 2013): 1 N nitric acid for 3 hours, 1 N acetone for 12 hours, 1 N ethanol for 3 hours, and finally 18 MΩ deionized water. The cathodes were stainless steel meshes (type 316, mesh 80 x 80, 0.0055” of wire diameter, McMaster-Carr, USA), and the separators were anion exchange membranes (AEM; AMI-7001, Membranes International, Glen Rock, NJ, USA). Each anode, cathode, and membrane has projected area was 100 cm^2, for a total of 200 cm^2 of projected area for the anode, the cathode, and the membrane.

For ARB acclimation, we inoculated the MEC with ADS (from MNWWRP) and the effluent from an MEC that has been continuously operated with acetate medium. The MEC anode was operated first with acetate medium in batch mode until the current was greater than 5 A/m^2. We then changed to continuous mode with acetate. The acetate medium consisted of 50 mM acetate, 100-mM phosphate buffer solution (PBS; 85% Na_2HPO_4 and 15% KH_2PO_4), 14 mM ammonium chloride, and trace minerals (Lee et al., 2008). The anode potential was poised -0.3 V (vs. Ag/AgCl) with a potentiostat (VMP3, BioLogic Science Instruments, Knoxville, TN) to create non-limiting conditions for ARB kinetics (Torres et al. 2008). After we operated the MEC with the acetate medium for two months, we allowed acetate to deplete in batch operation and changed the feed to the pre-fermented centrate. We conducted two batch runs with acetate prior to the control and PEF-treated centrate batch MEC runs to ensure that MEC anodes had similar conditions.

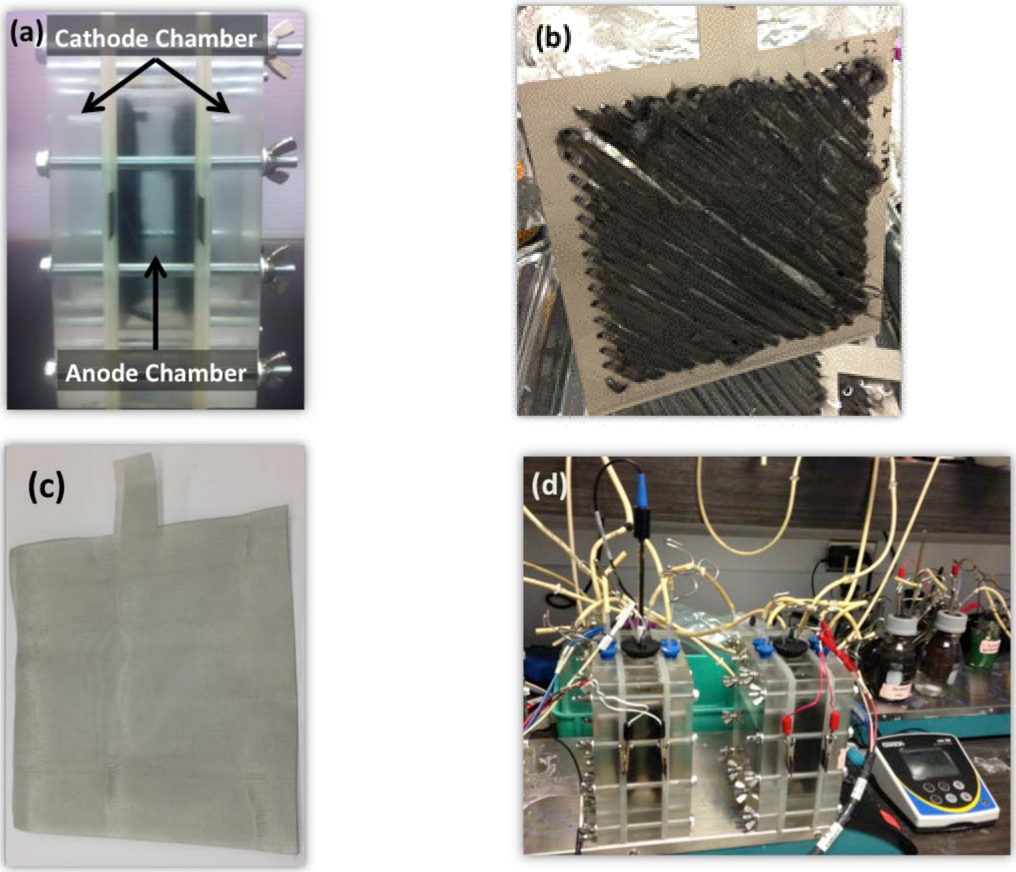

Figure 3. Pictures of flat-plate MECs. (a) Assembled MECs, (b) carbon fiber anode woven with titanium current collector, (c) SS cathode, and (d) MEC reactors equipped with a pH probe when fed with primary sludge.

Figure 4 is a schematic of the MEC experiments using fermented PS "centrate," which was generated by centrifuging (3220 x g) and then filtering (GF/C, Whatman®, UK) fermentation effluent. The centrate was composited for ~10 days to obtain enough liquid volume to be fed to the MEC anode chamber (~ 0.5 L). The centrate pH and alkalinity were ~6 and 300 mg/L as $CaCO_3$. Before being fed to the MEC, centrate pH was measured and adjusted to ~7 by adding sodium hydroxide. A pH probe was installed in the center of the anode chamber, and the pH was maintained between 6.5 and 8.5 with manual addition of sodium hydroxide or hydrochloric acid, as needed.

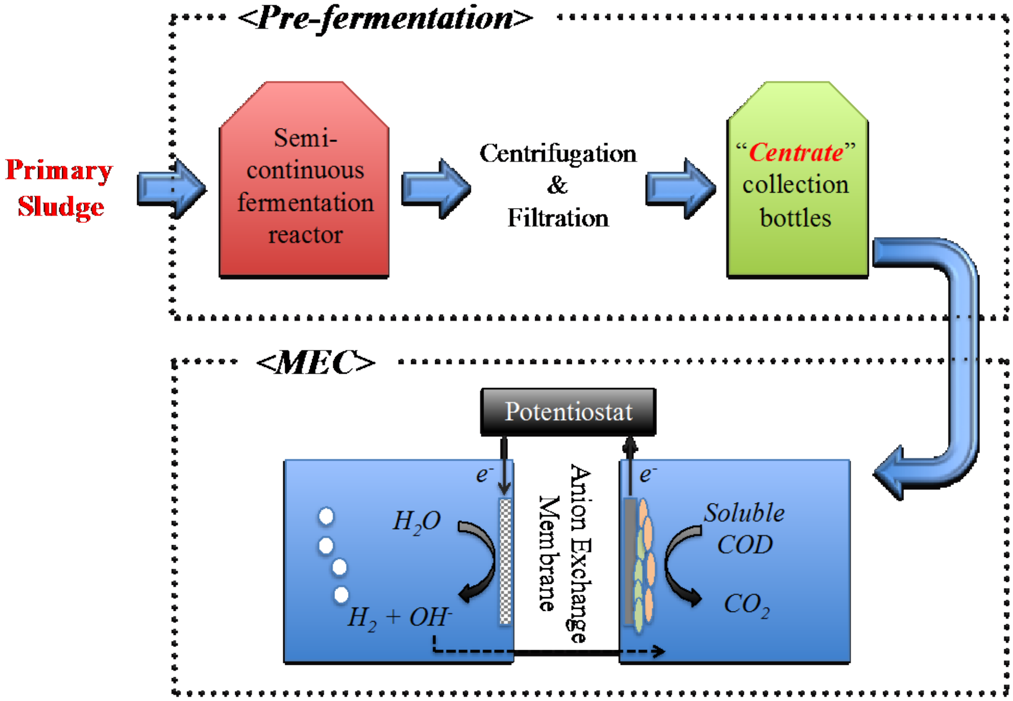

Figure 4. Schematic of the linkage between semi-continuous fermentation of PS and current capture from the fermentation centrate using an MEC.

Analytical methods. The volume of produced biogas was measured with a frictionless glass syringe (PERFEKTUM, Popper and Son, NY) by injecting it through the septum on the fermentation reactor and letting the gas pressure equilibrate with atmospheric pressure. Gas composition was analyzed with a gas sample taken with a 500-µL gas-tight syringe and using a gas chromatograph equipped with a thermal conductivity detector (GC-TCD, GC 2010, Shimadzu) and a packed column (Shincarbon ST 100/120, 2 m, Restek, Bellefonte, PA). N_2 was the carrier gas with a constant pressure and flow rate of 5.4 atm and 10 mL/min, respectively. Temperatures were 120, 145, and 150°C for injection port, column, and detector, respectively, and the current was 45 mA. Calibration was done with an analytical grade gas standard (CH_4: CO_2: H_2 = 40%: 30%: 30%, Matheson Tri-Gas, Twinsburg, Ohio).

PS characterization involved measuring TCOD, SSCOD, TSS, VSS, and VFAs as mentioned previously. COD was measured using spectrophotometric methods by HACH kit and spectrophotometer (DR0000, HACH, Loveland, CO). For the separation and quantification of VFAs from the fermentation experiments, an HPLC equipped with an AMINEX HPX-87H column was employed according to the conditions described in Parameswaran et al. (2009).

Calculations. The current density expressed in A/m^2 was calculated based on the projected area of the anode. Electron-equivalent mass balance on the fermentation reactors was expressed as mgCOD/L:

$$COD_{influent} = TCOD_{effluent} + CH_4 + Other = PCOD_{effluent} + SCOD_{effluent} + CH_4 + Other \quad \text{(Eqn. 4)}$$

where $COD_{influent}$ is the measured input PS TCOD concentration, $TCOD_{effluent}$ is the measured effluent TCOD concentration, $SCOD_{effluent}$ is the measured semi-soluble COD concentration, $PCOD_{effluent}$ is the computed particulate COD (PCOD; difference between $TCOD_{effluent}$ and $SCOD_{effluent}$), CH_4 is the COD equivalent of the CH_4 gas (mL),

$$1\ mL\ CH_4 \frac{1mmol\ CH_4}{24.86\ mL} \frac{8\ meq\ e^-}{mmol\ CH_4} \frac{8mg\ COD}{meq\ e^-} = 2.57\ mg\ COD\ at\ 30\ °C$$

and Other is any unaccounted COD sinks.

The electron-equivalent mass balance for MEC operation was also based on COD equivalents:

$$COD_{initial} = electrical\ current + COD_{final} + COD_{unaccounted} \qquad \text{(Eqn. 5)}$$

where $COD_{initial}$ is the measured mgCOD of the input centrate, electrical current is the COD equivalent of the Coulombs accumulated during the batch operation,

$$1\ Coulomb\ of\ current \frac{1e^-\ eq}{96485\ C} \frac{8g\ COD}{e^-\ eq} \frac{1000\ mg}{g} = 0.083\ mg\ COD$$

COD_{final} is the measured mgCOD at the end of batch MEC, and $COD_{unaccounted}$ is any unaccounted COD.

Coulombic efficiency (CE, the fraction of electrons recovered as electrical current at the anode of an MEC compared to the electrons removed from the substrate) and Coulombic recovery (CR, the fraction of electrons recovered as electrical current at the anode of an MEC compared to the total influent electrons in the substrate) were calculated based on Eqns. 6 and 7:

$$CE\ (\%) = \frac{electrical\ current}{(COD_{initial}-COD_{final})} \times 100 \qquad \text{(Eqn. 6)}$$

$$CR\ (\%) = \frac{electrical\ current}{COD_{initial}} \times 100 \qquad \text{(Eqn. 7)}$$

4.1.3. Semi-continuous operations of microbial electrolysis cells fed with primary sludge

Primary sludge (PS). We collected PS from the GWRP for semi-continuous experiments. We treated the PS with a full-scale pulsed-electric-field (PEF) unit (the OpenCEL Focused Pulsed alpha unit) and stored it in a temperature-controlled room at 4°C. Since a previous study showed that PEF pretreatment increased the bioavailability of PS by only 2%, we used PEF as a means to inactivate microorganisms in PS and, thus, to minimize the biodegradation of PS organic matter during storage, rather than as a true pretreatment method for improving performance (Ki et al., 2015).

MEC reactor set up and operation. We built two flat-plate microbial electrolysis cells (MECs) having one anode chamber in the center flanked by two cathode chambers on either side. The reactor design was the same as in Ki et al. (2016). We operated one MEC in batch mode and the other MEC in semi-continuous mode. In brief, the anode volume was ~500 mL, and the cathode at each side was ~50 mL. Carbon fibers and stainless-steel mesh were used as anode and cathode electrodes, respectively. AEMs (AMI-7001, Membranes International, Glen Rock, NJ, USA) were used as a separator between the anodes and cathodes. The anode, cathode, and membrane projected areas were 100 cm^2 each, which corresponded to a projected anode area to volume ratio of 40 m^2 m^{-3} reactor. The design of anode surface area (200 cm^2) for 500 mL of anode volume was based on the calculation of the expected current density from PS, along with the targeted HRTs.

ADS and biofilm scraped from a pre-acclimatized acetate-fed MEC were used for inoculating the MEC. We operated the MEC first with acetate medium (50 mM acetate, 100 mM PBS, 14 mM ammonium chloride, and trace minerals) (Ki et al., 2015) in continuous mode for approximately 2 months. The anode potential was poised at -0.03 V (vs. standard hydrogen electrode or SHE) with a potentiostat (VMP3, BioLogic Science Instruments, Knoxville, TN). Before changing the feed to PS, the MEC was operated with two cycles of acetate-fed batch until all the acetate was depleted.

We operated the MECs with PS feed in semi-continuous mode starting with a 15-day HRT and sequentially moving to 12-, 9-, and 6-day HRTs. After that, we resumed operation at 12-day HRT to evaluate the effect of pH by comparing pH 7.3 to pH 8.1. For all conditions, we fed PS to the MECs daily with varying volumes depending on the HRT studied, while removing the same volume of treated PS. At each feeding, we measured the effluent pH and added 5-M NaOH as needed to maintain the pH of 7.3 or 8.1 in the anode chamber.

We performed current density-voltage (j-V) experiments in triplicate, as described in Ki et al. (2016), when the current density reached a maximum when feeding PS at a 12-day HRT. j-V measurements were made with chronoamperometry, which began from the open-circuit potential of the anode and ramped up with increments of 30 to 100 mV until reaching an anode potential resulting in the highest current density.

Analytical methods. PS characterization included measurements of TCOD, SSCOD, TSS, and VSS. SSCOD, TSS, and VSS measurements were performed as described previously.

During semi-continuous operation, we attached a 500-mL bottle to the headspace of the anode chamber to measure biogas volume and composition. After stable operation was achieved at each HRT, we measured the gas volume and composition every day for one cycle of each HRT. During the 12-day HRT experiments with high pH, hydrogen (H_2) gas at the cathode also was collected and measured using a 1-L bottle. We used a 500-μL gas-tight syringe (PERFECTUM, New Hyde Park, NY) to collect gas samples and measured gas composition with gas chromatography and thermal conductivity detection

(GC-TCD, GC 2010, Shimadzu) after separation on a packed column (Carboxen^{TM} 1010 PLOT, Supelco, Bellefonte, PA). Argon was the carrier gas with a constant pressure and flow rate of 42.3 kPa and 10 mL/min, respectively. We employed temperatures of 150, 80, and 220 °C for injection port, column, and detector, respectively, and the current was 41 mA. CH_4 and CO_2 were also detected by GC-TCD. Calibration was performed using an analytical grade gas standard (CH_4: CO_2: H_2 = 40%: 30%: 30%, Matheson Tri-Gas, Twinsburg, Ohio).

We performed statistical analysis on TCOD- and VSS-removal efficiencies among the different HRT conditions tested. An independent-samples T-test was carried out using SPSS 24 (IBM, Armonk, New York). Also, we performed Spearman correlation analysis of the Coulombic and CH_4 recoveries with pH using with the same software, SPSS 24.

Calculations. Electron balances were made based on TCOD, as described Ki et al. (2015). CE, CR, cathodic H_2 recovery (or cathodic conversion efficiency, the ratio of electrons donated to H_2 normalized to the electrons transferred in the circuit from the anode to the cathode) were calculated as described in Ki et al. (2015) and Lee et al. (2009).

4.2 Integrate results into MFC kinetic models (Task 2)

4.2.1 Modeling system and assumptions

Table 2 summarizes the features of CASADM, PCIOBILM, and the PC incorporated into the MYAnode model developed for Task 2. The modeling foundation of the bulk liquid is based on CASADM, a non-steady-state model to describe typical aerobic, anoxic, and anaerobic biological phenomena exhibited in continuous stirred tank reactors (CSTRs) in WWTPs (Young et al. 2013b) and discussed in detail below. CASADM allows all biological mechanisms to occur in parallel, rather than assuming *a priori* the rate-limiting steps. We upgraded CASADM to include CCBATCH (Van Briesen and Rittmann, 1999) to efficiently link fast chemical speciation reactions, including acid-base equilibrium and complexation reactions, with slower microbial reactions.

For the model formulation, we applied the following assumptions. For the bulk solution, we assumed

- The anode chamber has ideal mixing and can be modelled as a CSTR.
- Gas formation does not occur within the diffusion layer to the biofilm or in the biofilm.
- The chemical formulas for various components include domestic wastewater are: $C_{10}H_{19}O_3N$ for PCOD and SCOD; $C_5H_7O_2N$ for biomass, biomass-associated products (BAP) and EPS; and $C_6H_{12}O_6$ for utilization-associated products (UAP) (Rittmann and McCarty 2001; Metcalf & Eddy 2014).

For the anode biofilm, we assumed

- The anode's biofilm consists of ARB only.
- We neglect ARB biomass synthesis. This allows the biofilm diffusion layer and biofilm thicknesses to be assumed as constant and modeled using ordinary differential equations.
- No biological reactions occur within the diffusion layer
- EET occurs through a conductive matrix or direct contact with anode. Thus, ARB oxidize donor substrate and respire electron only when in a biofilm is conductive and connected to an anode.

The modeling platform for the ARB biofilm is PCBIOFILM, which describes biological, chemical, and transport phenomena through an electricity-producing biofilm (Marcus et al. 2010; Marcus et al. 2011). The biofilm anode is modeled as two domains: an idealized 1D biofilm with constant thickness and uniform biofilm density that consists of ARB only, and a liquid-only diffusion layer. These two domains are located between the bulk liquid and anode surface.

Table 2. A summary of model features that are incorporated into MYAnode.

	CASADM	**CCBATCH**	**PCBIOFILM**
Types of reactions	• Biological mechanisms typical to WWTPs • Hydrolysis • EPS and SMP	• Fast chemical speciation of acids/bases	• Fast chemical speciation of acids/bases • ARB metabolism • Electrical migration
Transport phenomena	• Bulk liquid transport • Gas/liquid phase equilibrium	• No transport phenomena	• Diffusion through a biofilm
Biological mechanisms	• Aerobic oxidation by heterotrophic bacteria • Nitrification • Denitrification • Fermentation (acetogenesis) • Acetoclastic methanogenesis	• N/A	• N/A

MYAnode is a multi-component, non-steady state mathematical model that describes substrate utilization in the bulk anode chamber and in the biofilm, as illustrated in Figure 5. The reactor consists of two systems to be modeled: the bulk liquid within the anode chamber and the biofilm substrate consumption on the anode. Liquid flows into and out of the bulk liquid chamber. MYAnode is presented as four parts: (1) acid/base and chemical speciation using the PC, (2) biological processes in the bulk liquid, (3) anode biofilm processes, and (4) the coupling of slow biological reactions with transport.

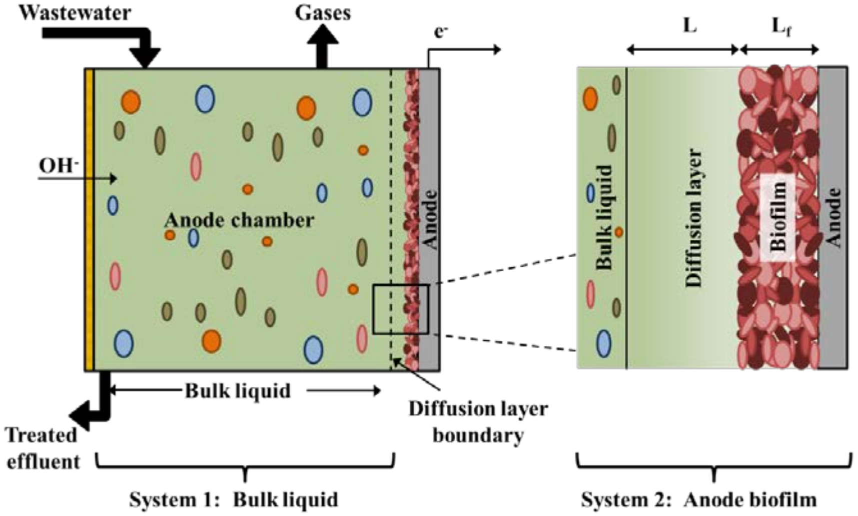

Figure 5. The reactors modelled, divided into two systems: the bulk liquid and the anode biofilm. L represents the length of the diffusion layer. L_f represents the length of the biofilm.

4.2.2 Chemical speciation using the proton condition in the bulk and biofilm

MYAnode calculates the chemical species concentrations in the bulk liquid and anode biofilm using the PC. The PC describes changes in acidity by performing a mass balance on protons generated or consumed, rather than basing a mass balance on charge. While not discussed in depth here, excellent references for utilizing the PC include Snoeyink and Jenkins (1980), Van Briesen and Rittmann (1999), and Benjamin (2015). As described in VanBriesen and Rittmann (1999) and Marcus et al. (2010), the model divides chemical species into two groups: components and complexes. A proton mass balance is calculated in relation to a "reference-level" for the protons and are neutral with respect to acidity, even though they are not necessarily neutral with respect to charge; these "reference-level" chemicals are the components. Components are combined together to describe other chemical species, or complexes, in the system. For simplicity, we chose components and complexes that can dissociate under acid/base conditions or are present as charge carriers, which affect ionic migration through the anode biofilm.

For MYAnode, we expanded Marcus et al. (2011) to include common ions present in WWT: all protonated forms of acetate (CH_3COO^-), phosphate, carbonate (CO_3^{2-}), NO_2^-, and NH_4^+; we also included the charged species NO_3^-, Na^+, and Cl^-, which do not participate in acid-base reactions at relevant pH values. The PC methodology is discussed in detail in the Appendix.

4.2.3 Bulk-liquid processes

ARB perform anode respiration in anaerobic conditions and depend upon other microorganisms in anaerobic WWT to hydrolyze and ferment complex organic compounds to simple substrates for their consumption (Rozendal et al. 2008; Parameswaran et al. 2009; Kiely et al. 2011; Parameswaran et al. 2011; Miceli et al. 2014). The model includes first-order hydrolysis of complex and particulate organic compounds. Since the kinetics of fermentation and the relationship between pH and fermentation are not well understood, the hydrolysis products are fermented by fermenting bacteria directly to acetate (Rittmann and McCarty 2001; Aquino and Stuckey 2008). This step is critical to providing substrate to most common ARB (Kiely et al. 2011; Parameswaran et al. 2011; Miceli et al. 2014). Two sets of microorganisms compete for acetate: acetoclastic methanogens to produce CH_4 and ARB to respire electrons to an anode.

We assume that the microbiological processes in the bulk liquid of the MEC are similar to those in WWT, which are the foundation of CASADM. CASADM is a non-steady-state mathematical model of biological kinetics typically found in WWT and is extensively discussed in Young et al. (2013b). CASADM is unique in that it assumes that all mechanisms can occur simultaneously rather than assuming *a priori* that any one rate is limiting and that it includes biomass-generated products like EPS and SMP, which are neglected in other models like ADM, ASM, and the Benchmark Simulation Models (Henze et al. 1999; Batstone et al. 2002; Nopens et al. 2009).

The components included in CASADM are summarized in Table 3. For solid materials, the model includes six components of active biomass – heterotrophic bacteria, ammonium-oxidizing bacteria (AOB), nitrite-oxidizing bacteria (NOB) fermenting bacteria, acetoclastic *Archaea*, and ARB – as well as EPS, inert (non-biodegradable) biomass, and PCOD. The soluble components include SCOD, CH_3COO^-, UAP, BAP, NH_4^+, NO_2^-, NO_3^-, O_2, HCO_3^-, Na^+, and Cl^-, as well as any complexes derived from them due to chemical speciation. Gas-phase materials include H_2, CO_2, O_2, N_2, NH_3, and CH_4. We omit H_2 production from fermentation due to undefined kinetics for H_2 production from SMP utilization and because the longer SRTs used during lab experiments allowing acetoclastic methanogenesis to dominate in anaerobic systems (Rittmann and McCarty, 2001), as observed by Ki et al. (2017).

Table 3. Materials (including all components and complexes) and biological mechanisms in MYAnode. Bolded entries delineate components for chemical speciation calculations.

Solid	Liquid		Gas/Liquid phase	Biological mechanisms
	Components	Complexes		
Heterotrophic bacteria	SCOD		O_2	Biomass synthesis
Ammonium-oxidizing bacteria (AOB)	UAP		CO_2	Endogenous decay
Nitrite-oxidizing bacteria (NOB)	BAP		NH_3	EPS and UAP generation
Fermenters	**CH_3COO^-**	CH_3COOH	N_2	Heterotrophic substrate consumption
Hydrogenotrophic methanogens	**NH_4^+**	NH_3	CH_4	Nitrification
Acetoclastic methanogens	**NO_2^-**	HNO_2		Denitrification
Anode-respiring bacteria (ARB)	**NO_3^-**			Fermentation
EPS	**HCO_3^-**	H_2CO_3		Hydrogenotrophic methanogenesis
Inert biomass		CO_3^{2-}		Acetoclastic methanogenesis
Particulate COD (PCOD)	**Na^+**			Anode respiration
	Cl^-			Hydrolysis
	HPO_4^{2-}	H_3PO_4		
		$H_2PO_4^-$		
		PO_4^{3-}		
	H^+			
	H_2O			

As described in Young et al. (2013b) and with exception of ARB, all biomass undergoes biomass synthesis based on Monod kinetics, first-order endogenous decay, and generation of EPS and UAP, as outlined in Laspidou and Rittmann (2002a, 2002b), but with two modifications: (1) UAP and BAP can be utilized as substrate by fermenters and heterotrophs, and (2) UAP and BAP utilization can result in the formation of additional EPS and BAP. Hydrolysis of PCOD and EPS to SCOD and BAP, respectively, can occur in any environment and follow first-order kinetics. When applicable, substrate utilization adheres to dual-limitation Monod kinetics dictated by electron donor and electron acceptor kinetics. We utilized the pH inhibition function developed by Park et al. (2007), in which the substrate utilization rate is multiplied by a factor, $I_{pH,}$ (unitless), according to the following conditions

$$I_{pH} = 0 \quad \text{for } pH < pH_{opt} - W \qquad \text{(Eqn. 8)}$$
$$I_{pH} = 1+\cos(\pi(pH-pH_{opt})/W) \quad \text{for } pH_{opt} - W < pH < pH_{opt} + W \qquad \text{(Eqn. 9)}$$
$$I_{pH} = 0 \quad \text{for } pH > pH_{opt} + W \qquad \text{(Eqn. 10)}$$

where pH_{opt} is the optimal pH for the bacteria and W is one-half the value of the difference between the upper and lower pH limits. I also utilize substrate limitation functions for reactions that can occur only when specific chemical components are not present, e.g. denitrification under anoxic conditions and fermentation and methanogenesis under anaerobic conditions. The substrate limitation function, S_{inh}, is described as

$$S_{h,inh} = \frac{K_{h,inh}}{K_{h,inh}+C_h} \qquad \text{(Eqn. 11)}$$

where h is a chemical or biological component, $K_{h,inh}$ is the inhibition factor (M/L^3) for component h, and C is concentration (M/L^3).

Since the biological reactions are slower than the chemical-speciation reactions, the change in concentration over time is described as

$$\frac{dC_h}{dt} = \sum_{g=1}^{g=N} \lambda_{hg} r_h \, I_{g,pH} S_{g,inh} \qquad \text{(Eqn. 12)}$$

where g is a chemical or biological reaction, C_h is concentration (M/L^3) of the solid or soluble components h, λ_{hg} is the stoichiometric coefficient of component h in reaction g, r is reaction rate (M/L^3-t), $I_{g,ph}$ is pH inhibition term for reaction g, and $S_{g,inh}$ is the substrate limitation factor.

4.2.4 Biofilm-anode processes

Biofilm-anode kinetics, mechanisms, and the impacts of charge migration are based largely on PCBIOFILM (Marcus et al. 2010; Marcus et al. 2011), with minor modifications to the ionic components (i.e., the addition of NO_2^-, NO_3^-, and NH_4^+) that can diffuse into the biofilm to maintain electrical neutrality. (See the Appendix for a description.) For ARB, all stoichiometry and kinetics are consistent with PCBIOFILM. Since the biofilm thickness is assumed, ARB performance is dictated by Monod kinetics with acetate being the lone electron donor for ARB. The effects of pH inhibition are corrected for using the inhibition functions described above.

4.2.5 The coupling of kinetically controlled reactions and transport

A differential mass balance containing transport and reaction terms describes the total analytical concentration of each component within the system

$$Vol\frac{\partial C_h}{\partial t} = Q_{in}C_{h,in} - Q_{out}C_{h,out} + SA\, J_{ion,h} + V\sum_{g=1}^{Ng} \lambda_{hg} r_h \, I_{g,pH} S_{g,inh} \qquad \text{(Eqn. 13)}$$

where Vol is the anode chamber volume (L^3), Q is the volumetric flow rate (L^3/T), and SA is the surface area of the anode (L^2). Within the diffusion layer and biofilm, a component's total analytical concentration is subject to changes due to chemical speciation, biological reactions and diffusion. Thus, Eqn. 13 within the biofilm and diffusion layers simplifies to

$$\frac{\partial C_h}{\partial t} = \frac{SAJ_{ion,h}}{Vol} + \sum_{g=1}^{Ng} \lambda_{hg} r_h\, I_{g,pH} S_g \qquad \text{(Eqn. 14)}$$

Assuming that length $x = L + L_f$ is the boundary between the bulk and diffusion layer, $x = L_f$ is the boundary between the diffusion layers and anode biofilm, and the anode surface is at $x = 0$, the following boundary conditions exist:

(1) Continuity of flux between the bulk liquid, the diffusion layer, anode biofilm:

$$-J_{bulk,h}\big|_{x=L+L_f} = -J_{ion,h}\big|_{x=L} = J_{ion,h}\big|_{x=L_f} \qquad \text{(Eqn. 15)}$$

(2) No flux at the anode surface:

$$J_{ion,h} = 0 \qquad \text{(Eqn. 16)}$$

Within the bulk liquid, advection, chemical speciation, and biological reactions affect a component's concentration, simplifying Eqn. 13 to:

$$\frac{\partial C_h}{\partial t} = \frac{1}{Vol}\left(Q_{in} C_{h,in} - Q_{out} C_{h,out}\right) + \sum_{g=1}^{Ng} \lambda_{hg} r_h\, I_{g,pH} S_g \qquad \text{(Eqn. 17)}$$

Gas-liquid phase equilibrium is described as

$$\frac{dC_i^L}{dt} = \frac{dC_i^G}{dt} = \frac{Vol_i^L}{Vol_i^G} K_L a_i\left(C_i^L - C_i^L H_i RT\right) \qquad \text{(Eqn. 18)}$$

where L represents the liquid phase, G represents the gas phase, C_i is the concentration of species i, K_La is the mass transfer coefficient of species i (1/t), and H is species i's Henry's law constant (M/L^3). Since the Henry's law constant for other species are relatively large, this model assumes that only the following species partition between gas and liquid phases: CH_4, CO_2, H_2, N_2, NH_3, and O_2.

4.2.6 Modeling approach and implementation

MYAnode consists of two main programs, as illustrated in Figure 6: CASADM and PCBIOFILM. CASADM has 40 nonlinear ODEs that describe the flow through the anode chamber using the chemical and biological components and complexes described in Table 2. The ODEs are solved using Euler's method using initial value conditions equal to the influent composition and time steps ≤ 1 min until the system obtained steady state, (i.e., a difference between data points $< 10^{-4}$). Mass balance checks were performed as part of each step's execution for each element within the model, with $< 10^{-12}$ error for any element.

For the initial time point, the free-component and complex concentrations are calculated to determine the amount of H^+ (also referred to as the "ACID" concentration) in the PC. The PC solves 16 nonlinear equations simultaneously using a modified Newton-Raphson method (Marcus et al. 2011) for the components acetate, phosphate, carbonate, nitrite, ammonium, and H^+. The total analytical component concentrations were used to calculate the bulk liquid concentrations for each free component and complex in the bulk. The bulk concentrations were used to evaluate the flux at the boundary layer between the bulk liquid and biofilm and concentrations of components with the biofilm using PCBIOFILM. The model was executed until steady-state was reached (~200-300 d).

PCBIOFILM's solver routine is described in depth in Marcus et al. (2011), with the diffusion layer broken into 10 nodes and the biofilm 20 nodes for computation accuracy. The finite-differences method was used to transform the set of boundary conditions and mass conservation equations into a set of algebraic equations. A modified Newton-Raphson method is used to find which component and complex values will set the objective functions equal to zero, with the initial conditions from the bulk as the starting point. Complex and component values are iterated on until the objective functions converge on the value of flux from the diffusion layer to the bulk is equal to the flux obtained from CASADM with an accuracy of 10^{-6} in the objective functions. The concentration values are then fed back to CASADM.

To test the accuracy of the model with realistic conditions, we utilized waste stream parameters outlined in Young et al. (2013b), Metcalf & Eddy (2014), and Ki (2017), as summarized in Table 4. Ki et al. (2017) operated a 0.5-L, dual-chamber MEC with two anodes and cathodes separated by AEMs. In Ki (2017), the reactor was fed daily with PEF PS. The anode geometric surface area was 200 cm^2. Mimicking Ki et al. (2017), the model is operated using varying HRTs from 6-15 d. The reactor is fed daily with influent PS, and the anode chamber pH is adjusted to 7.5 immediately after feeding. Hydrolysis kinetics were evaluated at 0.12 and 0.25/d, as determined by Ki et al. (2017) using CH_4 and VFA concentrations as the determining factors, respectively. Influent methanogen (X_m) concentration was varied from 1-100 mgVSS/L to determine how influent concentration affects diversion of substrate from current production.

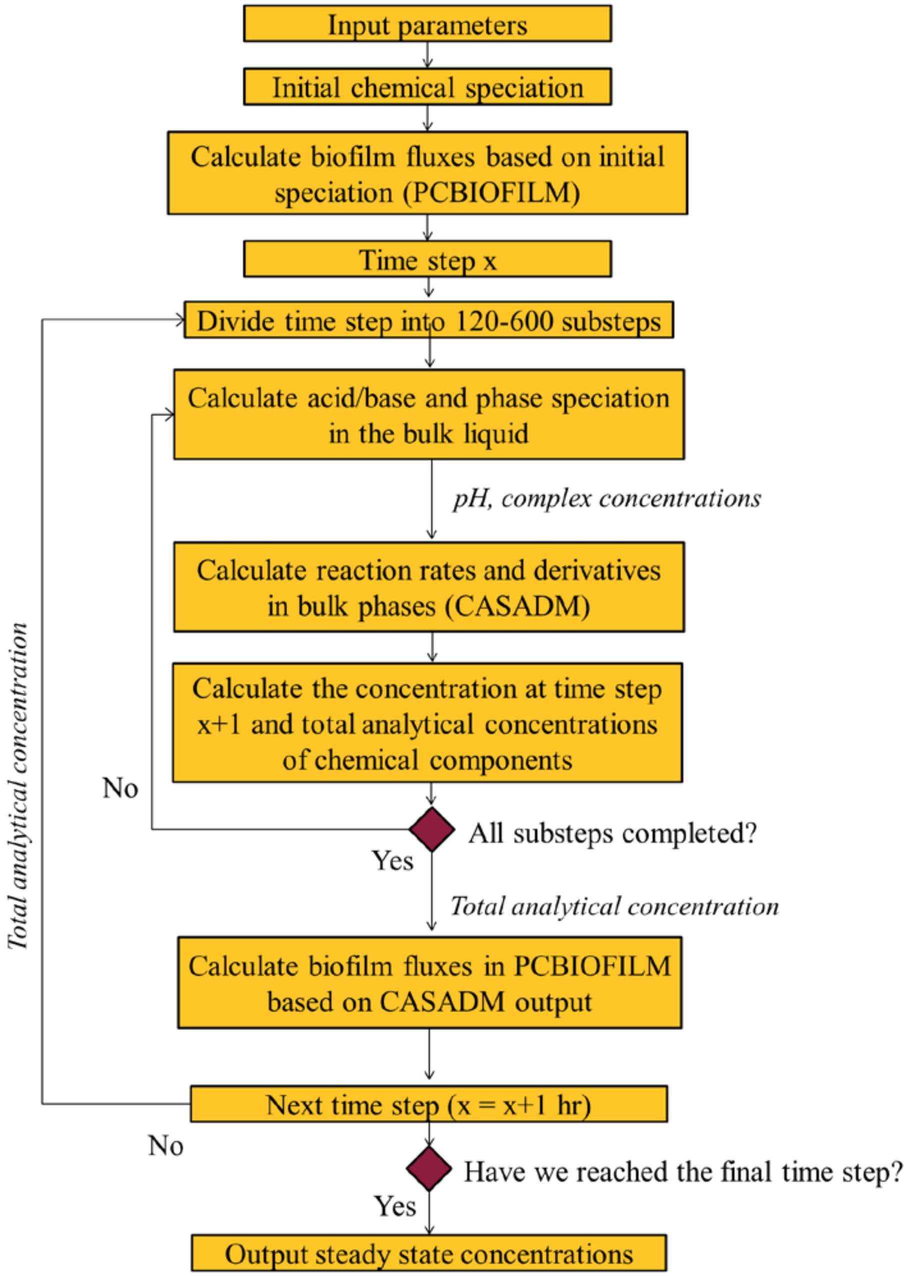

Figure 6. Flow chart of the solution procedure for MYAnode.

Table 4. Influent model parameters.

Parameter	Units	Scenario 1	Scenario 2	Scenario 3	Scenario 4
Influent wastewater					
Hydraulic retention time*	d	6	9	12	15
Anode chamber volume*	L	0.5	0.5	0.5	0.5
Influent pH*		6.9	6.9	6.9	6.9
Daily pH target*		7.5	7.5	7.5	7.5
SCOD*	mgCOD/L	1200	1500	1100	550
VSS*	mgVSS/L	4100	3300	3500	3700
TSS*	mgTSS/L	400	700	750	900
NH_4^+ **,†	mgN/L	50	50	50	50
NO_2^-, NO_3^- *	mgN/L	0	0	0	0
HCO_3^- *	mgHCO_3/L	300	300	300	300
Heterotrophic biomass**	mgVSS/L	50	50	50	50
AOB**	mgVSS/L	10	10	10	10
NOB**	mgVSS/L	5	5	5	5
Fermenting bacteria**	mgVSS/L	20	20	20	20
Acetoclastic methanogens**	mgVSS/L	0-100	0-100	0-100	0-100
Anode and biofilm					
Anode surface area*	cm^2	200	200	200	200
Anode potential*	V_{SHE}	-0.03	-0.03	-0.03	-0.03
Substrate utilization rate‡	mmol Ace/(cm^3 d)	17.5	17.5	17.5	17.5
Half-maximum rate concentration‡	mmol Ace/cm^3	0.002	0.002	0.002	0.002
Biofilm thickness*,‡	cm	0.015	0.015	0.015	0.015
Diffusion layer thickness‡	cm	0.01	0.01	0.01	0.01
pH optimal‡		7.5	7.5	7.5	7.5
pH inhibition range for ARB‡		2.1	2.1	2.1	2.1

* Ki et al. (2017), ** Young et al. (2013), †Metcalf & Eddy (2014), ‡Marcus et al. (2010)

4.3. Test Materials (Task 3)

4.3.1. Anode and membrane testing with primary sludge

We used carbon fiber anodes and membranes as separators in MECs fed with PS in batch and semi-continuous mode for up to ~1-year operations without changing materials. Also, we tested MPPCs fed with PS. The tests are related with Task 6~7.

4.3.2. Cathode and membrane testing with hydrogen peroxide

Membrane stability tests. We characterized five ion exchange membranes to determine their compatibility with H_2O_2: three AEMs including AMI-7001 (Membranes International, Inc.), Excellion I-200 (SnowPure LLC), and fumasep® FAA (fumatech GmbH); and two cation exchange membranes (CEMs) including CMI-7000 (Membranes International, Inc.) and Nafion-117 (Dupont™). We tested unconditioned membrane stability in solutions with H_2O_2 and pH 7 and 12. Membranes with surface areas of 9 cm^2 samples were cut, left at ambient lab conditions for 48 hours, and weighed. The membranes were placed in 25-mL serum bottles filled with 20 mL of 100 mM NaCl at pH 12, 100 mM NaCl with 10 g/L H_2O_2 at pH 12, or 100 mM NaCl with 10 g/L H_2O_2 at pH 7. We adjusted the electrolyte pH to 12, as it is the highest pH anticipated during MPPC operations. Bottles were prepared in triplicate, capped with butyl rubber stoppers and aluminum crimps, and degassed regularly. After 45 days, we emptied the bottles' contents and analyzed the solutions for H_2O_2 concentration and pH. Membranes were washed with deionized (DI) water and dried under ambient laboratory conditions prior to measuring the final mass.

Catalyst/binder characterization. We performed rotating-ring disk electrode (RRDE) tests using a RRDE-3A RRDE apparatus (ALS-Japan) to determine potential H_2O_2 production efficiency from different catalyst/binder combinations. We used a Vulcan carbon catalyst-Nafion binder mixture to coat the catalyst layer on the disk electrode at catalyst loadings of 0.22, 0.44, 0.67, 0.89, and 1.12 mg/cm^2. The ring/disk electrode was rotated at 1200 rpm for ~30 minutes until the ink dried. Once dried, the ring was submerged in 100-mM NaCl sparged with O_2 for >30 minutes to saturate the solution. We measured the ring and disk current densities at a disk speed of 1600 rpm and ring potential of 0.08 $V_{Ag/AgCl}$, and the disk potential was varied from -0.60 to 0 $V_{Ag/AgCl}$ at a scan rate of 10 mV/s to determine the number of electrons transferred to O_2.

H_2O_2 measurements and stability tests. For membrane stability experiments, we measured H_2O_2 concentration using the National Diagnostics Hydrogen Peroxide Assay Kit. For all other experiments, we analyzed H_2O_2 using the method of Graf and Penniston (1980). Colorimetric measurements were performed using a Cary 50-Bio UV-Visible spectrophotometer (Varian, Palo Alto, CA). When compared, these two methods demonstrated equivalent results (not presented here).

We evaluated H_2O_2 stability with different electrolytes. We prepared 200-mL solutions of 10 g/L H_2O_2 in five different electrolytes: 200 mM pH 4.5 PBS, 200 mM pH 7.5 PBS, 200 mM NaCl at pH 6.5, 200 mM NaCl at pH 12, and 200 mM Na_2CO_3 at pH 11.5. Sixty-five mL of each electrolyte combination were placed in three 100-mL glass serum bottles and corked with butyl-rubber stoppers (Bellco Glass, NJ) and aluminium caps. We removed 2-mL samples using a needle and syringe from each bottle at 2, 4, 6, and 12 h and every 12 h subsequently for 120 h. Samples were analysed for pH and H_2O_2 concentration.

4.4 Control strategies and design optimization algorithms (Task 4)

4.4.1 Analysis of pH neutralization process

Consider a 500-mL continuous stirred tank reactor ($CSTR$) with inlet streams of strong acid ($1M\ HCl$), weak acid 1($100mM\ H_2CO_3$), weak acid 2 ($100mM\ H_3PO_4$) and strong base ($1M\ NaOH$) and q_1,q_2, q_3 and q_4 being their flow rates, respectively. The schematic diagram of the reactor is shown in Figure 7. The combination of a strong acid, weak acid 1 and weak acid 2 simulates waste water and flow rate of the strong base is manipulated to control the pH of the liquid in the reactor. A variation of the buffering capacity of the wastewater is simulated by varying the flows of the weak acids. The volume of the liquid in the reactor and its temperature are kept constant. The pH of the liquid in the reactor is measured directly by a pH probe inserted in the reactor. It is assumed that perfect mixing occurs in the reactor and ions are completely soluble. The goal of pH control is to regulate pH of the liquid in the reactor by manipulating base flow rate.

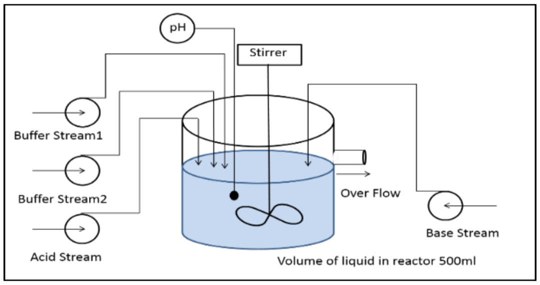

Figure 7. Schematic Diagram of the pH neutralization process CSTR.

A reaction invariant model is developed using reaction invariants of the reversible reaction components. In which chemical equilibrium is modeled based on the concept of reaction invariants (Gustafsson and Waller, 1983; McAvoy et al., 2000; Henson et al., 1994). Three reaction invariants (W_a is a charge-related quantity, W_b refers to the concentration of carbonate ions and, W_c refers to the concentration of phosphate ions) are involved for each stream (i = 1 to 4) in this system. The analytic expressions of the reaction invariants are listed below:

$$Wa_i = [H^+]_i - [OH^-]_i - [HCO_3^-]_i - 2[CO_3^{2-}]_i - [H_2PO_4^-]_i - 2[HPO_4^{2-}]_i - 3[PO_4^{3-}]_i$$

$$Wb_i = [H_2CO_3]_i + [HCO_3^-]_i + [CO_3^{2-}]_i$$

$$Wc_i = [H_3PO_4]_i + [H_2PO_4^-]_i + [HPO_4^{2-}]_i + [PO_4^{3-}]_i$$

A reaction invariant nonlinear model of pH neutralization process can be described using following differential equations:

$$\frac{dWa_5}{dt} = \frac{1}{V}[q_1(Wa_1 - Wa_5) + q_2(Wa_2 - Wa_5) + q_3(Wa_3 - Wa_5) + q_3(Wa_3 - Wa_5)]$$

$$\frac{dWb_5}{dt} = \frac{1}{V}[q_1(Wb_1 - Wb_5) + q_2(Wb_2 - Wb_5) + q_3(Wb_3 - Wb_5) + q_3(Wb_3 - Wb_5)]$$
$$\frac{dWa_5}{dt} = \frac{1}{V}[q_1(Wc_1 - Wc_5) + q_2(Wc_2 - Wc_5) + q_3(Wc_3 - Wc_5) + q_3(Wc_3 - Wc_5)]$$

The relationship between hydrogen-ion concentration and reaction invariants is given as follows

$$WC_i \frac{\frac{Ka_3}{[H^+]} + 2\frac{Ka_3Ka_4}{[H^+]^2} + 3\frac{Ka_3Ka_4Ka_5}{[H^+]^3}}{1 + \frac{Ka_3}{[H^+]} + \frac{Ka_3Ka_4}{[H^+]^2} + \frac{Ka_3Ka_4Ka_5}{[H^+]^3}} + Wb_i \frac{\frac{Ka_1}{[H^+]} + 2\frac{Ka_1Ka_2}{[H^+]^2}}{1 + \frac{Ka_1}{[H^+]} + 2\frac{Ka_1Ka_2}{[H^+]^2}} + Wc_i + \frac{K_w}{[H^+]} - [H^+]$$
$$= 0$$

Where $Ka_1 = \frac{[HCO_3^-][H^+]}{[H_2CO_3]}$, $Ka_2 = \frac{[CO_3^{2-}][H^+]}{[HCO_3^-]}$, $Ka_3 = \frac{[H_2PO_4^-][H^+]}{[H_3PO_4]}$, $Ka_4 = \frac{[HPO_4^{2-}][H^+]}{[H_2PO_4^-]}$
$Ka_5 = \frac{[PO_4^{3-}][H^+]}{[HPO_4^-]}$ and $K_w = [H^+][OH^-]$

And relationship between pH and hydrogen ion concentration is described as follows

$$pH = -\log_{10}([H^+])$$

The base flow is controlled by controlling voltage of the peristaltic pump's control terminal using a 12-bit digital to analog converter (DAC). Relationship between the DAC value and the base flow is given below.

$$Base\ flow\ \left(\frac{mL}{min}\right) = 7.45 \times \frac{DAC\ Value}{4095}$$

Nominal values of the model parameters are listed in Table 5.

Table 5. Model parameters.

Symbol	Value	Symbol	Value	Symbol	Value	Symbol	Value
Ka_1	4.47×10^{-7}	V	500 ml	Wa_1	1M	Wb_3	0M
Ka_2	5.62×10^{-11}	q_1	2.45 ml/min	Wa_2	−0.1M	Wb_4	0M
Ka_3	0.0072	q_2	2.45 ml/min	Wa_3	−0.18M	Wc_1	0M
Ka_4	1.6982×10^{-7}	q_3	2.45 ml/min	Wa_4	−1M	Wc_2	0M
Ka_5	2.6915×10^{-12}	q_4	2.45 ml/min	Wb_1	0M	Wc_3	0.1M
K_w	1.011×10^{-14}			Wb_2	0.1M	Wc_4	0M

To analyze the nonlinear model for pH control, it is linearized at different operating pH set-points and buffer flow combinations. Buffer flow rate combinations used to simulate variation in the buffering capacity are listed below.

- Case 1: $q_2 = 2.5\ mL/min$ and $q_3 = 2.5\ mL/min$
- Case 2: $q_2 = 0\ mL/min$ and $q_3 = 2.5\ mL/min$
- Case 3: $q_2 = 2.5\ mL/min$ and $q_3 = 0\ mL/min$
- Case 4: $q_2 = 0\ mL/min$ and $q_3 = 0\ mL/min$

The nonlinear model is linearized at the different pH operating points for all cases. Transfer functions of the linearized models can be expressed in the following format.

$$P(s) = \frac{K_g}{\mathrm{T}s + 1} e^{-\frac{s}{6}}$$

Where K_g is the plant gain and T is the plant time constant. Plots of gains and time constants of linearized plants are shown in Figure 8.

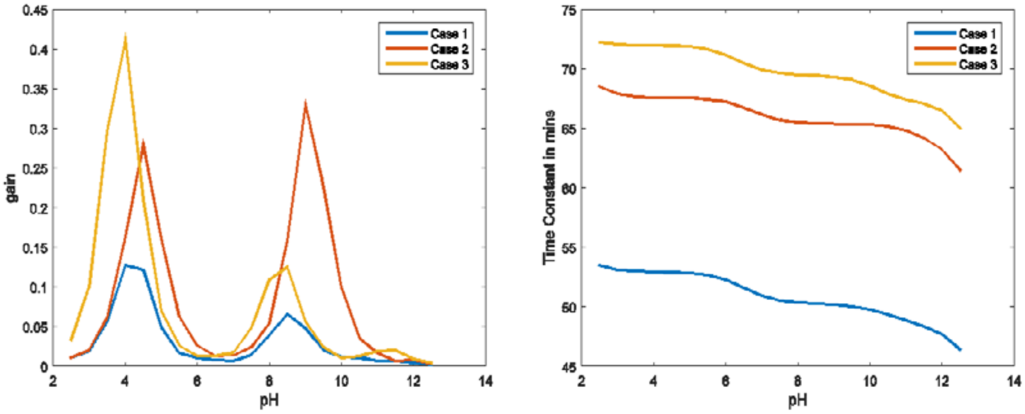

Figure 8. Left figure-pH vs gain plot; Right figure- pH vs time constant plot.

It can be seen from the above plots, only gain of the linearized plant models vary significantly. To compensate the variation in the gain of the plant it is sufficient to adapt the gain of the controller.

4.4.2 Direct adaptive pH Control algorithm

In this section, we summarize the formulation of controller gain adaptation as an approximate H_∞ loop shaping problem (Tsakalis and Dash, 2013) and discuss the necessary modifications for the practical implementation of the proposed algorithm in the pH control problem. For the tuning of the proportional integral derivative (PID) parameters, we adopt the Frequency Loop Shaping (FLS) approach, with a robust stability condition (RSC) metric described in Grassi and Tsakalis (2000).

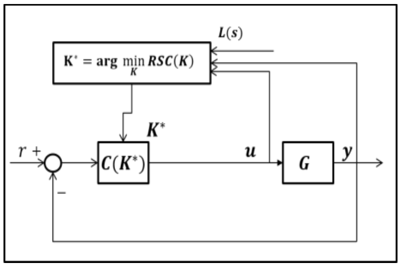

Figure 9. Block diagram of the closed-loop system with direct adaptive pH controller

PID controllers are some of the most extensively used algorithms in the process industry. PID tuning is a very well researched topic and some of the commonly used methods are discussed in Åström and Hägglund (2006); Rivera et al. (1986) and one such method is FLS. In FLS, closed-loop design specifications are specified in terms of a target open-loop transfer function and PID parameters are obtained by minimizing the distance between the target loop and the actual open-loop transfer function. More specifically, letting G be the plant and C the controller, the FLS objective is to minimize the distance between the loop transfer function GC and the target loop L.

A weighted H_∞ norm that corresponds to the small gain theorem called RSC metric provides a good measure of the distance between the actual and the target loop.

An extension of the offline FLS tuning for an online and adaptive implementation has been introduced in the paper by Tsakalis and Dash (2013), while the applicability and usage of the RSC metric in the monitoring of industrial process controllers have been discussed in Tsakalis and Dash (2007). The main idea in these studies was to estimate RSC values of using plant input-output data and use RSC to obtain PID parameters.

According to our model analysis, the process dynamics (pole, delay) change very little with the operating conditions. Therefore, non-adaptive part of the proportional integral (PI) controller is expressed as follows

$$\tilde{C} = \frac{(s+a)}{s}$$

Where $a = \frac{K_{in}}{K_{pn}}$, K_{in} and K_{pn} are the integral and the proportional gains of the nominal controller respectively.

For pH control, RSC minimization problem described in Tsakalis and Dash (2013) for the online implementation using a filter bank $\{F_i\}_i$ is rewritten to adapt only controller gain and is expressed as follows.

$$K^* = \arg \min_{K \in Mg} \max_{i} \frac{\left|\left|KS\tilde{C}F_i y - TsenF_i y\right|\right|_{2,\delta}}{\left|\left|F_i u\right|\right|_{2,\delta}}$$

K is the controller gain, Mg is the constraint set of the controller gain, S and $Tsen$ are sensitivity and complementary sensitivity of the target loop respectively. u is the plant input, y is the plant output and $\left|\left|\quad\right|\right|_{2,\delta}$ is exponentially weighted 2-norm with δ as the exponential weight. Above optimization problem is solved iteratively by computing the following at each time step k

$$\min_{K \in Mg} \max_{i} \frac{J_{i,k}}{m_{i,k}}$$

$$\mathrm{J_{i,k}(K_k)} = \sum_{\mathrm{n=0}}^{\mathrm{k}} \lambda^{\mathrm{k-n}} \left|\mathrm{z_{i,n}} - \mathrm{w_{i,n}^T K_k}\right|^2, \mathrm{m_{i,k}} = \lambda \mathrm{m_k} + |[\mathrm{F_i u}]_{\mathrm{k+1}}|^2$$

Where $\mathrm{z_{i,n}} = [\mathrm{TF_i u}]_{\mathrm{n}}, \mathrm{w_{i,n}} = \left[\mathrm{S\tilde{C}F_i y}\right]_{\mathrm{n}}$, and λ is the forgetting factor.

To make the proposed direct adaptive algorithm fast (to improve transient performance), but including some “sanity checks” to avoid misadjustment due to perturbations or measurement noise, the following refinements are introduced

- For faster convergence, the covariance P associated with the recursive least squares algorithm is reset periodically if one of the following conditions is met.
    - If the set-point variation exceeds a threshold.
    - If the time elapsed since the last reset exceeds a threshold.

  - If there is a significant change on the pH reading (accounting for disturbances).
- The estimated parameter is accepted as an update in the controller only if the value of the sum of squares of P for the entire filter bank exceeds a threshold.
- The plant input-output pair used in the adaptation algorithm is filtered using a band pass filter that attenuates frequencies of these signals outside the frequency range of interest.
- To ensure adaptation is active only when signals satisfy persistence of excitation, a dead zone is introduced in the cost function max [0;$\left(\frac{J_{i,k}}{m_{i,k}}\right) - \delta_{dzn}$]. Where δ_{dzn} is a small constant that represents a dead zone on the cost function.

This refined algorithm was tested using the lab-scale experiments and details are described in the next section.

4.4.3 Low-cost potentiostat construction

Our potentiostat design consists of a digital side and an analog side. The block diagram of the potentiostat is shown below in Figure 10. The digital side consists of an Analog to Digital Converter (ADC), a DAC, a microcontroller (Arduino Mega) and a personal computer. A personal computer or equivalent is also used to perform data acquisition, data storage, and data visualization tasks. The microcontroller receives potentiostat set-point and sends readings of the working electrode voltage, the reference electrode voltage and current between the anode and cathode back to the computer for the purpose of data logging. The microcontroller and the PC communicate using UART serial communication with a baud rate of 115200. The ADC and DAC are used to interface the analog side of the potentiostat with the micro controller and they communicate with the microcontroller using Serial Peripheral Interface (SPI) communication protocol. Both ADC and DAC are powered using the regulated voltage generated by the analog power circuit. Because they are powered using different digital voltage levels (generated from the analog power circuit), the SPI communication between the ADC/DAC and the microcontroller is digitally isolated using an isolator (IC ADUM7641). An integrated circuit (IC) ADS1248 is used as the ADC and another IC AD5752R is used as the DAC. The ADS1248 is a 24 bit ADC with 8 differential channels and it can support sampling rate up to 2000 samples/sec. The AD5752R is a 16 bit DAC with 2 channels and it can support sampling rate up to 10 mega samples/sec.

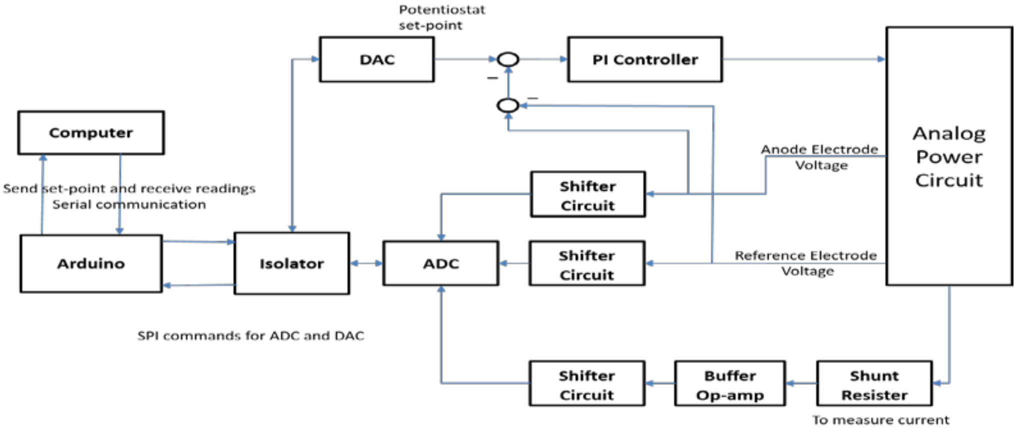

Figure 2. Schematic Diagram of the low-cost potentiostat.

The analog circuit is divided into three parts, an analog power circuit, a PI controller and shifter circuits. The analog power circuit converts a unipolar voltage source into bipolar voltage source, it translates an anode set-point voltage to an equivalent signal that is capable of driving current between an anode and a cathode, it also generates a regulated +5V signal (used to power ADC and DAC). The shifter circuit brings the voltage signals into the ADC range. In the proposed potentiostat we use an ADC with the range of 0 to 5V and our voltage signals (working/reference electrode) are between -2.5V to +2.5V. The shifter circuit brings signals from -2.5V to +2.5V range to 0V to +5V and the circuit diagram of the shifter circuit. To regulate the potential of the working electrode with respect to the reference close to the potentiostat set-point, we use a PI controller. The PI controller generates anode set-point based on the error $e(S - (R - A))$, where S, R and A are potentiostat's set point, reference electrode voltage, and anode voltage respectively.

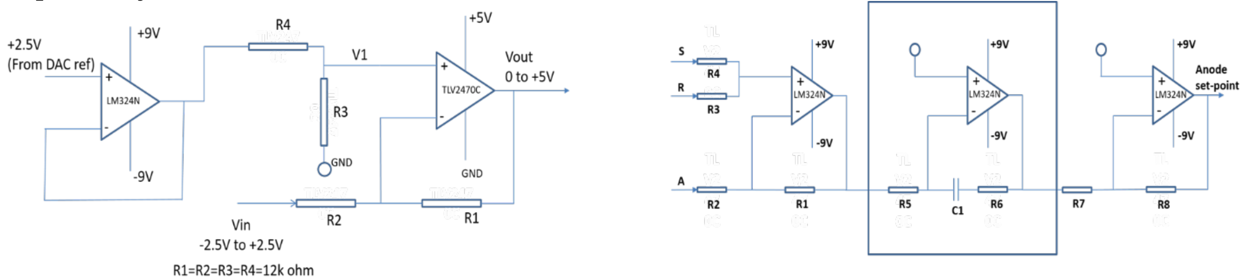

Figure 3. Left circuit- voltage shifter circuit; Right circuit- PI controller.

This potentiostat is tested using a ferricyanide reactor and results from set-point tracking experiments are discussed Section 4.4.

4.5. Design of Prototype MFCs and process control systems (Tasks 5 and 6)

4.5.1. Design, operation, and characterization of flat-plate reactors

Flat-plate MEC design. We designed a modular flat-plate MECs each with two anodes and two cathodes as described in our previous study (Ki et al., 2015). We provide a schematic in Figure 12. Briefly, the anodes were made of carbon fibers (24K Carbon Tow, FibreGlast, OH, USA) that were woven around a titanium plate that served as current collector (each anode was 10 cm x 10 cm, geometric area of 100 cm^2). The two anodes shared a common chamber. We used stainless steel meshes (Type 314, McMaster-Carr, USA) or nickel meshes (Ni 200, Unique Wire Weaving Co., Inc., USA) as the cathodes, and each cathode had a separate individual chamber. We cleaned the assembled anodes with 1 M nitric acid for 3 hours, 1 M acetone for 12 hours, 1 M ethanol for 3 hours, and deionized water (18 MΩ) overnight before using them. We equipped the anode chamber with a reference electrode (Ag/AgCl, MF-2052, Bioanalytical Systems, Inc., USA), which was at a ~2 cm distance from each anode. All potentials we report throughout are converted to vs. SHE using a conversion factor of +0.27 V. We determined this conversion factor as previously described for the medium we fed to the MECs (Torres et al., 2009). We used the AEMs AMI-7001 (Membrane International, Glen Rock, NJ) or Fumasep FAA (FuMa-Tech, Germany) to separate the anode and the cathode chambers. We maintained the distance between the anode and cathode at < 0.5 cm. The anode chamber volume was ~0.5 L and the cathode chamber volume (individual) was ~0.1 L (or 0.2 L total). The anode was fed with acetate as the electron donor (see medium composition below), while the cathode was fed with a 100-mM solution of NaCl or NaOH.

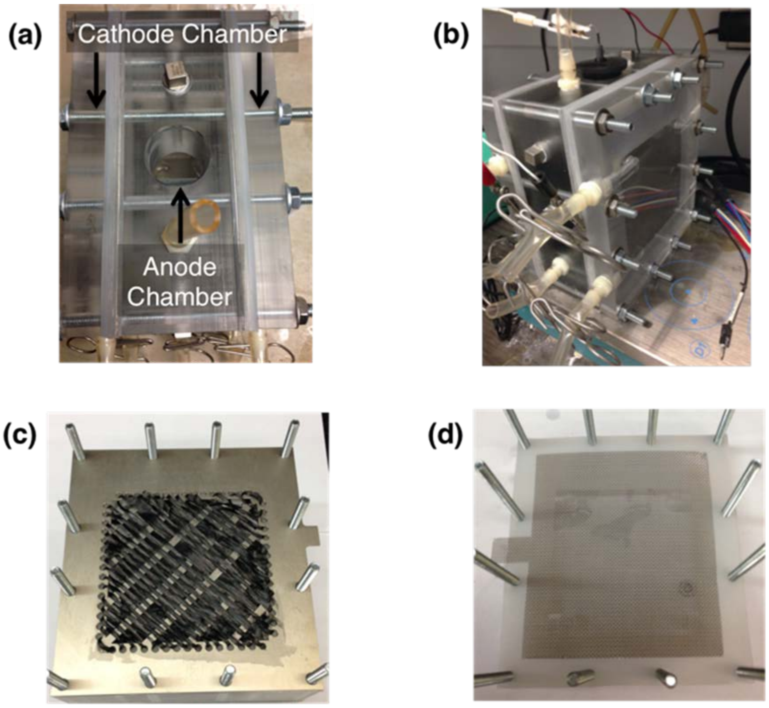

Figure 12. Pictures of modular flat-plate MEC (a) top view of the MEC with configuration of anode and cathode chambers, (b) assembled flat-plate MEC, (c) carbon fiber anode woven with titanium current collector, and (d) SS cathode.

We inoculated the MECs with a mixture of anaerobic digested sludge (2 mL, obtained from Mesa Northwest Wastewater Reclamation Plant in Mesa, AZ, USA) and the effluent from a continuously fed MEC in our laboratory fed with acetate as the electron donor (248 mL). We operated the MECs in batch mode initially, followed by continuous flow of the anode medium at a rate of 0.3-0.5 mL min^{-1}, resulting in a hydraulic retention time of 16.7-27.8 h. The anode feed consisted of 50 mM acetate, 100 mM phosphate buffer (PBS, 85 mM of KH_2PO_4 and 15 mM of Na_2HPO_4), 14 mM ammonium chloride, and trace minerals (Torres et al., 2007). The pH of the medium was ~7.6. We operated the MECs in a temperature-controlled room at 30 °C. We sparged the anolyte and catholyte with ultra-high purity nitrogen gas (>99.999%) to remove O_2 before feeding to each chamber. For experiments where we added CO_2 to the cathode, we used 100% CO_2 that was sparged into an external chamber containing the catholyte. The CO_2 flow rate was 250 mL min^{-1} and we recirculated the catholyte within the cathode chambers at 20 mL min^{-1} flow rate (Figure 13). We set the anode potential at -0.03 V with a multi-channel potentiostat (VMP3, BioLogic Science Instruments, Knoxville, TN), and recorded current, and anode and cathode potential every two minutes. This anode potential was selected on the basis of a previous study that has shown that the potential is oxidizing enough to allow optimum growth of known ARB (Torres et al., 2009).

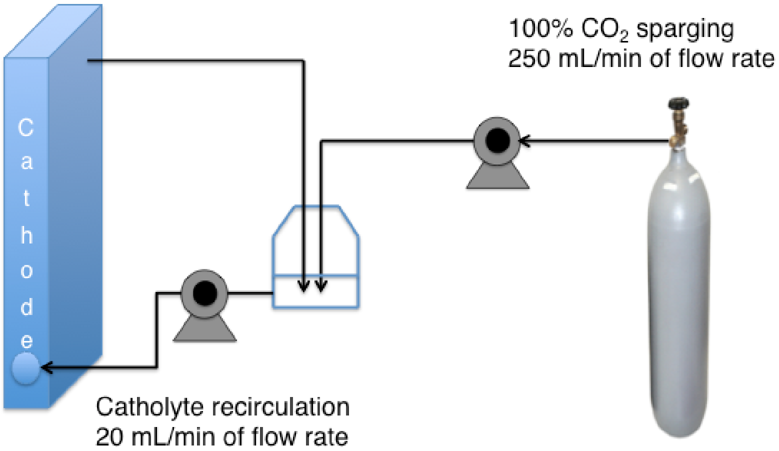

Figure 13. Schematic for CO_2 addition to cathode.

After a stable current was obtained, we developed *j*-*V* curves using chronoamperometry starting from the open circuit potential up to the anode potential resulting in the highest saturation current densities, stepping the potential 25 mV for each data point. We waited ~10 minutes for steady current at each potential before stepping up the anode potential. At the end of each experiment, we performed electrochemical impedance spectroscopy (EIS) measurements at 100 kHz with an amplitude of 10 mV, while using the anode as the working electrode and the cathode as the counter and reference electrode to determine the Ohmic resistance between the anode and the cathode. The Ohmic resistance used was an average value from 20 measurements. We also performed *iR* correction for all anode and cathodes potentials by doing EIS measurements in the same way as described above but with the anode or the cathode as the working electrode and the Ag/AgCl reference electrode as the reference.

Electrochemical impedance spectroscopy of MEC cathodes. To characterize the performance of the cathodes we used in the MECs during operation (with or without addition of CO_2 to the cathode), we performed potentiostatic EIS measurements at each condition at various cathode potentials. We used an amplitude of 10 mV, with a frequency range of 100 kHz to 10 mHz. We took six data measurements per decade of frequency. We fit the Nyquist plot data using an equivalent circuit model containing two charge transfer resistances in series with an Ohmic resistance. For each cathode potential, we report a total area-specific resistance, which is the sum of the two charge transfer resistances.

Characterization of anion exchange membranes. We characterized various commercially available AEMs (Table 6) to use in our MECs when adding CO_2 to the cathode. We used AEMs since it has been showed that when electroneutrality is maintained by transport of OH^- from the cathode chamber to the anode chamber, either directly or via carbonate and/or bicarbonate species, the pH on the anode can be maintained close to 7 (Torres et al., 2008; Fornero et al., 2010). For the AEM characterization, we used electrochemical cells containing two chambers filled with 100 mM $NaHCO_3$. We performed EIS on the cell with one stainless steel rod (≈9 cm^2, 5 mm diameter) as the working electrode, and another as the counter and reference electrode, using a frequency of 100 kHz and an amplitude of 10 mV. This allowed measurement of the Ohmic resistance between the two electrodes for the various AEMs. We also performed EIS analysis without a membrane to obtain the Ohmic resistance just from the liquid electrolyte used, thus making it possible to determine the resistance to ion transport from the AEMs only from subtraction. We show a list of the membranes tested in Table 6 along with their thickness and pH stability range.

Table 6. List of membranes tested, including their supplier and physical properties.

Type	Membrane	Supplier	Thickness (mm)	pH
Heterogeneous	AMI-7001	Membranes International, USA	0.50-0.51	1-10
	Excellion I-200	SnowPure, USA	0.32-0.34	NR
Homogenous	Fumasep FAA	FuMa-Tech, Germany	0.13-0.15	6-13
	Fumasep FAB	FuMa-Tech, Germany	0.10-0.13	0-14
	A201	Tokuyama, Japan	0.028	0-14

Characterization of cathode materials. For testing and comparing the performance of different cathodes for use in the MECs, we used a flat-plate two-chamber electrochemical cell having the same volume (100 mL) for each chamber. We used a stainless-steel mesh electrode (Super-Corrosion-Resistance Type 316 Stainless Steel Mesh, SS [20 x 20 wires/inch] (McMaster-Carr, USA) or a nickel mesh electrode, Ni 200 [70 x 70 wires/inch] (Unique Wire Weaving Co., Inc., USA) of size 7 cm x 7 cm (49 cm^2 projected area) as the cathodes. We provide more information on the two materials in Table 7. We used AMI-7001 as the membrane, and the same Ni mesh electrode as the counter electrode for all tests. For the electrolyte, we used 100 mM NaOH solution in both chambers. We performed linear sweep voltammetry (LSV) on the cathodes at 30 °C at a scan rate of 10 mV s^{-1}. Before performing LSV, we measured the Ohmic resistance by EIS and applied *iR* correction during the LSV. We repeated the LSV for at least three times for each material.

Table 7. Properties of cathode meshes tested in this study.

	Nickel	SS
Item	Nickel 200	Super-Corrosion-Resistance Type 316
Wire mesh (Wires/In.)	70 x 70	20 x 20
Wire diameter (In.)	0.004	0.018
Width opening	0.0103	0.032
% Open area	51.8	41
Cost ($/$ft^2$)	22.76	14.2
Company	UNIQUE WIRE WEAVING Co., Inc.	McMaster-Carr

4.5.2. Design of microbial H_2O_2 producing cells (MPPC)

Figure 14 illustrates our two-chamber, flat-plate MPPC operated at 30°C. The anode, cathode, and membrane had geometrical areas of 49 cm^2 at 30°C, shown in Figure 15. The anode chamber volume was 200 mL. The anode was composed of carbon fiber (24K Carbon Tow, Fibre Glast, OH, USA) woven through a titanium frame, as detailed in Ki et al. (2016). An AMI-7001 membrane was preconditioned in 2 M NaCl for one day prior to use. The cathode chamber consists of a 18-mL liquid serpentine flow cell and a serpentine air chamber supplied with 30 cm^3/min air (EcoPlus® Eco Air 3 commercial pump). The two cathode chambers are separated by the carbon cloth cathode (FuelCellsEtc GDL-CT). The liquid-exposed side of the cathode was coated with a slurry of 0.5 mg/cm^2 Vulcan carbon powder using a paint brush. The catalyst slurry consisted of 0.5 g Vulcan carbon powder, 3.5 mL 0.83 mL/cm^2 of 5% Nafion dispersion in alcohol (D521; FuelCellStore). The air-exposed MPL side is coated with 2 layers of 16 mg/cm^2 Teflon PTFE DISP 30 cured 15 minutes at 200°C and 1 hour at 280°C to improve cathode hydrophobicity. The distance separating the anode and cathode was ~0.5 cm. We used a Bioanalytical Systems, Inc. RE-5B Ag/AgCl reference electrode (+0.27 V_{SHE} in acetate media at 30°C) and a Bio-Logic VMP3 potentiostat to control anode potential at -0.30 $V_{Ag/AgCl}$ and monitored current production. We measured pH using Thermo Scientific, Inc.'s Orion 2 Star pH meter.

We inoculated the anode chamber with effluent from operating MECs in our laboratory to develop current-producing biofilms. The MPPC's anode was poised at -0.3 $V_{Ag/AgCl}$ and operated in batch mode until biofilms were formed and then placed into continuous-flow mode fed with 100-mM acetate medium (~pH 7) at a 0.5-h HRT (Parameswaran et al., 2012). The cathode was operated in continuous-flow mode and fed 200 mM NaCl catholyte with a 4-h HRT to the liquid chamber and 20 cm^3/min air to the air chamber. The MPPC operated in the peroxide-producing mode for more than three weeks.

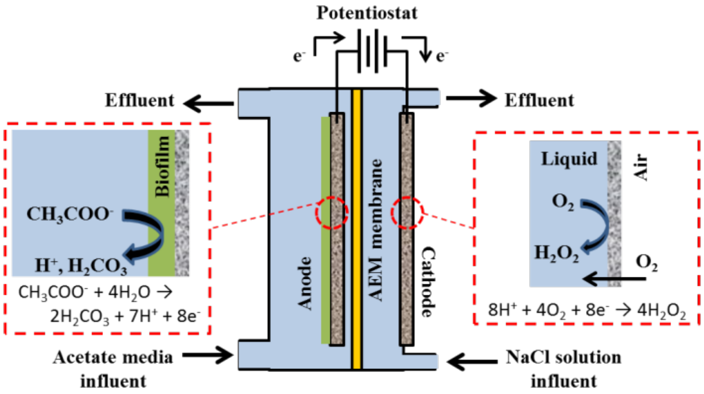

Figure 14. A schematic of the MPPC configuration used to produce H_2O_2 in the liquid cathode chamber.

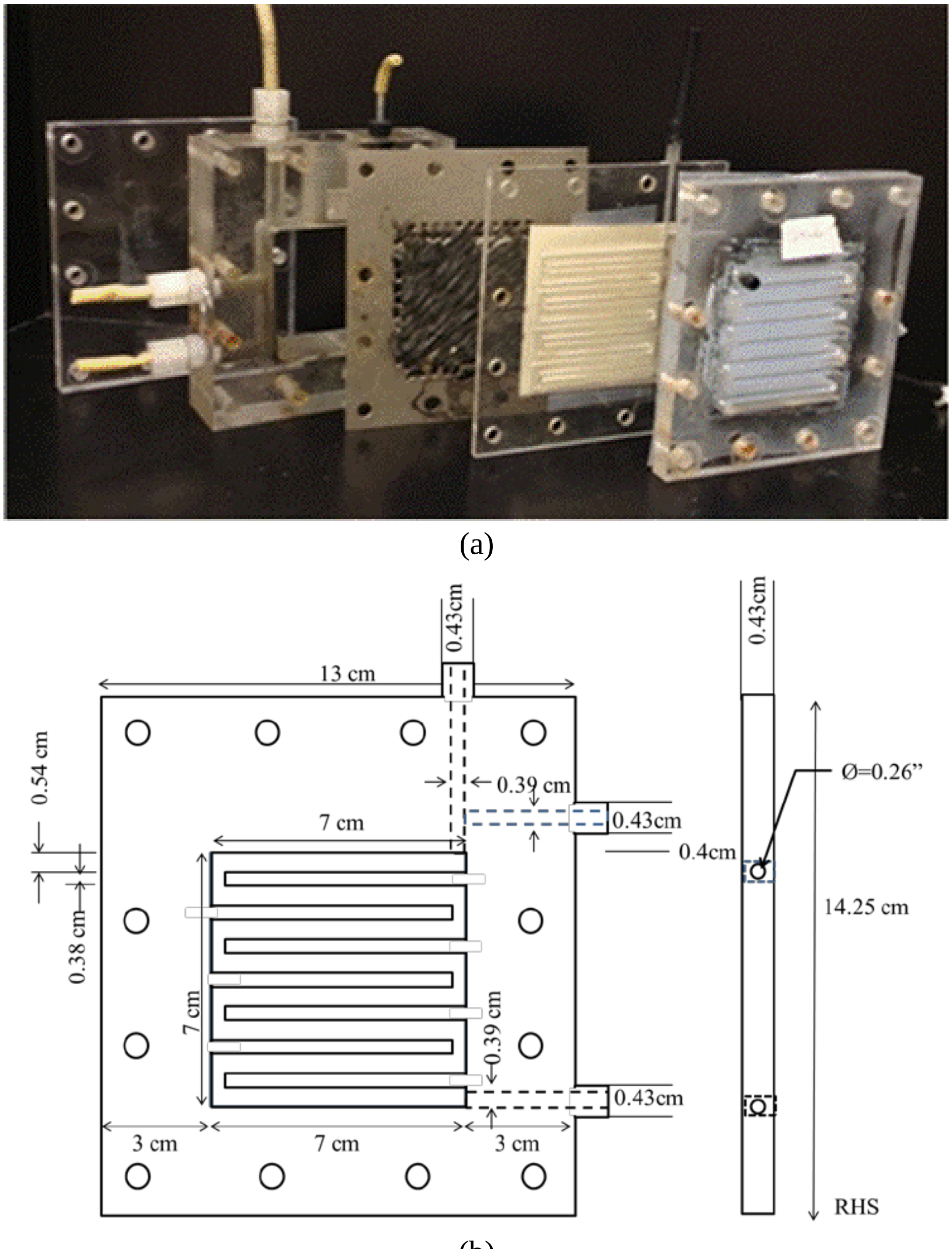

(a)

(b)

Figure 15. (a) The MPPC setup (from left to right): backing plate, anode chamber, anode, the liquid cathode chamber with AEM membrane attached between the anode and cathode, and the air cathode chamber with PTFE-coated cathode between the liquid and air cathode chambers. (b) A schematic of the serpentine cathode design.

4.6. Optimization of Prototype MFCs (Task 7)

4.6.1. Acetate-fed MPPC

We followed the same design of MPPC above. To inoculate the MPPC, we used 100-mL of inoculum grown from operating MEC reactors fed with acetate medium and 100-mL of 1-M acetate MEC media at pH 7 to develop current-producing biofilms. Once the biofilms achieved >10 A m^{-2}, we fed the anode continuously with 100-mM acetate medium with a 0.5-day HRT to provide additional mixing to improve current production. Throughout operations, the cathode was continuously fed with a catholyte solution. The air side of the cathode was supplied with air from an EcoPlus® Eco Air commercial pump and regulated using a Dwyer RMA-151-SSV 0-50 $cm^3\ min^{-1}$ flow meter.

The reactor operated for more than 7 months to determine long-term functionality and performance. Figure 16 summarizes the operating conditions and performance in terms of H_2O_2 concentration over the 7 months. Several catholytes were evaluated for H_2O_2 production using a 4-h HRT and no ethylenediaminetetraacetic acid (EDTA): 100-500-mM NaCl at pH 7; 100-mM H_3PO_4/KH_2PO_4 (PBS) at pH 2.5; 200-mM PBS at pH 2.5; 400-mM $NaHCO_3$ at pH 6.5; and 1-M $NaHCO_3$ at pH 8.5. We studied the effects of catholyte HRT from 1- to 6-h using 200-mM NaCl and no EDTA. We evaluated the use of EDTA as a stabilizer in 200-mM NaCl catholyte at concentrations ranging from 0- to 2-mM at a 4-h HRT. To obtain steady-state data, we waited at least 5 cathodic HRTs after each condition change prior to taking any H_2O_2 measurements. Reported cathode potentials were corrected for Ohmic resistance as established in Young et al. (2016).

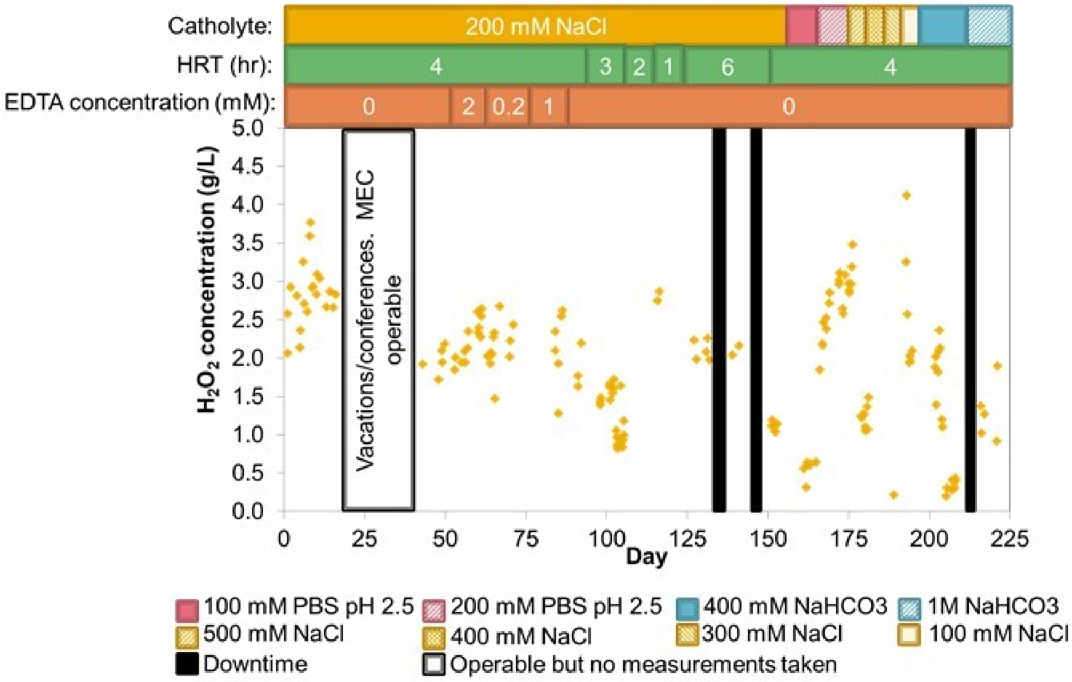

Figure 16. Graph summarizing the conditions during long-term MPPC operation. The first two downtime events were associated with membrane failures. The last downtime event was due to the catholyte chamber pump failing.

We performed cyclic voltammetry (CV) for different performance conditions to evaluate changes in cell overpotentials (Bard and Faulkner, 2001). CVs were performed at a 1 mV sec^{-1} rate from -0.55 to -0.1 V with the anode as the working electrode.

4.6.2. Primary sludge (PS)-fed MPPC (dual-chamber MPPC)

We operated a flat-plate microbial electrochemical cell with anode and cathode separated by an AEM AMI-7001 (Membranes International, Inc.). Following the same design described above, one central anode chamber contained two anodes, and the anode chamber was flanked by two separate cathode chambers with one cathode each. The same electrochemical cell was used as an MEC and an MPPC. The anodes were exactly the same, but the electrodes used for cathodes and the cathode chambers were modified for the MPPC. Experiments were first conducted in MEC mode, followed by MPPC mode. Enough time was allowed for operation under each condition to reach a pseudo-steady state: ~30 days for MEC and ~10 days for MPPC.

The anodes were fabricated using carbon fibers (24K Carbon Tow, FibreGlast, OH, USA) woven as a mesh through a titanium plate current collector (Ultra-Corrosion-Resistant Titanium Grade 2, 0.035" of thickness, McMaster-Carr, USA). The geometric surface area of each anode was 100 cm^2, and the anode chamber was 500 mL. The cathode for the MEC for H_2 production was the same as before (Ki et al., 2016; Ki et al., 2017), but the cathode chamber for the MPPC for H_2O_2 production consisted of a serpentine flow field having a ~120 mL volume between the AEM and cathode. Details on parts, configuration, and assembly of MPPC are provided in Figure 17.

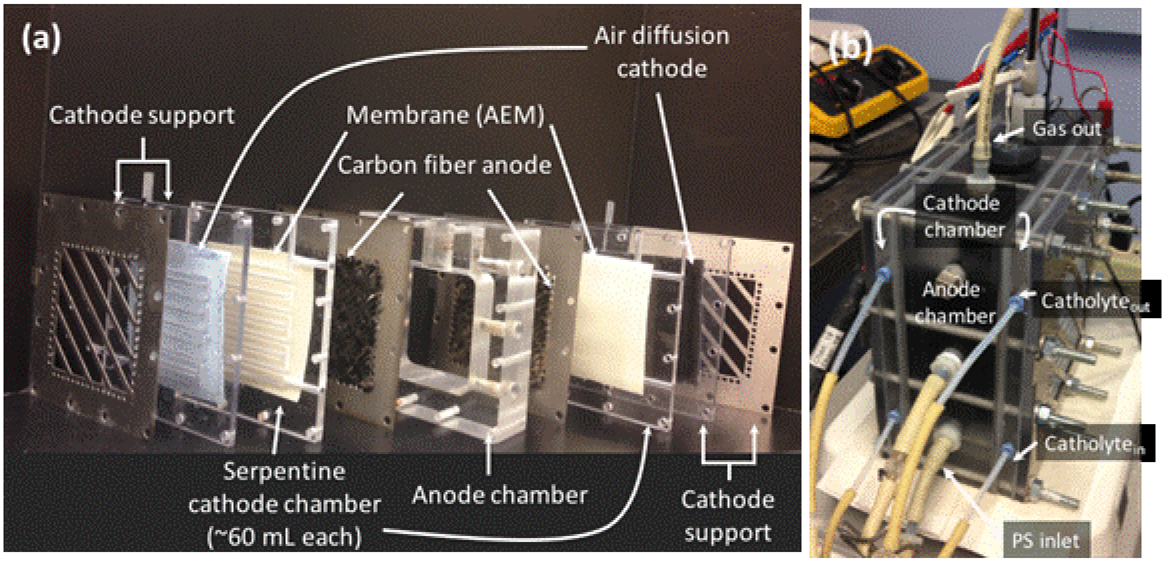

Figure 17. Microbial peroxide producing cell (MPPC) design. All reactor components (a) and the assembled system (b).

We used stainless-steel meshes (Super-Corrosion-Resistance type 316, McMaster-Carr, USA) as the cathodes for H_2 production in the MEC. The cathodes for H_2O_2 production in the MPPC were prepared with a carbon-cloth support (GDL-CT, Fuel Cells Etc, TX, USA), coated with a slurry of Vulcan carbon powder on the liquid-exposed side, and with a 30% PTFE microporous layer (MPL) on the air-exposed side; this was the same as used in Young et al. (2016). The area of each cathode was ~79 cm^2 (8.8 cm x 8.8 cm).

The distance between the anode and cathode was less than 0.5 cm in the MEC and ~1 cm in the MPPC. We included a reference electrode (Ag/AgCl, MF-2052, Bioanalytical Systems, Inc., USA), which was at a ~2 cm distance from each of the anodes. We used a multi-channel potentiostat (VMP3, BioLogic Science Instruments, Knoxville, TN) to control the anode potential at -0.3 V (versus Ag/AgCl) and recorded current, and anode and cathode potential, every two minutes with the EC-Lab software (v. 10.37).

We fed the MEC and the MPPC with PS semi-continuously at a 9-day HRT and with one feeding cycle per day; for example, we removed ~56 mL from the anode chamber and added the same volume of PS to the anode chamber every day. At each feeding, we maintained the pH of ~7.0 in the anode chamber with the addition of 5-M sodium hydroxide (NaOH) as needed (Ki et al., 2017). The electrolyte for the cathode (the catholyte) for MEC was 100-mM NaOH. The catholyte in the MPPC was 50-mM NaOH. We delivered the catholyte continuously in the serpentine cathode chamber of the MPPC with an ~1.5-h HRT for 18 days, and then we changed to batch mode with a one-day cycle. We collected catholyte samples of ~1 mL at 1.5, 3, 6, 12, and 24 hours during batch operation to measure pH, alkalinity, and H_2O_2 concentration.

Analytical methods. We characterized PS for TCOD, SSCOD, TSS, and VSS as described previously. We used colorimetric methods to determine the H_2O_2 concentration in the catholyte of the cathode chamber (Graf and Penniston, 1980). Briefly, the chemical solutions and samples were prepared in 1.5-mL cuvettes in the following order: 10 µL of sample (including H_2O_2 standard), 2 mL of HCl (50 mM), 0.2 mL of KI (1 M), 0.2 mL of ammonium molybdate (1M) in H_2SO_4 (0.5 M), and 0.2 mL of a starch solution (1%) as the indicator. H_2O_2 measurements were performed at a 570-nm wavelength using a Cary 50-Bio UV-Visible spectrophotometer (Varian, Palo Alto, CA). Total alkalinity was measured using spectrophotometric methods by HACH kit and spectrophotometer (DR2700, HACH, Loveland, CO).

Calculations. We calculated CR, anodic CE, and PPE. CR and CE were calculated as described previously in this report. The PPE was calculated for the batch-mode operation from the measured H_2O_2 concentration, the volume of the cathode chamber, and the recorded cumulative Coulombs as electrical current using Eq. (1),

$$H_2O_2\ production\ \ efficiency\ (\%) = \frac{n \times F \times C_{H2O2} \times V}{\int_0^t I dt} \times 100 \qquad (Eqn\ 1)$$

where n is the number of moles equivalent to moles of H_2O_2 (n = 2 here), F is the Faraday constant (96,485 Coulombs mol^{-1}), C_{H2O2} is the measured concentration of H_2O_2 (mol L^{-1}), and V is the volume of cathode chamber. If all the cumulative Coulombs measured were utilized for production of H_2O_2, the PPE would equal 100%.

Molecular microbial ecology. We collected biomass samples for analysis of microbial community structure in the anodes of the MEC and the MPPC; the samples were from the anode suspension (AnS), biofilm from the anode side facing the chamber (BfC), and biofilm from the anode side facing the membrane (BfM) on the carbon fiber electrodes. A schematic showing the sampling locations is provided in Figure 18. We centrifuged suspension samples to obtain pellets for DNA extraction. For the biofilm samples, we scraped off the anode surface using a pipette tip for at least 5 different positions. We prepared 0.17~0.27 gram of wet biomass by combining pellets or biofilm solids for each sample, and we added the combined biomass it to the bead tubes provided by a Power Soil DNA extraction kit (MoBio laboratories, Inc., Carlsbad, CA). We extracted DNA per the instructions provided with the kit, quantified DNA concentration with Nanodrop spectrophotometer, and stored DNA at -20 °C before sequencing.

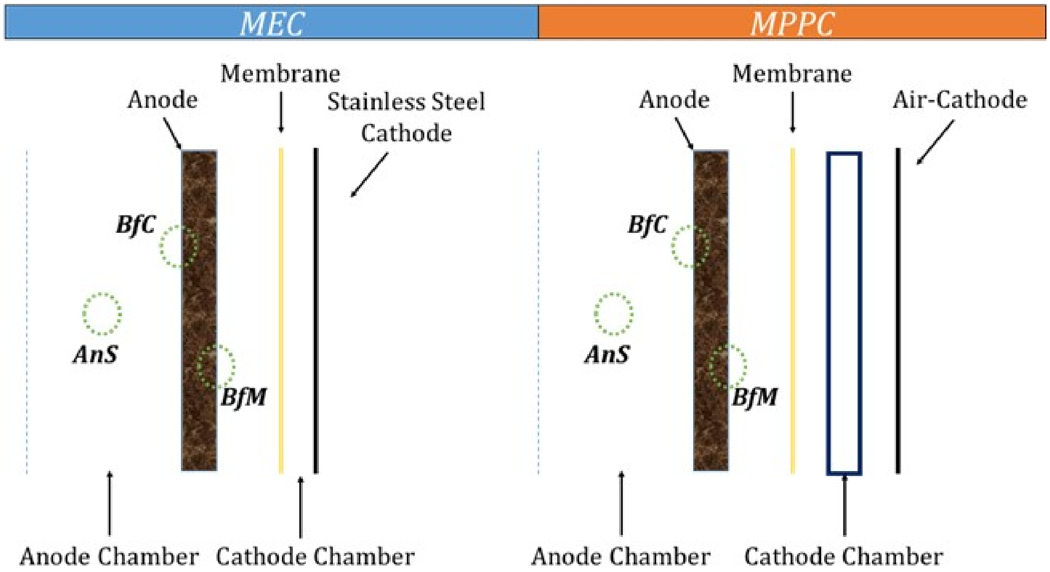

Figure 18. Schematic view for the sampling locations in the MEC and MPPC at the end of operation: anode suspension (AnS), biofilm of chamber side (BfC), and biofilm of membrane side (BfM).

We sent the extracted DNA to the Microbiome Analysis Laboratory at Arizona State University (ASU) for Illumina MiSeq sequencing. Amplicon sequencing of the V4 region of the 16S rRNA gene was performed with the barcoded primer set 515f/806r designed by Caporaso et al. (2012). Data received from the testing laboratory were analyzed using QIIME[29] after discarding sequences shorter than 25 base pairs (bp), longer than 450 bp, or labeled as chimeric sequences. After screening, primer sequences were trimmed off, and taxonomic classification was performed using RDP classifier at the 80%-confidence threshold (Cole et al., 2009). Operating taxonomic units (OTUs) were picked using the Greengenes database by UCLUST algorithm based on ≥97% identity (Edgar, 2010). We aligned the representative sequences for each OTU to the Greengenes database using PYNAST (DeSantis et al., 2006; Caporaso et al. 2010). Then, we made the OTU table and removed singletons. Lastly, the OTU table was rarefied to the minimum number of sequences among 6 samples (35,928 sequences); the total number of sequence reads for each sample after screenings were: MEC AnS = 58,557, MEC BfC = 64,681, MEC BfM = 56,365, MPPC AnS = 35,928, MPPC BfC = 58,902, and MPPC BfM = 55,570.

4.6.3. Primary sludge (PS)-fed MPPC (single-chamber MPPC, sMPPC)

Feed primary sludge. We obtained feed PS from GWRP and stored it in a temperature-controlled room at 4°C before use. We diluted the raw PS for the MPPC influent by ~2-fold with DI water providing an influent PS of 26-32 g/L of TCOD and 15-17 g/L of VSS. We measured the characteristics of the influent PS at the beginning and the end of each 6-day storage period. Characteristics of averaged influent PS are summarized in Table 8.

Table 8. Average of characteristics of influent PS fed to single-chamber MPPC (sMPPC).

Parameters	Unit	Average	Stdev
TCOD	mg/L	30,000	800
SCOD	mg/L	1400	100
TSS	mg/L	19,000	400
VSS	mg/L	16,000	300
pH	-	5.7	0.2

Design and operation of sMPPC. We operated a flat-plate microbial electrochemical cell with H_2O_2 production (MPPC), which was slightly modified from previous designs (Ki et al., 2016; Ki et al., 2017b). This design contained one central anode chamber with a 0.5 L volume, two anodes and was flanked by two separate air-cathodes. Carbon fibers woven on a titanium plate current collector were used for the anodes. Air-cathodes were fabricated in the lab with the protocol described in Young et al. (2016, 2017) and Ki et al. (2017b), optimized for H_2O_2 production. We coated a carbon-cloth with a slurry of Vulcan carbon powder on the liquid-exposed side and 30% PTFE MPL on the air-exposed side. The projected area of each anode and cathode was ~100 cm^2 (10 cm x 10 cm). Instead of using an AEM, we tested two different types of separators between the anode and cathode; eliminating the cathode chambers. The first separator tested was a glass fiber (GF, 1 µm pore size, 330 µm thickness, Type A/E, PALL Corporation) and the second was a stitchbond polyester fabric (SPF, Metacrylics, 360 µm thickness). Sludge liquid filled in the anode chamber and soaked through the separators to reach the cathode catalysts for electrochemical reactions. Figure 19 provides details on parts, configuration, and assembly of sMPPC. The distance between the anode and cathode was ~0.25 cm. A reference electrode (Ag/AgCl, MF-2052, Bioanalytical Systems, Inc., USA) was inserted in the middle of the anode chamber, at a ~2 cm distance from each of the anodes. We fixed the anode potential at -0.3 V (versus Ag/AgCl) using a multi-channel potentiostat (VMP3, BioLogic Science Instruments, Knoxville, TN) and recorded the current and anode and cathode potential every two minutes with EC-Lab software (v. 11.0).

We cultivated ARB first in MEC mode for 18 days by feeding an acetate medium (50 mM acetate, 100 mM PBS, 14 mM ammonium chloride, and trace minerals) with a biofilm scraped from pre-acclimatized MEC that was also fed with an acetate medium (Ki et al., 2017a). We then switched the reactor to sMPPC mode and operated the sMPPC with acetate medium for over 2 months. After the cultivation of ARB, we replaced the feed with PS, and operated the sMPPC semi-continuously; first at a 6-day HRT and then at a 3-day HRT for a minimum of 5 cycles at each HRT. We then analyzed characteristics of the PS effluent collected once the current had stabilized after each feeding. The anode chamber pH mas maintained at ~7 with the addition of NaOH (5M) during regular checks of the PS effluent. Table 9 details the variations in sMPPC construction and operation: filters (GF vs SPF, Exp. 1 & 2), HRTs (6- vs 3- HRT, Exp. 2 & 3), and circuit modes (closed vs open, Exp. 2 & 4). Electrons from the PS were captured for H_2O_2 production in closed circuit mode, while no electrons were captured in the open circuit mode.

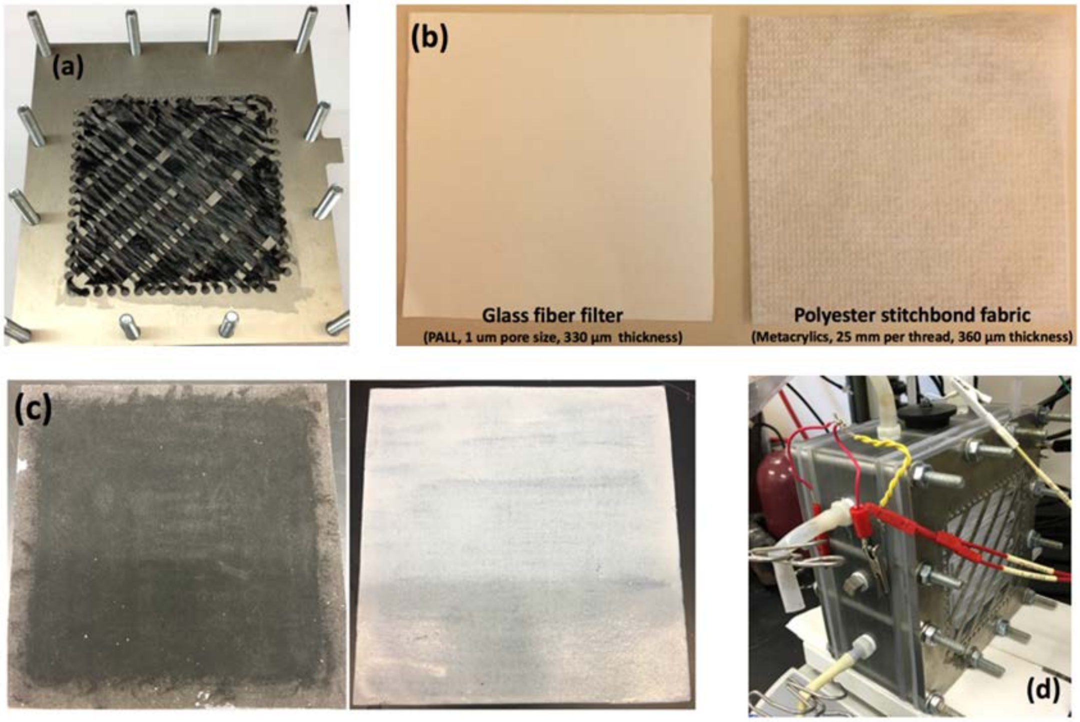

Figure 19. Details of single-chambered microbial H_2O_2 production cell (sMPPC): (a) carbon fiber anode woven with titanium plate, (b) two different filters used in the sMPPC, (c) cathode coated with Vulcan carbon with PTFE coating to air-side, and (d) assembled and potentiostat channel connected sMPPC.

Table 9. Design of experiments with separators, circuit connection, and PS loading rate.

Exp.	Separator	Circuit mode	PS loading rate
GF-Closed	GF	Closed	4.3 gCOD/L/d (2.5 gVSS/L/d)
SPF-Closed	SPF	Closed	5.0 gCOD/L/d (2.7 gVSS/L/d)
SPF-Open	SPF	Open	5.2 gCOD/L/d (2.8 gVSS/L/d)

GF: glass fiber, SPF: stitchbond polyester fabric

Analytical methods. TCOD, SCOD, TSS, VSS, VFAs, and total and fecal coliform of PS were characterized. We measured COD using spectrophotometric methods by a HACH kit (High Range Plus COD digestion vials) and spectrophotometer (DR2700, HACH, Loveland, CO). TSS, VSS, TCOD, and SCOD were prepared as previously discussed in this report. For total and fecal coliform enumeration, we followed *Standard Methods* (APHA, 2012); in brief, total coliforms were determined after 24-hour incubation at 37 °C on Difco^{TM} LB agar (Becton, Dickinson and Company, Sparks, MD), and fecal coliforms were determined using a multiple-tube fermentation technique with A-1 broth (Sigma-Aldrich, St. Louis, MO) after incubation for 3 hours at 35 °C and for 21 hours in a water bath at 44.5 °C.

4.7 Engineering Design and Life Cycle Analysis (Task 8)

4.7.1 Basis of Flows and Wastewater Compositions

Water and wastewater flows were developed from Noblis (2010) and are summarized in Table 10. The averages of these ranges were assumed for the population of company and battalion size bases. Noblis (2010) reports 35 gal/day/person wastewater production at military bases (Noblis, 2010). Based on Noblis (2010) and Metcalf & Eddy (2014), 15 percent of all wastewater is BW and 85% is GW. Based on data obtained during this project, 50% of the influent COD is influent biological oxygen demand as measured at 5 days (i.e., BOD_5). The wastewater composition used in the basis of design for the treatment alternatives is summarized in Table 11. For consistency, each scenario is bounded by the U.S. EPA's wastewater discharge standards of 30 mg BOD/L and 30 mg TSS/L (EPA, 1984) when the treated effluent is discharged to percolation fields or surface waters.

For each of the two (2) FOB scales, three scenarios were evaluated corresponding to: conventional treatment (CT), MFC with electricity production (MFC-E), and MPPC with H_2O_2 production (MEC-H2O2).

Table 10. Summary of FOB scales and Wastewater Flows.

		Graywater	Blackwater	Total
Scale	Soldiers	Gallons/day	Gallons/day	Gallons/day
Company	150	4,460	788	5,250
Battalion	600	17,900	3,150	21,000

Table 11. Wastewater Composition.

	COD (mg/L)	BOD_5 (mg/L)	TSS (mg/L)
Graywater	285	143	183
Blackwater	8350	4180	690
Combined Graywater/blackwater	1500	750	873

4.7.2 Conventional Wastewater Treatment Scenarios for LCA Analysis

Conventional WWT processes for company and battalion scales were based on current treatment methods at FOBs, where combined BW and GW is stored in a holding tank until it can be burned in a burn pit or the combined wastewater is treated in an aerated lagoon without further treatment. Process flow schematics for company and battalion scales are shown in Figure 20.

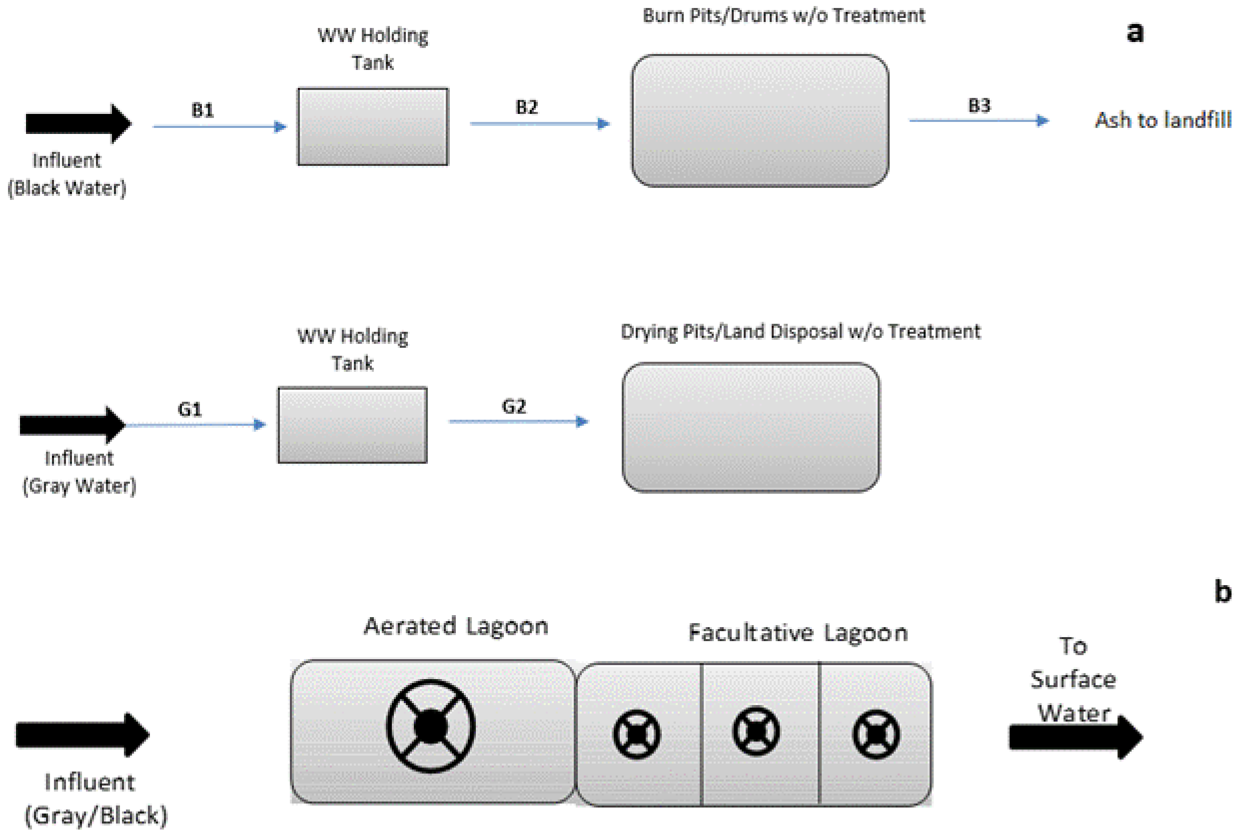

Figure 20. Company (a) and battalion (b) scales conventional treatment (CT) process flow diagrams.

MFCs with Electricity-Generation Wastewater Treatment Scenarios

Power generation is modeled in the LCA and represented in the node "Energy Recovery" in the process flow diagram figures. The second part of the MFC (separated by a membrane) contains an anaerobic anode chamber, which is where most reduction reactions occur. Research is being conducted on improving power production from anodes and eliminating costs from cathodes, which is assumed to be part of this MFC design. The combined BW/GW COD removal through the MFC was estimated to be 80% and TSS removal to be 40%, based on bench and pilot study results conducted by researchers at ASU. Also, a hydrolysis rate constant of 4.0 d^{-1} was assumed for combined BW/GW based on the same studies.

The MFCs (in this alternative) are assumed to have a potential difference between the anode and cathode reactions capable of generating electrical energy, rather than require more of it. As shown in Figure 21, this scenario combines BW and GW and sends the stream into a microbial fuel cell. A settling tank with coagulant addition is the next treatment step in this alternative, where it is assumed that 80% COD and 60% TSS are removed, based on general assumption guidelines provided in Metcalf & Eddy (2003) as well as data from the Pennsylvania State University research team. The solids from this process are pumped to a sludge disposal unit, which is assumed to run for only a few hours each week, just to load and unload the solids.

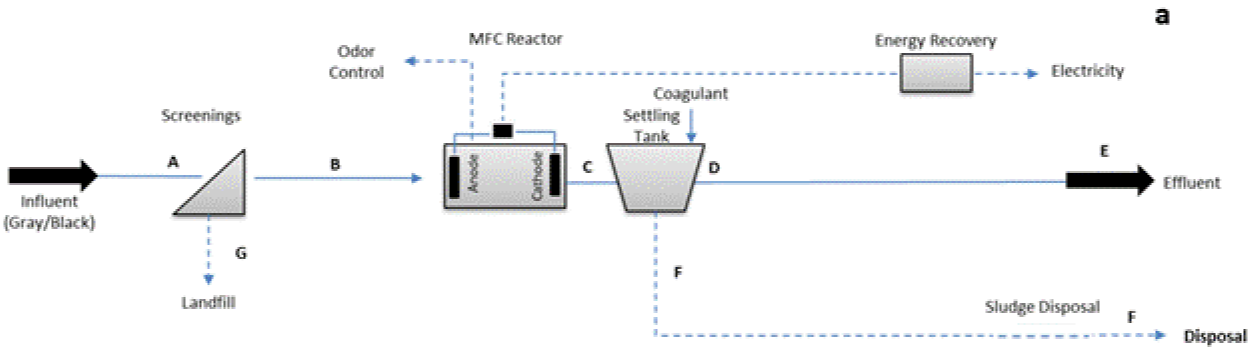

Figure 21. Company- and battalion-scale MFC with electricity production wastewater treatment (MFC-E) process flow diagrams.

MPPCs with Peroxide Production Wastewater Treatment Scenarios

The MFC can either create electricity or hydrogen peroxide, depending on the cathodic catalysts that allow for a $2e^-$ or $4e^-$ oxygen reduction. The following scenarios generally assume that the MFC favors the $2e^-$ reduction reaction in the cathode chamber, producing a net potential in favor of H_2O_2 production. Settling tanks with coagulation and solids disposal units were applied to these scenarios to provide some removal of TSS and COD. The same removal efficiencies from the MFC with electricity production scenario were also assumed for this scenario. This scenario assumed that the amount of hydrogen peroxide that is generated would be to be adequate for directly oxidizing the influent COD to desirable levels in the wastewater holding tanks.

Calculations were performed for each military group (based on the 0.85 lb H_2O_2 produced: lb COD removed and various literature sources) for alternatives favoring hydrogen peroxide production. Therefore, it was assumed that the hydrogen peroxide generated on the cathode would be treating (on average) 80% of the influent COD.

This alternative utilizes an MPPC reactor and subsequent settling tank (with coagulation and solids disposal) for treatment of BW to non-regulatory standards. This process is shown in Figure 22.

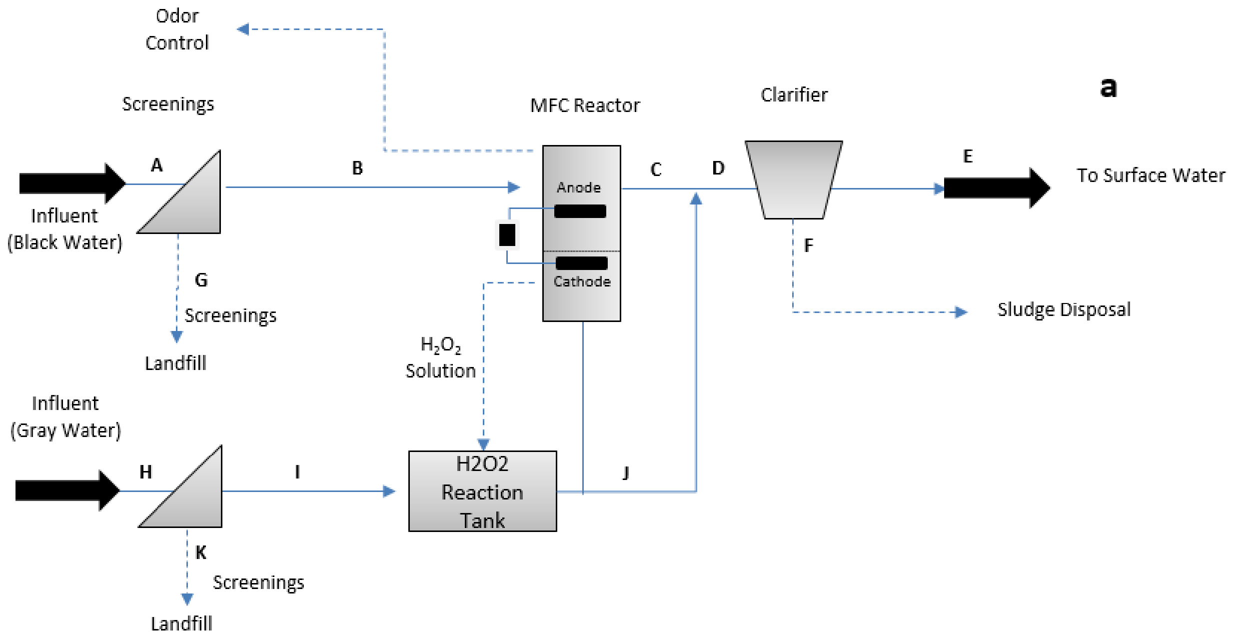

Figure 22. Company and battalion scale MPPC with H_2O_2 production wastewater treatment process flow diagrams.

4.7.3 Effluent Wastewater Compositions

The composition of the final effluent from of all scenarios is shown in Table 12. None of the treatment alternatives meets the U.S. EPA's wastewater discharge standards of 30 mg BOD_5/L and 30 mg TSS/L (EPA, 2014), but all could read the standards with additional polishing steps, such as biofiltration. Evaluation these additional steps were not with n this scope of work and are not discussed in this final report.

Table 12. Effluent Water Quality Summary.

	BOD_5 (mg/L)		COD (mg/L)		TSS (mg/L)		Sludge Flow (gal/year)		Sludge TSS (%)	
Scenario	Comp.	Batt.	Comp.	Batt.	Comp.	Batt.	Comp.	Batt.	Comp.	Batt.
CT	143[1]	92	285[1]	184	215[1]	90	NA	33,700	NA	10%
MFC-E	83	83	165	165	227	227	16,400	65,600	4%	4%
MPPC	76	76	151	151	253	253	18,300	73,300	4%	4%

1. Graywater only

4.7.4 Cost-estimate Methodology

Capital costs of alternatives were estimated using the best readily available information from manufacturers. The costing information is summarized in Table 13. For MFC and MPPC alternatives, we opted to utilize existing "package plants," whose costs were supplied by the manufacturer. For example, Contech, Inc. "Conex" modules were identified as compatible with MFC and MPPC technologies. The Conex units are used as the basis for MFC and MPPC process cost estimates in package plants (CONTECH, 2014). These mobile systems have analogous "base costs," which are based on each process required. The manufacturer noted that some processes required modifications to fulfill the treatment requirements of the proposed systems, which required some assumptions to be made for these additional modification costs. Unless indicated otherwise, the following costs from the manufacturer were used as a basis for capital cost estimates in the LCA.

The analysis of the capital costs of the microbial fuel cells required some more in-depth estimating, since these units usually require high cost specialty materials for proper functioning. Extensive research on MFCs from ASU and CDM Smith provided optimum material unit costs, which translated to volume-based unit costs (with a 1.5 safety factor applied). These were used to develop the cost basis below:

- MFC (for electricity production):
    - Anode: \$4.27/gal treated
    - Cathode: \$3.31/gal treated
- MPPC (for H_2O_2 production):
    - Anode: \$4.27/gal treated
    - Cathode: \$19.80/gal treated

This basis of unit capital-cost estimation for each process was utilized in a large cost-estimation spreadsheet, where the number of units determined the overall capital cost of each alternative. Based on flow rates and characteristics previously discussed, including required spare units for certain processes, total capital costs were developed for each process and therefore each alternative. aA scaling factor was applied for instances where an entire unit process would not be required to fulfill the design requirements of the unit process. Total capital costs were estimated from Eqn. 19 and the basis of design summary including costs is included in Appendix D.

$$Total\ Capital\ Cost = Unit\ Cost\ \left(\frac{\$}{unit}\right) * No.of\ Duty\ Units * scaling\ factor \qquad \text{(Eqn. 19)}$$

Table 13. Equipment Unit Costs.

Unit Process	$/unit
Plastic holding tank (8ft x 24 ft)	20,000
Plastic holding tank (8ft x 30 ft)	25,000
1 x Aerobic Pond 30-ft L x 30-ft W x 10-ft D 1 x Facultative Pond 30-ft L x 30-ft W x 10-ft D	250,000
Flow Equalization (including screenings, chemical addition and partitioning)	100,000
3-stage clarification	150,000
MPPC	136,000
MFC	300,000

4.7.5 Life-Cycle Assessment Methodology

Figure 23 illustrate the system boundary that defined the components included in the life cycle assessment of the three WWT alternatives for each of the FOB sizes.

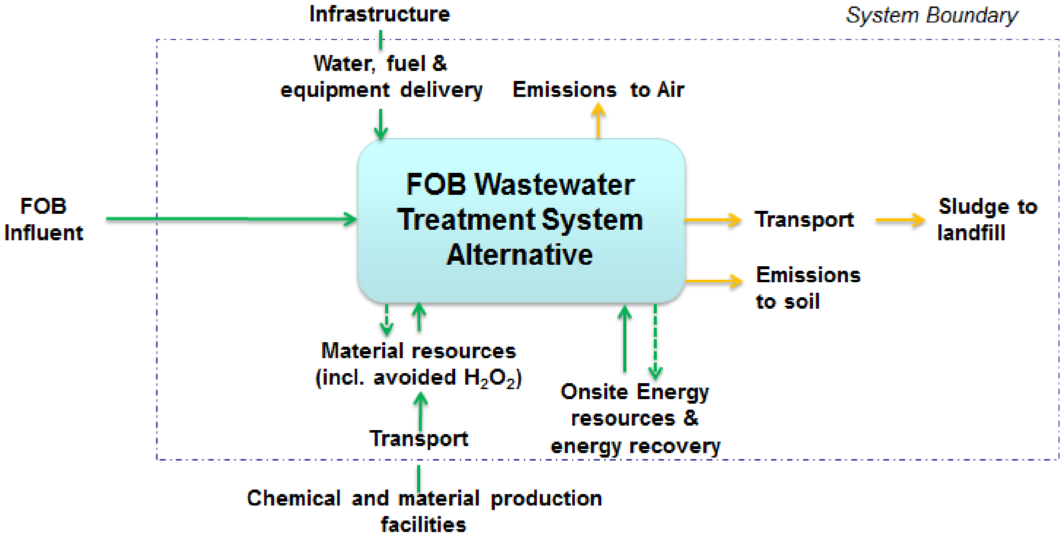

Figure 23. Schematic of LCA boundary.

4.7.6 Life Cycle Inventory

Data for the MFC and MEC life cycle inventories (LCIs) were obtained from laboratory research and institutional knowledge. Conventional WWT design was based primarily by design parameters found in Metcalf & Eddy (2014). Capital and operational data were compiled for each scenario and scale. A summary of this information can be found in Appendix D. LCI processes from Ecoinvent were used when available. Ecoinvent database unit processes were not altered for this study, with the exception of the transportation through trucks which was altered for the weight materials being delivered to the FOB. Due to the limited operational lives of FOBs, the LCI functional unit was 1m3 treated wastewater per year over a 1-year useful life. Capital construction goods are assumed to have a 15-year useful life. Second-order environmental impacts, such as emissions and resources required for production of chemicals and electricity used in construction and operation, were included in this assessment. First-order or direct emissions were not included for such aspects as sludge burning and discharge of treated effluent to receiving water bodies due to the varied composition of wastewater. As such, the impact from discharge of the treated effluent from each of the scenarios was not assessed in this LCA, as it is location specific and this study assesses the impact of theoretical FOBs of varying size. It was assumed that the travel distance for all goods to be used at the FOB, including chemicals, water and capital construction goods is 150 km, and the nearest landfill is 190 km (Noblis, 2010). We assume all onsite power generation is from diesel-burning electric generators. Transportation was assumed to be performed by a standard 32-ton lorry of European origin. Detailed construction and operational data can be found in the Appendix D.

4.7.7 Life Cycle Environmental Impact Assessment

This study broadly assessed the environmental and social impacts of varying WWT alternatives at different FOB scales and should be used as a starting point in more detailed LCA studies on these treatment technologies. Furthermore, as research of the two different types of MECs progresses, those results should be reassessed in the context of the LCA to see how they impact overall results. This analysis follows four stages of an LCA as defined in ISO 14040 standards: (1) definition of goals and scope; (2) LCI compilation using various databases available in SimaPro 7.3.3, the LCA software chosen to analyze the relative sustainability of the processed; (3) life cycle impact assessment (LCIA) using ReCiPe v1.08 method with a hierarchist model typically applied to scientific LCAs; and (4) interpretation of results. LCIA endpoint categories are expressed in terms of damage to human health (HH), damage to ecosystem diversity (ED), and damage to resource availability (RA). Within the HH endpoint, climate change HH, ozone depletion, human toxicity, particulate matter formation categories were assessed. Climate change ecosystem, terrestrial acidification, and terrestrial ecotoxicity were included in the ED endpoint. Fossil depletion was included in the RA endpoint (Goedkoop et al., 2008). We developed an additional endpoint category for soldier casualties based on casualty factors associated with water, fuel, and chemicals transport to and from the FOB and landfilling of sludge wastes based on values reported by the Army Environmental Policy Institute (AEPI, 2009).

5. RESULTS AND DISCUSSION

5.1. Studies on Hydrolysis of Blackwater (Task 1)

5.1.1. Batch methanogenic and fermentation reactors for hydrolysis on primary sludge

Primary sludge characteristics. Table 14 shows the comparison of PS before and after PEF treatment. TCOD and suspended solids have similar concentrations in both cases, which means that PEF did not cause net oxidation of volatile solids. However, soluble components such as SSCOD, VFAs, and proteins increased in PEF-treated PS by 78~86%, since microbial cell membranes and walls and macromolecules were disrupted. The increases of soluble organics were modest for PS compared to wasted activated sludge (WAS), which showed a 4800% increase of SCOD with a lower treatment intensity, ~19.8 kWh/m^3 (Salerno et al., 2009). PEF treatment also increased the sample temperature from 29°C to 49°C, although Sheng et al. (2011) showed that similar temperature increases were not responsible for changes of sludge characteristics.

Table 14. Primary sludge characteristics before and after PEF treatment.

Parameters	Control	PEF treated	Change (%)
TCOD (mg/L)	18,100 (± 92)	18,300 (± 424)	1.4
SSCOD (mg/L)	257 (± 3)	459 (± 2)	79
SSCOD/TCOD (%)	1.4	2.5	79
TSS (mg/L)	13,500	13,400 (± 102)	-0.7
VSS (mg/L)	10,300 (± 19)	10,200 (± 67)	-0.9
Protein (mg/L)	54 (± 1.2)	99 (± 0.9)	86
VFA (mg/L)	79	141	79
Temp. (°C)	29	49	-
pH	6.7	6.9	-

Stability of PEF-treated PS under psychrophilic conditions. A significant benefit of PEF treatment of PS could be microbial inactivation. Sheng et al. (2011) showed that PEF treatment inactivated the cyanobacterium *Synechocystis* PCC 6803, based on culture plating. Here, we evaluated microbial inactivation by monitoring for changes in soluble COD, VFAs, and volatile suspended solids for control and PEF-treated PS during storage at 4°C. Figure 24 shows that control PS underwent rapid degradation during storage at 4°C: SSCOD increased to about 2000 mg/L after 50 days of storage. In contrast, PEF-treated PS maintained stable SSCOD values of around 500 mg/L for the entire 54 days. The increase in SSCOD for the control PS was accompanied by a decrease in the VSS, while PEF-treated PS had a constant VSS concentration. Degradation also could be measured as VFAs, shown in Figure 25. Only the control PS had

VFA production, predominantly propionate. Inactivation by PEF was repeatable, as shown by data for a second trial (Figure 26).

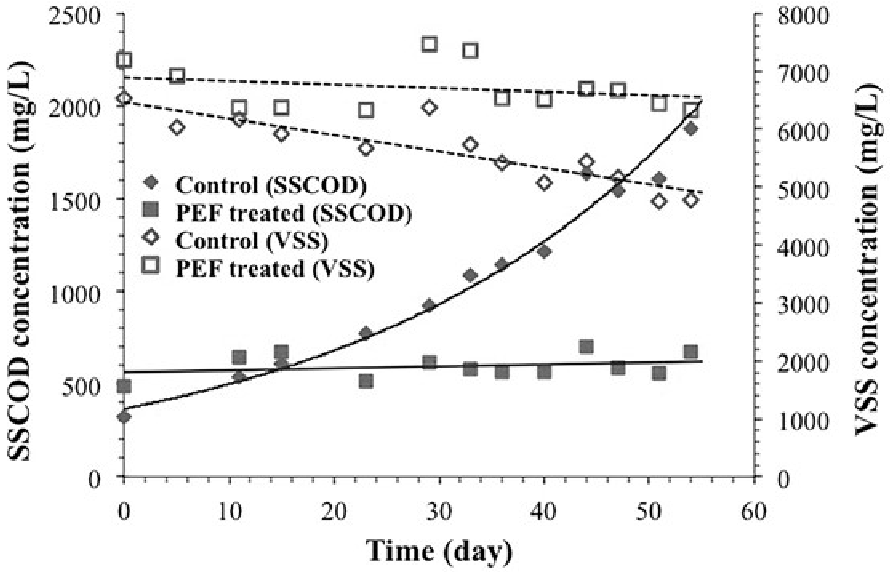

Figure 24. Changes of SSCOD and VSS concentrations of control and PEF-treated PS during storage at 4°C. Solid and dotted lines, used to highlight trends, were generated using the Trendline function in MS Excel.

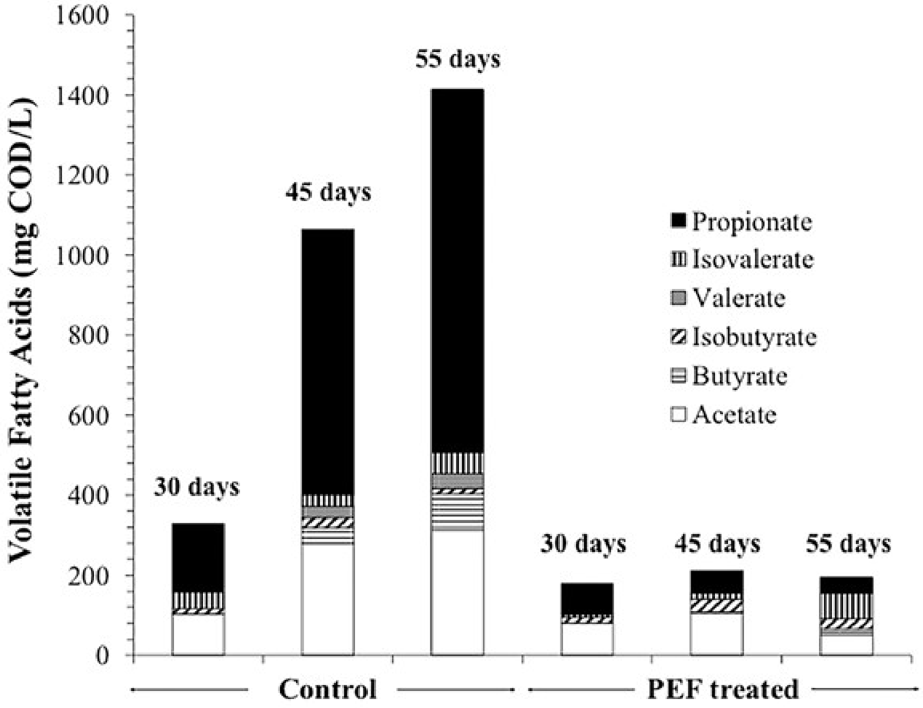

Figure 25. VFAs profiles of control and PEF-treated PS during storage at 4°C. The number of days on top of each bar graph corresponds to the time since storage began.

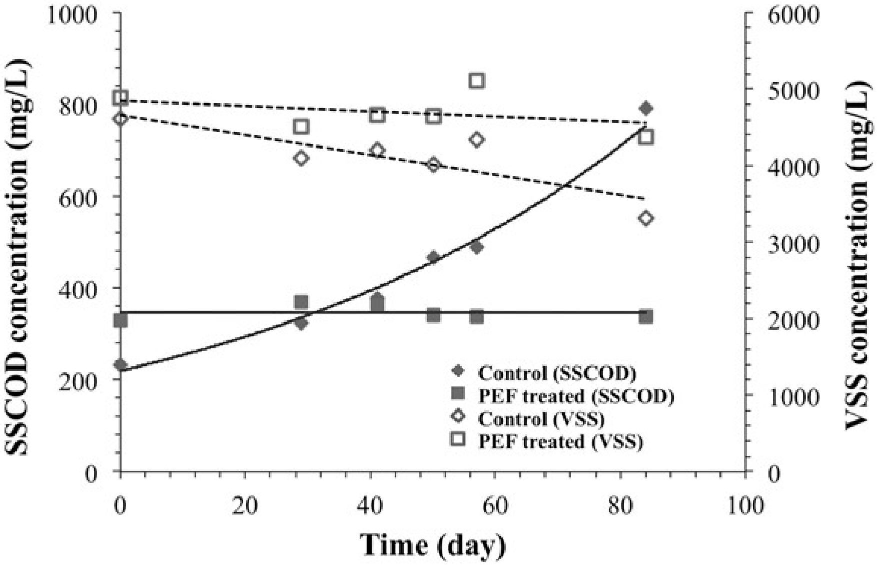

Figure 26. Inactivation of PEF treated PS compared to control PS in which had increase of soluble COD concentration and decrease of VSS concentration with time in the storage of psychrophilic condition with primary sludge.

Biochemical methane potential (BMP). As shown in Figure 27, the initial rate of CH_4 production in BMP assays was rapid for control and PEF-treated PS over ~10 days, after which the rate decreased. Even though the trends for control and PEF-treated PS are similar, the CH_4-production rate was higher for PEF-treated PS between 3 to 14 days, when particle hydrolysis likely played a major role for controlling the rate of methanogenesis. At the end of the BMP assay, the PEF-treated PS had yielded 8% more CH_4, and its fractional COD conversion increased from 32% to 34.5%, an 8% relative increment.

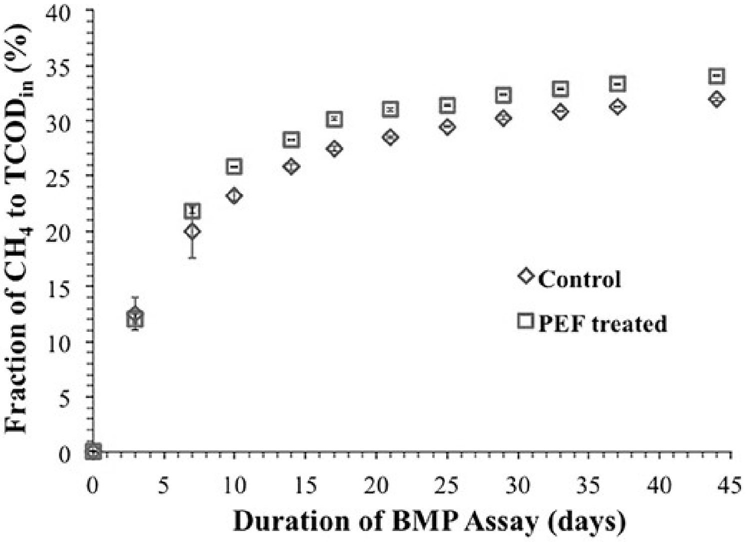

Figure 27. Cumulative CH_4 results for control and PEF-treated PS in BMP assays as a fraction of the TCOD of the starting PS.

Using the first-order model (Eqns. 2 and 3), we computed the hydrolysis rate constants ($k_{hyd\text{-}BMP}$) as 0.105 (± 0.005) and 0.119 (± 0.012) (day^{-1}) for control and PEF-treated PS, respectively.

Other studies place the PS-hydrolysis rate constants in a similar range, between 0.09 and 0.17 (day^{-1}) (Elbeshbishy et al., 2012; Ferreiro and Soto, 2003), with local differences arising due to differences in operational condition (e.g., temperature), particle size of the PS solids, and compositions of carbohydrate, protein, and lipid. The 13% increase in hydrolysis rate coefficient for PEF-treated PS, compared to control PS, may explain the increment to CH_4 conversion within the initial 14 days. CH_4 production from control PS slowly caught up with the PEF-treated PS between 14 and 44 days, resulting in the small decline in the relative increase in CH_4 production, to 8%. These trends indicate that PEF-treated PS may be modestly effective at only short SRT.

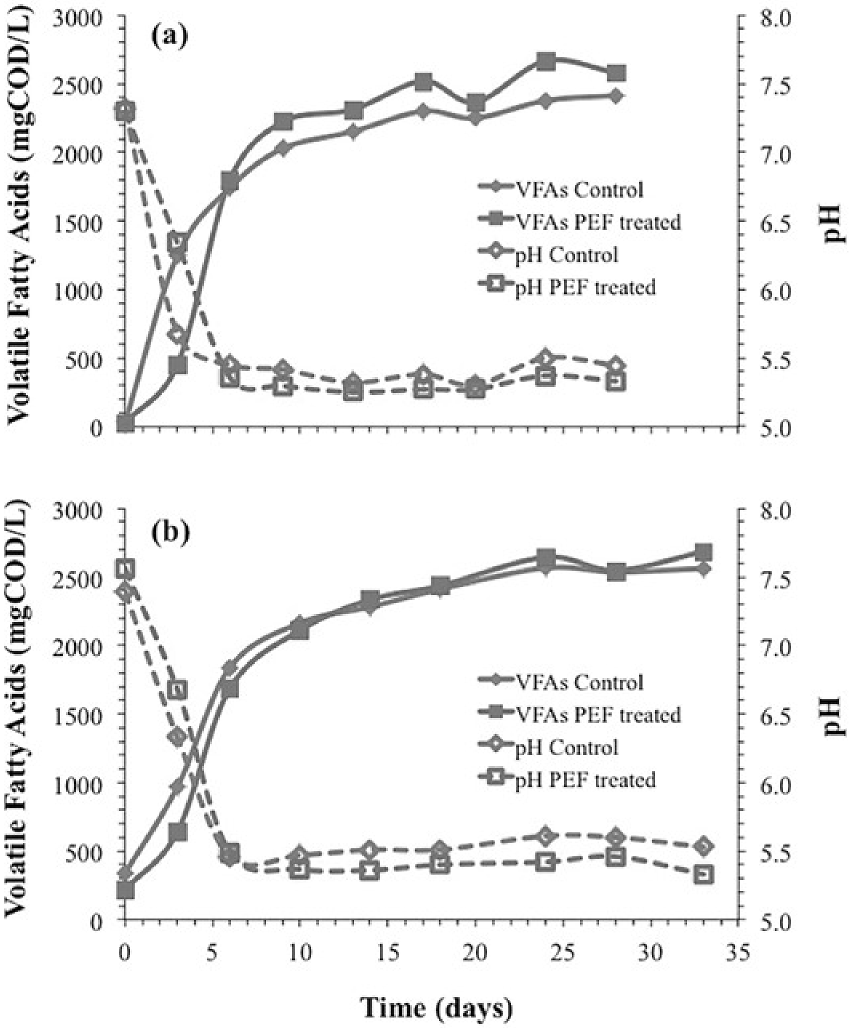

Figure 28. pH and volatile fatty acids (VFAs) concentrations produced in the fermentation batch bottles: (a) 1st enrichment fermentation and (b) 2nd enrichment fermentation.

Fermentation with methanogen inhibition. Figure 28 shows the results of batch fermentations over 30 days with 50 mM BES added to inhibit methanogenesis. The 1st and 2nd enrichments showed similar results for total VFAs and pH. After around 10 days, the pH declined to less than 5.5, and total VFAs stabilized. PEF-treated PS always had pH 0.1 to 0.2 units lower than control PS, one indication of higher fermentation efficiency (FE) to VFAs. After a short lag period, the

PEF-treated PS showed slightly, but consistently higher concentration of total VFA. Based on the VFA production, we also computed the hydrolysis rate constants ($k_{hyd\text{-}fermentation}$) using first-order model: 0.204 (± 0.009) and 0.254 (± 0.089) (day^{-1}) for control and PEF-treated PS, respectively. Thus, PEF-treated PS showed a 24% increase in hydrolysis rate coefficient, compared to control PS, over 10 days. Higher k_{hyd} based on fermentation compared to BMP is consistent to Pratt et al. (2012). At the end of batch fermentation, the PEF-treated PS had accumulated 7% more VFAs, and its fractional COD conversion (gVFA-COD/gTCOD$_{in}$) increased from 13 to 14%, a 7% relative increment. Though the relative increment after PEF treatment by fermentation is similar to the one in BMP assay, the actual magnitude of ~13% conversion in fermentation is much lower, compared to ~30% in BMP during 30 days operation. Hydrolysis and fermentation may have been limited due to three reasons. First, PS may have a substantial fraction of organic solids that resist hydrolysis (Rulkens, 2008; Jones et al., 2008). Second, the low pH after 10 days may have inhibited hydrolytic bacteria (Veeken et al., 2000). Third is feedback inhibition by the fermentation products (Pratt et al., 2012; Raposo et al., 2006).

Even though VFAs accumulation with time had similar trends to CH_4 production in BMP assays, total VFAs produced in control and PEF-treated PS started to stabilize earlier (between 6 to 10 days), compared to BMP (after 10 days) (Figure 27 and 28). Correspondingly, we also show in Figure 29 that acetate production in all cases (control and PEF-treated PS of the 1st and 2nd enrichments) stabilized in less than 10 days of batch operation. On the other hand, other fatty acids (propionate, butyrate, iso-butyrate, valerate, and iso-valerate) increased to the end of the batch experiments (Figure 30). These results support a possible thermodynamic feedback inhibition of β-oxidation that converts longer fatty acids (e.g., butyrate) to acetate (Rittmann and McCarty, 2001; McCarty and Smith, 1986).

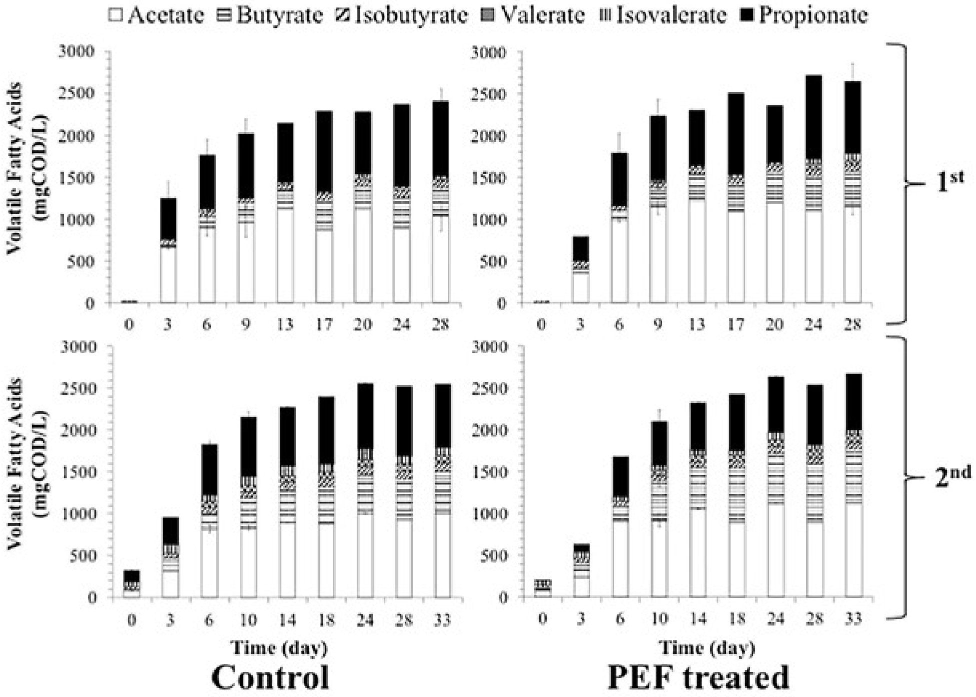

Figure 29. Changes of VFAs profiles during the 1st and 2nd enrichment fermentations for control and PEF-treated PS.

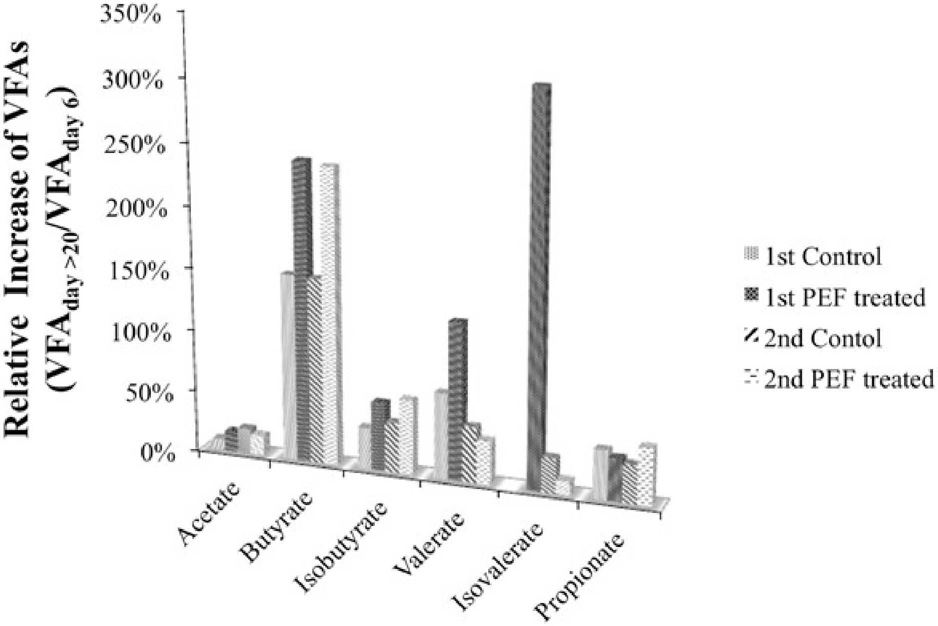

Figure 30. Relative increase of volatile fatty acids (VFAs) with the ratio of the average VFAs over 20 days to VFA at day 6.

PEF treatment effectiveness. Table 15 shows that the methane-production rate (MPR) for PEF-treated sludges were 1.6, 1.7, and 1.1 times higher than the respective controls for thickened mixed sludge (50:50 ratio of WAS:PS), WAS alone, and PS alone, respectively. This highlights that WAS contributed significantly to the positive impacts observed with PEF treatment of thickened mixed sludge (Rittmann et al., 2008). Consistent with the impact of PEF on CH_4 production are the much larger increases in soluble COD after PEF treatment of WAS (4800%) (Salerno et al., 2009), compared to PS (79%) (Table 14). This large difference results from the severe disruption of WAS flocs and bacterial cells (Salerno et al., 2009). In contrast, PS has relatively more non-cellular organic solids, and the organic solids are more readily biodegradable. Thus, PEF treatment of PS did not result in a big increase in SSCOD or a large increment of CH_4 production.

Table 15. Comparisons of methane production rate with different sludge types in anaerobic digestion.

Sludge type	Methane production rate (L/kg VS/ day)		Ratio of MPR increase	Reference
	Control	PEF treated		
WAS + PS (1:1)	794	1270	1.6	Rittmann et al. (2008)
Only WAS	0.0421	0.0724	1.7	Salerno et al. (2009)
Only PS	0.0120	0.0133	1.1	This study

5.1.2. Continuous operations of fermentation reactors for microbial electrolysis cells

Optimizing the pre-fermentation stage. We performed a comprehensive evaluation of the pre-fermentation SRT = HRT with methanogenic inhibition. Batch fermentations were performed in

250-mL serum bottles having a working volume of 180 mL, with ADS from MNWWRP. Three serial enrichments of batch fermentation were performed, all under selective methanogenic inhibition using 50 mM BES. At the end of batch fermentations, we carried out semi-continuous fermentation in the same serum bottles at 6-, 3-, and 2-day solid retention times. Each condition was maintained for 5x SRTs to ensure steady state.

Volatile-Solids Destruction was computed based on the averaged change of VSS concentration for each SRT;

$$Voltile\ Solids\ Destruction\ [VSD](\%) = \frac{(VSS_{in} - VSS_{out})}{VSS_{in}} \times 100 \qquad \text{(Eqn. 20)}$$

We showed VSD results at each SRT for both control and PEF-treated PS. In control PS, the VSD decreased with shorter SRTs from 27% at 6 days to 14% at 3-day SRT. On the other hand, VSD was maintained at around 25% at 3-day SRT for PEF-treated PS (1.8 fold higher than control), indicating its greater biodegradability. However, both control and PEF-treated PS showed only 4% VSD at 2-day SRT, likely due to washout of fermenters and the need for appropriate active biomass.

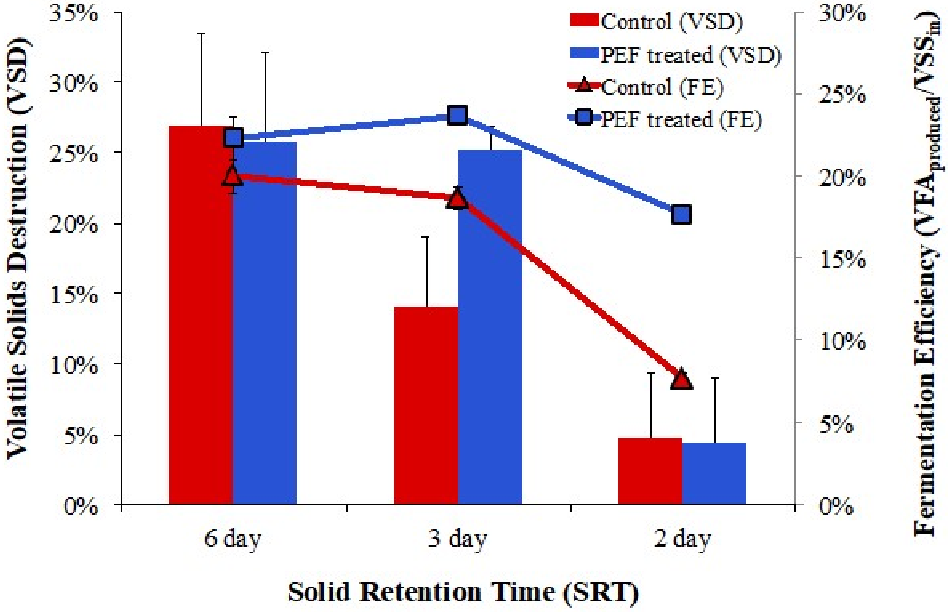

Figure 31. Volatile Solids Destruction (VSD) and fermentation efficiency (FE) (defined as the ratio of $VFA_{produced}/VSS_{in}$) in control and PEF-treated PS, at different solid retention times (SRTs).

This study shows that a relatively longer HRT (=SRT) of 6 days led to the highest fermentation efficiency or FE ($VFA_{produced}/VSS_{in}$) of 20% in the control PS reactor, while PEF treatment shortened it to 3 days, with an FE of 23%. The VFAs - acetate, butyrate, and propionate - are the dominant VFAs in the effluent of the semi-continuous fermentation reactors (Figure 32). The proportion of acetate increased, while that of butyrate decreased when the SRT became shorter, for both control and PEF-treated reactors. Propionate decreased in the control reactors with shorter SRT, while the opposite trend was observed in PEF-treated reactors. PEF-treated PS fermentation at 3-day SRT (= HRT) was the optimum for allowing efficient hydrolysis from PS organic solids and achieving higher VSD and FE (Figure 31).

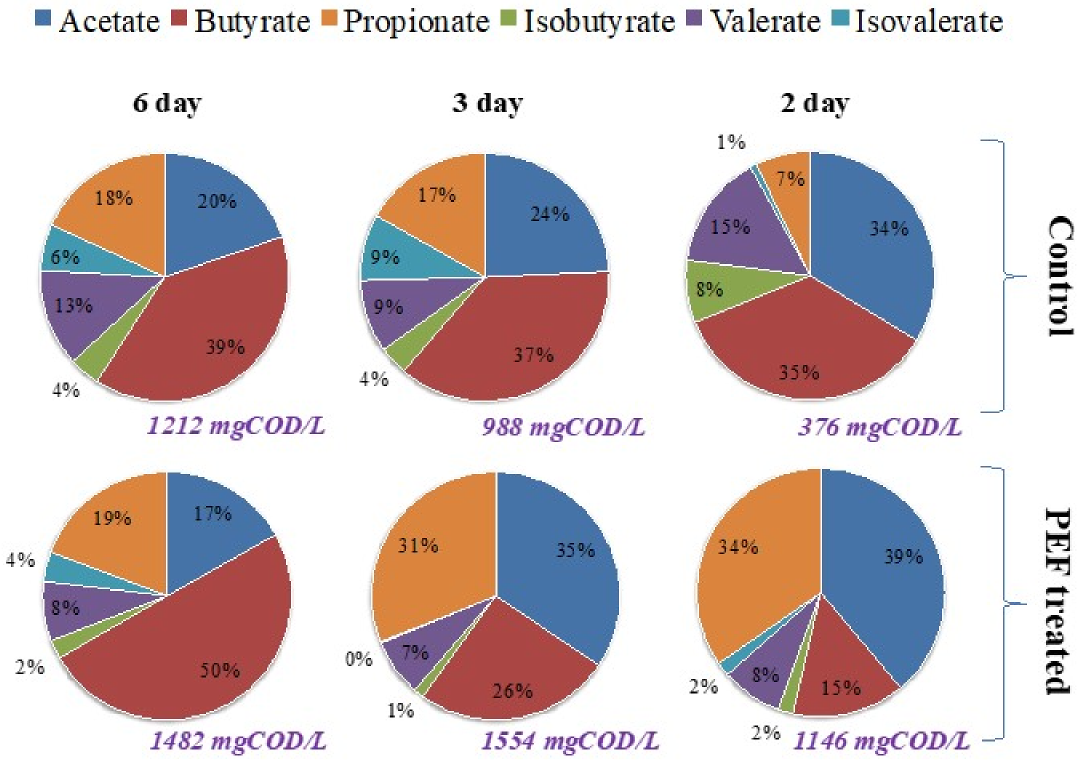

Figure 32. Volatile fatty acids (VFAs) produced and its proportion after stabilization of each SRT (Total VFA concentrations at the bottom of pie charts represent the average of duplicate measurements).

From this analysis, we concluded that 3-day is the shortest SRT allowing efficient hydrolysis from PS organic solids: ~25% of volatile solids destruction and ~23% fermentation efficiency. Thus, we evaluated SRTs of 3 and 15 days without inhibition of methanogenesis. Figure 33 shows the distribution of VFAs and methane produced at the different HRTs and SRTs tested in the fermentation reactors. The 3-day SRT resulted in much more VFAs accumulation (by 1.4~2.5 fold) and less methane production (by 2~7.5 fold). While the longer SRT increased overall hydrolysis of PS, a significant fraction of VFAs available for feeding to the MECs was diverted to methane gas. Furthermore, the increase in SRT did not bring about a large increase in the overall TCOD removal as VFAs or methane, suggesting a higher fraction of recalcitrant compounds in the PS studied. Based on the semi-continuous fermentation experiments, the 3-day SRT (= HRT) was the best condition tested for pre-treatment of PS before MEC.

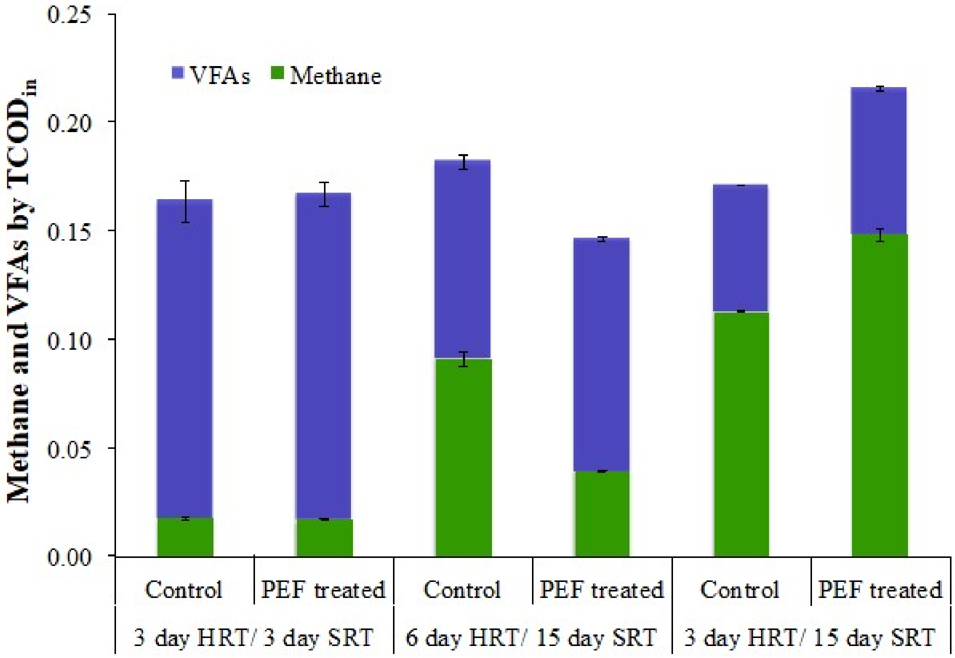

Figure 33. Steady-state fermentation efficiencies to VFAs and methane (g COD of the product normalized to $TCOD_{in}$) for the different fermentation condition (SRT and HRT). The initial $TCOD_{in}$ values ranged from 9400 to 12000 mgCOD/L.

Fermentation reactors fed with control and PEF-treated PS had similar fermentation efficiencies (~17% by $TCOD_{in}$), indicating that the impact of PEF was not manifested by methane and total VFAs productions. However, PEF exacerbated methanogenesis for the 15-day SRT, probably due to lack of washout of methanogens, although the difference also might be associated with a longer adaptation time, as the experiments were done sequentially in the same bottle.

Centrate characterization from pre-fermentation reactors. Based on the trends in Figure 33, we repeated the fermentation studies with a 3-day SRT to generate enough effluent for operating the centrate-fed MECs. Figure 34a shows COD mass balances for these 3-day fermentations. The fraction of produced methane and VFAs (~15% by $TCOD_{in}$) in both fermentations was similar to the results (~17% by $TCOD_{in}$) in Figure 33, confirming minimal impact of PEF on these parameters. Around 15% of $TCOD_{in}$ was converted to semi-soluble COD (centrate) and, thus, available to be an electron donor in the MEC. The semi-soluble COD was mainly VFAs, at 57% and 76% of SSCOD in control and PEF-treated centrates, respectively. Acetate was the dominant VFA in both cases, followed by propionate. PEF treatment increased the fraction of acetate in total VFAs by ~35%, compared to control (Figure 34b). This indicates that PEF led to selective enrichment of a microbial community that promoted acetate accumulation.

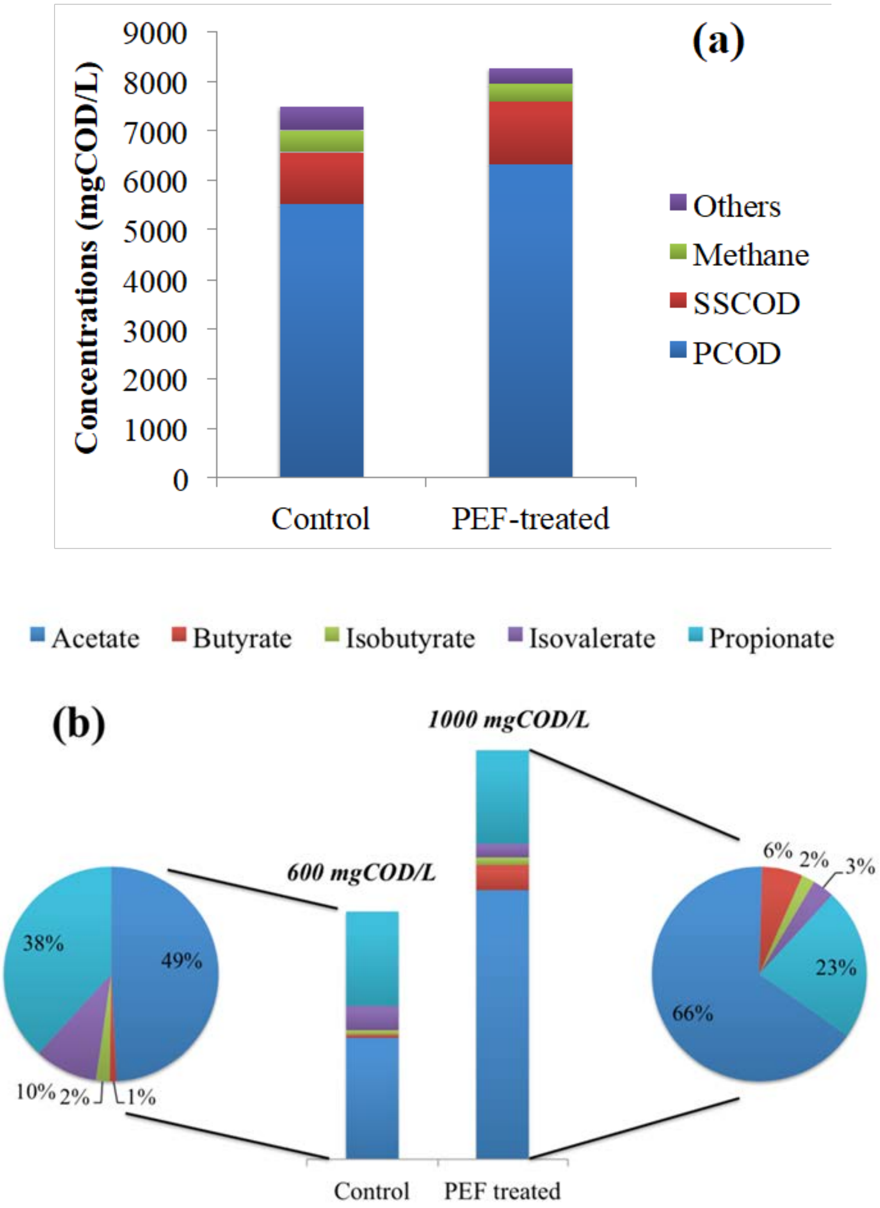

Figure 34. Detailed characterization of the performance of pre-fermentation reactors operated with a 3-day SRT. (a) COD mass balance for control and PEF-treated PS. (b) Volatile fatty acids (VFAs) profiles and total VFAs concentrations as COD.

Performance of the MECs fed control and PEF-treated PS centrate. Figure 35a shows the current densities and the Coulombs recovered as COD in MECs fed with control and PEF-treated PS centrate. With the pH maintained near neutral, the current densities increased to as high as 1.3 and 3.1 A/m^2 for control and PEF-treated centrate, although they declined to the background current by ~1.5 and 2.0 days, respectively. Correspondingly, VFAs were hardly detected at the end of both batch experiments: control: 47 mg COD/L, PEF-treated: 0 mg COD/L. The higher concentrations of SSCOD and VFAs and, particularly, the 2.2-fold higher acetate concentration in the PEF-treated centrate led to the 2.4-fold higher peak current density (294 and 660 mgCOD/L as acetate for control and PEF treated, respectively). Since ARB prefer acetate as their electron donor (Torres et al., 2007; Lee et al., 2008; Liu et al., 2005; Oh and Logan, 2005), the selective accumulation of acetate in PEF-treated PS centrate (2.2-fold higher than control) probably was the factor for the much faster rate of anode respiration (2.4-fold higher maximum current density) in the MEC.

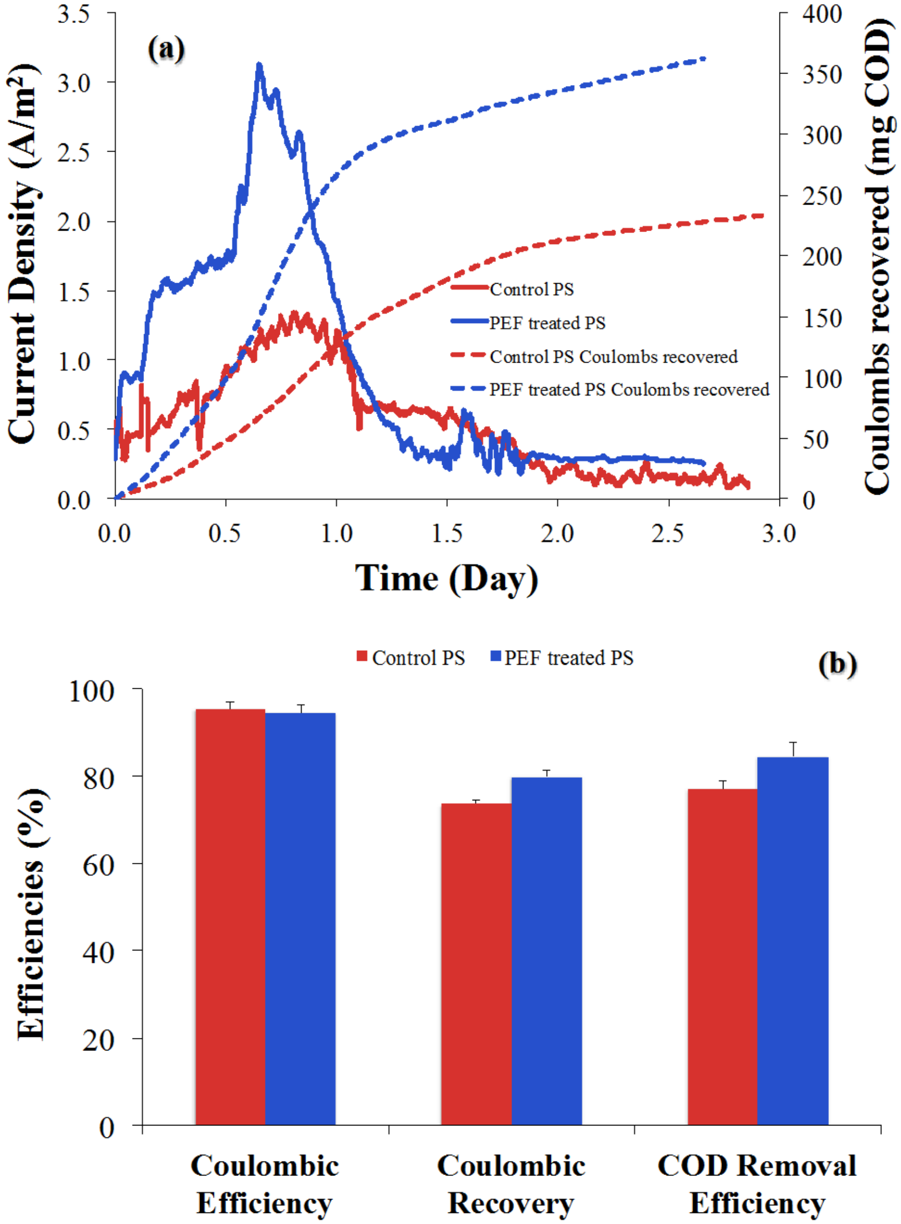

Figure 35. Performance of MECs fed with control and PEF-treated PS centrate operated with pH control: (a) current density and Coulombs recovered as mg COD and (b) efficiencies by normalized to the initial centrate SSCOD.

Higher initial SSCOD was important for allowing the PEF-treated PS centrate to have a faster rate of electron recovery. Because the volume of the anode chamber for the PEF-treated centrate was larger (0.35 versus 0.30 L), the starting mass of SSCOD was greater for the PEF-treated centrate: 459 versus 315 mg SSCOD. Integration of the currents in Figure 34a indicates that the Coulombs recovered were 360 and 232 mg COD for PEF-treated and control centrates, respectively. The 55% larger input of SSCOD with the PEF-treated centrate is consistent with the 55% more electrons captured as current.

Figure 35b shows that the MECs fed control and PEF-treated PS centrate gave good performance with similar efficiencies, CE, CR, and COD removal: 95, 74, and 77% for control and 95, 80, and 85% for PEF, respectively. Thus, the ARB could use the centrate's SSCOD efficiently as an electron donor. Although PEF pre-treatment had a strong positive effect on the maximum current density (Figure 35a), it gave only a small increase in CR and COD removal and had no effect on CE.

Table 16 summarizes the electron flows from SSCOD in centrate, as well as from the original TCOD of the PS. Although only 14 or 16% of PS TCOD ended up as the centrate after pre-fermentation, most of the SSCOD was recovered as current in the MEC (74% and 80% for control and PEF-treated, respectively). Between control and PEF-treated, PEF treatment had modest improvement of CR by 6% although the absolute CR was 34% higher in PEF-treated centrate fed MEC, which is likely due to ~1.5 (or ~1.9) times more SSCOD (or acetate) fed in the MEC as described earlier. Correspondingly, 7% lesser SSCOD in PEF-treated centrate fed MEC was detected at the end of the batch (23% and 16% for control and PEF-treated, respectively).

Table 16. Summary of COD flows in mg/L of the pre-fermented centrate fed MEC and normalized to the initial centrate SSCOD in the MEC and to the input PS TCOD in the two-stage system.

	Control			PEF-treated		
	COD (mg/L)[a]	Fraction by $\mathrm{SSCOD_{in}}$ (%)[b]	Fraction by $\mathrm{TCOD_{in}}$ (%)[c]	COD (mg/L)[a]	Fraction by $\mathrm{SSCOD_{in}}$ (%)[b]	Fraction by $\mathrm{TCOD_{in}}$ (%)[c]
Initial centrate SSCOD	1050 (±16)	100	14	1310 (±27)	100	16
Final centrate SSCOD	241 (±1)	23	3	202 (±25)	16	2
Final centrate PCOD	51	5	0	52	3	0
Current as COD	774	74	10	1040	80	13
Unaccounted COD	-14	-1	0	9	1	0

[a] Anode volume was 0.3 and 0.35 L for control and PEF-treated PS centrate fed MEC

[b] Fraction by initial centrate SSCOD of the MEC stage

[c] Fraction by starting TCOD in the PS of the pre-fermentation stage (control PS: 7500 (± 300) mgCOD/L, PEF-treated PS: 8300 (± 600) mgCOD/L)

In this sub-task, semi-continuous pre-fermentation of PS as a means to enhance electron recovery as current in an MEC was evaluated. Pre-fermentation with a 3-day SRT (=HRT) led to more VFA accumulation and less methane production. Although PEF treatment before fermentation did not alter the production of VFAs and methane for the 3-day SRT, it yielded more of the most desirable fermentation product, acetate. This resulted in higher maximum current density in the batch MEC experiments. Over the full duration of the MEC batch experiments, CE, CR, and COD-removal efficiency were high for the pre-fermented centrate and hardly affected by PEF pre-treatment. However, the overall recoveries from the sludge were low (Figure 34a), which is why we continued testing the direct addition of sludge into the MEC in section 5.1.3.

5.1.3. Semi-continuous operations of microbial electrolysis cells fed with primary sludge

Current density for the PS-fed semi-continuous MEC. We operated the MECs semi-continuously with HRTs starting at 15 days and changing sequentially to 12, 9, 6, and 12 days; the last 12-day experiments were conducted at neutral pH (~7.3) and then high pH (~8.1). The PS used for semi-continuous operation contained ~8 g COD L^{-1} and ~3.6 g VSS L^{-1}. The PS loading rates were 0.53, 0.67, 0.89, and 1.33 g COD L^{-1} d^{-1}, and 0.24, 0.3, 0.4, and 0.6 g VSS L^{-1} d^{-1} for 15, 12, 9, and 6-day HRTs, respectively.

Current density for each HRT, presented in Figure 36, increased with decreasing HRT: from ~0.35 A m^{-2} at 15-day HRT to ~2.2 A m^{-2} at 9- and 6-day HRTs. This resulted from the increased organic loading of PS from ~0.53 g COD L^{-1} d^{-1} at 15-day HRT to over 0.89 g COD L^{-1} d^{-1} for 9- and 6-day HRTs. Each feeding cycle started with a high current density that subsequently decayed as COD was consumed. The maximum current density during semi-continuous mode of operation was 2.2 A m^{-2}. During the final 12-day-HRT experiments with pH 7.3 or 8.1, the maximum current densities were similar to each other and slightly greater than during the earlier 12-day HRT experiment.

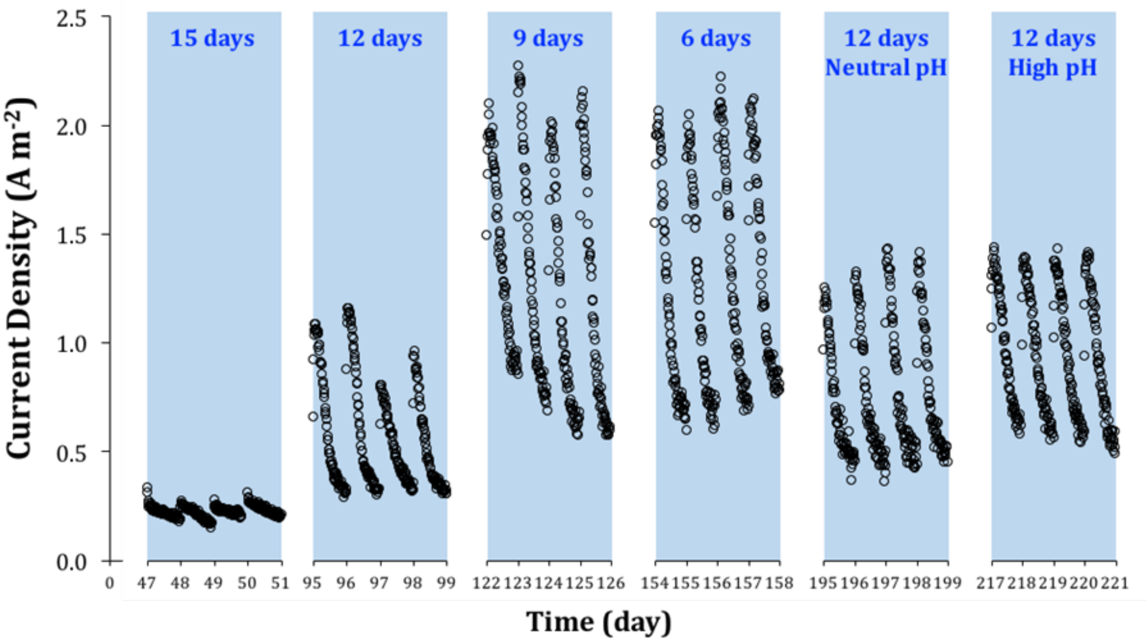

Figure 36. Current density with time for different HRTs during semi-continuous MEC operation with PS. The gaps in time between different HRTs were the adaptation periods for the new HRT. Data shown in this figure correspond to the last 4 days of operation for each HRT, when current had stabilized from cycle to cycle.

Electron partitioning to electrical current and methane. We performed electron balances during the last 6 to 15 days of operation for each HRT, when performance was stable. A minimum of six measurements were averaged to generate the electron balances in Figure 37a. We show in Figure 37b how the recovered electron equivalents were apportioned between current and CH_4. Semi-continuous MEC operation achieved over 60% TCOD removal, and at least 40% out of the 60% was conversion to either CH_4 or Coulombs. The missing $\leq$ 20% (out of 60%), an unaccounted fraction annotated as Others in Figure 37a, could include electron equivalents routed to biomass synthesis and to accumulation and retention of solids inside the reactor. The CR was only 13% for the 15-day HRT, while methanogenesis was 33% of influent electrons. Thus, the MEC behaved largely as an AD at this relatively long HRT. CR increased with shorter HRTs: 28%, 34%, and 32% for 12-, 9-, and 6-day HRTs, respectively, and CH_4 fractions declined proportionally. Thus, lower HRT favored ARB activity by increasing the substrate loading. Concurrently, methanogen washout could have become important for SRT $\leq$ 8-day (Miron et al., 2000; Lee et al., 2011). We were unable to estimate SRT for methanogens, which were in suspension and the biofilm, but the low methanogenic activity at an HRT of 6 days suggests that their SRT was not much larger than HRT. Thus, the lower HRTs not only benefited ARB, but also helped decrease diversion of electrons to CH_4. Even though the current density and CR at the 6-day HRT were similar to those of the 9-day HRT, the sum of CH_4 and Coulombic recoveries decreased to ~41%, and effluent COD increased to ~36%. The cause was less solids hydrolysis at the short HRT, a phenomenon seen before for HRT below ~8 days (Rittmann and McCarty, 2001; Lee et al., 2011).

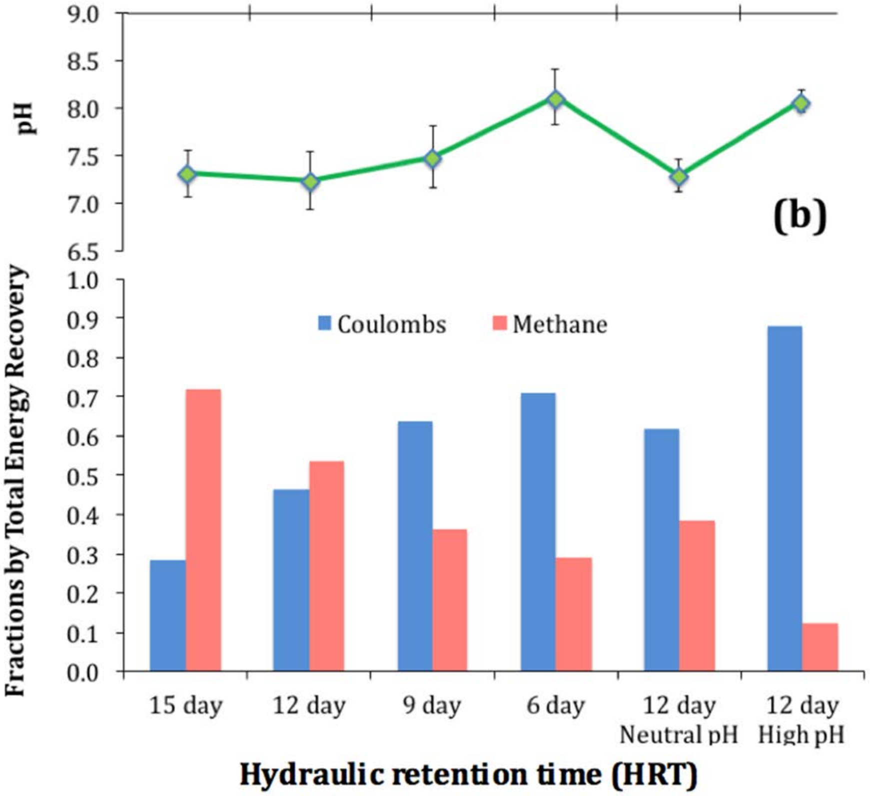

Figure 37. Electron balances for semi-continuous MECs fed with PS at each HRT (a), and fractional distributions between electrical current and methane (b).

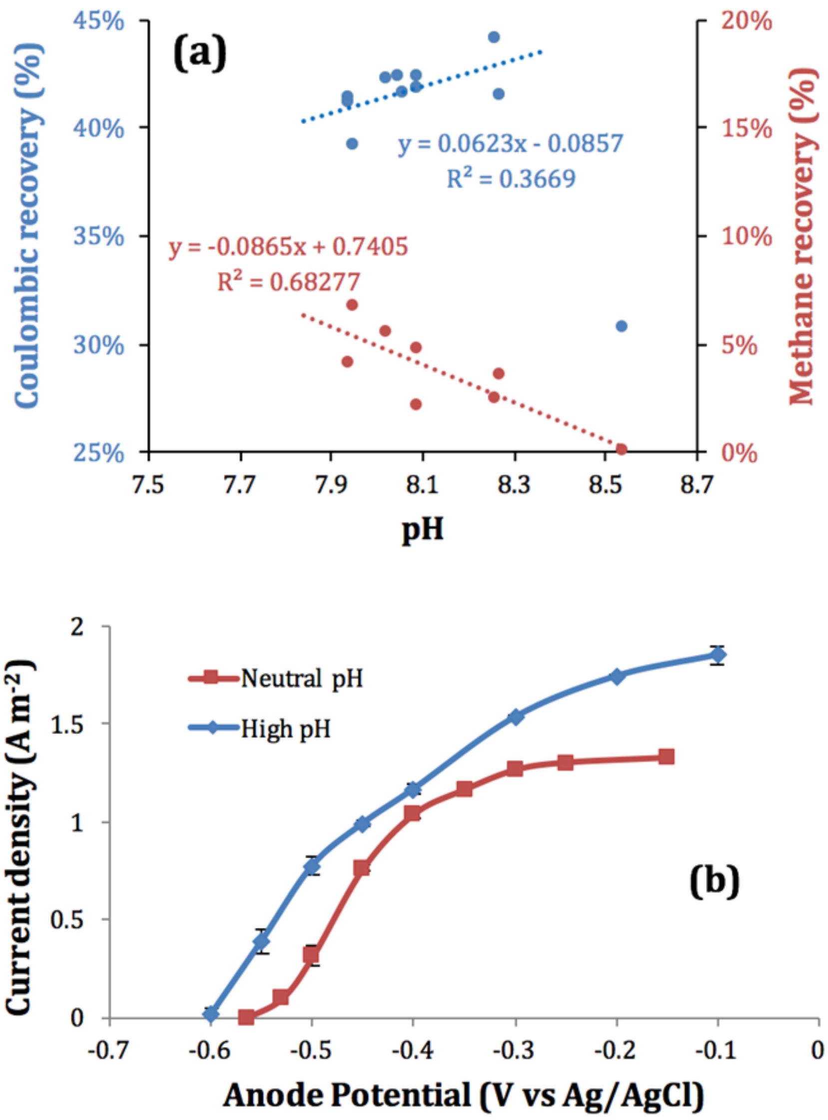

Figure 38. Effect of pH on the electron recovery and *j*-*V* response. (a) Relationship between Coulombic and methane recovery and pH of the anode chamber for high pH semi-continuous experiments. The datum for pH ~8.5 was excluded from the correlation. (b) Comparison of the *j*-*V* response for high and neutral pH at stabilized condition of 12-day HRT.

Importance of pH management. Apart from the effect of the HRT on the PS conversion, pH conditions, which were manually controlled, were different for each HRT, as reported in Figure 37b. To address directly the impact of pH on electron recovery as current and CH_4, we operated the last two runs at the 12-day HRT, but with markedly different pH values. The distribution of electron equivalents was changed markedly by high pH when the HRT was fixed at 12 days in the last two runs (Figure 37). An anode chamber pH of ~8.1 (high pH) gave a sharp increase in CR, to ~42%, with a proportional decrease of CH_4 recovery, to ~6%. Correspondingly, CE increased up to 61% at pH 8.1 from 50% at pH 7.3. Thus, keeping the anode pH above ~8 significantly favored anode respiration over methanogenesis for the same HRT. This result could have been due to inhibition of the methanogens, a benefit to the ARB, or both, at higher pH. The optimal range of pH for methanogens is between 6.5 and 7.6 (Rittmann and McCarty, 2001), which lends support that the methanogens may have been inhibited at the anode chamber pH of ~8.1. The higher alkalinity associated with higher pH also increases proton transport out of the biofilm (Torres et al., 2008; Marcus et al., 2011), and this may have provided a benefit to the ARB. Yuan et al, (2012) also reported a positive impact of high pH for an anode fed sewage sludge in an MFC; they attributed the effect to inhibition of methanogens and solubilization of sludge solids, which would provide more substrate for ARB or methanogens. We demonstrate in Figure 38a that, for all experiments, methanogenesis had a strong negative correlation with measured anode-chamber pH (in the range of 7.9 to 8.5), while the CR increased in the pH range of 7.9 and 8.3, although the CR declined at the highest pH (8.5), perhaps due to a pH inhibition on ARB metabolic activity. Statistical analysis using Spearman correlation coefficient also shows a negative relationship between pH and CH_4 ($p < 0.05$) and a positive relationship between pH and CR ($p = 0.063$).

The *j-V* curves in Figure 38b show that higher pH benefited anode respiration in two ways: a higher maximum *j* and a wider range of anode potentials giving current. More alkalinity at higher pH, which enhanced proton transport from the biofilm anode, probably was the main cause for a higher maximum *j* (Torres et al., 2008; Marcus et al., 2011). When pH was increased in the anode, the open circuit potential (OCP) was shifted to a more negative value by 56 mV compared to neutral pH; this is nearly the same as the theoretical decrease of ~60 mV per one pH unit (Ki et al., 2016). This shift to the left for the OCP and the *j-V* curve indicates that more energy was available at the same potential for high pH.

Sludge treatment. TCOD removal and VSS reduction are shown in Table 17 for all HRTs. TCOD and VSS reductions were statistically not different (*p* value > 0.05) and in relatively narrow ranges: 62-71% for TCOD and 54-61% for VSS. The range for VSS reduction is similar to a previous report for an MFC treating sewage sludge: ~63% and 55% without and with 2-bromoethane sulfonate (a methanogen inhibitor), but with 37-day batch operation (Xiao et al., 2014). However, our results were substantially superior to most other reports treating PS: 32% VSS reduction in batch operation (Vologni et al., 2013) and 37-51% of TCOD removal and 51-57% of VSS reduction from the first-stage MFC unit fed with PS at 7-day HRT despite a very low CE, ~2% (Ge et al., 2013).

Typical VSS reduction in AD is ~50% (Cao and Pawłowski, 2012), although it depends on HRT and the input sludge composition: e.g., 56~65% VS reduction at a 15- ~ 30-day HRT (Tchobanoglous et al., 2003), and 35% VS reduction from PS at a 20-day HRT (Ghyoot and Verstraete, 1997). Also, the effect of SRT (= HRT in a completely mixed AD reactor) on VSS reduction, investigated systematically for thickened primary + waste activated sludge by Lee et al. (2011), showed a substantial increase -- from 34 to 50% -- as SRT increased from 4 to 20 days. Poorer VSS removal was linked to less hydrolysis at the lower SRT, and washout of methanogens also was a factor. Thus, our results for VSS removal with the MEC were as good as or better than typically seen with AD.

Since the ARB were initially acclimated with acetate for about 2 months, the anode biofilm was likely comprised mostly of ARB at first, and then PS solids, along with other microorganisms (e.g., methanogens and fermenters), might have accumulated on top of the ARB. As explained earlier, SRT might not be the same as HRT because of detachment or attachment of active biomass on the biofilm. After opening the reactor at the end of the experiment, we found on the anode surface a very thick layer of solids pictured. The solids presumably were comprised of the aforementioned microbes and some PS solids.

Table 17. Changes of PS-TCOD and VSS concentration in the anode chamber for the different HRTs.

	HRTs	TCOD (mgCOD L^{-1})	VSS (mg L^{-1})	TCOD removal (%)	TCOD consumption rate (gCOD m^{-3} d^{-1})	VSS reduction (%)	VSS removal rate (gVSS m^{-3} d^{-1})
Influent	-	8000 (± 110)	3600 (± 270)	-	-	-	-
Effluent	15 day	2900 (± 1800)	1600 (± 710)	64 (± 23)	340 (± 120)	55 (± 21)	130 (± 51)
	12 day	3000 (± 720)	1700 (± 270)	62 (± 9)	420 (± 61)	54 (± 11)	160 (± 32)
	9 day	2400 (± 280)	1400 (± 100)	70 (± 4)	620 (± 33)	61 (± 9)	240 (± 32)
	6 day	2600 (± 400)	1500 (± 190)	67 (± 5)	900 (± 69)	59 (± 10)	350 (± 55)
	12 day neutral pH	2300 (± 250)	1500 (± 170)	71 (± 3)	480 (± 23)	60 (± 10)	180 (± 27)
	12 day high pH	2300 (± 240)	1400 (± 150)	71 (± 3)	480 (± 22)	61 (± 10)	180 (± 26)

MEC design and long-term operation. The MEC design we used contributed to high H_2 production with semi-continuous operation: cathodic H_2 recovery and CE were 93 (± 15) and 61 (± 6) %, respectively; thus, overall H_2 recovery from PS was 57 (± 11) %, which is higher than the most cathodic H_2 recoveries in previous studies using municipal wastewater with dual-chamber MECs (Ditzig et al., 2007; Heidrich et al., 2013). The rates measured for experiments with a 12-day HRT and high-pH were 0.37 m^3 H_2 m^{-3} day^{-1} for the anode chamber volume and 1.2 L H_2 g VSS^{-1} day^{-1} for the influent PS-VSS. The electrical energy input calculated with ~1.1 V of applied voltage was 2.7 kWh m^{-3} H_2, which is comparable with previous MEC performance, ~2.1 kWh m-^{3} H_2[47] and much lower than the typical energy input for water electrolysis, 5.6 kWh m^{-3} H_2 (Call and Logan, 2008).

We achieved long-term MEC operation with direct feeding of PS for ~300 days: ~75 days of two-consecutive batch runs (data not shown) and ~221 days of semi-continuous operation (Figure 36). We had no reactor downtime, did not need to replace any reactor parts, and observed minimal membrane fouling. The flat-surface anode served as a barrier between the PS solids and the membrane. At the end of semi-continuous operation, when we disassembled the MEC after 12-day HRT at high pH, we could see that the PS solids did not penetrate through the anode to the membrane side.

This study documented TCOD removals, VSS reductions, current densities, and electron balances achieve with long-term, semi-continuous operation of a flat-plate MEC fed with PS and having HRTs between 6- and 15-days. The maximum current density exceeded 2 A m^{-2} for the 6- and 9-day HRTs, and the CR was the highest with an 9-day HRT (34%). For a 12-day HRT, maintaining pH over 8 in the anode chamber reduced electron diversion to methane and shifted electron flow to current. PS-fed MECs had VSS reduction ~60%, which is a good as or better than AD. As a first report of long-term semi-continuous MEC operation using PS, this study demonstrated that CR and sludge treatment could be enhanced by increasing pH and decreasing HRT in the flat-plate MEC. We use this data as a basis for our kinetic models in Section 5.2 and the development of MPPC reactors fed with sludge as a surrogate for blackwater.

5.2 Integrate results into MFC kinetic models (Task 2)

5.2.1 General modeling results versus experimental data

We compared the modeling results to Ki et al. (2016) results for a 12-d HRT, since the mass balance was most complete for that data set than for the other HRTs. The model predicts correct trends for the amounts of current and CH_4 produced in the system, as well as effluent TSS, VSS, and SCOD concentrations (Appendix A Figure A1). Figure 39a illustrates the modeling results at hydrolysis rates of 0.12/d and 0.25/d for HRT 12 d using a diffusion layer thickness of 0.4 cm. X_m concentration influenced the accuracy of the model predictions, with the best fit occurring between 10 and 25 mg X_m as VSS/L. X_m concentrations in PS are listed in literature from 0.1 to 10 mg VSS/L (Batstone et al. 2002; Nopens et al. 2009; Young et al. 2013b); thus, additional X_m likely represents X_m present in the anode's biofilm, which is not included in the model.

Figure 39b illustrates that reducing the diffusion layer thickness from 0.4 to 0.1 cm increases current production by ARB. Although higher acetate concentrations may be available in the bulk liquid at larger diffusion layer thicknesses, Figure 39c shows that higher acetate concentrations reach the biofilm surface when the diffusion layer is 0.1 cm, increasing ARB consumption of acetate and current production. This increase is due to higher concentrations of acetate being available to the ARB biofilm, as seen in Figure 39c. Coulombic recovery increased from 41% to 49% at X_m = 10 mg/L and from 98 to 128% at X_m = 25 mgVSS/L as the hydrolysis rate increased from 0.12/d to 0.25/d, respectively. Consequently, CH_4 production decreased between 20% and 34%.

The model results indicate that the hydrolysis rate had a lower impact on diversion of electrons to ARB consumption than the influent X_m concentration or diffusion layer thickness. Little difference is observed with increasing X_m concentration: the fraction of electrons diverted to current production decreases 37% to 13% at a hydrolysis rate of 0.12/d versus 38% to 15% at a hydrolysis rate of 0.25/d when the diffusion layer thickness is held constant at 0.4 cm. The impact of hydrolysis rate is greater with decreasing diffusion layer thickness, as more available acetate in the bulk liquid reaches the biofilm surface. Thus, optimizing reactor design should prioritize methods to reduce X_m concentrations and decrease diffusion layer thickness rather than improving hydrolysis rate.

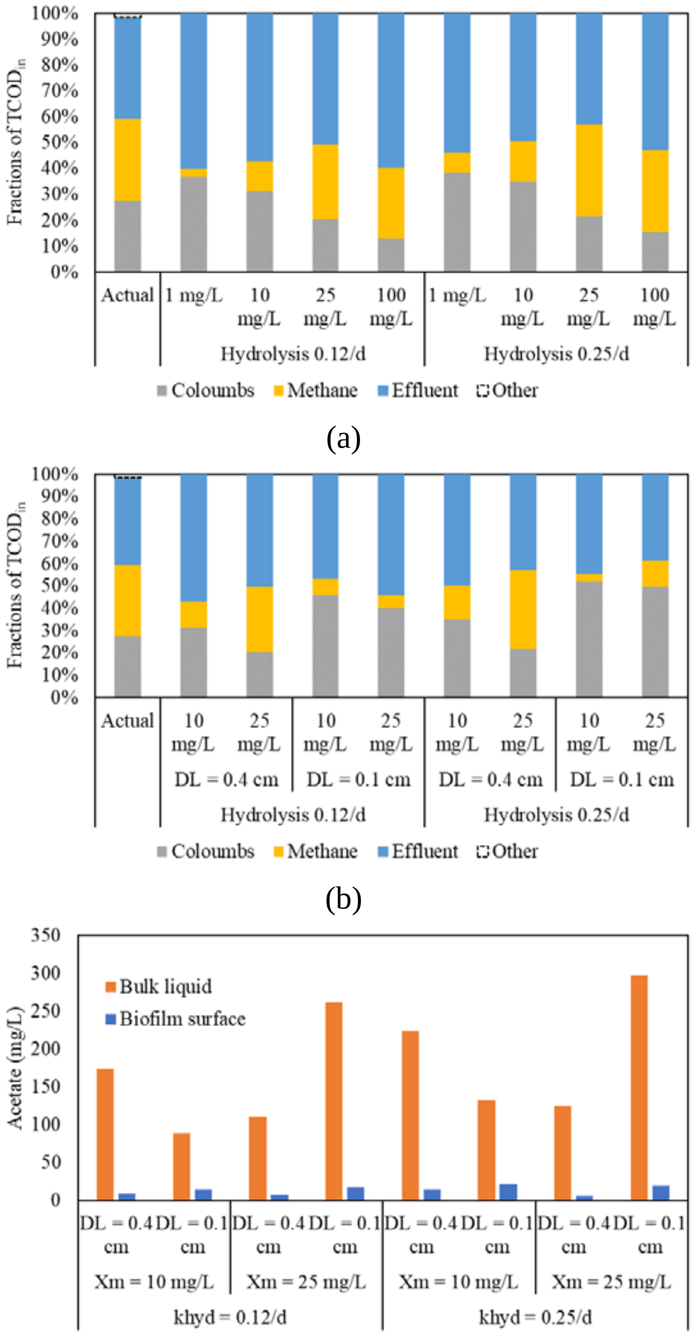

(a)

(b)

(c)

Figure 39. Electron balances on respiration products based on TCOD$_{in}$ concentrations at a 12 d HRT (a) at varying influent methanogen concentrations (X_m = 1 to 100 mg/L) and hydrolysis rates (k_{hyd} = 0.12 and 0.25/d) at a constant diffusion layer (DL) thickness = 0.4 cm and (b) at DL = 0.4 and 0.1 cm at influent methanogen concentrations of 10 and 25 mgVSS/L and hydrolysis rates of 0.12 and 0.25/d. (c) Acetate concentrations in the bulk liquid and at the biofilm surface at influent X_m concentrations of 10 and 25 mgVSS/L and hydrolysis rates for DL = 0.4 cm and 0.1 cm. Effluent represents SCOD and TSS concentrations removed from the reactor. "Actual" refers to experimental results and "Other" to unaccounted TCOD as reported in Ki et al. (2017).

5.2.2 Influent methanogen concentrations affect methane production and bulk pH

Similar to the 12-day HRT results, the best model fits for CH_4 production and coulombic recovery for 9-day and 15-day HRT occur at X_m concentrations between 10 and 25 mgVSS/L. These results are summarized in Figure 40. While the model appears to predict higher CH_4 production than Ki et al. (2016) at a 9-d HRT and lower coulombic recovery at a 15-day HRT, the discrepancies are in part due to unaccounted for electrons in the mass balance.

Increasing influent X_m concentration resulted in increases in overall CH_4 and coulombic recoveries for the 9-day HRT, and this apparently contradictory trend was due to increases in alkalinity, which provided more suitable pH ranges for X_m and ARB respiration. Although the pH was adjusted to 7.5 daily, Figure 41a shows that the low influent alkalinity and X_m concentrations in the bulk at an HRT of 9 days were unable to prevent a significant decrease in anode chamber pH. At an influent X_m concentration of 1 mg/L, < 400 mg $CaCO_3$ alkalinity was available to buffer the acetate production of 450-600 mg/L-d, causing the pH to decrease rapidly from pH 7.5 to less than 6. The low pH results in metabolic inhibition of methanogens and ARB respiration; consequently, X_m are washed out of the anode chamber, reducing overall CH_4 and current production to <1% each. As X_m increased to $\geq$ 10 mg VSS/L, HCO_3^- from Xm acetate utilization and NH_4^+ from endogenous decay provide additional alkalinity, reducing the daily pH fluctuations to a range more suitable for X_m and ARB respiration (pH 6.3-7.5).

At the 12 and 15-day HRTs, MEC performance was similar regardless of hydrolysis rate or influent X_m concentration. Figures 41a and 41b show that, with increased HRT, the daily bulk pH concentrations become increasing more stable above pH 6.5, improving the likelihood of ARB and X_m respiration. pH stability is facilitated by higher and more consistent daily alkalinity concentrations regardless of X_m concentration. Interestingly, the model predicts higher coulombic recovery at a 15-day HRT versus experimental results.

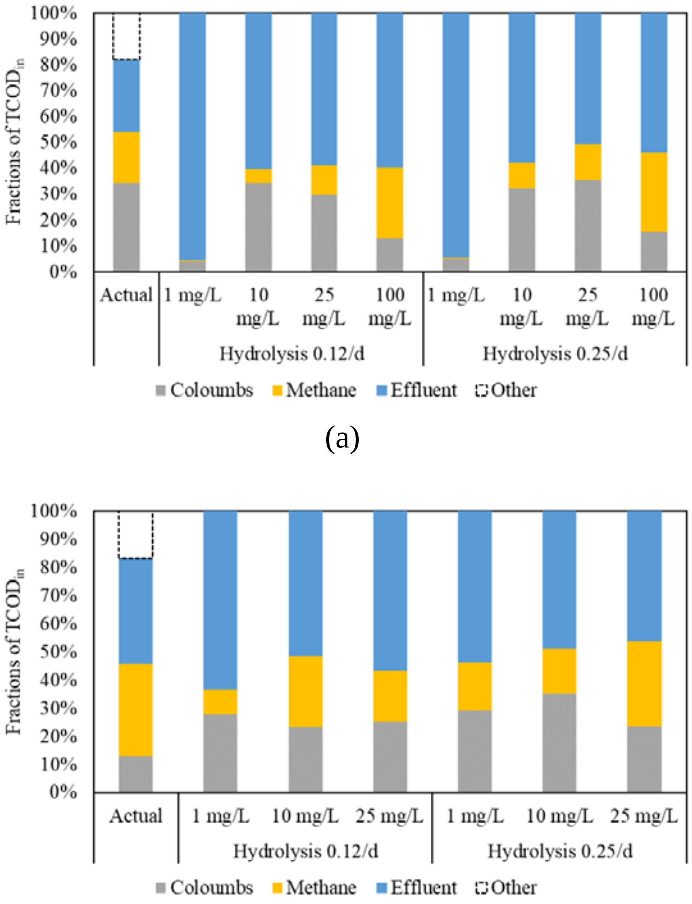

(a)

(b)

Figure 40. Electron balances on respiration products based on TCOD$_{in}$ concentrations at a (a) 9 d and (b) 15 d HRT. Effluent represents SCOD and PCOD concentrations removed from the reactor. “Actual” refers to experimental results and “Other” to unaccounted TCOD as reported in Ki et al. (2017).

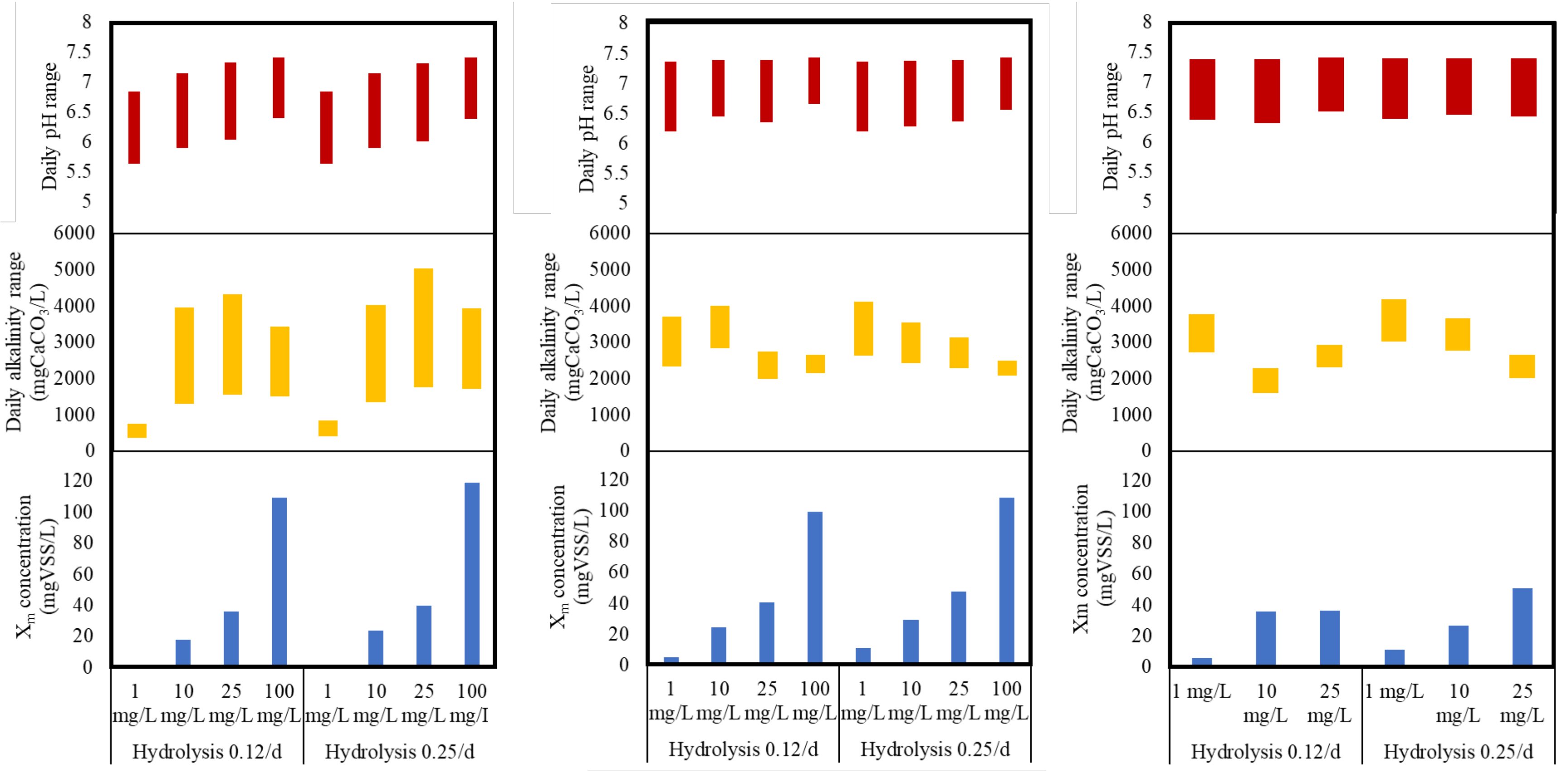

(a) (b) (c)

Figure 41. Daily pH range, daily alkalinity range, and % of methanogens present expressed in terms of influent TCOD (TCOD$_{in}$) at HRTs of (a) 9 days, (b) 12 days, and (c) 15 days.

5.3. Test Materials (Task 3)

5.3.1. Anode and membrane testing with primary sludge

PS-fed MEC. Figure 42 and 43 are the photos of carbon fiber anodes woven with titanium plates and AEMs (AMI-7001). We had no reactor downtime, did not need to replace any reactor parts, and observed minimal membrane fouling. The flat-surface anode served as a barrier between the PS solids and the membrane. At the end of semi-continuous operation, when we disassembled the MEC after 12-day HRT at high pH, we could see that the PS solids did not penetrate through the anode to the membrane side, as shown in Figures 42 and 43.

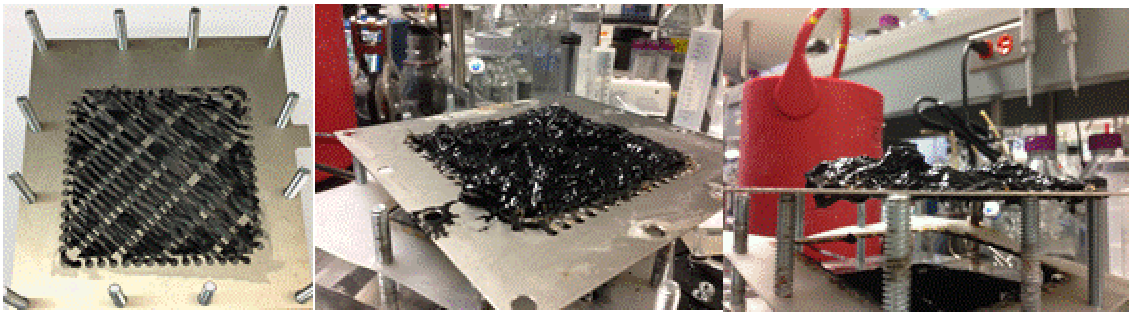

Figure 42. Photos of anode fibers: i) initial (left) and ii) after 12-day HRT at high pH (right).

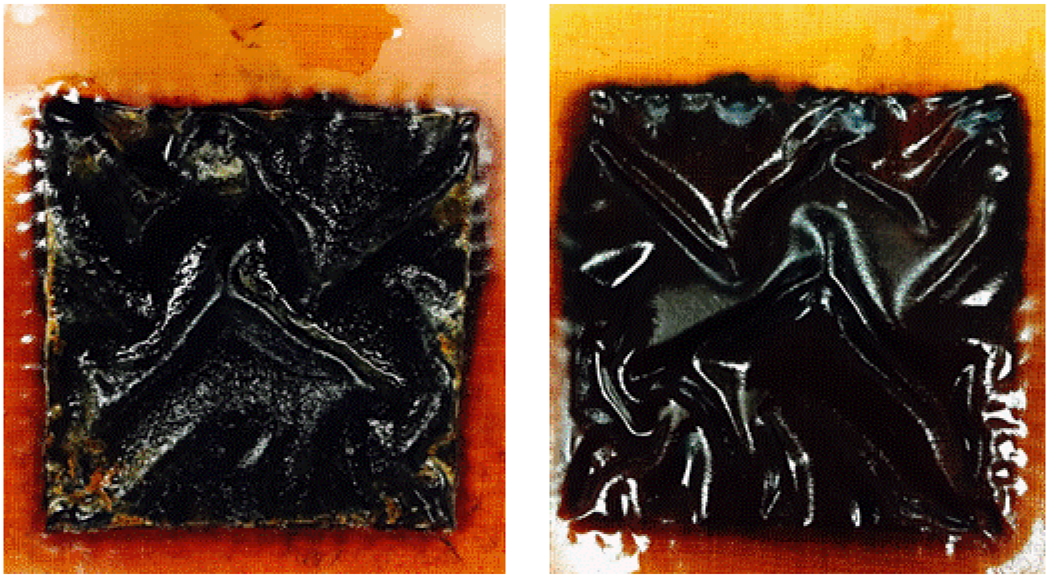

Figure 43. Photos of the membrane at the end of the long-term operation for ~1 year: anode side (left) and cathode side (right).

PS-fed MPPC. As shown in Figure 44, we saw no evidence of membrane deterioration or chemical deposits after running 27 days in the MPPC fed with PS. PS-fed anodes were deposited on the surface of carbon fiber anodes like the case of PS-fed MEC, thus anode reactions in the anode chambers in MEC and MPPC are the same.

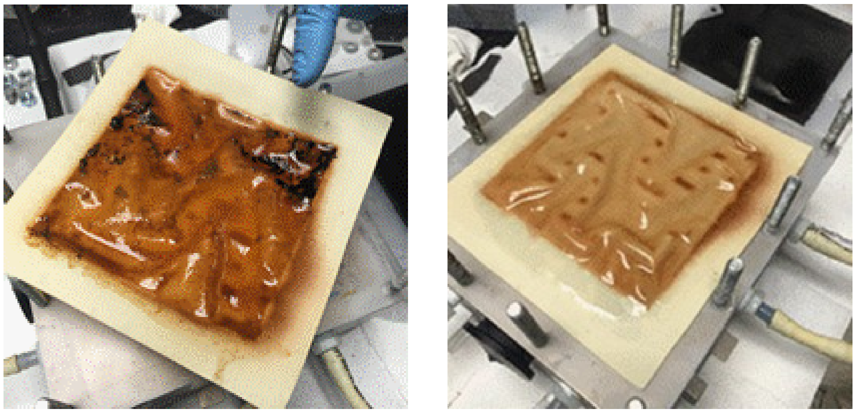

Figure 44. Anion exchange membrane used during MPPC fed with PS for 27 days. Left (anode side) and Right (cathode-chamber side).

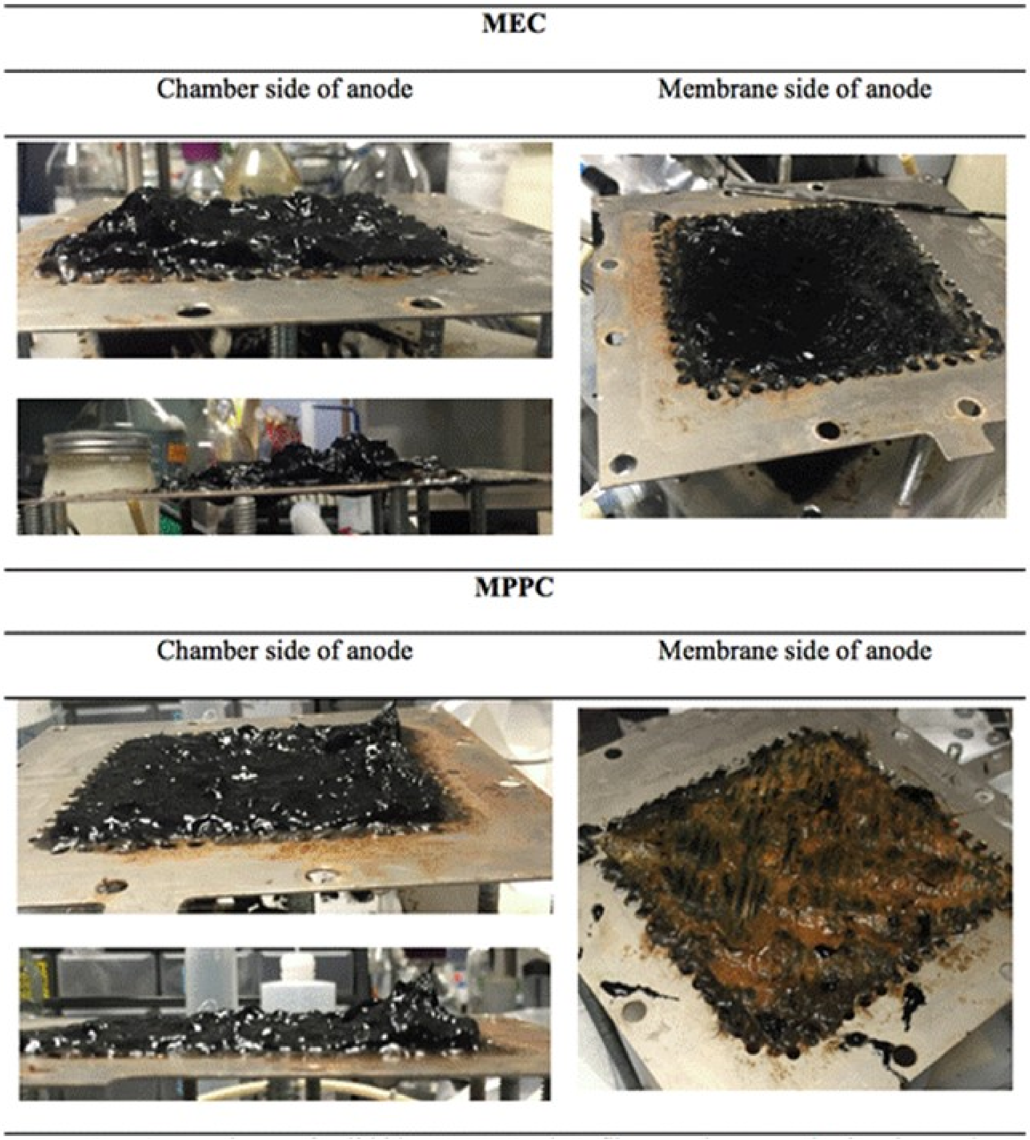

Figure 45. Comparisons of solid biomass on carbon fiber anodes towards chamber and membrane after MEC (top) and MPPC (bottom) operation.

5.3.2. Cathode and membrane testing with hydrogen peroxide

Membrane materials selection. Several factors are considered important in membrane selection. Membrane compatibility with H_2O_2 is the most important factor as contaminants or functional groups on the membrane may potentially contribute to H_2O_2 degradation either catalytically or through a decomposition reaction with the membrane itself. H_2O_2 reacting with the membrane may destabilize the membrane's integrity, leading to membrane failures. Membrane compatibility at different pHs is also important since the OH^- produced during the oxygen reduction reaction (ORR) has the potential to significantly increase the catholyte pH, and H_2O_2 deprotonates to the more reactive HO_2^- at the pK_a of 11.8. Therefore, we evaluated H_2O_2 degradation and membrane weight loss over a 45-day exposure period at pH 7 and 12. We tested the membranes in a 100-mM $NaHCO_3$ solution using EIS to determine their ionic transport resistances. EIS was performed at 100 kHz and 10 mV amplitude with the anode as the working electrode and the cathode as the counter electrode. As illustrated in 39, heterogeneous membranes exhibited 45-85 ohm-cm^2 in resistance. Homogeneous membranes demonstrated resistances <20 ohm-cm^2. For perspective, at 10 A/m^2, the homogeneous membranes have Ohmic overpotential <20 mV and heterogeneous membranes between 50-85 mV.

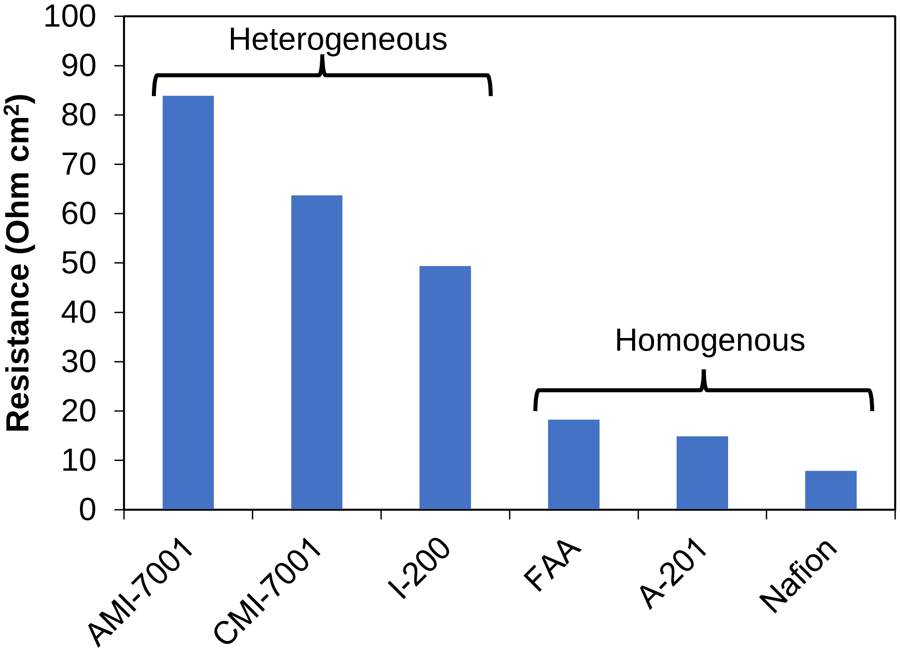

Figure 46. Area-specific resistances determined using electrochemical impedance spectroscopy for seven different heterogeneous and homogenous membranes in 100 mM $NaHCO_3$.

Finally, the choice of using an AEM or CEM results in operational trade-offs. HO_2^- produced at high pH can potentially diffuse across an AEM. However, a CEM provides preferential diffusion of cations other than H^+ to the cathode to maintain electroneutrality, potentially lowering the pH below an acceptable threshold for ARB. AMI-7001, CMI-700, and FAA membranes were evaluated for stability in a 10 g/L H_2O_2 solution at pH 7. After 45 days of exposure, there was negligible H_2O_2 degradation at pH 7 (Figure 47a), and the membranes experienced negligible mass loss (Figure 47b). This stability was likely due to the membranes being well suited for use near neutral pH and increased H_2O_2 stability at pH 7.

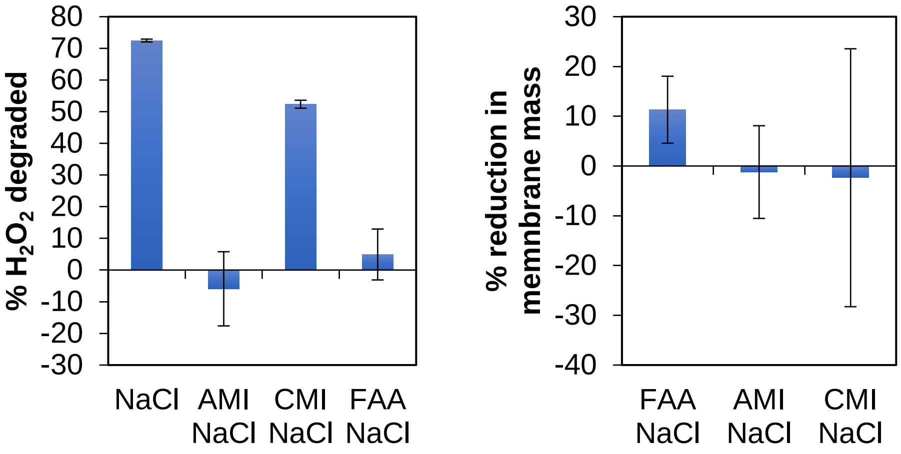

(a) (b)

Figure 47. (a) Percent H_2O_2 degraded and (b) membrane weight loss for FAA, AMI, and CMI membranes at pH 7 and 10 g/L H_2O_2.

Since OH^- production due to H_2O_2 formation at the cathode would likely increase catholyte pH during MPPC operations, membranes were evaluated for compatibility and H_2O_2 degradation at pH 12. Figure 48 illustrates that H_2O_2 was most stable in the presence of the Nafion membrane: ~11% of the total H_2O_2 was degraded over 45 days while the electrolyte pH decreased from pH 12 at day zero to pH 2.5 at day 45. This degradation was significantly lower than the 91% degradation exhibited during H_2O_2 stability tests without the membrane (Figure 49). All other membranes exhibited >85% H_2O_2 degradation, values similar to the 91% degradation measured during H_2O_2/NaCl stability tests without a membrane without significant pH change between days 0 and 45. Thus, the lack of degradation with Nafion was likely due to acidification of the electrolyte.

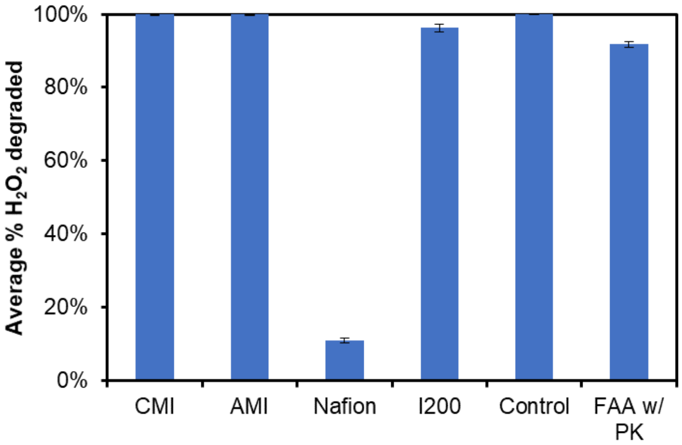

Figure 48. H_2O_2 degraded during batch bottle tests for membrane stabilities at pH 12.

H_2O_2 degradation did not necessarily correlate with membrane mass loss during the stability tests. Figure 49 illustrates that all membranes had weight loss at pH 12, regardless of the presence of H_2O_2. Except CMI-7000, all other membranes exposed to H_2O_2 experienced higher weight loss than membranes exposed to electrolyte only. The CEM membranes demonstrated lower differences in weights (<5% for both CEMs) than AEMs, since the CEMs' negatively charged active sites likely repelled HO_2^- ions from the membrane. For AEMs, the I-200 membrane had a 14% difference between the H_2O_2-exposed and electrolyte-only masses, making it the AEM with the smallest change in mass when exposed to H_2O_2. AMI-7001 and FAA lost 39% and 44% more mass, respectively, when exposed to H_2O_2 versus pH only.

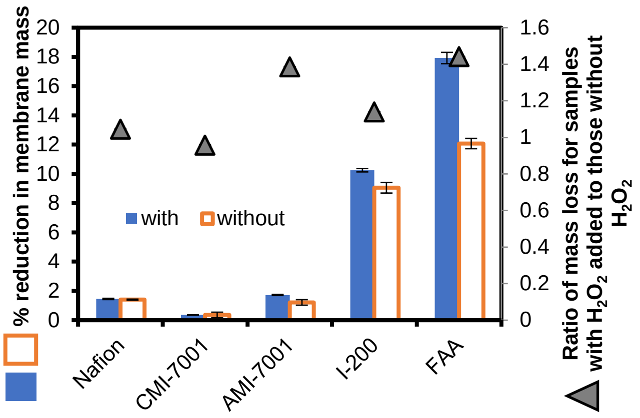

Figure 49. (left axis) Percent reduction in membrane mass during batch bottle tests for membrane stabilities with 10 g/L H_2O_2 at pH 12 and (right axis) ratio of mass loss for membranes exposed to H_2O_2 versus membranes exposed to pH 12 only. Values >1 indicate that membranes exposed to H_2O_2 lost more weight than membranes exposed to electrolyte only. Values <1 indicate that membranes exposed to electrolyte only lost more weight than membranes exposed to H_2O_2.

While FAA is rated by the manufacturer as stable at pH 12, FAA's lower thickness (130 μm) may have contributed to a lower structural integrity, causing the membrane to disintegrate when exposed to H_2O_2 at pH 12 (Figure 50). AMI-7001 experienced the lowest absolute mass loss (0.69 mg/cm^2 with and 0.96 mg/cm^2 without H_2O_2), which we speculate is due to either AMI-7001 being a less reactive material or its greater thickness (3.5x thicker than FAA), which hampered H_2O_2 permeation into and, therefore, decomposition of the membrane. Total organic carbon (TOC) analyses (detailed in SI) revealed that membranes exposed to H_2O_2 and/or high pH consistently produced more TOC over the duration of the experiment, likely caused by the release of complex soluble organics into solution during polymer deterioration (Figure 51).

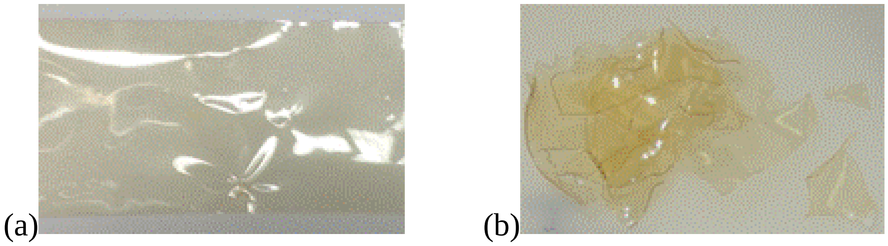

Figure 50. FAA (a) before and (b) after pH 12 100-mM NaCl and 10 g/L H_2O_2 stability tests. The stability tests used a 3 cm x 3 cm square that deteriorated to pieces by the end of the 45-day test.

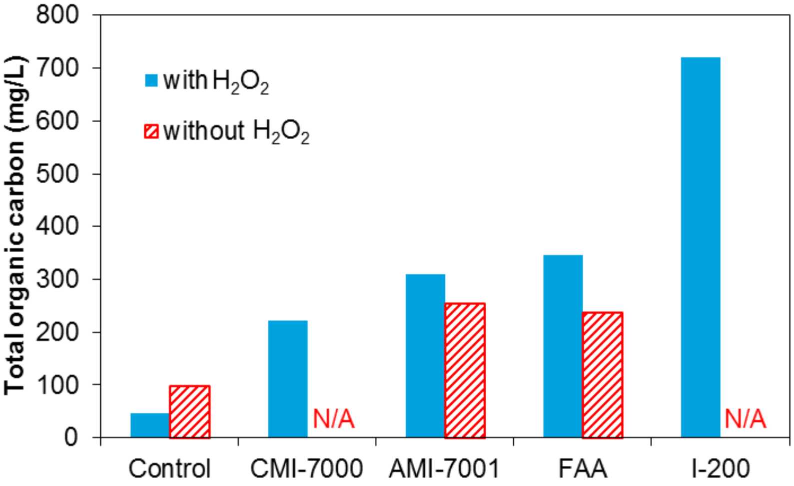

Figure 51. Total organic carbon (TOC) from batch bottle tests of membrane stabilities with and without 10 g/L H_2O_2 present in the solution at pH 12. TOC measurements were obtained using a Shimadzu TOC-V CSH Total Organic Carbon analyzer. Tests were not performed on CMI-7000 and I-200 at pH 12 only.

Nafion, AMI-7001, and FAA demonstrated greater H_2O_2 stability in the short term, making them the most viable candidates for an MPPC. In addition, all membranes exhibited low Ohmic losses <85 Ω-cm^2. Based on this evaluation, we opted to use an AEM in the MPPC to provide easy regulation of anode pH. Based on its low reactivity with H_2O_2, we chose to utilize AMI-7001 for MPPC experiments. If pH rises at the cathode, catholyte choice could help regulate the pH near neutral to reduce concentration overpotentials.

Cathode materials characterization. We utilized LSV in a half-cell with 100-mM sodium perchlorate to narrow our catalyst and binder choices to Vulcan carbon and Nafion, respectively. The Vulcan carbon had ~0.4V lower activation potential than graphite carbon using the same binder (Figure 52).

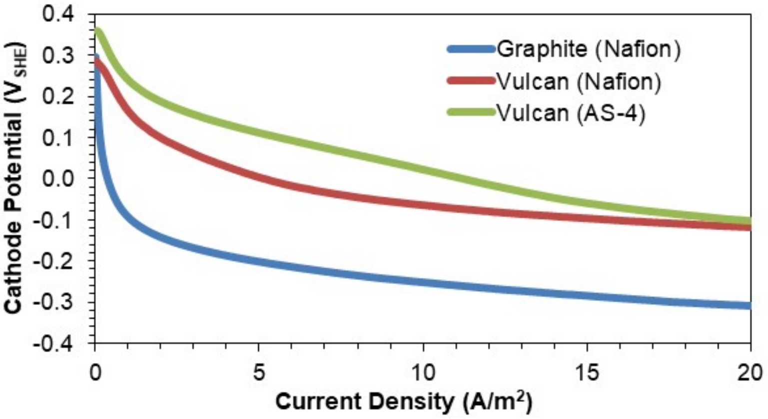

Figure 52. Cathode potentials (up to 20 A m^{-2}) established using linear sweep voltammetry with three catalyst/binder combinations: 50 g/L Vulcan carbon in a 5% Nafion solution (labeled Vulcan (Nafion)); 62.5 g/L of Vulcan carbon in an 3.13% AS-4 solution (labeled Vulcan (AS-4)); and 87.7 g/L of graphite in an 8.77% Nafion solution (labeled Graphite (Nafion)).

We used RRDE testing to determine the optimal Vulcan carbon loading, as it distinguishes between 2-electron and 4-electron ORR. Consistent with Bonakdarpour et al. (2008) and Paulus et al. (2001), lower catalyst loadings routed a higher number of electrons to H_2O_2, instead of to H_2O. Between -0.37 to -0.57 $V_{Ag/AgCl}$ (Figure 53), loadings of 0.22 and 0.45 mg/cm^2 provided the lowest average catalyst loading, 0.22 mg/cm^2, yielded an average of 2.04 ± 0.03 electrons per O_2 reduced, or almost 100% delivery of electrons to the 2-electron reduction to H_2O_2. The highest catalyst loading (1.12 mg/cm^2) yielded an average of 2.72 ± 0.06 electrons per O_2 reduced, or about two-thirds of the electrons were routed to H_2O. At higher loadings, the produced H_2O_2 must be transported through a thick catalyst layer, providing additional catalyst-contact time that increases the likelihood H_2O_2 is reduced again through Eqn. 1 to H_2O. Figure 53 also demonstrates the disk potentials because the cell required current input regardless of operating potential in order to operate. At an E_{KA} (the anode potential at one-half of the maximum current density) of -0.42 $V_{Ag/AgCl}$ for *Geobacter sulfurreducens*, the MPPC will likely require some small power input to produce H_2O_2 (Torres et al., 2008).

To summarize, the Vulcan carbon/Nafion binder combination produced the lowest cathodic overpotentials with an optimal Vulcan carbon loading of ~0.45 mg/cm^2 for the highest H_2O_2 production over a wide range of cathode potentials. Based on these results, we applied ~0.5 mg/cm^2 Vulcan carbon to the cathode for MPPC operations.

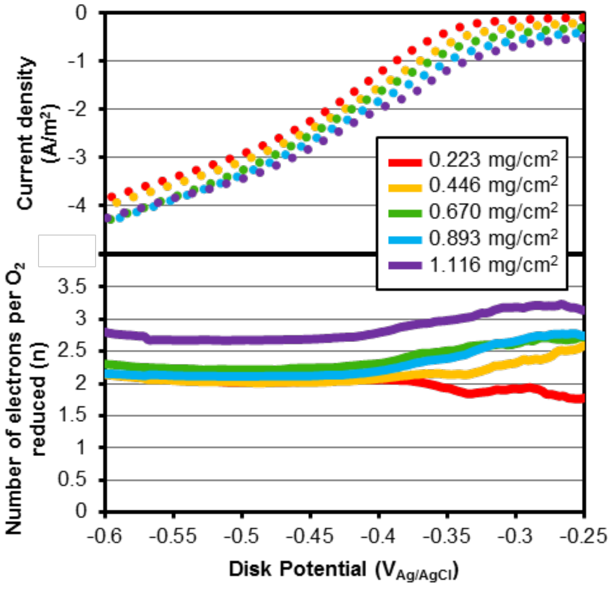

Figure 53. Ring current density (dotted lines) and the number of electrons per O_2 reduced (n; solid lines) as a function of disk potential for Vulcan carbon catalyst loadings ranging from 0.22 to 1.12 mg/cm^2.

H_2O_2 stability tests. Figure 54 illustrates that H_2O_2 was more stable at lower pH in 120-h stability tests. Phosphate buffers performed well, with pH 4.5 PBS resulting in no H_2O_2 detectable degradation in 24 h and 7% degradation over 120 h, while pH 7.5 PBS resulted in 6% degradation over 24 h and 21% degradation over 120 h, which is consistent with Yang et al. (2014). A NaCl solution at pH 6.5 also resulted in short-term stability of H_2O_2, as H_2O_2

degraded 13% in 24 h and 62% in 120 h. H_2O_2 became increasingly unstable as pH increased to alkaline conditions in the presence of Na_2CO_3 and NaCl. H_2O_2 in pH 11.5 Na_2CO_3 degraded 31% within the first 2 h and 99% within 24 h. Similarly, 49% of H_2O_2 degraded in pH 12 NaCl within 24 h. The susceptibility of H_2O_2 to degradation under alkaline conditions is consistent with Abbot and Brown (1990) and Qiang et al. (2002). Worsening stability with CO_3^{2-} may be attributed to increased H_2O_2 decomposition rates caused by the formation of metal-hydrogen-carbonate complexes in alkaline conditions (Torres et al., 2008).

From a broader perspective, the decreasing stability of H_2O_2 at higher pH becomes a processing and storage issue. Our stability tests confirm that alkaline-produced H_2O_2 cannot be stored long-term without significant degradation. Thus, maintaining a relatively low or neutral pH at the cathode is optimal for H_2O_2 production and stability.

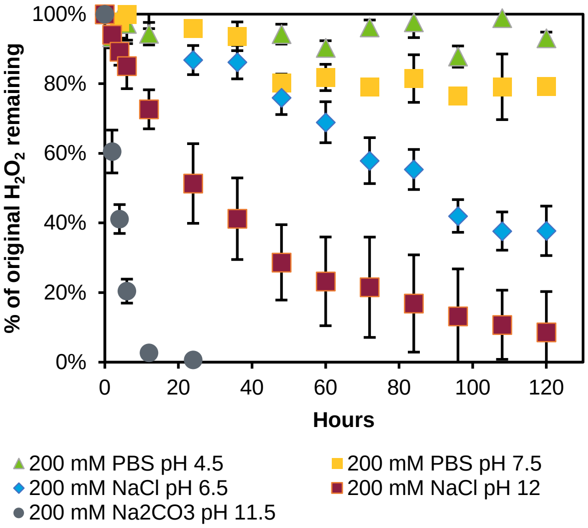

Figure 54. H_2O_2 stability in different electrolytes at different pHs.

In this Task, we outlined a methodology for designing MPPCs. We described the material characterization required to design MPPCs to continuously produce H_2O_2. The Vulcan carbon/Nafion binder combination provided chemical stability with H_2O_2 while producing minimal activation overpotentials compared to graphite catalyst. Using a rotating-ring-disk electrode (RRDE), we determined that the optimal catalyst loading to achieve the 2-electron oxygen reduction reaction (ORR) was approximately 0.5 mg cm^{-2}. Anion-exchange-membrane (AEM) stability tests established AMI-7001 as the optimal membrane to resist H_2O_2 degradation and promote long-term MPPC performance due to its high structural integrity. These materials were used in Tasks 6 and 7 for the construction and optimization of MPPC prototypes.

5.4. Process control strategies and design optimization algorithms (Task 4)

5.4.1 Experimental evaluation of the direct adaptive pH controller

In this section, we discuss the experimental evaluation of the direct adaptive controller. The experimental setup used is shown in Figure 55. In the laboratory experimental setup, the peristaltic Pump1 is used to control flow rates of the acid, the buffer stream1, and the buffer stream2, the peristaltic Pump2 is used to control the base flow rate. Pump2 and the pH sensor are interfaced with Microcontroller1. The pH sensor has a quantization of 0.04 pH and sampling time of 1 second. Pump2 is interfaced with the Microcontroller1 using an MCP4725 12-Bit DAC. Microcontroller1 communicates with the DAC using I2C protocol and it communicates with the pH sensor using UART serial. An Arduino DUE micro-controller (Microcontroller1) is used to implement the control algorithm and another Arduino DUE micro-controller (Microcontroller2) is used to implement the adaptation algorithm. Microcontroller1 acquires the pH value from the pH sensor, computes and outputs control commands to the Pump2, it also transmits the sensor and the control values to a supervisor PC for logging using UART serial communication. Microcontroller2 receives input and output values from the Microcontroller1, computes the controller gain (K) based on the proposed direct adaptive control algorithm and sends the computed controller gain value to the Microcontroller1. Data transfer between Microcontroller1 and Microcontroller2 is also done using UART serial communication protocol. The main motivation behind this experiment is to examine the behavior of the adaptive controller under realistic conditions and establish reasonable expectations as well as limitations of performance. It is shown that the linearized model of the plant, combined with controller gain adaptation, is sufficient to achieve uniform performance across a wide range of operating points. At the same time, undesirable performance effects caused by the simultaneous lack of excitation and disturbances appear to be within practically tolerable limits. The settings of the direct adaptive control algorithm for the experimentation are listed below.

- A nominal data-driven plant model is identified at the pH of 6 and for buffer flow Case1.
- Bandwidth of the target loop shape is chosen based on the uncertainty characterization of the residues from the system identification.
- A nominal PI controller is designed for the nominal plant using offline FLS algorithm using a target loop shape
- The nominal PI controller and the target loop shape used in the design of the nominal PI controller are used in the formulation of the direct adaptive control algorithm.
- A Filter Bank for the direct adaptive control algorithm is constructed using 20 all pass filters with the logarithmic interval between 0.1BW to 10BW, where BW is the bandwidth of the nominal target loop shape.
- Controller gains are restricted to a set $[10\ 10^6]$.
- To provide excitation, a square with small amplitude is superimposed on the step signals used for the set-point transition

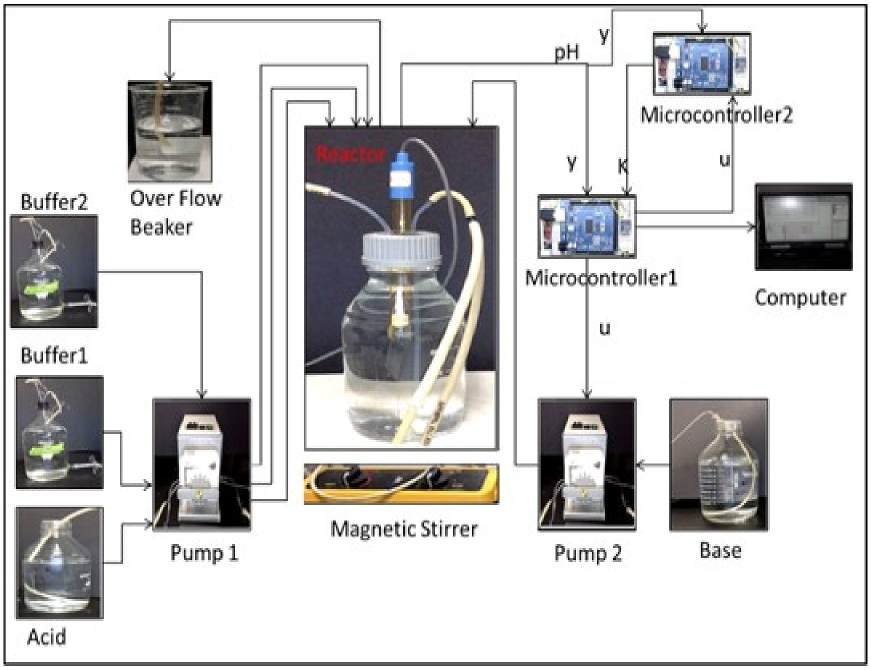

Figure 55. Block diagram of the lab -scale pH neutralization process CSTR.

The transfer functions for pH = 6 (Case 1) of the identified plant ($\hat{G}_6(s)$), controller ($\hat{C}_6(s)$) and target loop ($\hat{L}_6(s)$) are given below.

$$\hat{G}_6(s) = \frac{7.63\times10^{-5}(-s+1.53)}{(s+4.26)(s+0.018)}, \qquad \hat{L}_6(s) = \frac{0.8273\,(s+4.28)(s+0.409)}{s(s+4.26)(s+0.018)}$$

$$\hat{C}_6(s) = \frac{2.124\times10^{4}(s+0.273)}{s}$$

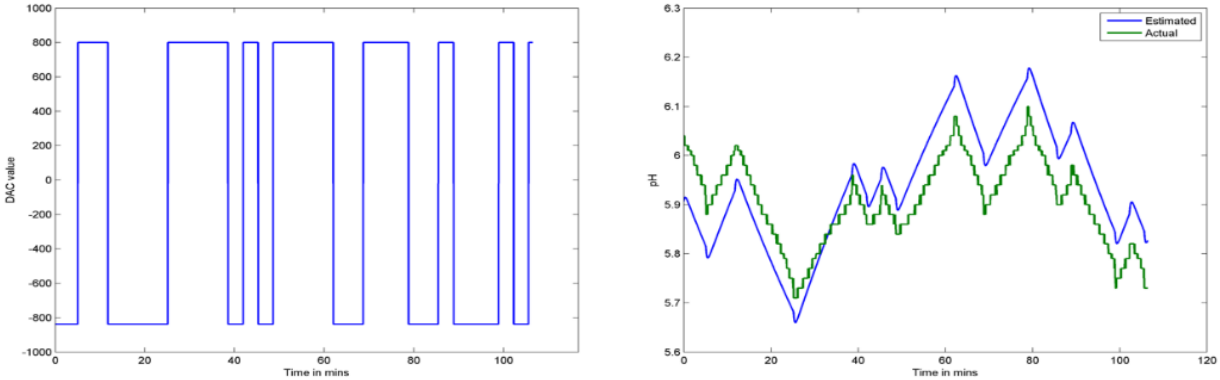

Figure 56. System identification signals; left- PRBS input; right- actual output (green trace) and predicted output (blue trace).

A Direct Adaptive pH control algorithm is used to control pH of the liquid in the reactor with $\hat{C}_6$ and $\hat{L}_6$ as base controller and target loop shape respectively. Results for Case1 and Case2 of buffer flows are shown below

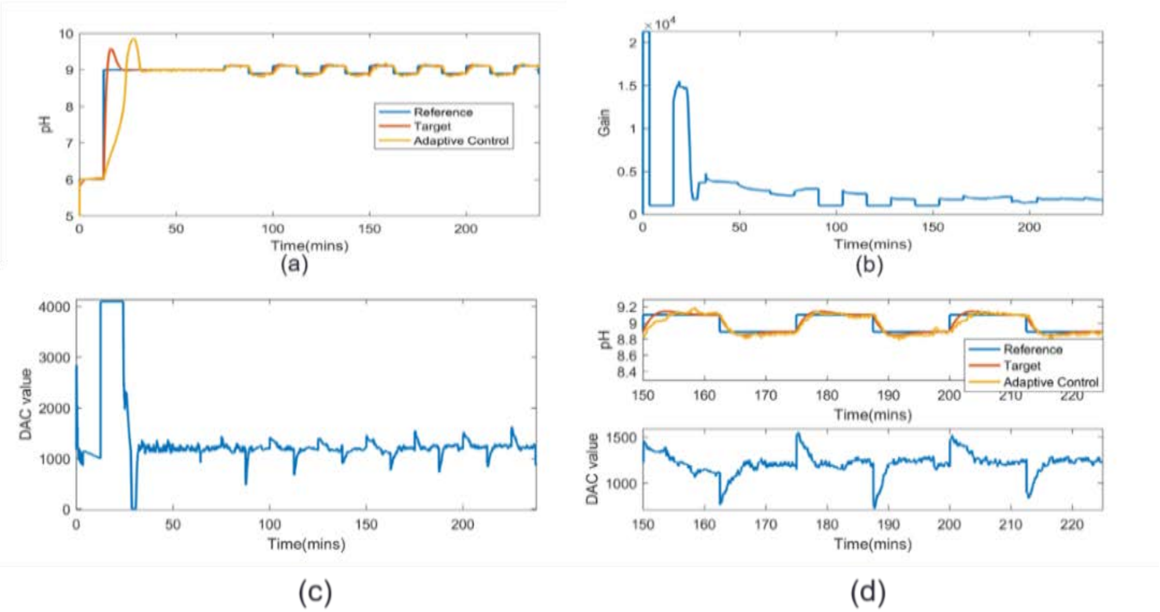

Figure 57. Closed-loop adaption results for Case 1 (a) plant output plot (b) controller gain plot (c) plant input plot (d) zoomed input-output plot.

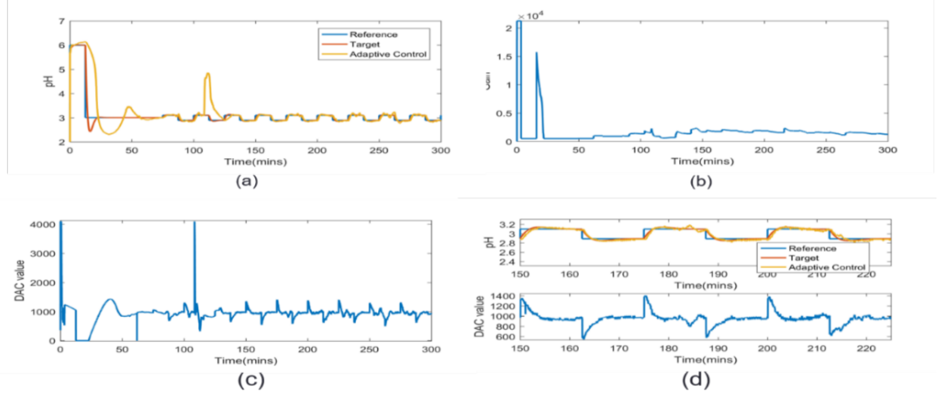

Figure 58. Closed-loop adaption results for Case 2 (a) plant output plot (b) controller gain plot (c) plant input plot (d) zoomed input-output plot.

The experimental results with the direct adaptive pH controller are shown Figures 56-58. We observe that the proposed controller able to adapt reasonably well to the gain changes in the plant with the operating points and with the change in buffering capacity. Undesirable characteristics of the response include the rather large overshoot during the step change of the set point from pH 6 to 9. This is not unreasonable since even the nominal loop exhibits some overshoot (red trace), but the overshoot is exacerbated by the slow adaptation of the gain. In such transitions, the transient response offers very little information on the plant around the step point and the adaptation cannot be expected to converge very quickly. We also observe that the controller gain convergence time depends on the input and parameter saturation. We conclude that using a single data-driven linear model (obtained using a system identification experiment) along with the proposed direct adaptive algorithm to update the gain, we achieve successful closed-loop pH control over a wide range of operating conditions including variations in the pH, as well as in the buffer flows. The proposed algorithm is further tested using computer simulations and results from these simulations are discussed in the next section.

4.4.2 Direct adaptive pH control simulation results

The experimental results are qualitatively very similar to the simulations of the model derived from first-principles, even though it requires detailed modeling to achieve quantitative matching. This similarity allows us to investigate the behavior of the proposed adaptive controller under a much wider set of conditions. The simulations are also used to examine the effectiveness of alternative schemes and the determination of sound principles for their practical implementation. For our simulation study, we begin again with the derivation of the model for the simulated system (described in the previous section). The linearized plant at pH = 6 (Case 1) is used as a nominal plant (G_6) and a PI controller (C_6) is designed using an offline FLS algorithm for the target loop L_6

$$G_6(s) = \frac{0.000197}{(s+0.0191)} \times e^{-s/6} \quad C_6(s) = \frac{4206(s+0.434)}{s} \quad L_6(s) = \frac{0.83\,(s+0.434)}{s(s+0.0191)}$$

Using C_6 as the nominal controller in the proposed direct adaptive control algorithm and L_6 as the target loop, we simulate the transitions to other operating points, namely pH 3, 4.5, 6, 9, 12. A small square wave with a 25min period is also injected after the transition to assess the speed of convergence. The results from the simulation show the adaptive controller performs well and the controller gain adaptation compensates for variation in the plant gain because of changes in the operating point and buffer flows, as anticipated. Some sample results of the simulations are shown below

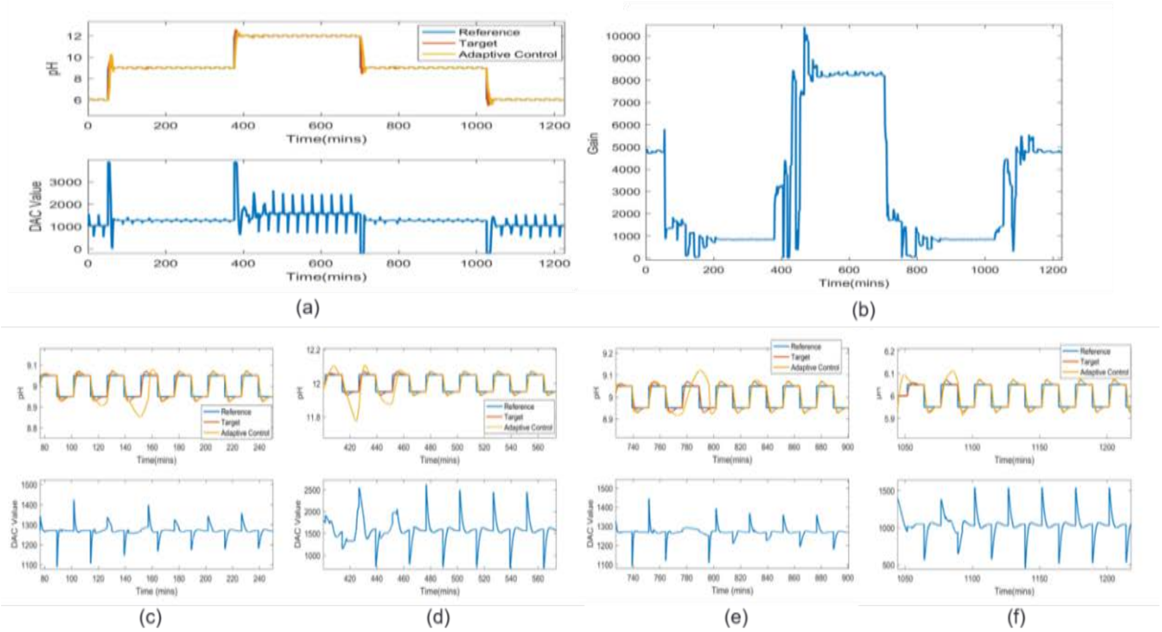

Figure 59. Direct adaptive pH control results for case 1 (a) Input output plot (b) controller gain plot (c-f) Zoomed in input-output plots after each big transition step.

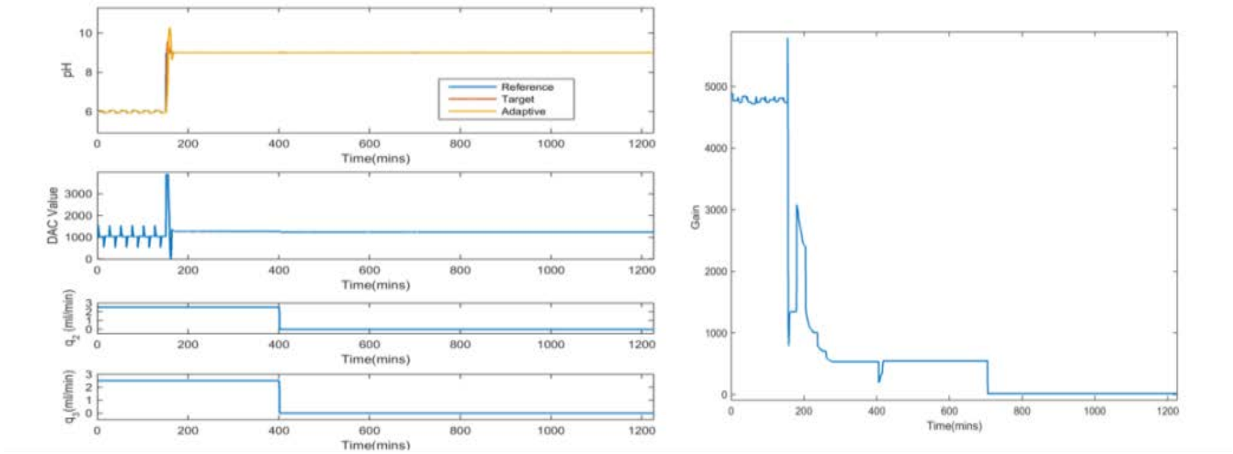

(a) (b)

Figure 60. Direct adaptive pH control with buffer flow changes (a) Input output plot (b) controller gain plot.

Set-point transitions and adaptation convergence are shown in Figures 59 and 60. We observe the similarity with the experimental results and the quick adaptation as it takes approximately 2-3 cycles of the square wave for the controller gain to converge. We also note a significant overshoot during the step change, this results from the inability to estimate the correct gain in such a short time. The results also show direct adaptive algorithm successfully compensates gain changes in the plant because of change in the buffer flow rates.

Simulation results reinforce our conclusions from the experimental results, that the proposed direct adaptive control algorithm is able to achieve reasonable and uniform performance, while relatively weak excitation requirements (e.g., small square wave) can yield quick parameter convergence.

The pH neutralization process with high retention time is studied in detail and it is shown that only the gain of the plant changes significantly with the operating point and the buffering capacity. The gain changes are so large that the usual process delays caused by pump actuators and sensor sampling can cause instability with a fixed or a scheduled controller that does not account for buffering changes. To avoid excessive performance degradation due to a conservative controller gain selection, a direct adaptive controller is considered. The PI controller is tuned using a FLS objective and the online optimization based on the approximation of a H_∞ Robust Stability Condition from input-output data. Experimental and simulation results indicate that the adaptive control solution can provide similar, practically acceptable performance over a wide operating range. The algorithm developed along with hardware implementation can be readily used to control pH of a MFC.

4.4.3 Low-cost potentiostat test results

It can be seen from plots in Figure 61 our potentiostat performs reasonably well in tracking set-points. There is an offset in our potentiostat response; this is a result of the shifter circuit and a variation in the reference electrode potential over time. Some of the bias can be corrected by calibrating potentiostat measurements. Statistical analysis of the proposed potentiostat performance is discussed in the next paragraph.

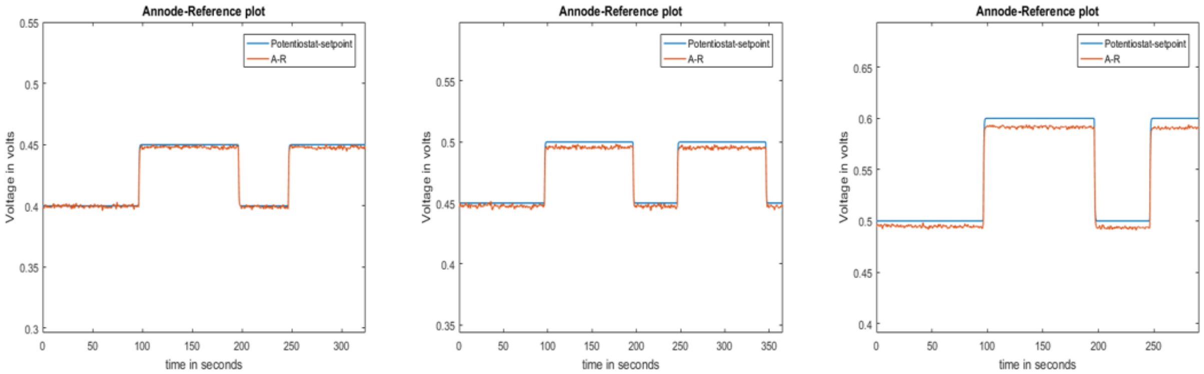

Figure 61. The low-cost potentiostat set-point tracking plots.

We use an ADC with an effective resolution of 17 bits and a range of 0 to 2.048 V in our potentiostat to measure potentials of the anode and the reference electrodes and the ADC least significant bit (LSB) represents a voltage of $1.5625\times10^{-5}V$. If the ADC quantization error is modelled as a uniform random variable [-0.5LSB, +0.5LSB], then the theoretical standard deviation value of an ADC voltage reading resulting from the quantization is $4.5105\times10^{-5}V$. Table 18 shows the standard deviation of the cathode potential readings, where it is observed that its value is higher than the theoretical value (standard deviation because of quantization); this is a result of the presence of external noise. The effect of external noise can be decreased by migrating our potentiostat's analog circuit from a bread board to a printed circuit board (PCB).

Table 18. Standard deviation of cathode potential measurements.

Potentiostat set-point(V)	Proposed potentiostat(V)	Biologic-vmp3(V)
0.4	5.5575×10^{-4}	4.3489×10^{-4}
0.45	5.5964×10^{-4}	4.1844×10^{-4}
0.5	5.9194×10^{-4}	3.5317×10^{-4}
0.6	5.8798×10^{-4}	4.4608×10^{-4}

As compared to Biologic-vmp3 cathode potential measurements, the standard deviation of our potential is slightly higher. There is an expected trade-off between the cost of a potentiostat and its accuracy. Even though the analytical grade potentiostat is more accurate (the standard deviation values of voltage readings of the analytical grade potentiostat are lower than our potentiostat) and can sample potentials faster, the cost of the analytical grade potentiostat is significantly higher than the proposed low cost potentiostat ($6000 vs $200). We conclude that the proposed potentiostat gives satisfactory performance at a fraction of the cost.

In this subtask, we show that, in the typical industrial environment, the proposed potentiostat performance is practically similar to an analytical grade potentiostat. The trade-offs between the proposed potentiostat and an analytical grade potentiostats are also discussed. Moreover, the separation of analog, digital and processor hardware allows this potentiostat to be easily integrated with any hardware components used in the future projects.

5.5. Design of Prototype MFCs and Process Control Systems (Tasks 5 and 6)

5.5.1. Design, operation, and characterization of flat-plate reactors

Characterization of overpotentials in MECs. We first performed chronoamperometry to obtain *j*-*V* curves for an MEC constructed with stainless steel mesh cathodes (SS-1) and AMI-7001 membranes (Figure 62a). We performed at least two replicate measurements to obtain the curves for each condition and show only one representative set here.

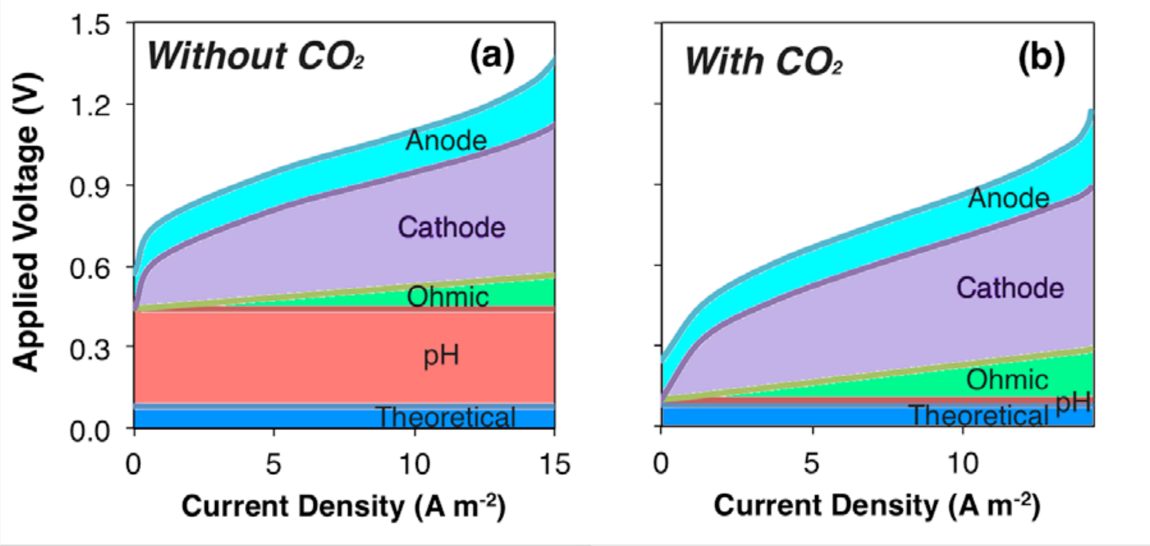

Figure 62 Characterization of the applied voltage in the flat-plate MEC with AMI-70001 membrane and stainless-steel mesh cathode (a) without and (b) with CO_2 addition to cathode. We performed chronoamperometry to plot *j*-*V* curves after producing high current densities (> 15 A m^{-2}) in the MEC.

We divided the total overpotential into four individual overpotentials: (i) anode overpotential resulting from ARB metabolism, (ii) Ohmic overpotential, which is related to ion transport between the anode and the cathode, (iii) concentration overpotential related to an increase in the cathode chamber pH due to low concentration of H^+ or high concentration of OH^-, and (iv) cathode overpotential, which includes cathode activation losses and potentially any concentration losses related to different local concentrations of reactants and products from the bulk electrolyte. The overall applied voltage in the MECs is then the sum of all overpotentials and the theoretical applied voltage necessary, as per the following equation.

$$E_{ap} = E_{Th} + \eta_{pH} + \eta_{Ohmic} + \eta_{cathode} + \eta_{anode} \qquad \text{(Eqn. 21)}$$

where E_{ap} is the applied voltage, E_{Th} is the theoretical voltage necessary, η_{Ohmic} is the Ohmic overpotential, η_{pH} is the concentration overpotential due to increased cathode pH, $\eta_{cathode}$ is the cathode overpotential, and η_{anode} is the anode overpotential. The applied voltage (E_{ap}) was the difference between the anode and cathode potentials measured with the potentiostat. The theoretical voltage (E_{Th}) is the energy needed to overcome the thermodynamic barrier for H_2 production in MECs. We calculated this with the Nernst equation with known acetate and bicarbonate concentrations, and pH,

$$E_{Th} = E_{ca} - E_{an} = \left(E_{ca}^{0} - \frac{RT}{2F}\ln\frac{pH}{[10^{-7}]^{2}}\right) - \left(E_{an}^{0} - \frac{RT}{8F}\ln\frac{[CH_3COO^{-}]}{[HCO_3^{-}]^{2}[10^{-7}]^{9}}\right) \qquad \text{(Eqn. 22)}$$

where E_{ca} and E_{an} represent the theoretical cathode and anode potential from the Nernst equation.

We calculated concentration overpotential related to a high cathode pH (η_{pH}) by measuring the observed pH difference between bulk liquid in the anode and cathode, and using the relationship of 60.1 mV of overpotential per one unit that the cathode pH is higher than the anode pH at 30 °C. We determined Ohmic overpotential from the Ohmic resistance (R_{Ohmic}; Ohm cm^2) measured using EIS.

$$\eta_{Ohmic} = j \cdot R_{Ohmic} \qquad \text{(Eqn. 23)}$$

We calculated the anode overpotential from the following equation,

$$\eta_{anode} = E_{an,observed} - E_{an} \qquad \text{(Eqn. 24)}$$

We assumed that the remainder of the applied voltage is due to the cathode overpotential.

For the *j*-*V* curve shown in Figure 62a, we used 100 mM NaOH as the catholyte. This in itself creates the concentration overpotential due to a high cathode pH. However, this was out of convenience for the experimental protocol. Even for MECs that are operated with NaCl electrolyte or buffers, the increase in cathode pH is a widely observed phenomenon (Rozendal et al., 2008; Sleutels et al., 2009; Nam and Logan, 2012). We show in Figure 63 how the cathode pH increases over time up to almost 13 if we use a 100 mM NaCl solution at the cathode.

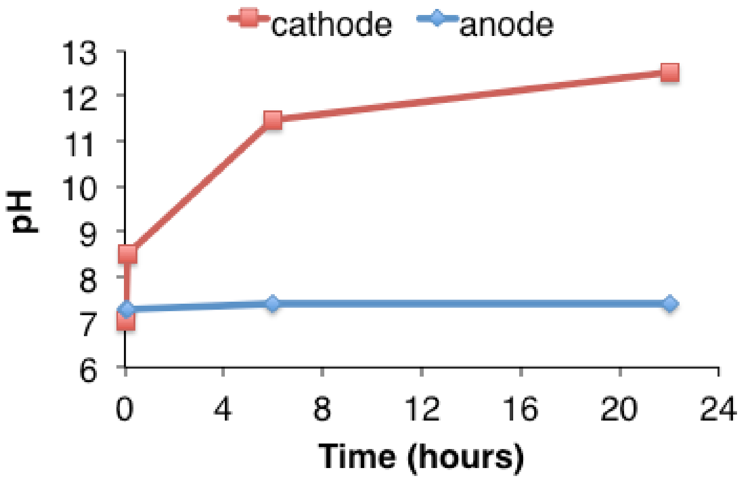

Figure 63. pH increase in flat-plate MEC cathode. pH in cathode fed with 100 mM NaCl increased up to >12.5 within 24 hours at ~10 A m^{-2}.

As shown in Figure 62a, at a high current density (~10 A m^{-2}) where the total applied potential was 1.092 ± 0.017 V, the cathode has the largest fraction of the overpotential (0.429 ± 0.040 V), followed by the concentration overpotential due to a high cathode pH (0.344 ± 0.019V), the anode overpotential (0.153 ± 0.012 V), and the Ohmic overpotential (0.085 ± 0.002 V). Energy losses associated with the anode are usually not avoidable because they relate to the concentration gradients of reactants and products in the anode biofilm (substrate and proton), intracellular potential losses (ARB metabolism), and the extracellular potential losses (EET to anode) (Torres et al., 2010; Lee and Rittmann, 2010). The anode overpotential is typically 0.1-0.3 V depending on the current density (Lee and Rittmann, 2010; Jeremiasse et al., 2010). This is reflected in the Nernst-Monod equation used for modeling ARB, in which the mid-point potential, which results in half the maximum current density production, is only ~0.1 to 0.15 V more positive of the theoretical anode potential for many pure and mixed cultures (Yoho et al., 2014; Torres et al., 2008; Torres et al., 2008). In this case, the anode overpotential (0.153 ± 0.012 V) is within range of what is known for ARB with an efficient metabolism and EET mechanism. Therefore, we should focus on the energy losses from concentration overpotential due to a high cathode pH and cathode overpotential to improve the voltage efficiency.

Effect of CO_2 addition to the cathode. The pH imbalance between the anode and the cathode in MXCs always results in a higher pH at the cathode (Rozendal et al., 2006; Popat et al., 2012). Since an increase in one pH unit decreases the redox potential for the hydrogen evolution reaction by 60.1 mV (at 30 °C), this results in a large concentration overpotential. In the case shown in Figure 62a, the pH difference between the two chambers was 6.0 units, and so the concentration overpotential was 0.361 V. We have previously tested a strategy whereby adding CO_2 to the cathode can reduce the pH, and thus reduce the concentration overpotential in air-cathode MFCs which include the oxygen reduction reaction (Popat et al., 2012; Torres et al., 2009). We tested this strategy for our flat-plate MEC design. In MECs with a liquid catholyte, hydroxide ion (OH^-) can be combined with the added CO_2 to form bicarbonate (HCO_3^-) and/or carbonate (CO_3^-) anions (Figure 64). These anions dissolved in catholyte will buffer the pH close to their pK_a values of 10.3 and 6.3 for the HCO_3^-/CO_3^- and CO_2/ HCO_3^- couples, respectively. This is advantageous in decreasing the pH-related concentration overpotential. A previous study shows that the pHs of catholytes were ~5.9 and ~6.5 of non-buffer and buffer solution with CO_2 addition to cathode in MFC (Fornero et al., 2010).

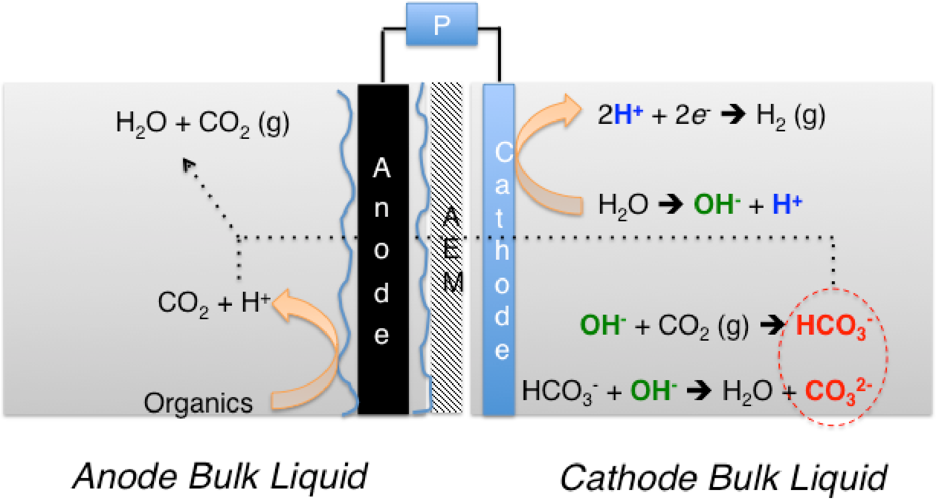

Figure 64. Mechanism of CO_2 in decreasing the concentration overpotential.

We show in Figure 65 the effect of adding CO_2 to the cathode on the applied voltage and the cathode pH at a high current density (~18.5 A m^{-2}). As soon as we introduced CO_2 into the cathode chambers of the MEC, the applied voltage decreased from 1.285 to 1.083 V. This represents a decrease in the overpotential of 0.202 V. The cathode pH decreased by roughly 5 units. This should result in a decrease in the applied voltage of ~ 0.301 V. While the change we observe is smaller than this, it could be due to a higher local cathode pH than that measured in the bulk solution of the cathode chambers. This overpotential could then thus be included in the cathode overpotential for which we do not distinguish between the activation losses and the concentration overpotential due to higher surface pH than bulk solution. We have observed such phenomenon in MFC cathodes before (Popat et al., 2012). Nonetheless, we confirmed that adding CO_2 to the cathode represents a great opportunity to reduce significantly the applied voltage in MECs. This improvement is greater than the previous report in air-cathode MFCs (Torres et al., 2008), which shows the improvement of the operational voltage of the MFC by 0.08 and 0.12 V with 5 and 10% of CO_2 addition to the MFC cathode, respectively. The larger improvement we observed could be due to higher concentration of CO_2 (100%) added to the cathode in our study.

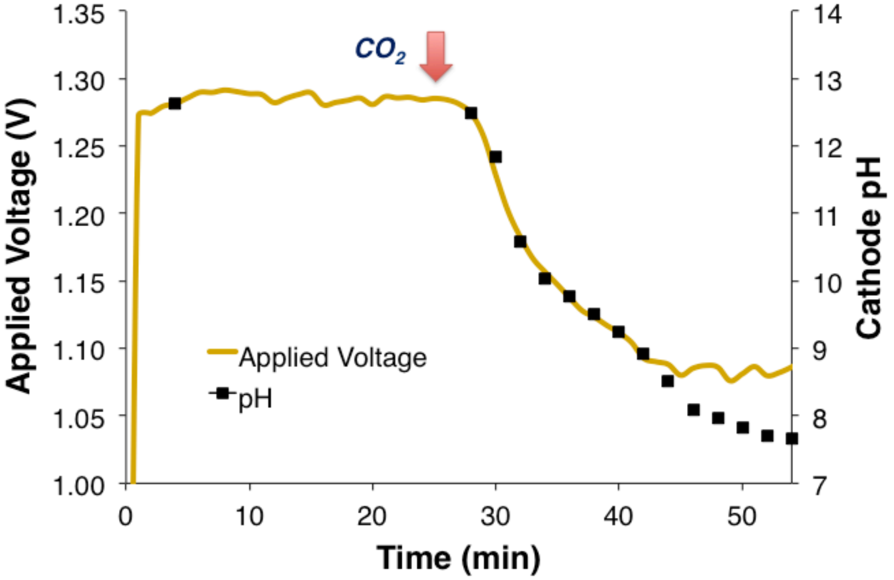

Figure 65. Decrease in applied voltage and cathode pH with CO_2 addition to cathode. Current density was 18.5 ± 0.3 A m^{-2}.

To further confirm that the benefit of CO_2 is primarily on the pH, and not necessarily on the cathode activation overpotential, we performed EIS measurements on the cathode, at various cathode potentials. Through these measurements, we determined the overall cathode resistance at each potential. The results from these measurements are shown in Figure 66. In Figure 66a, we show the cathode potential vs. the cathode area-specific resistance, from which it is apparent that the main impact of CO_2 is on changing the cathode potential at which a given current density is obtained. However, the overall shape of the curve remains similar, suggesting that the catalyst properties have not changed. This is further exemplified in Figure 66b, where the current density vs. the cathode area-specific resistance relationship stays the same irrespective of adding CO_2. These results indicate that CO_2 only affects the performance by decreasing the pH in the cathode chamber without resulting in any cathode catalytic changes.

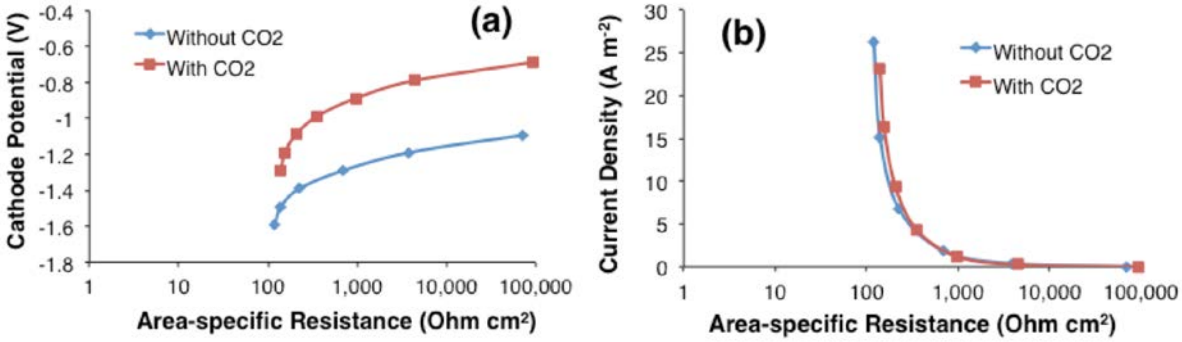

Figure 66. Effect of CO_2 on the cathode catalytic reaction: (a) cathode potential vs. the cathode area-specific resistance, (b) current density vs. the cathode area-specific resistance.

Next, we characterized the flat-plate MEC the same way as in Figure 62a, but this time while continuously adding CO_2 to the cathode chambers. A comparison of the complete characterization with (Figure 62b) and without CO_2 is shown in Figure 62. Adding CO_2 to the cathode chamber almost completely eliminated pH-related concentration overpotential (only 0.027 ± 0.013 V). At a current density of 10 A m^{-2}, we reduced the total applied voltage from 1.092 to 0.859 V, which is amongst the best reported performances for MECs in literature (An and Lee, 2013; Tartakovsky et al., 2011; Sleutels et al., 2013; Zhang et al., 2010). There are few studies having exceptional high current densities (> 16 A m^{-2}) with 1 V of applied voltage (Jeremiasse et al., 2010; Sleutels et al., 2009). The high performance might result from a good reactor design with a high rate of flow through recirculation of anolyte and catholyte (hydraulic retention times [HRTs] ≈ 1~2 minutes). The recirculation helps mass transport of reactants and products to and from anode and cathode; this might be one of the reasons for their high performance. The energy usage for high rate of recirculation with pump was not evaluated.

Even though the overall overpotential was reduced with addition of CO_2 to the cathode chamber, the Ohmic overpotential increased, and this is likely due to a shift in the predominant species being transported through the AEM from OH^- to carbonate or bicarbonate. We next focused on decreasing this Ohmic overpotential to ensure the maximum benefit of adding CO_2 for pH control. In addition, this leaves cathode overpotential as the major overpotential in the system (0.457 ± 0.023 V), and thus we focused also on testing other cathode catalysts with the aim of reducing the overall applied voltage.

Material selection for reducing the Ohmic and cathode overpotentials. We show in Figure 67 the area specific resistance to ion transport for five different AEMs in 100 mM bicarbonate solution. While AMI-7001 is a standard AEM that have been used in various laboratory MXC studies (Parameswaran et al., 2009; Fornero et al., 2010; Vyas et al., 2001), it had the largest resistances to transport of bicarbonate of all the membranes we tested. The FAA, FAB, and A201 membranes provided significantly less resistance to bicarbonate transport compared to the AMI-7001 and I-200 membranes. The result is consistent with the type of membrane, i.e. "homogeneous" or "heterogeneous." Heterogeneous membranes (AMI-7001 and I-200) have a backing material, providing greater mechanical strength but an increase in thickness and thus higher ion transport resistance. On the other hand, homogeneous membranes (FAA, FAB, and A201) are the opposite since they are made from finer resin particles, thus resulting in thinner and flexible membranes with lower resistance (Güler, 2014; Krstajic et al., 2011) (see Table 6 for thicknesses for each membrane). Since FAA has also better stability at higher pH compared to AMI-7001 (Table 6), we selected FAA as the membrane to replace AMI-7001 in the next phase of our MEC testing.

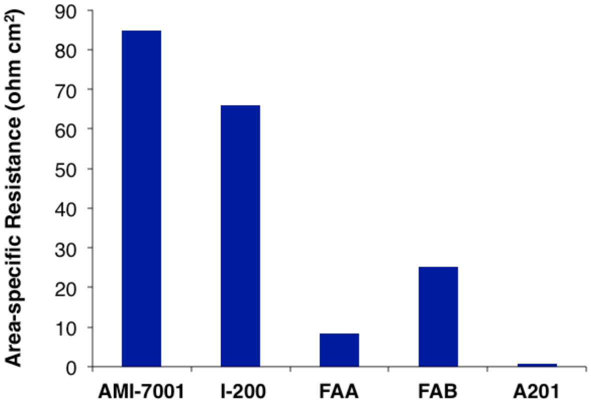

Figure 67. Resistances of various membranes tested in 100 mM $NaHCO_3$.

Even though CO_2 has a benefit in decreasing the concentration overpotential, the cathode overpotential also represents one of the major overpotentials. A Pt-based cathode can decrease the cathodic activation losses most effectively, but Pt is expensive. Thus, there have been many studies to develop efficient catalysts for reducing cathodic activation overpotential with non-noble metals (Jeremiasse et al., 2010; Hu et al., 2009; Couper et al., 1990; Selembo et al., 2010). Many reports show that nickel or Ni-based cathodes are effective in decreasing the hydrogen evolution reaction overpotential (Jeremiasse et al., 2010; Hu et al., 2010; Rozendal et al., 2008). Therefore, to decrease the cathode overpotential by selecting a good low-cost catalyst, we chose a commercially available Ni mesh, and tested its performance against the SS mesh as a comparison (Figure 68). The nickel mesh (Ni 200) had less overpotential compared to the SS mesh especially at high current density. At 10 A m^{-2}, cathode potential is higher by 0.12 (± 0.002) V with Ni 200 mesh indicating a lower activation barrier to produce H_2. This could be because of higher catalytic activity of pure nickel vs. in an alloy, such as in stainless steel, or related to the specific configuration we used for the meshes (for e.g. open area, mesh size etc. – see Table 7).

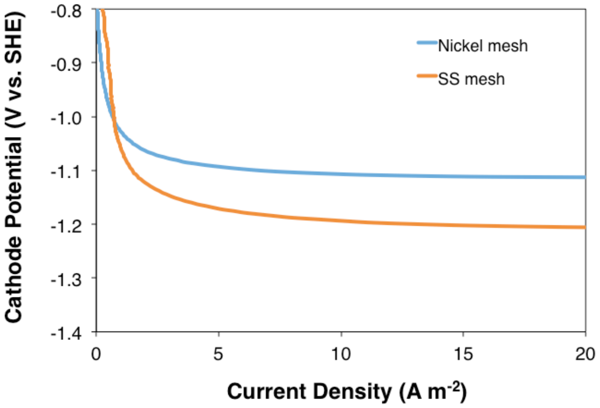

Figure 68. Linear sweep voltammograms (LSVs) of stainless steel and nickel mesh cathodes at pH 13.

Characterization of overpotentials in MEC with improved materials. With the Ni mesh cathode and FAA membrane, we performed the same characterization experiments for the MEC as we did with the MEC with stainless steel mesh cathode and AMI-7001 membrane, both with and without adding CO_2 to the cathode chambers. Figure 69 shows the *j-V* curve with the applied voltage separated into the various overpotentials. We also summarize each individual overpotential at 10 A m^{-2} in Table 19.

At 10 A m^{-2}, the total overpotential without adding CO_2 to the cathode was 0.989 ± 0.017 V, a significant decrease over the values obtained before the materials improvement (1.092 ± 0.017 V). The FAA membrane decreased the Ohmic overpotential by ~ 52 mV from 0.085 ± 0.002 V with AMI-7001 to 0.033 ± 0.004 V at 10 A m^{-2}. The cathode overpotential decreased from 0.429 ± 0.040 V to 0.405 ± 0.036 V. The FAA membrane allowed for a slightly lower pH in the cathode chamber, which also resulted in a decrease in the concentration overpotential due to a higher cathode pH (0.279 ± 0.011 V overpotential with FAA vs. 0.344 ± 0.019 V overpotential with AMI-7001). The overall reduction in the applied voltage however was smaller than the improvements in these overpotentials, because the anode overpotential was slightly higher at 0.199 ± 0.013 V vs. 0.153 ± 0.012 V.

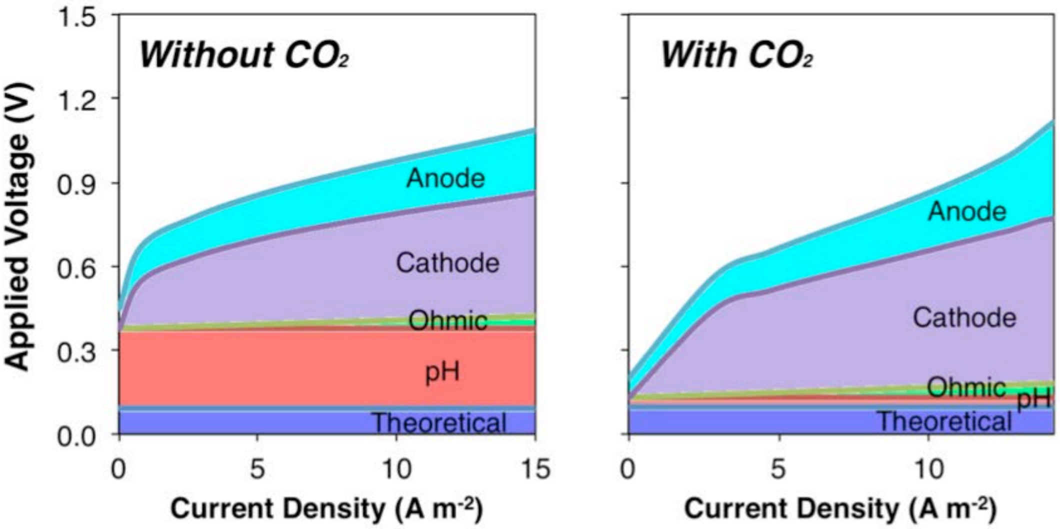

Figure 69. Characterization of applied voltage in flat-plate MEC with FAA membrane and nickel mesh cathode.

Table 19. Individual overpotential characterized in flat-plate MEC at 10 A m^{-2} with and without CO_2 addition to different cathodes (SS = stainless steel and Ni = nickel).

Overpotential	SS without CO_2	SS with CO_2	Ni without CO_2	Ni with CO_2
Anode	0.153 (± 0.012)	0.168 (± 0.016)	0.199 (± 0.013)	0.210 (± 0.014)
Cathode	0.429 (± 0.040)	0.457 (± 0.023)	0.405 (± 0.036)	0.513 (± 0.021)
Ohmic	0.085 (± 0.002)	0.125 (± 0.007)	0.033 (± 0.004)	0.035 (± 0.003)
pH	0.344 (± 0.019)	0.027 (± 0.013)	0.279 (± 0.011)	0.032 (± 0.002)
Theoretical	0.081 (± 0.000)	0.081 (± 0.000)	0.091 (± 0.001)	0.098 (± 0.001)
Total	1.092 (± 0.017)	0.859 (± 0.001)	0.989 (± 0.017)	0.888 (± 0.022)

When adding CO_2 to the cathode chambers, the applied voltage at 10 A m^{-2} was 0.888 ± 0.022 V, which does not represent an improvement over the previous MEC before including new materials (0.859 ± 0.001 V). This was despite improvement in the Ohmic overpotential, which decreased from 0.125 V ± 0.007 to 0.035 ± 0.003 V with the FAA membrane. The largest part of the overpotential (0.513 ± 0.021 V) in this case was from the cathode overpotential. There are several possible reasons for this. It is possible that there was a local high pH on the cathode surface, despite a lower bulk pH with adding CO_2, which could result in a higher cathode overpotential, which includes any losses due to local concentration gradients.

In addition, the characterization with CO_2 added to the cathode was done after several days of operation of the MEC, which could have resulted in inhibition of the nickel catalyst. It has previously been reported that with long-term operation (> 1 month) with a Ni foam cathode, the overpotential increased, but the exact mechanisms of this change in performance are not known (Jeremiasse et al., 2010). One possible mechanism is the formation of nickel hydride, which has been shown to diminish the catalytic properties of Ni (Couper et al., 1990). In addition, another possible cause could be the decrease of active surface area due to either the H_2 or CO_2 bubbles trapped in the mesh, which were evident while operating the cathode in this fashion. This would result not only in higher activation losses due to reduced surface area, but also possibly concentration overpotential due to accumulation of H_2 on the reaction surface.

In this Subtask, we characterized the applied voltage in flat-plate MECs as individual overpotentials from different phenomena. This is of great theoretical and practical importance for MPPC development that also requires a design optimization and increase in voltage efficiency. In our flat-plate MECs, low overpotentials at high current densities were observed with (i) high-surface area anode, (ii) commercially available cathodes and membranes, and (iii) CO_2 addition to the cathode.

CO_2 (100%) addition to the cathode eliminated concentration overpotential due to a high cathode pH, just like in air-cathode MFCs. We want to note here that while we used a two-chambered MEC where pH difference between the anode and cathode is directly apparent due to the use of a membrane, we have shown that local gradients could also cause a Nernstian concentration overpotential at the cathode in single-chambered systems, which can be decreased or eliminated using CO_2. Recycle of the CO_2 produced in the anode from oxidation of organics would be the ideal scenario. In the present study, we use the optimum system using pure CO_2 and fast recirculation with pump. However, how CO_2 is returned from the anode to the cathode needs to be optimized further, especially when dealing with real wastes at the anode.

5.5.2. Design of microbial H_2O_2 producing cells (MPPC)

We assembled a MPPC using the optimal conditions from our previous testing: 200 mM NaCl at pH 7, which demonstrated good stability with H_2O_2 in the short term; the AMI-7001 AEM, which demonstrated low mass loss; and 0.5 mg/cm^2 of Vulcan carbon catalyst with Nafion binder, which maintained lowest cathodic overpotentials over the largest range while partitioning the highest number of electrons to H_2O_2. We operated the MPPC continuously for 18 days with a 4-h HRT in the liquid cathode chamber and air flow rates of 10, 20, and 30 cm^3/min through the air cathode chamber. Prior to anode inoculation, we quantified the total cell abiotic Ohmic overpotential using EIS as 75.0 Ω-cm^2.

As demonstrated in 63, the MPPC gave good performance with the optimized design variables. Varying the air supply rate had minimal effect on H_2O_2 concentration: the average effluent H_2O_2 ranged from 2.5 ± 0.4 to 3.1 ± 0.4 g/L, with the highest H_2O_2 concentration (3.8 g/L) achieved at 20 cm^3/min. These high concentrations were achieved even though the effluent catholyte pH ranged from 12.1 to 12.4. While the cathode potential decreased from -0.54 to -0.50 $V_{Ag/AgCl}$, the H_2O_2 concentration decrease from 20 to 30 cm^3/min likely was due to the 1 A/m^2 decrease in current density. For comparison, our cell used 18% more energy to produce 3 times the amount of H_2O_2 compared to Rozendal et al. (2009).

We used CVs to understand our MPPC's performance. The CVs illustrated that the MPPC achieved higher energy-neutral current densities (i.e., the current at which the reactor experiences 0 V cell potential) than other systems due to reduced overpotentials, and cathodic overpotentials are still the limiting factor in MPPC performance. Figure 70 shows a CV of our MPPC at a 1 mV/s scan rate. Correcting for Ohmic losses in the system, the open-circuit potential was 0.20 V for all scans, which is lower than the theoretical potential of 0.56 V. The ~0.3 V difference is associated with the equilibrium pH difference between the anode and cathode since there was a ~5 pH unit difference between the anode and cathode. Energy neutral operations occurred at 3.72 ± 0.29 A/m^2, which is significantly larger than that achieved by Rozendal et al. (2009), at 1.6 A/m^2, and Modin and Fukushi (2012), 0.54 A/m^2. The superior energy-neutral performance indicates that H_2O_2 could be produced at up to 3.72 A/m^2 without requiring energy input, and the cell had significantly lower overpotentials versus previous studies. Based on the theoretical potentials at the anode and cathode and not corrected for Ohmic losses, Figure 70a demonstrates that, at energy neutral conditions, the anode overpotential was 0.149 V and cathode overpotential was 0.379 V. Concentration overpotential due to pH differences between the anode and cathode chambers account for 0.27 V or 51% of cathode overpotentials. Therefore, 0.029 V of Ohmic overpotential exists at energy neutral conditions, reiterating that our cell design significantly decreases Ohmic losses within the MPPC. While small, these Ohmic losses significantly affected cell performance: adjusted for Ohmic losses, Figure 70b shows that the anode and cathode overpotentials increase to 0.157 V and 0.403 V, respectively, and that the cell could operate at 4.58 A/m^2 before drawing additional energy to produce H_2O_2. At our operating current density of ~ 10 A/m^2 and pH 12.08-12.43, the cathode overpotential increased to 0.524 V, of which 58% was due to pH differences between the anode and cathode chambers. As discussed in Popat and Torres (2016), the production of OH^- ions during the oxygen reduction reaction increases pH at the cathode, making it more difficult to reduce the cathode operating pH and, consequently, concentration overpotential.

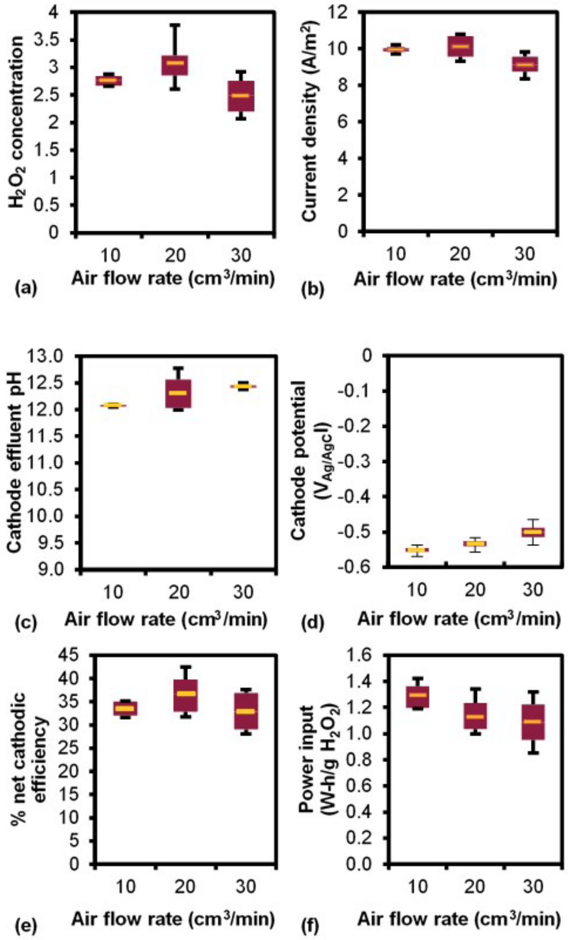

Figure 70. Performance during continuous operations with varying air flow rate: (a) H_2O_2 concentration, (b) current density, (c) pH, (d) cathode potential, (e) percent net cathodic efficiency (as H_2O_2), and (f) power input required to produce 1 g of H_2O_2.

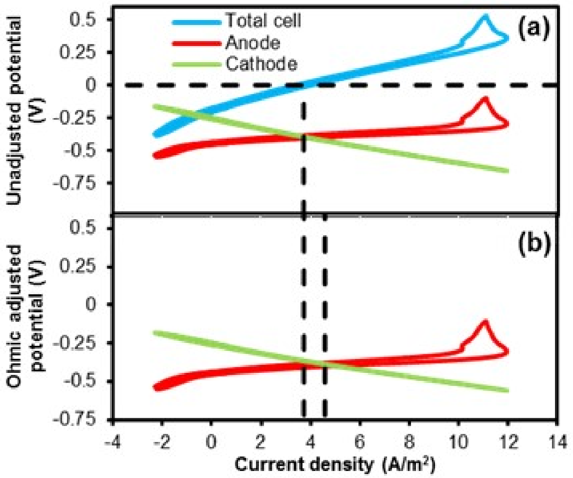

Figure 71. Cyclic voltammetry of the MPPC for (a) unadjusted cell and (b) Ohmic corrected potentials, with cell (blue), anode (red), and cathode (green) potentials. For the cell potentials, positive voltages represent power consumption and negative voltages represent power production.

The superior performance of the MPPC we report here likely was due to a combination of several factors. The improvement in energy-neutral operations was largely driven by the decreased distance between anode and cathode: When the distance was decreased from 1 to 0.5 cm in the MPPC, the energy-neutral current density increased from 1.63 (± 0.03) to 3.72 A/m^2 (Figure 72). Catalyst selection tailored to H_2O_2 production resulted in low cathode potentials and good net cathodic efficiencies with little power input. The use of AMI-7001 membrane provided long term, stable performance while having minimal effect on H_2O_2 production versus other membranes, as shown is Figure 72. Nevertheless, performance could be further improved by reducing the pH gradient between the anode and cathode chambers, consequently reducing the MPPC's concentration overpotential.

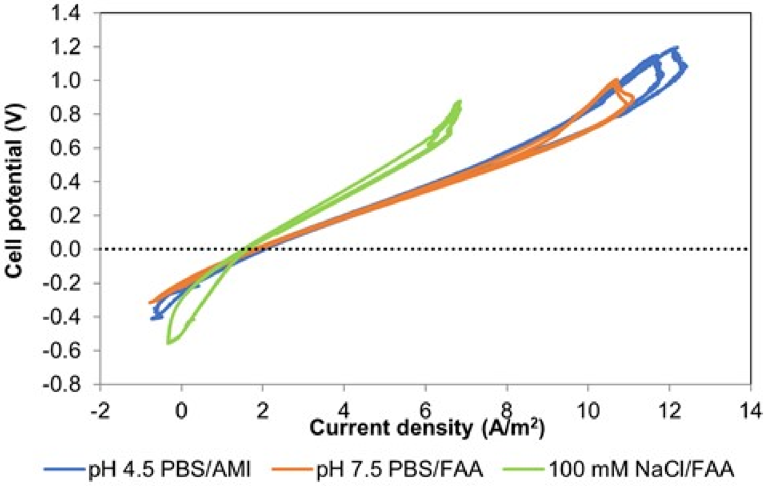

Figure 72. CVs of preliminary reactor design. The MPPC CVs were performed with two different membranes (FAA and AMI-7001) and three different catholytes: 100 mM NaCl, pH 4.5 PBS, and pH 7.5 PBS. The MPPC was operated at a 4 hr HRT and 30 cm^3/min air flow rate. The reactor design was the same as the reactor presented in this paper, except there was 1 cm distance between the anode and cathode. The FAA membrane is ~1/3 the thickness of the AMI membrane and has a lower resistance.

In this Task, we combined the findings of previous Tasks into an MPPC design, which we operated using 200 mM NaCl catholyte at different air-flow rates to optimize H_2O_2 concentration. The air-flow rate did not drastically change MPPC performance: The MEC produced H_2O_2 at a concentration as high as 3.8 g L^{-1} and an average of 2.5±0.4 to 3.1 g L^{-1} at different air-flow rates. The MPPC's Ohmic overpotentials were small at 69.1 Ω cm^2. During operation, anodic overpotentials were approximately 42 % lower than cathodic overpotentials, and >58 % of cathodic overpotential was caused by the pH gradient between the anode and cathode chambers. Thus, we assert that continuous H_2O_2 production in MECs is achievable if materials are optimized for compatibility with and production of H_2O_2.

For perspective, our MPPC is capable of producing H_2O_2 at concentrations more than adequate for water and wastewater treatment. H_2O_2 concentrations of 2.5–3.0 g L^{-1} are five- to tenfold higher than the doses required to remove 90+ % chemical oxygen demand (COD) from wastewater streams, 20-fold greater than required for 99+ % removal of micropollutants and 10–100-fold higher than required for UV disinfection.

5.6. Optimization of Prototype MFCs (Task 7)

5.6.1. Acetate-fed MPPC

Effects of varying cathode HRT. Based on the favorable results using NaCl as the catholyte in Young et al. (2016), we explored the impact of catholyte HRT with a fixed NaCl concentration of 200-mM on sustained performance. Figure 74a illustrates excellent H_2O_2 production: the concentration increased almost linearly from 1.0 to 3.1 g H_2O_2 L^{-1} as the catholyte HRT increased from 1- to 4-h at similar current densities (Figure 74c). For perspective, these concentrations are more than adequate for disinfection (30-50 mg H_2O_2 L^{-1}) and micro-pollutant removal (5-20 mg H_2O_2 L^{-1}) when coupled with UV and Fenton processes (Yang et al., 2014; Rajala-Mustonen and Heinonen-Tanski, 1995). The increases in H_2O_2 concentration were coupled with pH increases from 11.8 to 12.3 (Figure 73), since OH^- was produced during O_2 reduction and the catholyte was unbuffered. System overpotentials did not demonstrate any clear trends with any of the parameters evaluated (Figure 74).

As expected, an optimal HRT existed due to a tradeoff between H_2O_2 production rate, which is highest at the lowest HRTs, and decay rate, which outpaces the production rate at longer HRTs. Figure 73e illustrates that the net production rate of H_2O_2 decreased from 1.02 to 0.76 g $L_{cathode}^{-1}$ d^{-1} as HRT increases from 1- to 4-h. There was a corresponding decrease in Figure 74b shows the power required to produce H_2O_2 increased from 0.42 to 1.13 Wh g^{-1} H_2O_2 and cathodic coulombic efficiency (CCE) from 57% to 21%. The decrease in net production rate with increasing HRT was a result of H_2O_2 decomposition that could have had several causes: (1) H_2O_2 dissociating to HO_2^- at high pH and diffusing across the AEM, (2) H_2O_2 reacting with the AMI membrane as illustrated in Young et al. (Young et al., 2016), and (3) H_2O_2 auto-decaying to H_2O and O_2 due to prolonged exposure to the carbon catalyst or metals (Drogui et al., 2001):

$$H_2O_2 \rightarrow 2H_2O + O_2 \qquad \text{(Eqn. 25)}$$

Above a 4-h HRT, the effluent H_2O_2 concentration decreased to 2.3 g H_2O_2 L^{-1}, leading to a pH decrease to 12.2 via Eqn. 26, even though the cathode potential was consistent with the other HRTs (-0.52 V) and current density was similar to the 2- and 3-h HRTs (8.5 A m^{-2}). The deteriorating performance likely was due to the reduction of H_2O_2 to H_2O via the 2-electron ORR:

$$H_2O_2 + 2e^- \rightarrow 2OH^- \qquad \text{(Eqn. 26)}$$

due to increased exposure to electrons at the cathode at the long HRT. We observed membrane failures only during the experiment operated at the 6-h HRT. The membrane failed twice in 6 days while operating at the 6-h HRT, and the total down time was 2% of the total operating time. We suspect that the long HRT may have also promoted H_2O_2 auto-decay by reacting with the membrane itself to form O_2 by Eqn. 25.

The MPPC design was efficient for sustained operation: the open-circuit potential was 0.18-0.20 V versus the theoretical value of 0.56 V, and the ~0.3 V difference was caused by the ~ 5-unit pH difference between the anode and cathode. Consistent with the results in Section 5.5, the MPPC achieved high current density in energy-neutral situations (i.e., when the reactor experiences 0 V cell potential) ranging from 3.24 A m^{-2} at 1-h and 2-h HRT and 3.73 A m^{-2} at 4-h HRT.

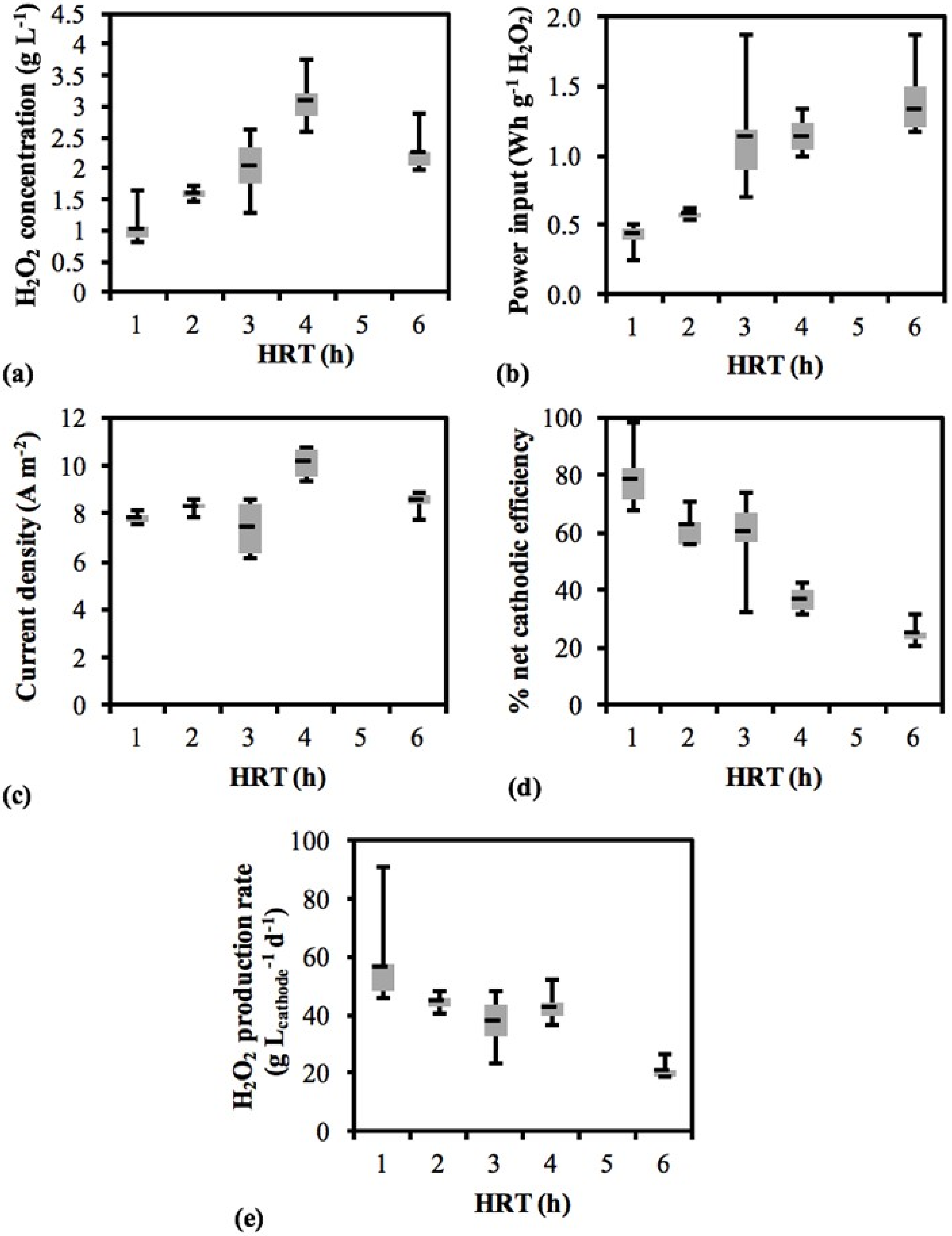

Figure 73. Results for the experiment with a range of HRT from 1- to 6-h using 200-mM NaCl catholyte: (a) H_2O_2 concentration, (b) power input, (c) current density, (d) net cathodic

coulombic efficiency, and (e) H_2O_2 production. The light gray boxes represent the first and third quartiles, and the black point represents the average value. The whiskers represent the maximum and minimum data points.

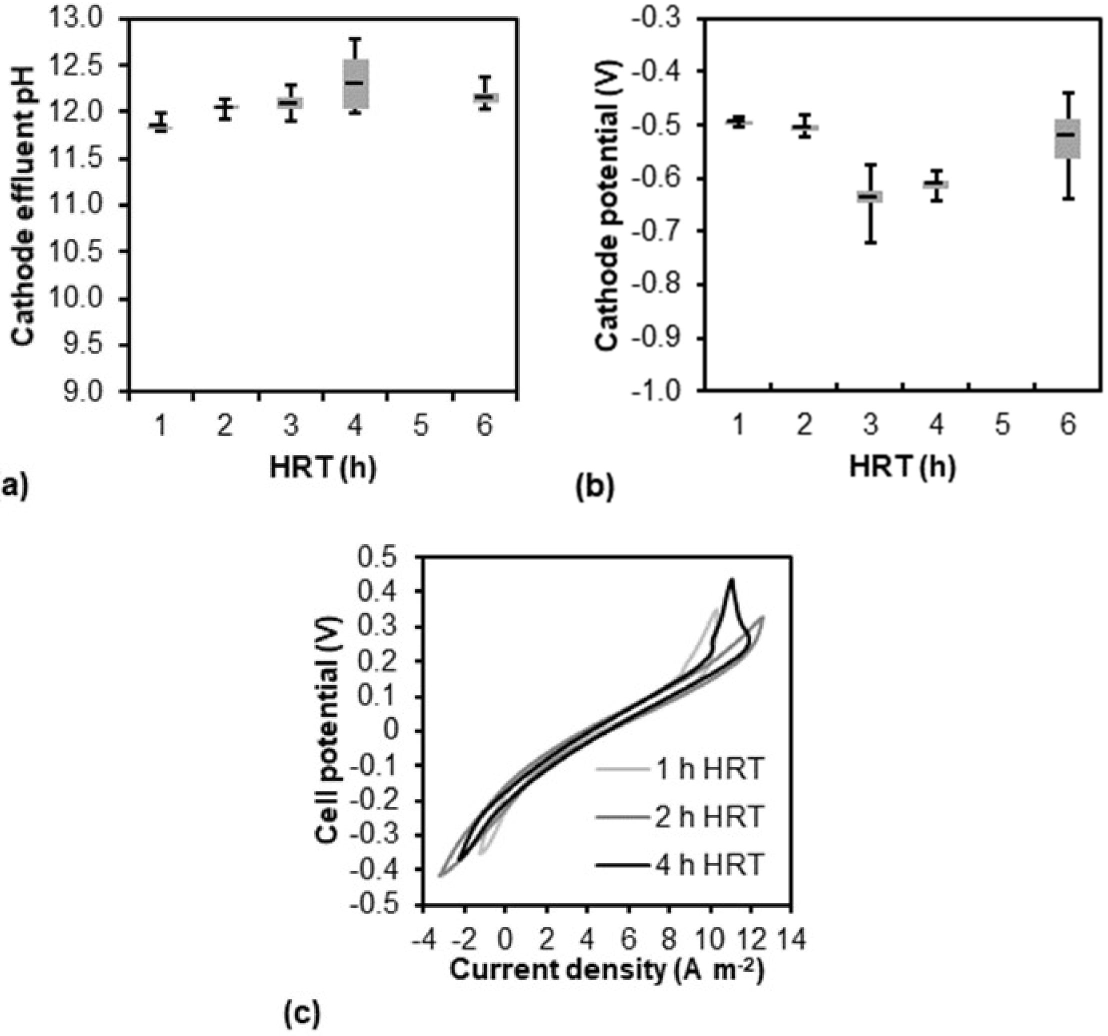

Figure 74. Results for the experiment with a range of HRT from 1- to 6-h using 200-mM NaCl catholyte: (a) cathode effluent pH, (b) cathode potential, (c) net cathodic efficiency, and (d) cyclic voltammetry of cell performance. The light gray boxes represent the first and third quartiles, and the black point represents the average value. The whiskers represent the maximum and minimum data points.

Effects of varying NaCl catholyte concentrations. As expected, increasing the electrolyte concentration improved MPPC power efficiency, although H_2O_2 production did not change. Figure 75a shows that NaCl concentration ≥ 200-mM had little effect on H_2O_2 effluent concentration (2.4-3.1 g L^{-1}), but the required power input declined from 1.1 to 0.4 Wh g^{-1} H_2O_2 (Figure 75b). This improvement was observed even though there was a small decrease in current density from 10.1 to 9.1 A m^{-2} (Figure 75c) and CCE stabilized between 37% and 43% (Figure 75d). 100-mM NaCl catholyte produced a lower average H_2O_2 concentration than ≥ 200-mM NaCl (~1.2 versus ~3.1 g L^{-1}), largely due to a limiting concentration of Cl^- ions to maintain electroneutrality; on an electron basis, 100-mM of NaCl supports the production of 1.7 g H_2O_2 L^{-}

^{1} (50-mM). Above 100-mM, cathode potential improved as expected from -0.54 V at 200-mM to -0.33 V at 500-mM NaCl (Figure 75e) at similar current densities, indicating reduced Ohmic losses.

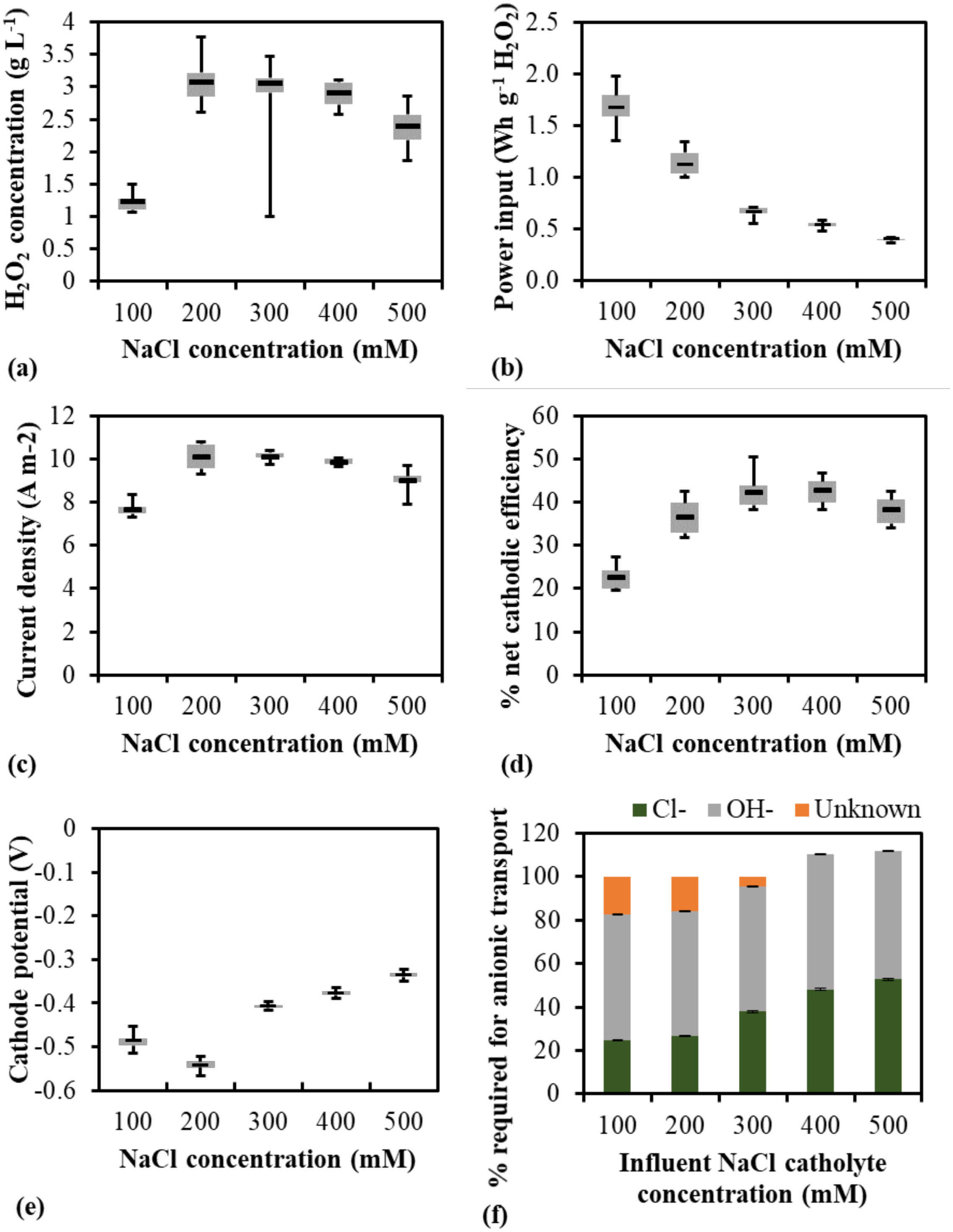

Figure 75. Results for varied NaCl concentrations from 100- to 500-mM: (a) H_2O_2 concentration, (b) power input, (c) current density, (d) net cathodic coulombic efficiency, (e) cathode potential, (f) and the percent of anionic transport from the cathode chamber to the anode

chamber required to maintain electroneutrality. The light gray boxes represent the first and third quartiles, and the black point represents the average value. The whiskers represent the maximum and minimum data points.

Figure 75f shows that, regardless of NaCl concentration, OH^- was the primary ion migrating from the cathode to the anode chamber, ranging from 56% to 60%. OH^- as the dominant anion also explains why all conditions achieved approximately the same pH (12.14-12.23): Cl^- migrated from the cathode chamber until the catholyte achieved a stable pH ~12.2-12.3, at which concentration the OH^- overcame the migration barrier to begin diffusing to the anode. Cl^- migration and/or diffusion increased 20-44% with increasing catholyte concentration and reduced ionic Ohmic overpotentials: Each 100-mM of NaCl present in the catholyte led to a linear increase of ~6% in Cl- anions migrating to the anode and ~ 50 mV decrease in cathode overpotential. The linear declines of Ohmic losses are consistent with the linear CVs in (Figure 76b). Consequently, reduced cathodic overpotentials led to a smaller power input for H_2O_2 production.

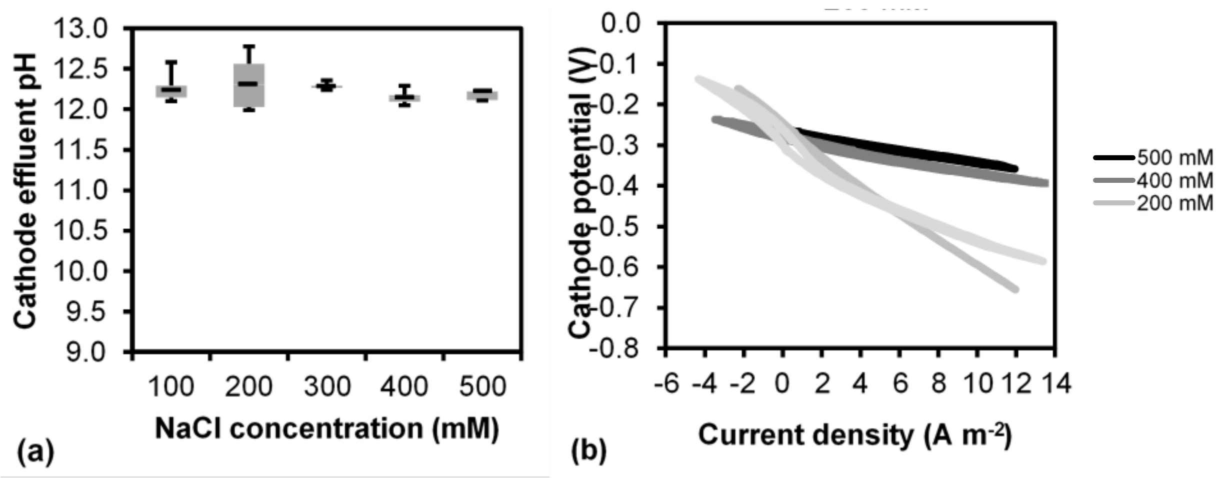

Figure 76. Results for varied NaCl concentrations from 100- to 500-mM: (a) cathode effluent pH and (b) the cathode CV. The light gray boxes represent the first and third quartiles, and the black point represents the average value. The whiskers represent the maximum and minimum data points.

Since Cl^- and OH^- did not account for the total number of anions required to maintain electroneutrality in the cell, additional unidentified ions, identified as the "unknown" fraction in Figure 75f, must have diffused between the anion and cathode chambers. These unidentified ions represented 17% of the migrating ions at 100-mM NaCl, but they steadily decreased to 0% at higher NaCl catholyte concentrations. The unidentified ions could have been HO_2^-, present at the cathode due to the pH being greater than the H_2O_2's pK_a, or counter diffusing cations like Na^+ from the anode chamber. It is more likely that HO_2^- anions were migrating to the anode, since the concentration of unidentified ions linearly decreased from 17% at 100-mM NaCl to 0% at 400-mM NaCl; if Na^+ had dominated the unidentified ions, then having more Na^+ in the anode chamber should have made them more important.

Effects of applying EDTA as an H_2O_2 stabilizer. Metal chelators often are used to stabilize H_2O_2 solutions by preventing H_2O_2 from oxidizing metals (Campos-Martin et al., 2006). Based on stability testing in NaCl and PBS solutions in serum bottles (Young et al., 2016), EDTA increased H_2O_2 stability over a range of pH values in comparison with solutions without EDTA (Figure 77). Therefore, we hypothesized that EDTA addition to the catholyte would further stabilize and improve H_2O_2 production.

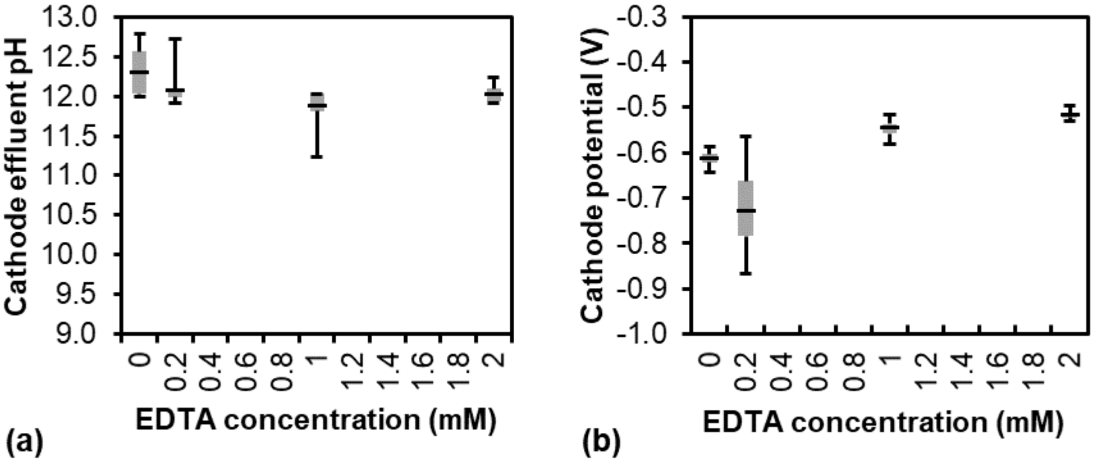

Figure 77. Results for the experiment varying EDTA concentrations from 0- to 2-mM: (a) cathode effluent pH and (b) cathode potential. The light gray boxes represent the first and third quartiles, and the black point represents the average value. The whiskers represent the maximum and minimum data points.

Even though EDTA improved the CCE from 37 to 52% (Figure 78d), Figure 75a illustrates that the highest H_2O_2 concentrations were produced without EDTA: H_2O_2 concentration decreasing from 3.1 to 2.0 g L^{-1} with increasing EDTA concentration due in part to current densities decreasing from 10.1 to 4.6 A m^{-2} (Figure 75c). Nonetheless, EDTA addition improved the energy efficiency of the MPPC from 1.13 to 0.54 Wh g^{-1} H_2O_2 and CCE from 37 to 52% (Figure 77). The increased cathodic efficiency likely was due to EDTA slowing the decomposition of H_2O_2 and improving CCE and power performance. This reiterates the trade off in operating MPPC: without EDTA, the MPPC achieved higher effluent concentrations, but adding EDTA reduced power requirements.

Decreased H_2O_2 concentrations were caused by EDTA diffusion to the anode, reducing current production. At the cathode, effluent pH was in the range of 11.8-12.3 (Figure 77), meaning that EDTA was completely deprotonated and could diffuse through the AEM to the anode. Figure 78e shows that GC-FID analysis detected EDTA in the anode chamber at concentrations ranging from 0.030- to 0.043-mM when EDTA was present in the catholyte. In the anode chamber, EDTA likely chelated with Fe^{2+} supplied as a nutrient for ARB to facilitate EET or with the iron in the cells involved with EET (Estevez-Canales et al., 2015). The detected EDTA concentrations exceeded the 0.021-mM concentration required to chelate all Fe^{2+} present in the anode medium. In addition, Figure 79 illustrates little change in E_{KA} at any concentration of EDTA, further indicating that the decrease in current likely was not due to modification of the metabolic EET pathway. Iron has been identified as an important nutrient in the EET mechanism of a variety of ARB (Estevez-Canales et al., 2015; Kato et al., 2013; Shi et al., 2016).

Estevez-Canales et al. (2015) demonstrated decreased current production due to a reduction in c-type cytochromes in ARB cells when iron-containing media was supplemented with the metal chelator 2,2′-bipyridine, and these cytochromes are critical for EET. Based on the CV results (Figure 79), it is likely that reduced current production was a result of ferrochelation rather than a change in metabolic pathway, as in Estevez-Canales et al. (2015). While EDTA can be effective when added to the catholyte after it leaves the cathode chamber, it can harm MPPC performance if added with the catholyte. Future research should explore the utilization of non-metal-chelating stabilizers to improve H_2O_2 concentrations.

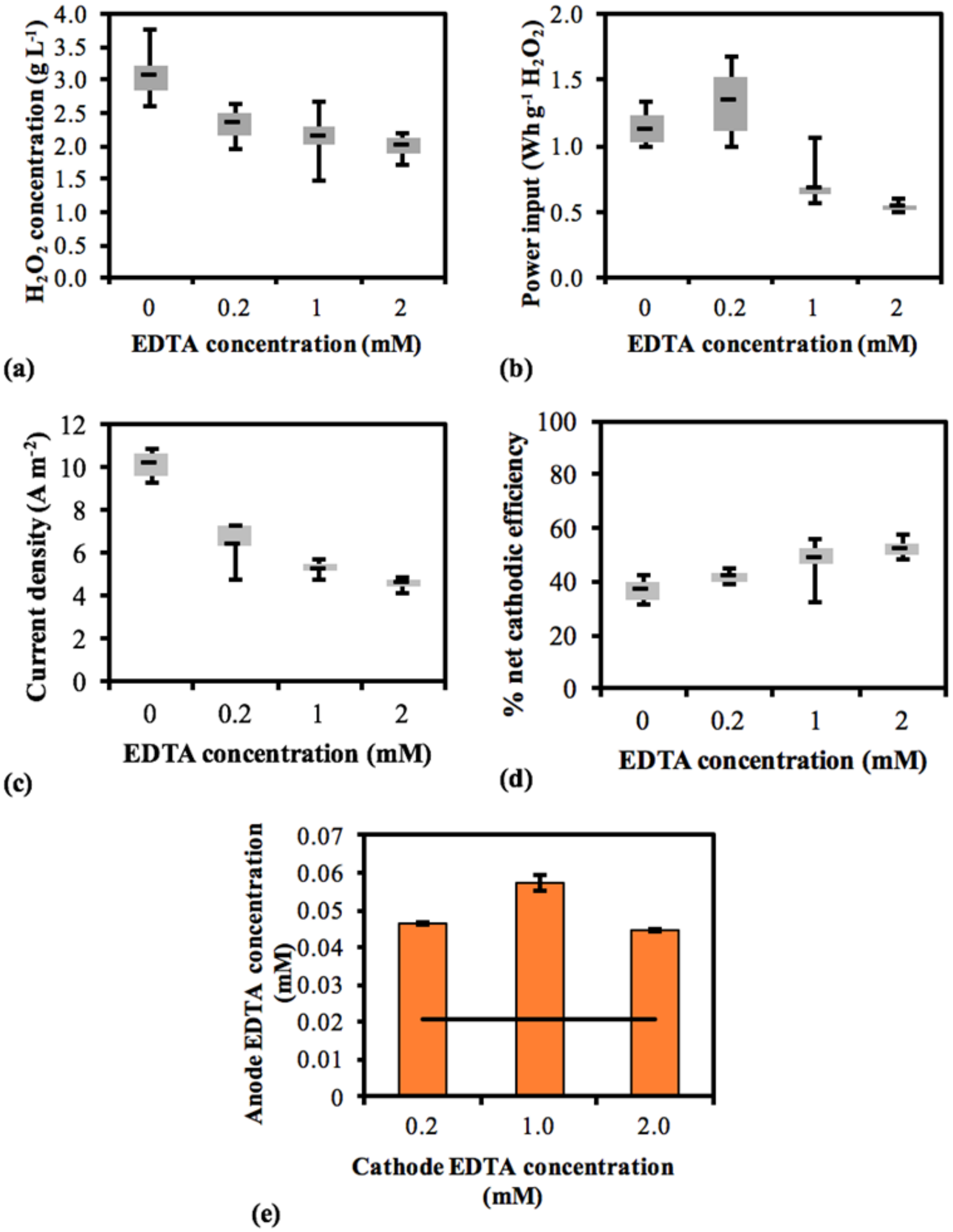

Figure 78. Results for the experiment varying EDTA concentrations from 0 to 2-mM: (a) H_2O_2 concentration, (b) power input, (c) current density, (d) net cathodic coulombic efficiency, and (e) EDTA concentrations in the catholyte and anolyte, where the black line represents the amount of

EDTA required to chelate with all Fe^{2+} added in the anolyte. The light gray boxes represent the first and third quartiles, and the black point represents the average value. The whiskers represent the maximum and minimum data points.

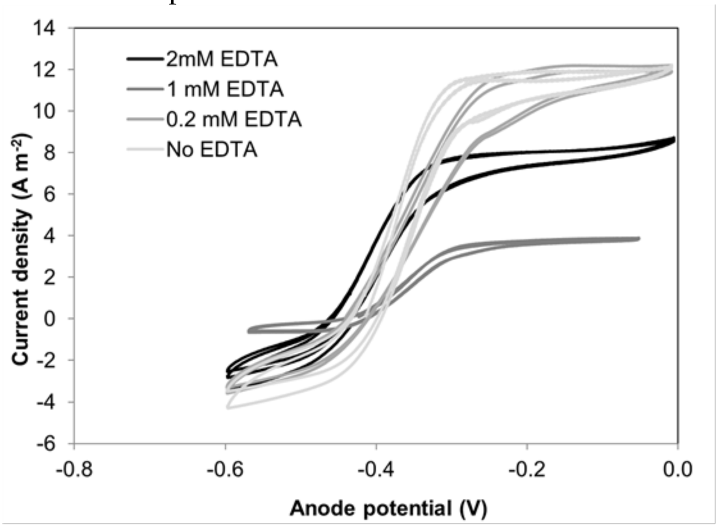

Figure 79. Cyclic voltammetry of anode performance as a function of EDTA concentration.

Effects of buffering catholytes. Reducing the pH difference between the anode and cathode chambers decreases pH concentration overpotentials and potentially leads to increased energy efficiency for H_2O_2 production. Based on this concept, we evaluated adding acid-base buffers to the catholyte to reduce concentration overpotentials. Although adding the buffers improved several performance variables -- including pH, current density, and cathode potentials -- acidic buffers failed to produce as much H_2O_2 as NaCl. Figure 80b shows that PBS catholyte lowered the pH to 12.13 and 10.36 with 100- and 200-mM PBS, respectively, and to 11.4 and 9.4 with 400-mM and 1-M $NaHCO_3$, respectively, which are lower than NaCl's pH of 12.3. Cathode potentials improved to -0.49 V with 200-mM PBS versus 200-mM NaCl (Figure 80c). Current densities were 2-3 A m^{-2} higher with $NaHCO_3$ than NaCl, since the $NaHCO_3$ diffused to the anode and improved mass transport through the anode biofilm. In addition, Figure 77f illustrates that more phosphate anions and OH^- anions were removed from the catholyte, versus with the NaCl electrolyte, which should have reduced Ohmic resistances in a method similar to that observed at the higher NaCl concentrations.

Regardless of these improvements, Figure 80a shows that using PBS and $NaHCO_3$ catholytes produced H_2O_2 concentrations ranging 0.34-2.54 g H_2O_2 L^{-1} (p-value <0.003), values significantly less than 3.10 g H_2O_2 L^{-1} with 200-mM NaCl. Since less H_2O_2 was produced, Figure 80d shows that the CCE decreased from 37% with 200-mM NaCl to 15% and 8% with 100- and 200-mM PBS and 26% and 4% with 400- and 1000-mM $NaHCO_3$. Correspondingly, power input was higher for all buffering catholytes versus NaCl (Figure 80e).

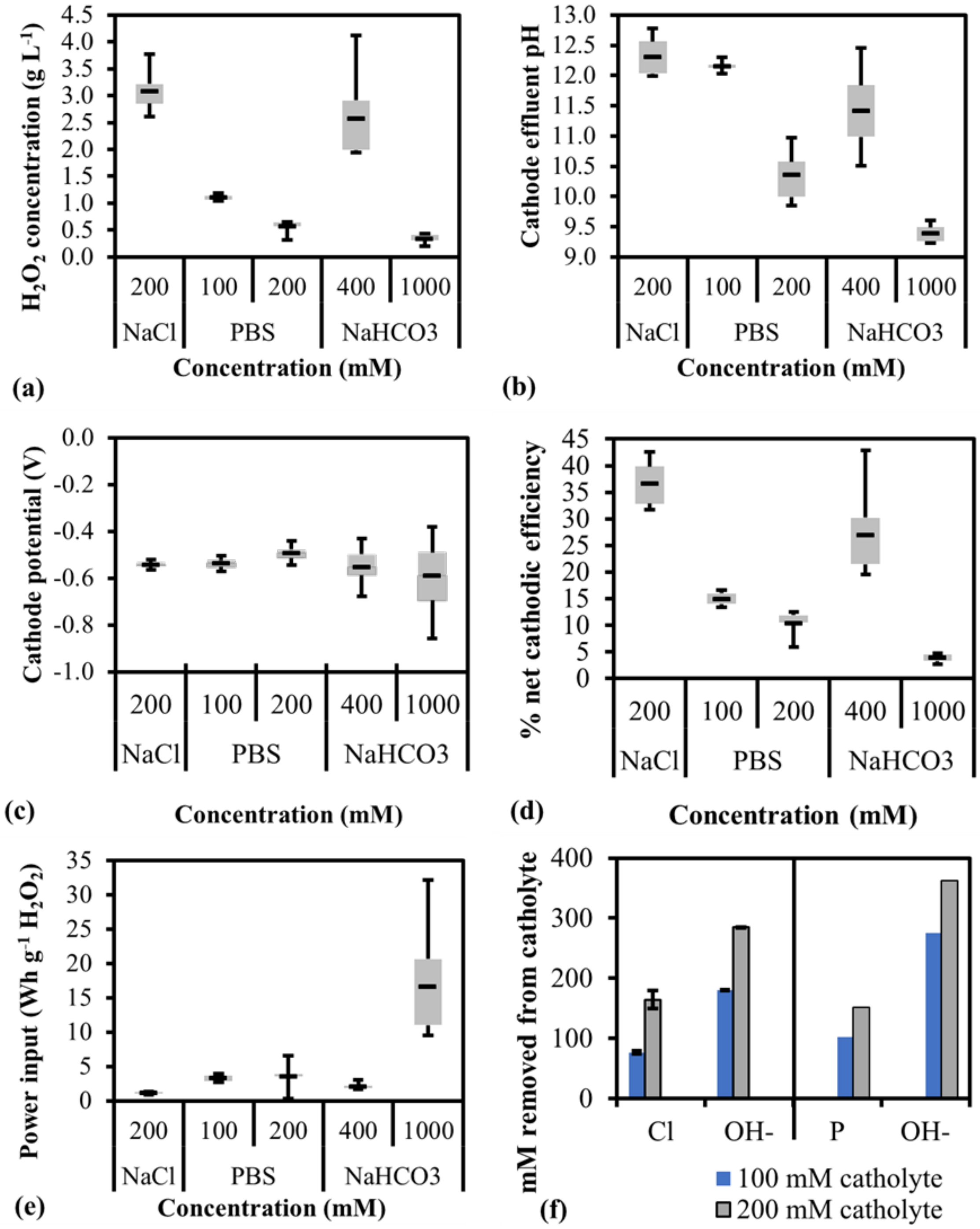

Figure 80. PBS and $NaHCO_3$ catholyte experiments results: (a) H_2O_2 concentration, (b) cathode effluent pH, (c) cathode potential, (d) net cathodic efficiency, (e) power input, and (f) the composition of anions that diffused from the cathode to the anode. The light gray boxes represent the first and third quartiles, and the black point represents the average value. The whiskers represent the maximum and minimum data points.

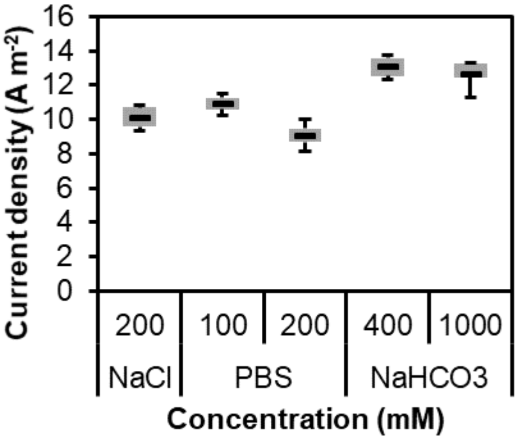

Figure 81. Current density for varied buffering electrolyte concentrations. The light gray boxes represent the first and third quartiles, and the black point represents the average value. The whiskers represent the maximum and minimum data points.

Because anode performance did not deteriorate (it even improved a small amount), the poor performance for H_2O_2 production was caused by a net loss of H_2O_2 in the cathode chamber. With the buffering catholytes, the net loss probably was due to increased auto-decay of H_2O_2 to O_2 or the 2-electron ORR of H_2O_2 to H_2O at the influent end of the cathode chamber, where the pH was 2.5, even though the effluent pH exceeded 10. At the entrance, pH 2.5 PBS is thermodynamically more favorable for the 4-electon and 2-electron ORR reactions than at higher pHs. Consequently, the kinetics of these reactions are faster, likely resulting in the reduction of H_2O_2 to H_2O via Eqn. 1. With $NaHCO_3$, we hypothesize that H_2O_2 auto-decayed to O_2 in the presence of carbonate and bicarbonate, since both compounds have been shown to decrease H_2O_2 stability (Young et al., 2016; Nicoll and Smith, 1955; Abbot and Brown, 1990; Qiang et al., 2002). Auto-decay of H_2O_2 to O_2 is further supported by our observations of gas flowing out of the cathode chamber when $NaHCO_3$ was used as the catholyte.

A perspective for the application of MPPCs in wastewater applications. MPPCs have the potential to provide cost savings to WWT plants that utilize H_2O_2 for disinfection. Since cathode performance is independent of the anode substrate content, we evaluated the potential for H_2O_2 production at WWT plants utilizing primary and waste-activated sludge. We estimated the amount of H_2O_2 produced in a MPPC treating either primary sludge or WAS in a 10 million L d^{-1} municipal WWT plant. Depending upon the catholyte HRT, a WWT plant could produce 890–1900 kg d^{-1} of H_2O_2 (or 89–191 mg d^{-1} L^{-1} of influent wastewater) while consuming 1200 kg COD d^{-1} from primary sludge, a surrogate for blackwater.

The flat-plate MPPC design demonstrated continuous H_2O_2 production at concentrations (3.1 g L^{-1}) sufficient for disinfection and micropollutant removal and with low power input (1.1 Wh g^{-1} H_2O_2). This H_2O_2 concentration is ~30-fold more than required for disinfection and micro-pollutant removal during water and wastewater treatment. The MPPC performed well using a simple NaCl catholyte with a 1- to 4-h HRT and no stabilizers. At a 1-h HRT, the H_2O_2 production rate provides more than 3 times the H_2O_2 required for disinfection and micro-pollutant removal at a power input 5- to 25-fold lower than required in the conventional anthraquinone process for H_2O_2 production. The addition of the metal-chelating stabilizer EDTA inhibited current production at the anode by chelating Fe^{2+} at the anode, reducing the amount of current produced by ARB and, consequently, reducing the number of electrons available for H_2O_2 production at the cathode. In the current reactor configuration, weak acid buffers provided no performance benefit versus a NaCl catholyte, largely due to increasing H_2O_2 auto-decay either due to pH gradients along the cathode or the presence of compounds reducing H_2O_2 stability. Ultimately, the best conditions for MPPC operation will depend upon the operational goals of the process. High HRTs generally favor higher effluent concentrations. However, the MPPC will require larger power inputs to achieve the necessary concentration and operate at lower net cathodic coulombic efficiencies. High production rates can be achieved at low HRTs with lower power inputs, but produce lower effluent H_2O_2concentrations. Given its *in situ* consumption, FOBs and WWT plants would benefit from operating at lower HRTs to produce more H_2O_2 for use in advanced oxidation processes or sludge pretreatment.

5.6.2. Primary sludge (PS)-fed MPPC

The PS was diluted ~3.8-fold with distilled water, and the influent PS fed to the MPPCs had ~7.6 g/L of TCOD and ~3.8 g/L of VSS. PS characteristics are provided in Table 20.

Table 20. Characteristics of PS influent and MEC and MPPC effluents for experiments with a 9-day HRT.

	MEC		MPPC	
	Influent	Effluent	Influent	Effluent
TCOD	7450 (±330)	2860 (±20)	7700 (±90)	3940 (±40)
SSCOD	370	280	420 (±20)	340 (±20)
TSS	4260 (±40)	1880 (±20)	4590 (±140)	2650 (±70)
VSS	3740 (±20)	1680 (±10)	3890 (±130)	2210 (±60)

H_2O_2 production and efficiency. Figure 82a shows H_2O_2 concentrations (theoretical and measured) and H_2O_2 production efficiency (PPE, based on Eq (1)) during batch operation of the cathode in the MPPC. The H_2O_2 concentration increased up to ~230 mg L^{-1} by 6 hours, but then decreased to ~121 mg L^{-1} by 24 hours. The theoretical H_2O_2 produced, based on the electrical current produced at the anode, increased linearly up ~2300 mg L^{-1}, indicating that the PPE kept decreasing with time, from 72% at 1.5 hours to 5% at 24 hours. Clearly, H_2O_2 decomposition became increasingly important in the cathode chamber over 1 day of batch cathode operation.

Catholyte pH in the MPPC decreased with time from ~12.6 (0 hour) to 10.4 (24 hour), as shown in Figure 82b. This is contrary to the expected pH increase with time, since O_2 reduction to H_2O_2 generates OH^- (Eqn. 26). Ion migration caused the decline in pH. Specifically, OH^- could have diffused from the cathode to the anode due to the large pH difference (~12.6 at the cathode and ~7 at the anode), and HCO_3- could have diffused from the anode to the cathode due to its concentration gradient. Either transport mechanism would have contributed to a pH decrease at the cathode: loss of alkalinity due to OH^- transport out of the cathode and pH buffering due to import of HCO_3^-. Based on the measured pH and total alkalinity of the catholyte (Figure 82b), OH^- decreased significantly, while other alkalinity species (CO_3^{2-} and HCO_3^-) increased with time. Thus, both ion-migration mechanisms appear to have been at work.

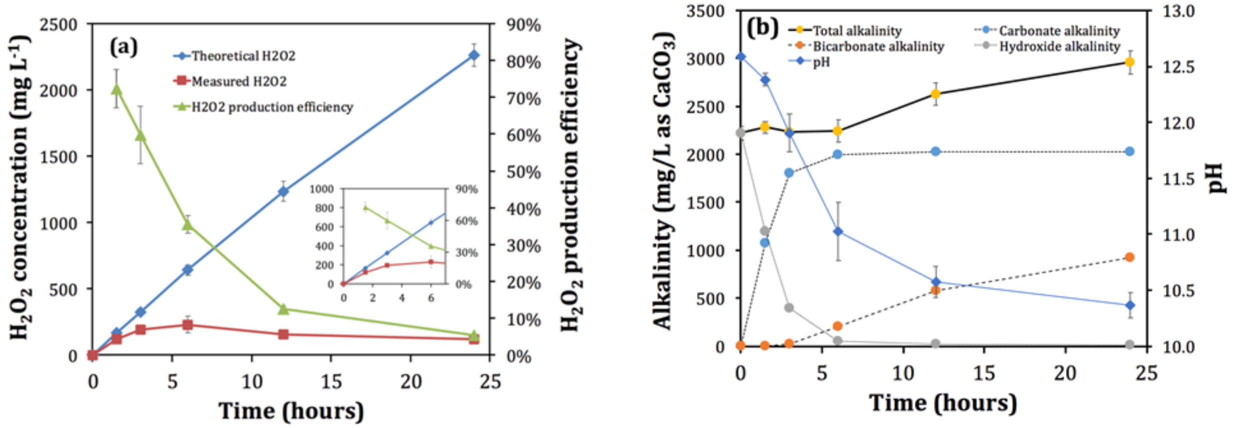

Figure 82. Results of cathode batch operation of a microbial peroxide producing cell (MPPC): (a) theoretical and measured H_2O_2 concentrations based on 100% conversion from cumulative coulombs and detection method, respectively, and H_2O_2 production efficiency (PPE) (number of measurements, N = 3). The inset zooms in on the first 6 hours' operation in the MPPC. (b) pH and alkalinity of catholyte over the 24-hour batch runs.

During the first ~6 hours, the total alkalinity stayed approximately constant, while OH^- and CO_3^{2-} drastically decreased and increased, respectively, especially during the first 3 hours. The increase in CO_3^{2-} indicates that HCO_3^- was moving from the anode to the cathode, and the stability of total alkalinity means that transport of OH^- to the anode was off-setting the generation of OH^- at the cathode and the input of HCO_3^- from the anode.

After ~6 hours, the pH was ≤ 11, and HCO_3^- steadily increased due to a combination of an increase of the concentration of inorganic C and a shifting of the speciation of inorganic carbon towards, HCO_3^-, since the pK_a of the HCO_3^-/CO_3^{2-} couple is ~10.3. Due to continued import of HCO_3^- and generation of base, the CO_3^{2-} alkalinity remained high. High CO_3^{2-} is important, because CO_3^{2-} can be responsible for H_2O_2 decay (Lee et al., 2000); this is discussed more below. The decrease in H_2O_2 concentration after 6 h means that the H_2O_2-decay rate was faster than the H_2O_2-generation rate at the cathode. H_2O_2 decay could have been accelerated by four mechanisms: 1) metal cations in PS diffusing from anode to the cathode and catalyzing H_2O_2 auto-decay, 2) membrane degradation with consumption of H_2O_2, 3) reaction of H_2O_2 with carbonate ions, and 4) diffusion of the HO_2^- ion to the anode. Direct movement of metal cations should not have been important, because we used an AEM. As exemplified in Figure 44, we saw no evidence of membrane deterioration or chemical deposits after running 27 days in the MPPC fed with PS. Thus, the first two mechanisms were unlikely.

Accelerated loss of H_2O_2 by reaction with carbonate is supported by prior studies and special tests we carried out. Lee et al. (2000) reported that the rate of decomposition of H_2O_2 loss was ~9-fold faster in a carbonate solution than in a caustic solution (NaOH) when the pH was 10~10.6, the temperature was 30~50 ˚C, and the ionic strength was 1.5~3 M. Since the mechanism of H_2O_2 decay in the presence of carbonate ions has not been elucidated yet, we performed H_2O_2-decay tests to confirm that accelerated H_2O_2 decay was linked to the carbonate concentration. Figure 83 shows that H_2O_2 decomposed quickly during ~1 day in a sodium carbonate solution. Finally, produced H_2O_2 can dissociate to HO_2^- ion at high pH (pK_a ~ 11.8)

(Young et al., 2016), and the HO_2^- anions could have diffused to the anode chamber. We explore below evidence supporting this mechanism.

Abiotic H_2O_2 decay tests in different salt solutions. We performed H_2O_2-decay tests in 100-mM solutions of sodium carbonate, sodium bicarbonate, and sodium hydroxide with ~2700 mg L^{-1} of H_2O_2. Although pH was maintained stable during ~1 day operation, the H_2O_2 concentration in sodium carbonate decreased very rapidly (99% removed in 23 hours), while H_2O_2 in the positive control with deionized water was very stable. H_2O_2 concentrations in sodium hydroxide and sodium bicarbonate were relatively stable, with 9 and 28% removals in 23 hours.

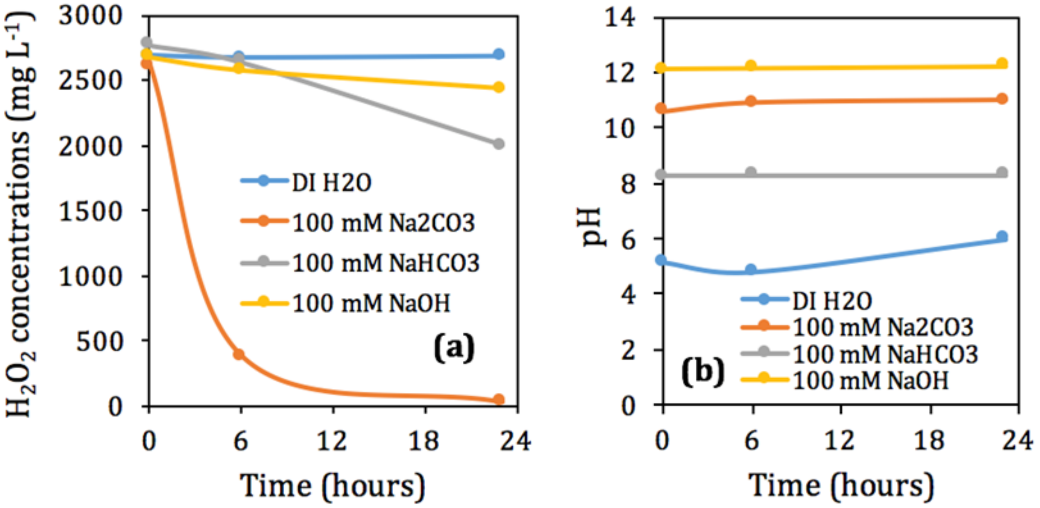

Figure 83. H_2O_2 decay with time in different solutions: 100 mM sodium carbonate, sodium bicarbonate, and sodium hydroxide. (a) H_2O_2 concentration and (b) pH.

Comparison of MEC and MPPC operation. Figure 84 shows current densities and applied voltages over three one-day feeding cycles for the MEC and the MPPC pseudo-steady state operation periods. The pattern of current density was the same for both modes: high current at start of a one-day cycle and a decrease due to the consumption of PS-COD. The maximum current densities were similar, ~1 A m^{-2}.

The applied voltage for the MPPC was ~0.2 V, a value much lower than that of the MEC, ~1.04V. The theoretical applied voltage for H_2 production in MEC is 0.14 V (Ki et al., 2016), which means that the total overpotential in the MEC was 0.9 V. Likewise, the theoretical potential for H_2O_2 production in MPPC is +0.56 V (Rozendal et al., 2009), making the total overpotential 0.76 V, a value smaller than with the MEC. In our previous study (Ki et al., 2016), we characterized the applied voltage of the same design of flat-plate MECs and categorized into anode overpotential (η_{anode}), cathode overpotential ($\eta_{cathode}$), Ohmic overpotential (η_{Ohmic}), pH-related concentration overpotentials (η_{pH}), and theoretical voltage (E_{Th}). The largest overpotentials were η_{cat} and η_{pH}, and that should be the same here for an MEC and an MPPC. Since we poised the anode potential at -0.3 V (vs Ag/AgCl) in both cases and used the same substrate, η_{an} should be similar. η_{Ohmic} should be small for current densities of ~1 A m^{-2} (in both reactors), although the distance between anode and cathode was ~0.5 cm larger with the MPPC.

Thus, the observed improvement of ~0.14 V of total overpotential with the MPPC should have been related to better cathodic catalysis with H_2O_2 production, compared to H_2 production in the MEC (Young et al., 2016; Ki et al., 2016).

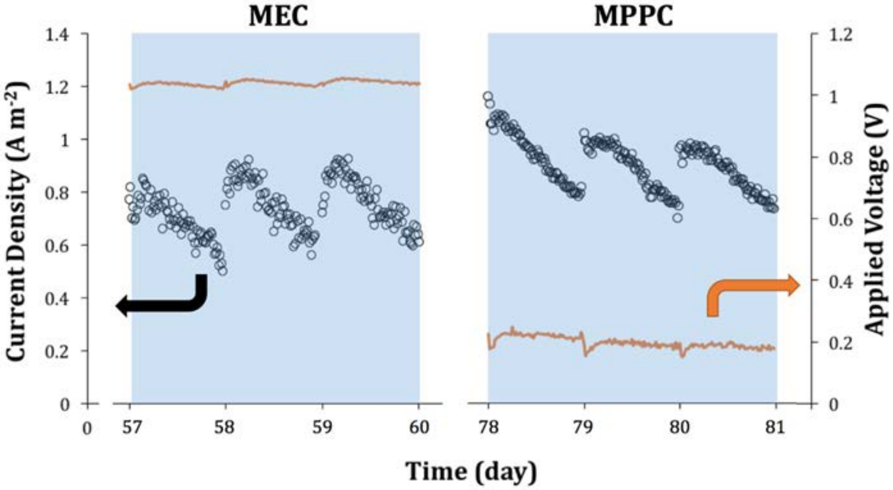

Figure 84. Current densities and applied voltages in the MEC and MPPC operated with semi-continuous feeding (one-day cycle) and a 9-day HRT. Data are for the last 3 days of operation after the current stabilized for successive cycles.

Figure 85 summarizes performance parameters for the effluent from the MPPC and MEC. Influent concentrations did not differ much between the two conditions, but the COD-removal in MPPC was 49 (±1)% and 62 (±5)% in the MEC. This difference was due to inhibition of methanogenesis in the MPPC, since the anode chamber of the MEC produced 27 ± 4 mL d^{-1} of biogas, versus only 2 ± 4 mL d^{-1} for the MPPC. CH_4 generation accounted for higher COD removal in the anode of the MEC. Although CRs were similar in the MEC and MPPC, ~30%, the CE was higher in the MPPC: 64% versus 48%. Higher CE in the MPCC was from lower COD removal efficiency due to the decline in methanogenesis.

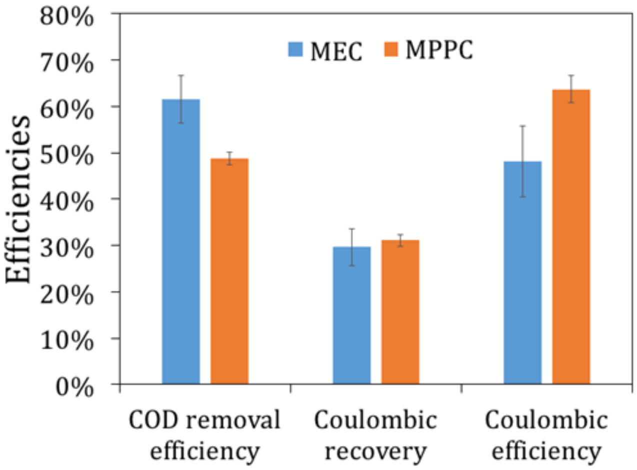

Figure 85. COD-removal efficiency, CR, and CE for the MEC and MPPC for a 9-day HRT during semi-continuous operation with one-day feeding cycle of PS.

Inhibition of methanogenesis could have been caused by H_2O_2 and O_2 diffusion into the anode chamber through the membrane from the air-cathode. Most MFC studies using an air-cathode reported high COD-removal efficiency, but low CE, because O_2 diffusing into the anode chamber allowed rapid aerobic biodegradation, which out-competed anode respiration (Angosto et al., 2015; Ge et al., 2013; Zhuang et al., 2012). Since the MPPC in our study had lower COD removal than the MEC, the difference in performance between the MPPC and MEC probably was caused by diffusion of H_2O_2, not O_2.

Microbial phylotypes relevant to community structure and function. Figure 86 shows the taxonomy of the microbial communities, classified at the order level, in 6 samples: AnS and two sets of BfS for the MEC and MPPC. Biofilm samples were taken from the BfC and BfM of the anode. The AnS and BfC communities were similar between the MEC and MPPC, but the BfM communities were significantly different.

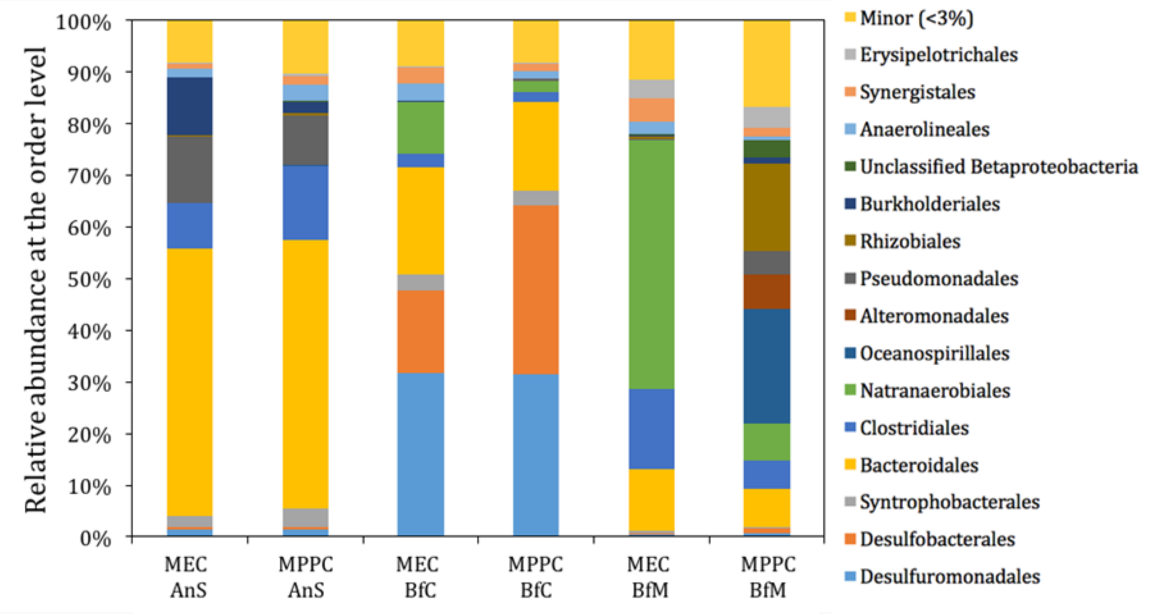

Figure 86. Microbial community structure at the order level for anode suspension (AnS), biofilm of chamber side (BfC), and biofilm of membrane side (BfM) in the MEC and MPPC at the end of operation.

The dominant phylotype in AnS was *Bacteroidales*, which includes bacteria well-known for carrying out hydrolysis and fermentation of complex organics (Jia et al., 2013; Rismani-Yazdi et al., 2013). For the BfC in both systems, *Desulfuromonadales* and *Desulfobacterales* were dominant orders. *Geobacter*, unclassified *Pelobacteraceae*, and unclassified *Desulfobulbaceae* were dominant at the genus level. These genera contain species that typically are found in anode biofilms (Jia et al., 2013; Kiely et al., 2011; Torres et al., 2009; Wang et al., 2014).

Despite being at the same anode surface, the BfM communities were different from the BfC communities of each system, and the two BfM communities (MEC vs MPPC) were very different from each other. *Natranaerobiales* was the most abundant phylotype in the MEC BfM, with *Dethiobacter* (Family *Anaerobrancaceae*) and unclassified *Anaerobrancaceae* being the largest fractions at the genus level, 23 and 25%, respectively. *Dethiobacter alkaliphilus*, which is 96% similarity to the representative sequence in the MEC BfM, is an obligate anaerobe that uses H_2 as an electron donor and thiosulfate, elemental sulfur, and polysulfide as electron acceptors in high-pH (~10) and high-salt (~0.6 M of sodium) environments (Sorokin et al., 2008).

In contrast, *Oceanospirillales* and *Rhizobiales* were predominant in the MPPC BfM, and *Halomonas* and *Parvibaculum* were the largest fractions at the genus level, 17 and 16%, respectively. *Halomonas* species are aerobes living in saline conditions. Some species, such as *Halomonas salaria* sp. and *Halomonas denitrificans* sp., have a yellow or brown-yellow color (Kim et al., 2007) that corresponded to the appearance of the membrane-side anode at the end of the experiments with the MPPC, shown in Figure 45. *Parvibaculum lavamentivorans* DS-1 also is an aerobe known for biodegrading synthetic laundry detergents (e.g., linear alkylbenzenesulfonate, LAS) (Schleheck et al., 2011).

The different community structures of BfM from BfC in the MEC and MPPC correlate to the very different environments of the cathode chamber. In particular, BfM in the MPPC included a majority of aerobic bacteria, since O_2 and H_2O_2, which can degrade to O_2, diffused through the air-cathode and AEM. Although H_2O_2 and O_2 diffusion was not significant enough to change the microbial community structure of AnS and BfC or divert electron flow away from anode respiration (similar CRs of ~30%, Figure 85), it profoundly altered the BfM community.

Low energy requirement. With a 6-hour cathode HRT that produced ~230 mg H_2O_2 L^{-1} in the MPPC, the cathode potential was around -0.5 V (vs. Ag/AgCl). Since the anode potential was fixed at -0.3 V (vs. Ag/AgCl), the applied voltage was 0.2 V, resulting in ~0.87 kWh per kgH_2O_2 for ~1 A m^{-2} current density. This value is consistent with the ~1 kWh per kg H_2O_2 measured by Young et al. (2016) using the same reactor design (flat-plate MEC), but fed with acetate as the electron donor. This energy requirement for H_2O_2 production is relatively low compared to other published studies using actual wastewaters: 2.5-78 kWh per kg H_2O_2 using real wastewater (Modin and Fukushi, 2012; Modin and Fukushi, 2013; Arends et al., 2014; Sim et al., 2015) and similar to when using synthetic wastewater (acetate) of ~0.93, 3, and 0.659 kWh per kg H_2O_2 (Rozendal et al., 2009; Modin and Fukushi, 2013; Chen et al., 2014). The low energy input can be attributed to the relatively small distance (~1 cm) between the anode and cathode, which minimized the energy loss of ion transport (Young et al., 2016; Ki et al., 2016).

Modin and Fukushi (2013) demonstrated production of > 9 g L^{-1} of H_2O_2 (highest concentration reported so far using MPPC fed with acetate) with a rate of > 11 g L^{-1} d^{-1}. However, they needed a high energy input, ~3 kWh per kg H_2O_2. Even though we demonstrate that we can produce H_2O_2 at ~1 kWh per kg H_2O_2, H_2O_2 can be theoretically produced with the production of power or at least with little or no energy input (Rozendal et al., 2009; Young et al., 2016). A systematic investigation of cell design and materials (e.g., membranes, catalysts) may lead to a higher concentration of H_2O_2 with lower or zero net energy input (Young et al., 2016). The energy input for H_2O_2 production using MPPC would be a significant improvement compared to conventional H_2O_2 production methods: 2-10 kWh per kg H_2O_2 by AO and 4-5 kWh per kg H_2O_2 by electrochemical technologies (Althaus et al., 2007; Goor et al., 2000; Eul et al., 2001; Foller and Bombard, 1995). However, continuous H_2O_2 production in an MPPC using real wastewater needs to be studied and optimized in the future.

In summary, we demonstrated H_2O_2 production using PS in a flat-plate, dual-chambered MPPC. The maximum H_2O_2 concentration achieved ~230 mg/L in 6 h of batch catholyte operation, but H_2O_2 net-decomposed for longer catholyte times; the main cause of H_2O_2 loss was reaction with carbonate ions that moved from the anode to the cathode and to diffusion of H_2O_2 from the cathode to the anode. The energy requirement for H_2O_2 production was relatively low, ~0.87 kWh per kgH_2O_2, compared to other H_2O_2-producing microbial electrochemical cells using real wastewater. While the MPPC and an MEC achieved ~30% Coulombic recovery, the Coulombic efficiency was ~12% higher in the MPPC than in the MEC due to lower TCOD removal from suppression of methanogenesis in the MPPC. Even though the microbial communities of the anode suspension and anode biofilm for both cells were similar, aerobic bacteria were significant only on the side of the anode facing the membrane in the MPPC. The presence of aerobic bacteria and the suppression of methanogenesis in the MPPC support that H_2O_2 diffused to the anode side.

Transport of ions across the membranes was of importance in producing H_2O_2 when using real wastewater. When we use an AEM, carbonate and bicarbonate ions can move from the anode to the cathode; if we were to use a cation-exchange membrane (CEM), other cations, such as K^+, Na^+, and metals, would diffuse from the anode to the cathode to maintain electroneutrality. Transport of the cations would bring about two possible negative effects: (1) lowering the pH below an acceptable threshold for anode respiring bacteria (ARB) and (2) accelerated H_2O_2 decay with metal catalysis.

5.6.3. Primary sludge-fed MPPC (single-chamber MPPC, sMPPC)

Effect of separator for sludge treatment. Figure 87 details the results of the mass balances of input to and output from the sMPPC for various experimental designs. In Figure 87, electrons captured on anodes (i.e, CR) are similar at ~20% using both GF and SPF. COD and VSS removals also were similar at ~50% and ~55%, respectively (Table 21). The values met one of two requirements for Class B biosolids (> 38% of volatile solids). The use of the GF and SPF separators yielded effluents with similar levels of total coliforms, but the SPF effluent was shown to have a ~30-fold reduction in fecal coliforms when compared to the GF filter effluent. This indicates two effects; (1) H_2O_2 produced at the cathodes was likely transported to the anode chamber more efficiently through the SPF than through the GF and (2) anode respiration is not affected by H_2O_2 based on the Coulombic recovery and efficiency (Table 21) as well as the current density (Figure 88). Efficient transport of H_2O_2 from the cathodes to the anode chamber in the sMPPC equipped with SPF is likely be due to its larger pores, increasing H_2O_2-to-pathogen contact with a reduced decay of H_2O_2. The Ohmic resistance between the anode and cathode decreased also when changing from GF to SPF, from 5.4 to 2.2 Ohms, supporting an increased transport through the SPF as compared to the GF. There are several mechanisms of H_2O_2 decomposition: metal catalysis, material degradation, carbonate ion catalysis, and hydroperoxyl anion (HO_2^-) migration (Ki et al., 2017b).

In GF-equipped-sMPPC, slow diffusion of H_2O_2 or HO_2^- along with a high pH might result in H_2O_2 decay with carbonate coming from the anode chamber as described in the previous study (Ki et al., 2017). On the other hand, there was higher reduction of pathogens in the SPF-equipped-sMPPC despite the same anodic performance including CR, CE, COD and VSS removal. The value of fecal coliform in the PS effluent with SPF was met with Class B biosolids (< 2 x 10^6 CFU or MPN per gram of biosolids, dry-weight basis) (US EPA, 2003).

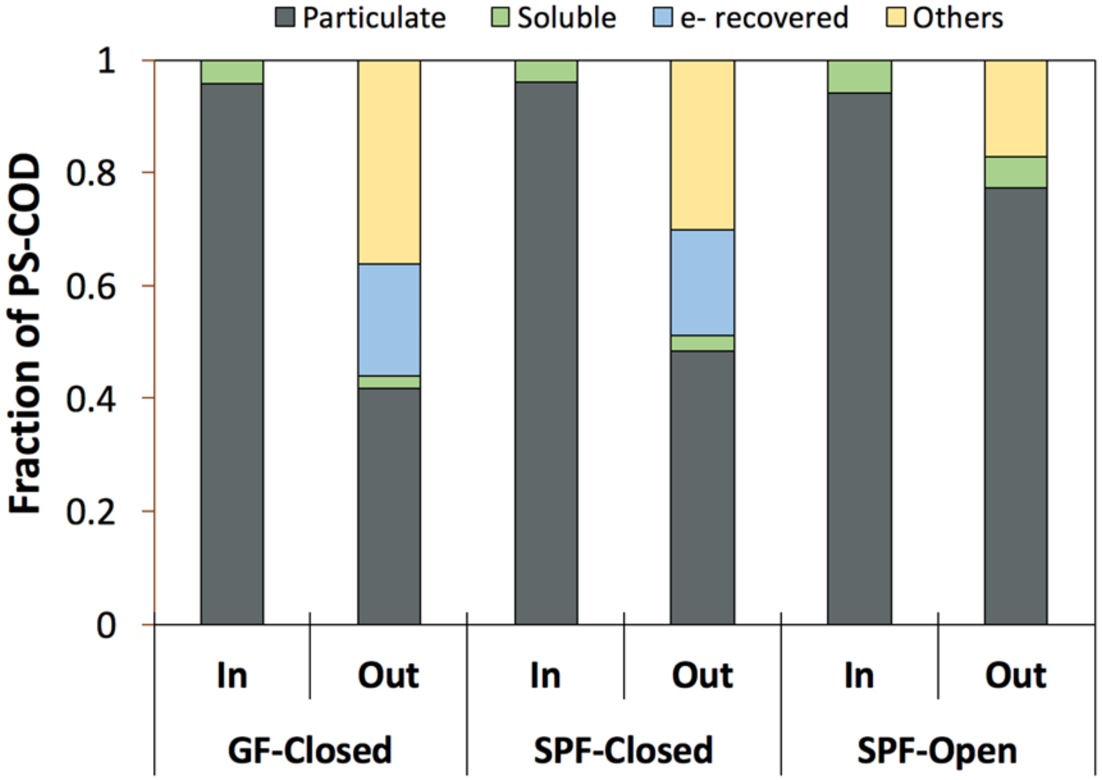

Figure 87. COD-based mass balances of PS_{in} and PS_{out} in three experiments at 6-day HRT. Particulate is the solids fraction of PS; soluble is the soluble fraction of PS; e^- recovered is accumulated Coulombs; Other is the unaccounted fraction of PS.

Table 21. Summary of performances in single- and dual-chambered MPPCs.

MPPCs		sMPPC (this study)			dMPPC*
Exp.		GF-Closed	SPF-Closed	SPF-Open	
CR	%	20 (±1)	19 (±2)	0	31 (±1)
CE	%	35 (±3)	38 (±6)	0	64 (±3)
COD removal	%	56 (±4)	49 (±8)	17 (±7)	49 (±1)
VSS removal	%	61 (±5)	52 (±5)	28 (±8)	43 (±4)
Total coliform	MPN /GDW	$6.3x10^7$ ($\pm 4.5x10^6$)	$5.6x10^7$ ($\pm 4.0x10^7$)	2.9×10^8 ($\pm 3.5x10^7$)	-
Fecal coliform	MPN /GDW	3.91×10^6	1.2×10^5 ($\pm 1.2x10^4$)	1.4×10^7 ($\pm 4.0x10^6$)	-

* Operating conditions: 9-day HRT, 8 gCOD/L and 4 gVSS/L as influent PS, 0.89 gCOD/L/d and 0.44 gVSS/L/d as organic loading rate (Ki et al., 2017)
MPN: most probable number
GDW: gram of solids, dry-weight basis

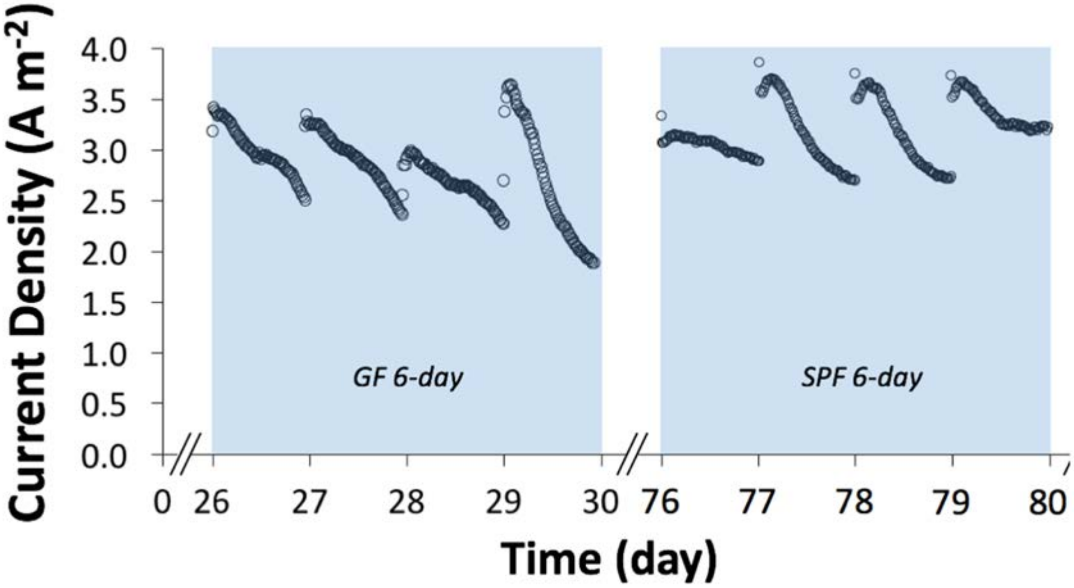

Figure 88. Current densities under stabilized conditions at 6-dayHRTs in the sMPPC equipped with GF or SPF filter.

Closed vs open circuit at 6-day HRTs. We operated the sMPPC at 6-day HRT in open-circuit condition (no current production) to investigate how much current recovery and H_2O_2 produced contributed to PS destruction. When equipped with the SPF, SPF-Closed and SPF-Open are comparable (Figure 87). PS destruction still occurred through anaerobic hydrolysis or aerobic oxidation with O_2 from air-cathodes despite relatively lower COD and VSS removals (17 and 28%, Table 21). Since no CH_4 was produced, a possible COD sink at the anode, we hypothesize that most of the unaccounted COD decrease in SPF-Open is due to aerobic degradation. If we assume a similar O_2 diffusion rate occurred in the other experiments, then we propose ~13% of PS-COD were degraded only with the contribution of H_2O_2 produced in the sMPPC. Except the electron consumption by ARB, the degradation of PS-COD might have resulted from 1) mineralization with H_2O_2 or reactive oxygen species (ROS or radicals) derived from H_2O_2 or 2) oxidation by O_2 after breaking down from H_2O_2.

This is the first demonstration of sludge stabilization with H_2O_2 produced in a sMPPC fed with PS. The SPF-filter equipped sMPPC had 19% of CR, 38% of CE, 49% of COD removal and 52% of VSS removal along with 1.2×10^5 MPN/gram dry solid of fecal coliform at 6-day HRT (5 gCOD/L/day or 2.7g VSS/L/day). Sludge stabilization met the requirement of Class B biosolids. The microbial consortium of the sMPPC worked capturing energy for H_2O_2 production and treated and stabilized PS in better effluent sludge quality.

5.7 Engineering Design and Life Cycle Analysis

5.7.1. Engineering Design of a Pilot-Scale MPPC

The main objective of this task was to develop an engineering design for a pilot-scale MPPC that can be demonstrated under ESTCP. To achieve these objectives, the following subtasks were conducted and are described in the following sections:

- Develop the design concept for the MPPC.
- Develop a design basis for the MPPC concept.
- Prepare engineering drawings and specifications suitable for pilot-scale system fabrication by a design-build contractor.

Engineering design concept. The conceptual design for the pilot-scale MPPC is illustrated in Figure 89. This conceptual design is based on multiple fluidized-bed reactors in series with recycle and has several attributes that are intended to promote solids flow, distribution, residence time and hydrolysis; mass transfer; COD removal; operational flexibility; and ease of operations and maintenance. Blackwater is pumped to the first subreactor and enters it from the bottom through a liquid distributor. The recycle pump flow rate is adjusted to induce an upward water velocity in each subreactor. An optimal upward velocity is one that: 1) keeps most of the solids suspended, and 2) maximizes solids retention time in the subreactors. By achieving these two goals, the solids settling and deposition in each subreactor is minimized and solids hydrolysis is maximized. The water containing some of the partially hydrolyzed solids overflows a weir in the first subreactor into a downcomer. This water and solids mixture then enters the second subreactor for further treatment. Additional subreactors are used to achieve treatment goals.

Multiple electrode modules are situated in each subreactor (Figure 89b). Two electrode modules are shown as an example only, and further discussion on their design and construction is presented below. The electrode modules oxidize the BW and reduce water to hydrogen peroxide. Catholyte is pumped into each electrode module and hydrogen-peroxide containing catholyte exits for subsequent use (e.g., GW oxidation or disinfection).

Specific process-mechanical attributes of the design concept include:

- Modular construction to promote scalability.
- Closely spaced and removable electrode modules to maximize cathode area per unit volume and simultaneously facilitate maintenance and management of accumulated solids.
- Controllable recycle rate to optimize solids hydrolysis, mixing, and energy consumption.
- Minimization of head loss through each subreactor to enable use of gravity-overflow weirs between subreactors rather than pumps.

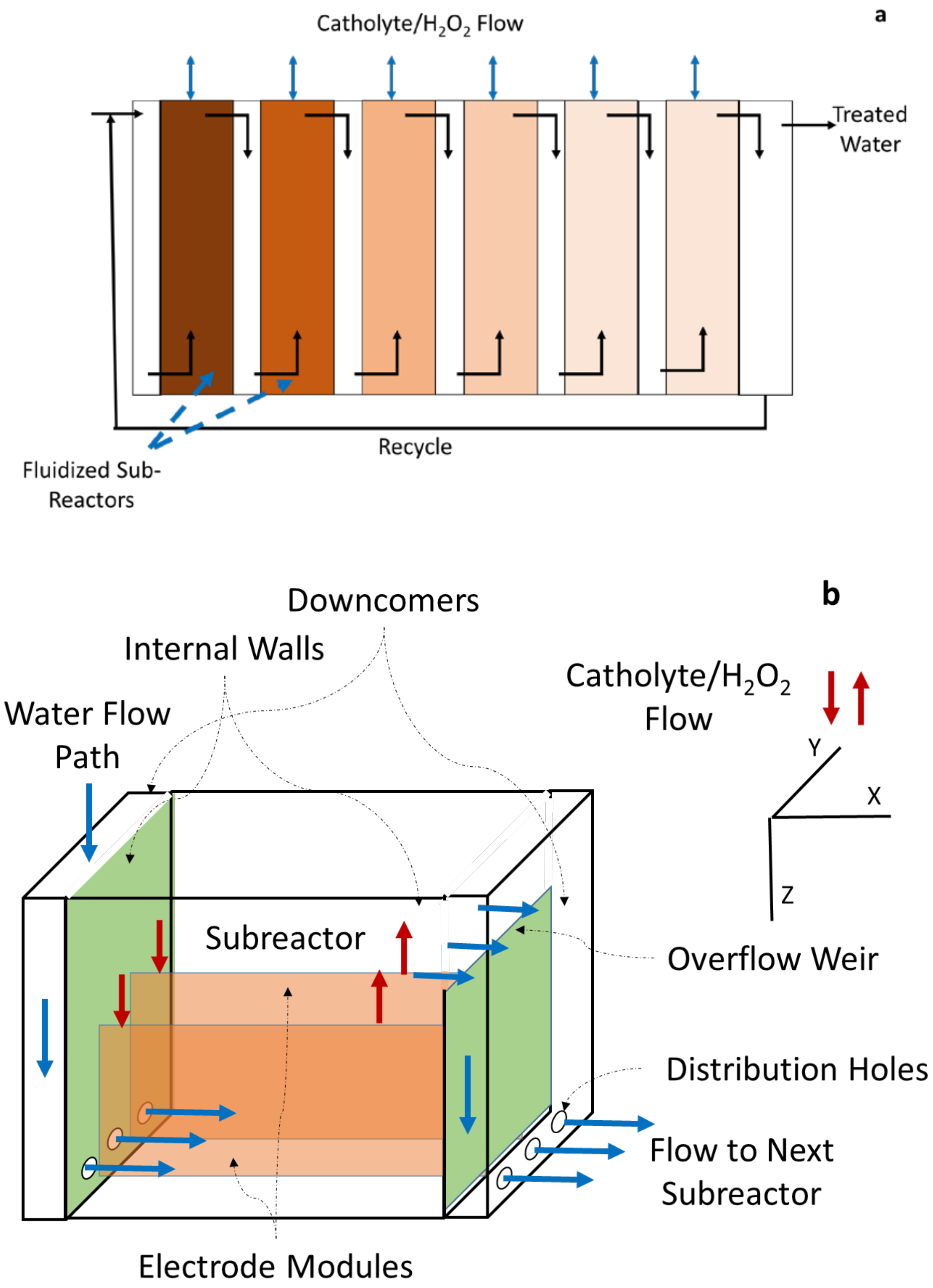

Figure 89. Conceptual design of the pilot-scale MPPC showing (a) multiple fluidized bed subreactors in series with recycle and (b) a single fluidized bed subreactor containing electrode modules. The number of subreactors and electrode modules are for illustration only and do not reflect the actual pilot-scale MPPC design.

The concept for the electrode module is illustrated in Figure 90. The concept is based on the laboratory MPPC design described previously. Details are provided in later sections, while a general overview is presented here. The expanded titanium mesh serves as an inert and rigid current collector with high open area that presses against the carbon cloth anode. This is the face that is in contact with the upward-flowing BW. The carbon cloth is separated from the catholyte flow cell by an ion exchange membrane. Catholyte is pumped into a port in the top of the catholyte flow cell and hydrogen peroxide-laden catholyte exits a second port. Adjacent to the catholyte flow cell is the cathode constructed of carbon cloth with a Vulcan carbon catalyst. In the middle of the electrode module sandwich is a porous spacer that promotes air flow and oxygen reactions at the cathode surface.

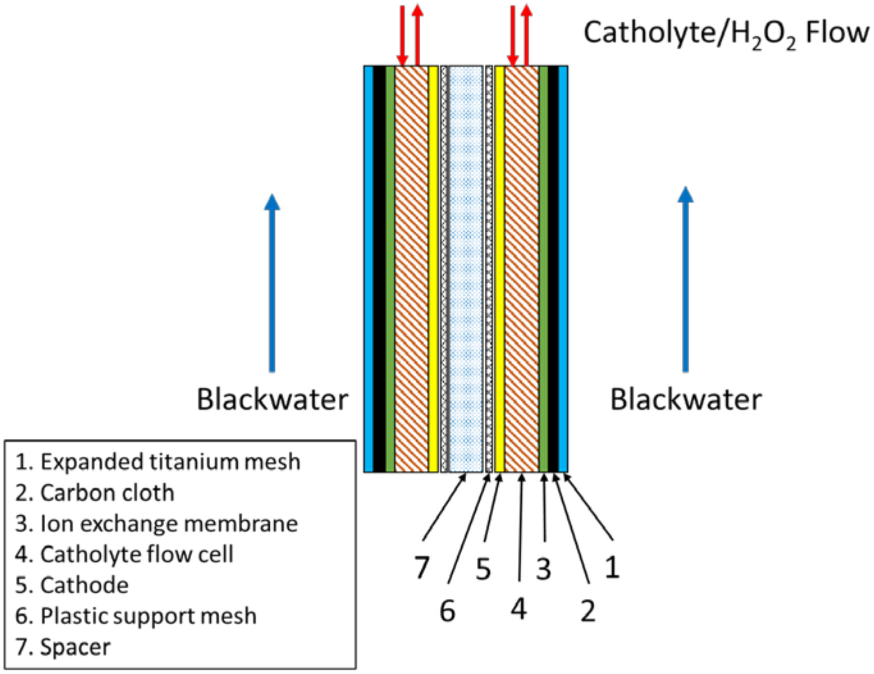

Figure 90. Cross section of MPPC electrode module concept. Point of view is in the X direction as illustrated in Figure 89a above.

Solids settling is an important issue that was identified during laboratory testing. Laboratory reactors used a magnetic stir bar to keep the solids suspended which is not practical for a pilot-scale or full-scale system. Mechanical mixing systems are commercially available but involve moving parts that are subject to failure and require regular maintenance. Hydraulic mixing is often used in full-scale anaerobic digesters successfully. Fluidization of the solids can be induced by an upward liquid velocity gradient. Validation of the fluidization concept involved laboratory experiments to estimate BW settling velocities.

Estimation of Blackwater Settling Velocity. PS was used to estimate the BW settling velocity. The method of Gerges et al. (1999) was followed. It involved placing PS (250 mL) in a graduated cylinder and measuring COD in samples 5 cm from the top of the water level. Figure 91 shows the COD removal efficiency along with fit to the model:

$$Eff = Eff_{max}(1 - e^{-\lambda t}) \qquad \text{(Eqn. 27)}$$

where, *Eff* is the removal efficiency, *Eff$_{max}$* is the maximum removal efficiency (ratio of nonsettleable COD to initial COD and assumed to be 0.75), λ is the settling parameter, and *t* is the settling time. λ was estimated to be 0.024 min^{-1}.

A frequency distribution of settling velocities was then developed Figure 92. As a design basis, we decided that 85% of the solids must be fluidized which translates to a settling velocity of 0.53 cm/min. This value was used to size the recycle flow rate as described below.

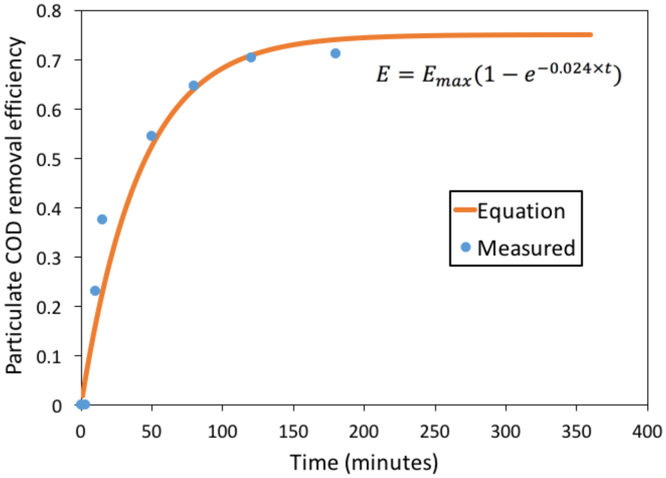

Figure 91. Relationship between settling time and particulate COD removal efficiency.

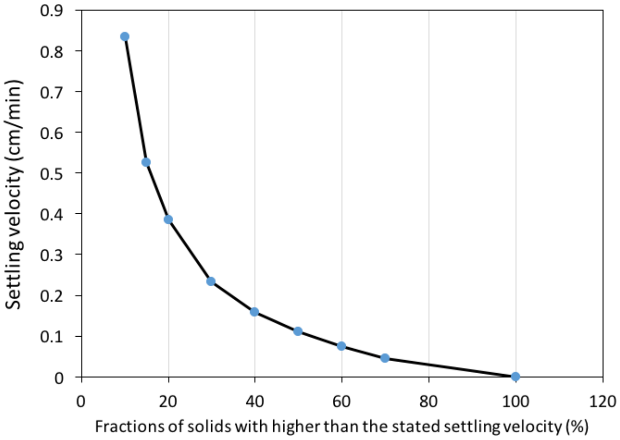

Figure 92. Frequency distribution of settling velocity and COD-based solids fraction.

Engineering Design Basis. The design basis was developed for a system capable of treating blackwater and producing hydrogen peroxide that could be used to treat graywater.

Anticipated wastewater composition and treatment requirements. Estimates for wastewater composition is challenging and varies widely. Anticipated wastewater composition with respect to COD, BOD$_5$, and TSS was evaluated using a variety of data sources. These sources included engineering handbooks, USEPA publications, journal articles, theses, and engineering reports.

The results are summarized in Table 22. A conservative estimate of 10,000 mg/L volatile suspended solids (VSS) was used as the design basis.

Table 22. Graywater and blackwater composition documented in a selection of the literature.

Wastewater type	Source	COD (mg/L)	BOD_5 (mg/L)	TSS (mg/L)
Blackwater	European vacuum toilets (Wendland, 2008)	9,500 to 19,000	NA	NA
Blackwater	Nature park toilets (Oarga, 2013)	1,700±700* to 2,700±1,000	1,100±580 to 1,500±6000	720±160 to 1,700±680
Blackwater	Vacuum toilets (Elimitwalli, 2006)	10,000±8,900 to 39,000±20,000	NA	NA
Blackwater	Vacuum toilets (de Graaff, 2010)	7,700 to 9,800	NA	NA
Blackwater	Vacuum toilets (Wendland et al., 2007)	8,700±3,980	NA	NA
Blackwater	Naval shipboard (Lerke et al., 2010)	NA	780 to 1,700	2,100 to 3,500
Blackwater	U.S. Septage (US EPA, 1984)	1,500 to 703,000 (average 31,900)	440 to 78,600 (average 6,480)	310 to 93,000 (average 12,900)
Blackwater	Lodging house (Atasoy et al., 2007)	1,200	406	560
Blackwater	Housing area (Palmquist and Hanaeus, 2005)	806 to 3,100	410 to 1,400**	920 to 4,300**
Blackwater	Cruise ship (CDM Stmith, 2000)	NA	1,950	1,510
Graywater	Lodging house (Atasoy et al., 2007)	245	90	48
Graywater	Bath and shower (Atasoy et al., 2007)	100 to 200	50 to 100	NA
Graywater	Hand basin (Atasoy et al., 2007)	263	109	NA
Graywater	Shower (Atasoy et al., 2007)	109	59	NA
Graywater	Housing area (Palmquist and Hanaeus, 2005)	495 to 680	350 to 500***	570 to 700**
Graywater	Cruise ship (CDM Stmith, 2000)	NA	153 to 270	85 to 170
Combined black and graywater	Naval shipboard (Lerke et al., 2010)	NA	530 to 1,300	700 to 2,400
Combined black and graywater	Untreated domestic strong wastewater (Tchobanoglous et al., 2003)	1000	400	350

*± Reported standard deviation.

**Total solids

***BOD_7

Treatment requirements depend on ultimate end use and disposition. Treated water that is discharged to surface water will need to meet requirements of the USEPA National Discharge Pollution Elimination System (NPDES). Blackwater is highly concentrated and laboratory results typically showed about 50% destruction of organics. Therefore, meeting NPDES permit limits was not considered reasonable. Rather, stabilization was elected as the goal in general accordance with EPA Part 503 biosolids regulations. Specifically, these regulations stipulate 38% volatile solids destruction for vector attraction reduction assuming the treated BW was land disposed in an area that would be restricted from human contact. This goal was selected as the design basis for this design.

Process engineering calculations. Engineering calculations were conducted to finalize the design basis and estimate reactor size and performance. These calculations are included in Appendix B and results are summarized in Table 23.

Table 23. MPPC design basis summary.

Parameter	Units	Value	Notes
VSS influent	mg/L	10,000	Conservative assumption for blackwater
Minimum VSS removal	%	38	EPA Part 503 Biosolids rule
First-order rate constant for VSS	day^{-1}	0.1	Based on laboratory experiments
Hydraulic residence time	day	7	Optimal based on laboratory experiments
Flow rate	gal/day	144	Assumed
Predicted VSS removal	%	50	Calculated
Reactor water volume	gal	1000	Calculated
Fluidization velocity	cm/min	0.53	Equal to laboratory-determined solids settling velocity
Number of subreactors	-	6	Assumed
Recycle ratio ($Q_{reactor}/Q_{influent}$)	-	10	Assumed
Subreactor flow rate	gpm	1.0	Calculated
Recycle flow rate	gpm	0.9	Calculated
Current density	A/m^2	4	Based on laboratory experiments
Area per electrode module (both sides)	ft^2	24	Based on 3-ft by 4-ft electrode module
Total number of cathodes	-	36	Calculated
Number of cathode modules per subreactor	-	6	Calculated
Catholyte flow rate in each electrode module	mL/min	190	Calculated
Total catholyte flow rate	gpm	1.8	Calculated
Current delivered to each electrode module (both anode-cathode pairs)	A	9	Calculated
Total delivered current	A	324	Calculated
Controlled anode voltage relative to reference electrode	V	0.2 to 0.5 ± 0.05	Based on laboratory experiments
Hydrogen peroxide concentration generated	mg/L	380	Calculated

Engineering Design Drawings and Specifications

Process and instrumentation. The main components of the MPPC are subreactor tanks, electrode modules and associated reference electrodes, catholyte tankage and pumps, and recycle pump. In addition, provisions using the generated hydrogen peroxide to treat GW in a separate tank was also included. The design builds upon the concept presented above in Figure 93. Figure 93 is a process flow diagram (PFD) for the system, and Figures 94 and 95 are process and instrumentation diagram (P&ID) and associated legend for the system.

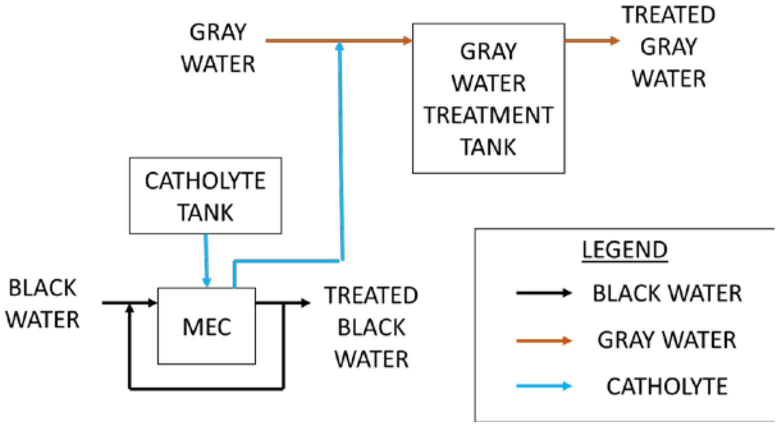

Figure 93. Simplified process flow diagram.

The PFD simply shows that BW is treated by the MPPC conceptually described above, and hydrogen peroxide is generated in catholyte that is then used to treat GW in a separate tank. The P&ID provides additional details of the physical process including all process equipment and pumps, shows the instruments, and shows how the information flows around the system. Major process equipment and pumps in addition to the MPPC (labelled microbial fuel cell reactor on the drawing) include:

- Feed pumps for black (PMP-103) and gray (PMP-100) for conveying wastewater to the process.
- Self-cleaning strainers for BW (STR-133) and GW (STR-130) to remove grit and larger particulates.
- MPPC recycle pump (PMP-106).
- Catholyte concentrate tank (TNK-150) for manual preparation of the concentrated catholyte.
- Catholyte pump (PMP-102) for conveying the concentrate to the catholyte equalization tank (TNK-152).
- Blend pump (PMP-101) for conveying GW to be used for diluting the catholyte. Alternatively, potable water can be used for dilution.
- Static mixer (MXR-131) and strainer (STR-132) for the diluted catholyte.
- Pumps for catholyte deliver to (PMP-104) and from (PMP-105) the MPPC.
- Mixer (MXR-134) and reaction tank (TNK-155) for mixing hydrogen peroxide-laden catholyte with GW and providing residence time and storage.

The P&ID also shows the instruments (e.g., flow rate, pressure, temperature) and controls (e.g., flow control, high/low level) for the system. The destination / source of all signals (analog [solid triangle] and digital [open triangle]) is represented at the top of the drawing. In addition, the electrical connections to the anodes, cathodes and reference electrodes (Ag/AgCl) are shown.

Local and remote monitoring of flow rates, pressures, liquid levels, temperature, current and voltage are shown as well as control of motor operation, flow rates, strainer cleaning, and electrode potentials. The control architecture drawing (Figure 96) provides a conceptual visualization of how the components of the system are connected on the network. The boundaries of the physical locations are shown in dashed lines.

A Keithley 2750 digital multimeter will be used as the data acquisition tool and will be connected to the operator workstation for data storage and analysis. The 2750 is designed to sense low voltages; leads from the fuel cells are connected directly to expansion cards which plug in to the back of the 2750. 7708 multiplexer module expansion cards will be used to provide sufficient I/O channels. For current measurement, a shunt with known resistance will be installed in the anode lead and the voltage drop across it measured. The current channels will be programmed in the Keithley to divide the measured voltage by the known resistance to calculate current.

KickStart control software from Keithley will be installed on the Operator Workstation to view, process, and export the recorded data. The software can be configured to record data at specified intervals to collect “snapshots” of the process over time. It can also be automated to export data to the hard drive of the operator workstation at specified times.

The Vision 1040 PLC/HMI with I/O expansion card V200-18-E3XB from Unitronics will collect the flowrate, temperature, pressure and liquid level data from the process sensors and output them to the Keithley 2750. The main purpose of the PLC is to communicate with the influent pumps over ethernet: sending start/stop and speed commands and receiving fault, running, and speed feedback commands. A low flow alarm will be configured in the PLC to shut down the pump should the flowrate remain below a configurable set point for a configurable time.

The Vision HMI graphics will display the flowrates, pressures, temperature, currents and voltages. An alarm screen will show flow, level, and pressure alarms that are user-configurable.

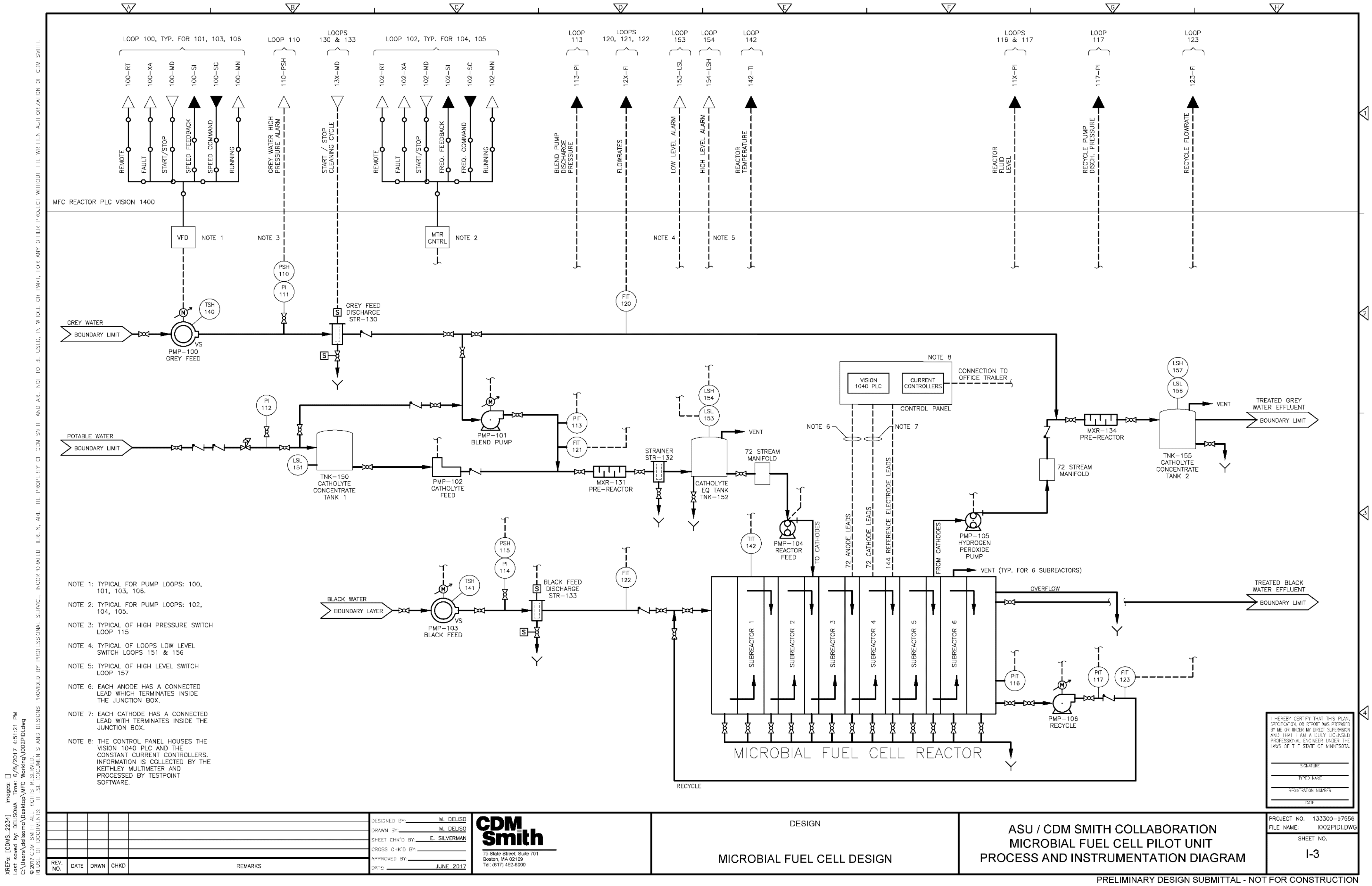

NOTE 1: TYPICAL FOR PUMP LOOPS: 100, 101, 103, 106.

NOTE 2: TYPICAL FOR PUMP LOOPS: 102, 104, 105.

NOTE 3: TYPICAL OF HIGH PRESSURE SWITCH LOOP 115

NOTE 4: TYPICAL OF LOOPS LOW LEVEL SWITCH LOOPS 151 & 156

NOTE 5: TYPICAL OF HIGH LEVEL SWITCH LOOP 157

NOTE 6: EACH ANODE HAS A CONNECTED LEAD WHICH TERMINATES INSIDE THE JUNCTION BOX.

NOTE 7: EACH CATHODE HAS A CONNECTED LEAD WITH TERMINATES INSIDE THE JUNCTION BOX.

NOTE 8: THE CONTROL PANEL HOUSES THE VISION 1040 PLC AND THE CONSTANT CURRENT CONTROLLERS. INFORMATION IS COLLECTED BY THE KEITHLEY MULTIMETER AND PROCESSED BY TESTPOINT SOFTWARE.

I HEREBY CERTIFY THAT THIS PLAN, SPECIFICATION, OR REPORT WAS PREPARED BY ME OR UNDER MY DIRECT SUPERVISION AND THAT I AM A DULY LICENSED PROFESSIONAL ENGINEER UNDER THE LAWS OF THE STATE OF MINNESOTA.

SIGNATURE

TYPED NAME

REGISTRATION NUMBER

DATE

DESIGNED BY: M. DELISO
DRAWN BY: M. DELISO
SHEET CHK'D BY: E. SILVERMAN
CROSS CHK'D BY:
APPROVED BY:
DATE: JUNE 2017

75 State Street, Suite 701
Boston, MA 02109
Tel: (617) 452-6000

DESIGN

MICROBIAL FUEL CELL DESIGN

ASU / CDM SMITH COLLABORATION
MICROBIAL FUEL CELL PILOT UNIT
PROCESS AND INSTRUMENTATION DIAGRAM

PROJECT NO. 133300-97556
FILE NAME: I002PIDI.DWG
SHEET NO.
I-3

PRELIMINARY DESIGN SUBMITTAL - NOT FOR CONSTRUCTION

Figure 94. Process and instrumentation diagram for the MPPC system.

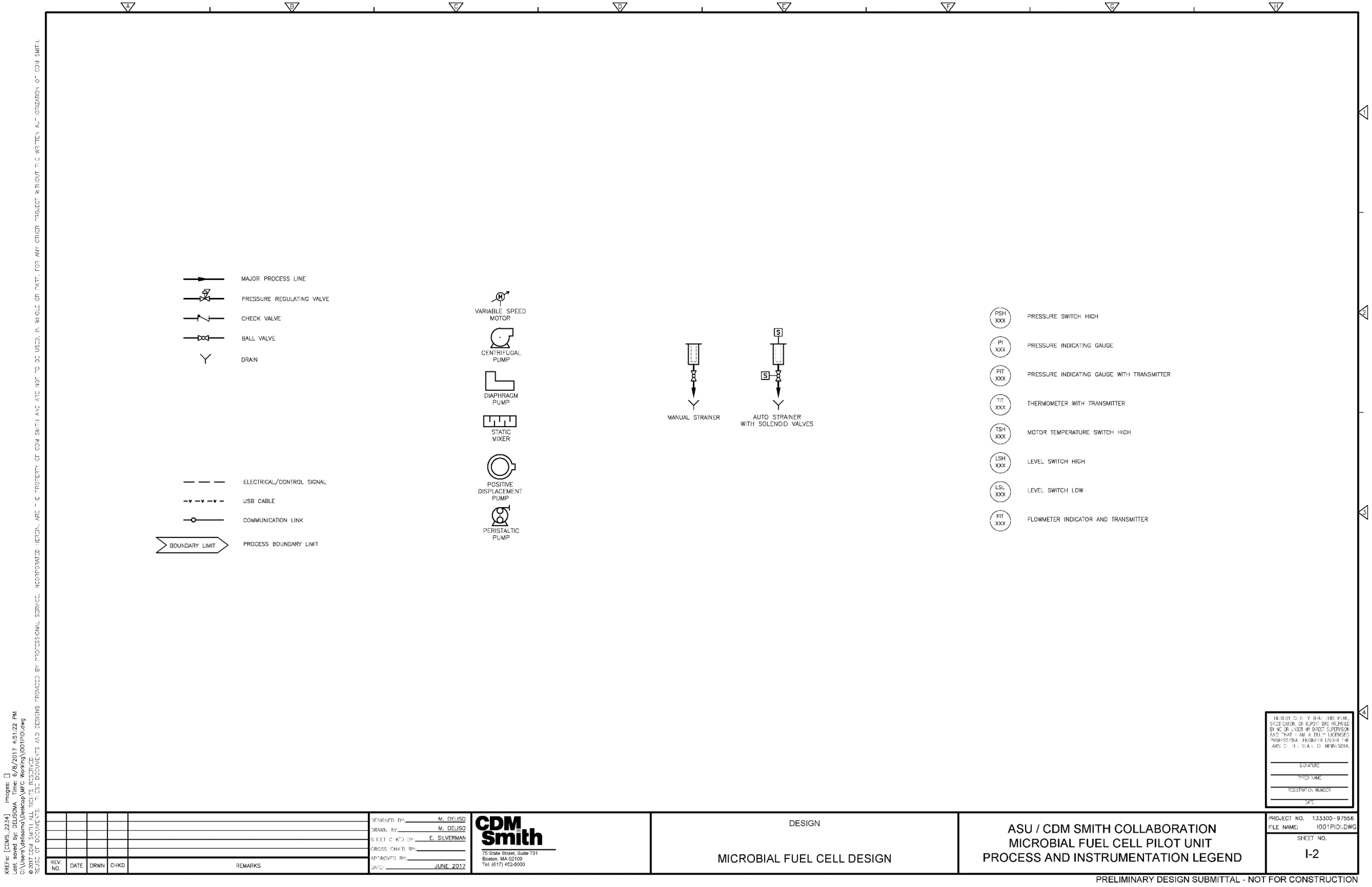

Figure 95. Process and instrumentation legend.

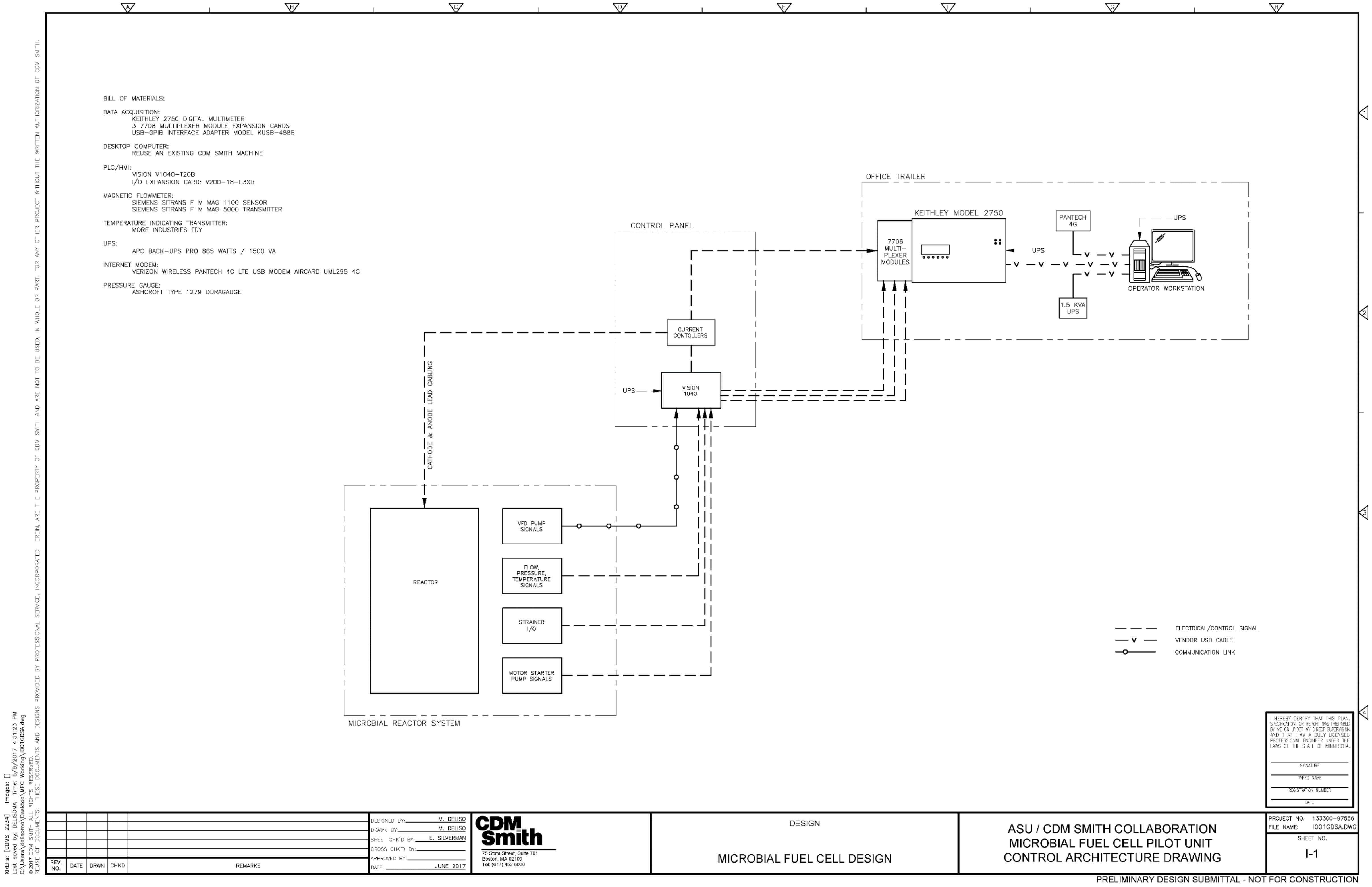

BILL OF MATERIALS:

DATA ACQUISITION:
    KEITHLEY 2750 DIGITAL MULTIMETER
    3 7708 MULTIPLEXER MODULE EXPANSION CARDS
    USB–GPIB INTERFACE ADAPTER MODEL KUSB–488B

DESKTOP COMPUTER:
    REUSE AN EXISTING CDM SMITH MACHINE

PLC/HMI:
    VISION V1040–T20B
    I/O EXPANSION CARD: V200–18–E3XB

MAGNETIC FLOWMETER:
    SIEMENS SITRANS F M MAG 1100 SENSOR
    SIEMENS SITRANS F M MAG 5000 TRANSMITTER

TEMPERATURE INDICATING TRANSMITTER:
    MORE INDUSTRIES TDY

UPS:
    APC BACK–UPS PRO 865 WATTS / 1500 VA

INTERNET MODEM:
    VERIZON WIRELESS PANTECH 4G LTE USB MODEM AIRCARD UML295 4G

PRESSURE GAUGE:
    ASHCROFT TYPE 1279 DURAGAUGE

I HEREBY CERTIFY THAT THIS PLAN, SPECIFICATION, OR REPORT WAS PREPARED BY ME OR UNDER MY DIRECT SUPERVISION AND THAT I AM A DULY LICENSED PROFESSIONAL ENGINEER UNDER THE LAWS OF THE STATE OF MINNESOTA.

SIGNATURE
TYPED NAME
REGISTRATION NUMBER
DATE

DESIGNED BY: M. DELISO
DRAWN BY: M. DELISO
SHEET CHK'D BY: E. SILVERMAN
CROSS CHK'D BY:
APPROVED BY:
DATE: JUNE 2017

CDM Smith
75 State Street, Suite 701
Boston, MA 02109
Tel: (617) 452-6000

DESIGN

MICROBIAL FUEL CELL DESIGN

ASU / CDM SMITH COLLABORATION
MICROBIAL FUEL CELL PILOT UNIT
CONTROL ARCHITECTURE DRAWING

PROJECT NO. 133300–97556
FILE NAME: I001GDSA.DWG
SHEET NO.
I-1

PRELIMINARY DESIGN SUBMITTAL - NOT FOR CONSTRUCTION

Figure 96. Control architecture**.**

Mechanical engineering design. The general approach to mechanical design was to have a modular system that is easily maintainable with removable electrode modules. Figure 97 shows plan, elevation, and isometric views of the reactor tank showing the 6 subreactors and 36 electrode modules.

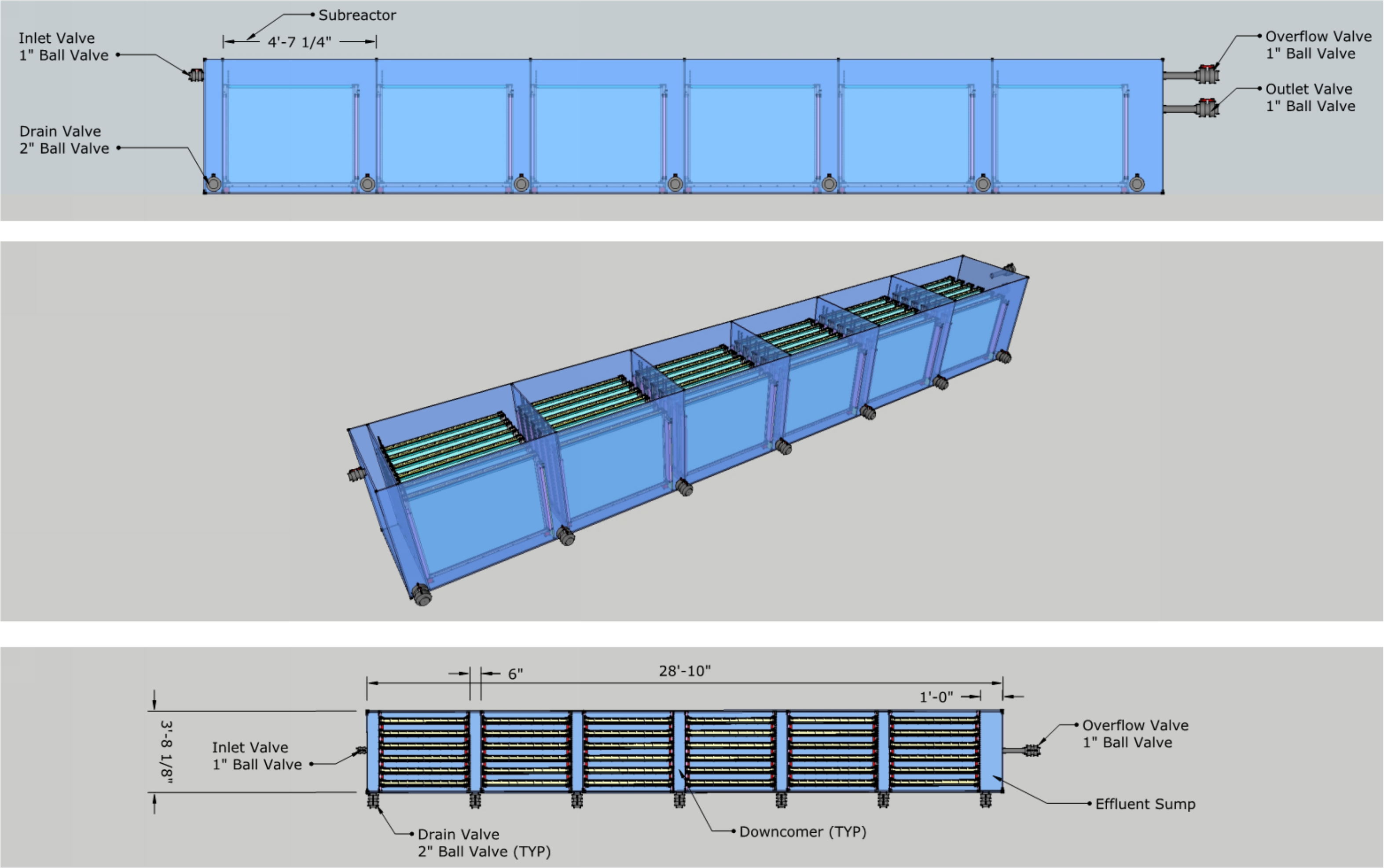

Figure 97. Plan, elevation, and isometrics views of the MEC reactor showing six subreactors, each preceded by a downcomer, and an effluent sump (right). Inlet and outlet valves are shown as well as drain valves for each downcomer, subreactor, and sump.

Figures 98 and 99 are isometric drawings of a subreactor from two perspectives.

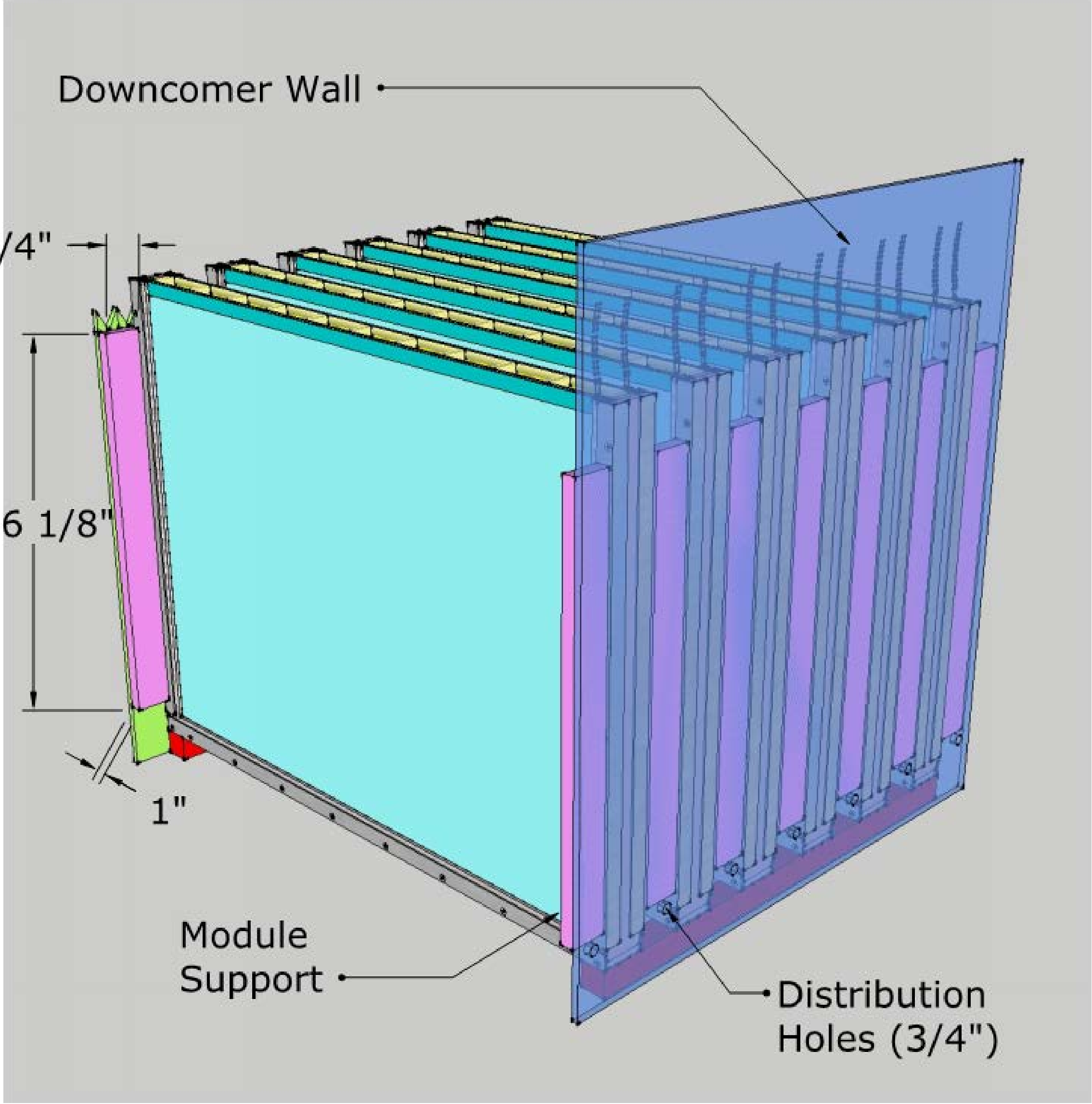

Figure 98. Isometric cutaway view (tank bottom and sides removed for clarity) of a single MEC subreactor showing the upstream downcomer wall with distribution holes located near the bottom, six electrode modules (light blue) with structural supports (pink) allowing for easy electrode removal from above, an overflow weir (green), and electrode floor supports (red) used to adjust the electrode height as necessary.

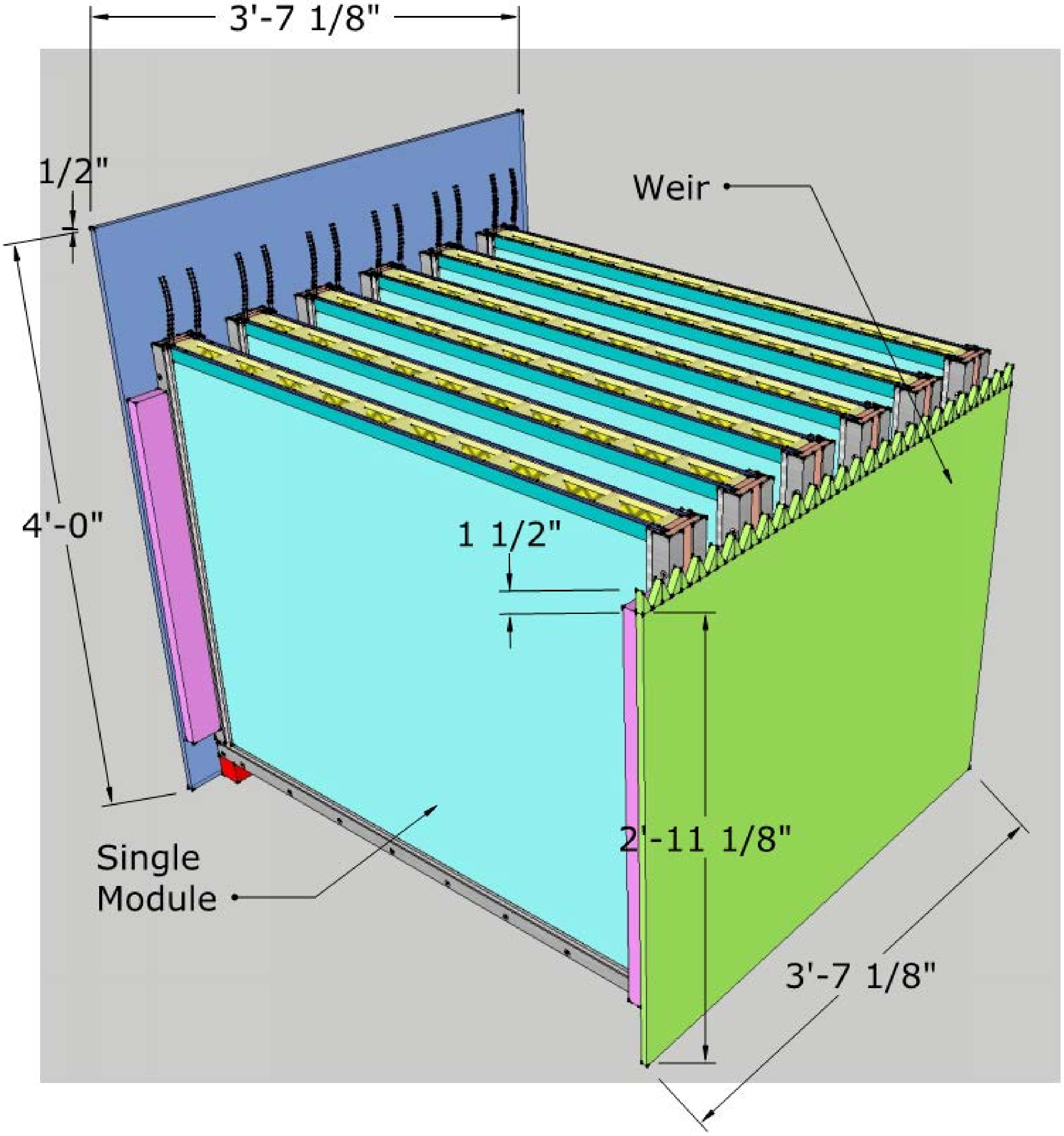

Figure 99. Isometric cutaway view of the MPPC subreactor shown above from a different perspective.

Figure 100 shows not-to-scale sketches further illustrating the electrode module design and manufacturing sequence. Figure 101 is a to-scale isometric view of a single electrode module and Figure 102 illustrates the individual electrode module components and its manufacturing sequence, each component detailed in Figures 103-112. Figure 113 is a detailed isometric view of the electrode module.

Step 1 – Spacer, cathode support mesh, and plastic frame

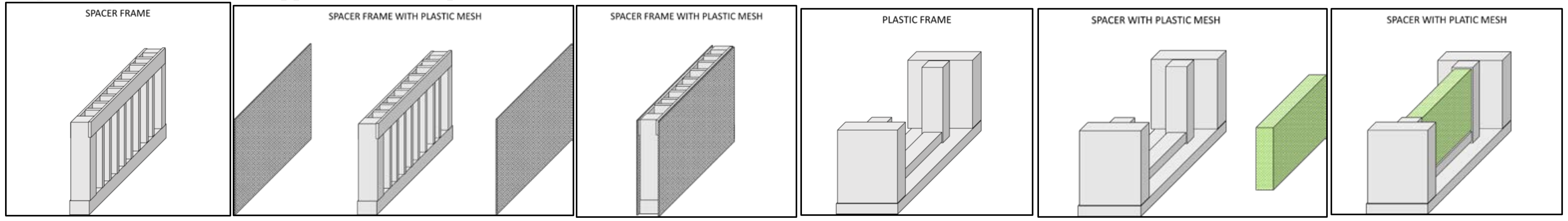

Step 2 – Catholyte flow cell

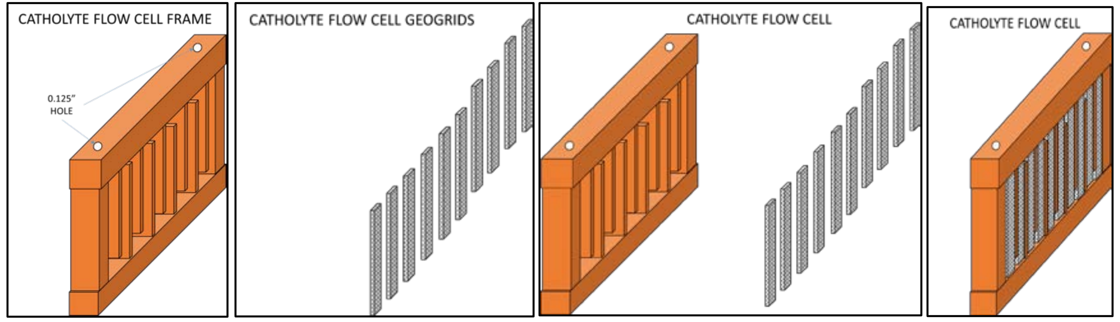

Step 3 – Cathodes and catholyte flow cells

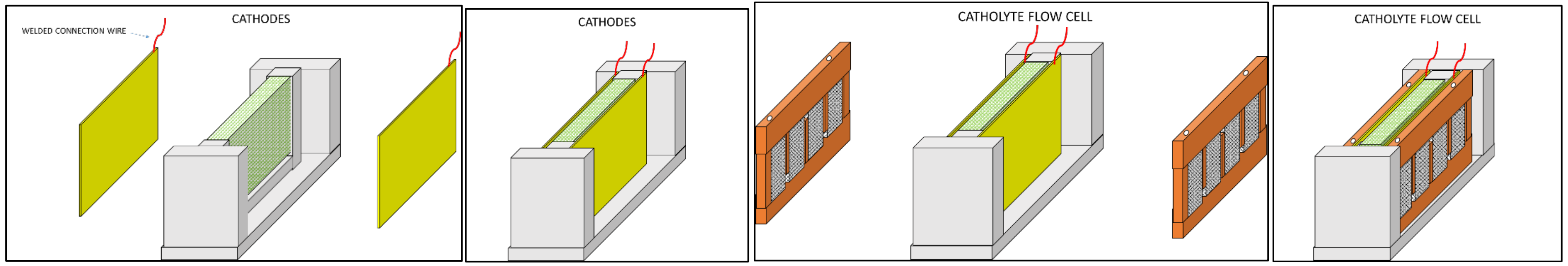

Step 4 – Anion exchange membrane, carbon cloth anode, and expanded titanium mesh current collector

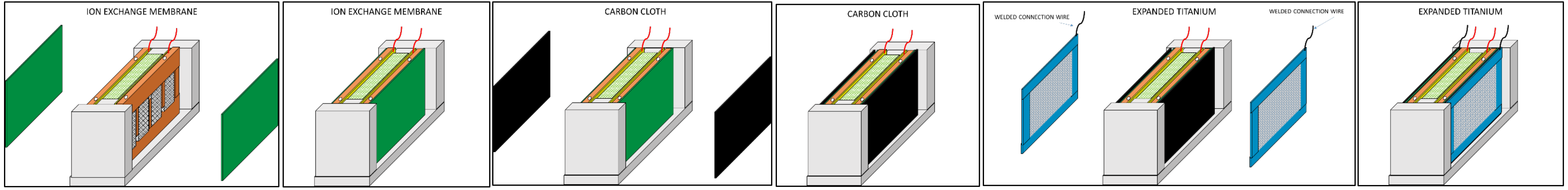

Step 5 – Sealing gasket, securement angle brackets, and finished electrode module

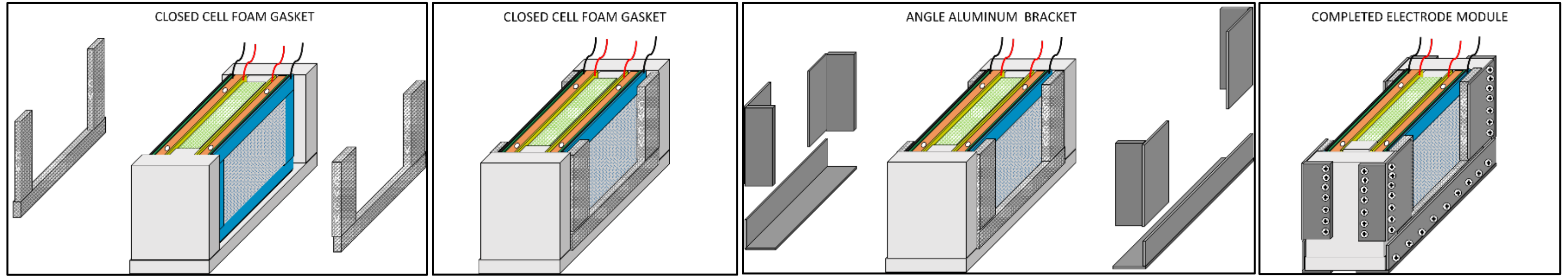

Figure 100. Electrode module components and manufacturing sequence. For illustration purposes only. Not to scale. Sequence reads each row sequentially.

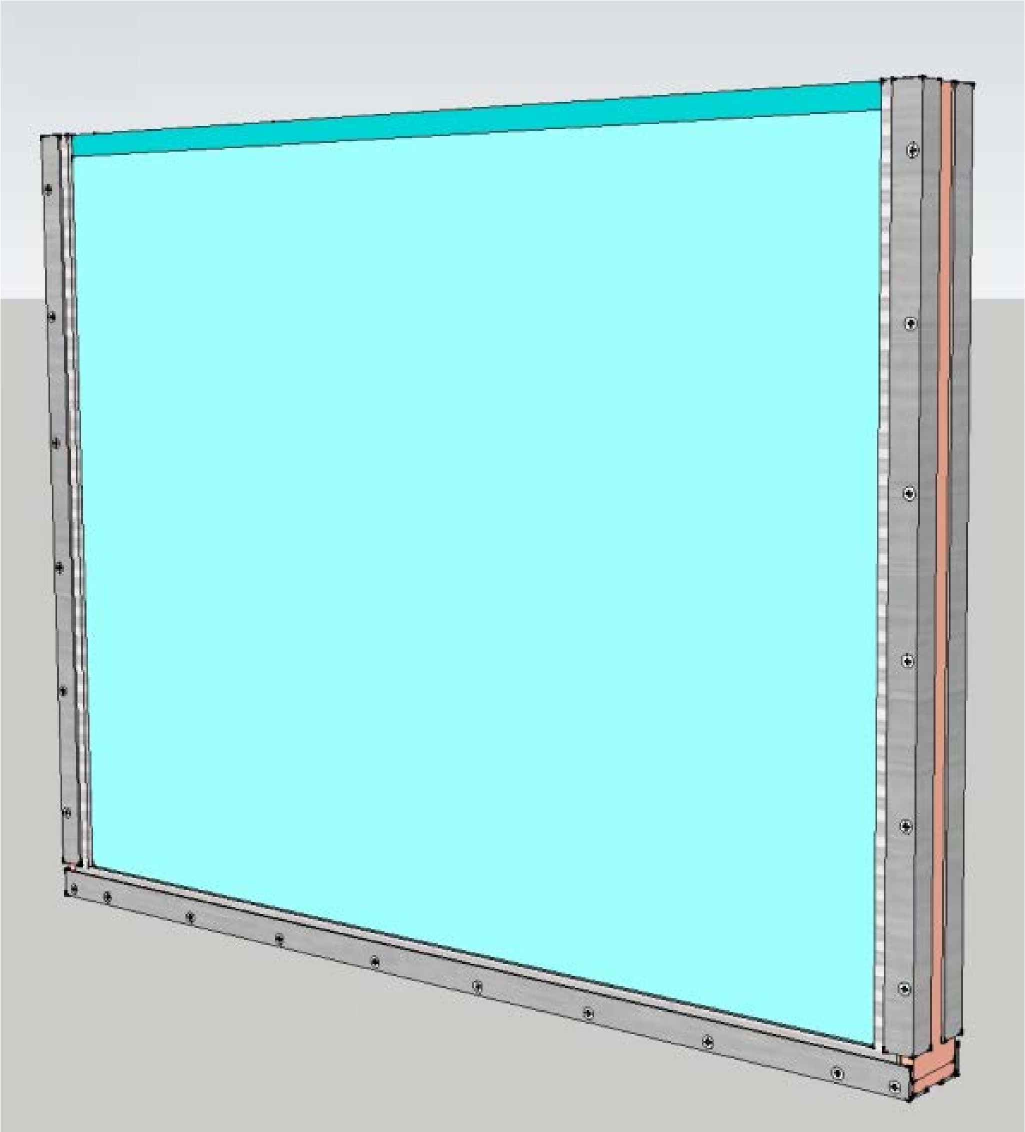

Figure 101. Isometric view of an electrode module illustrating the expanded titanium mesh (light blue) and the angle aluminum securement brackets (gray). The securement angle brackets are secured by countersunk screws into the plastic support frame.

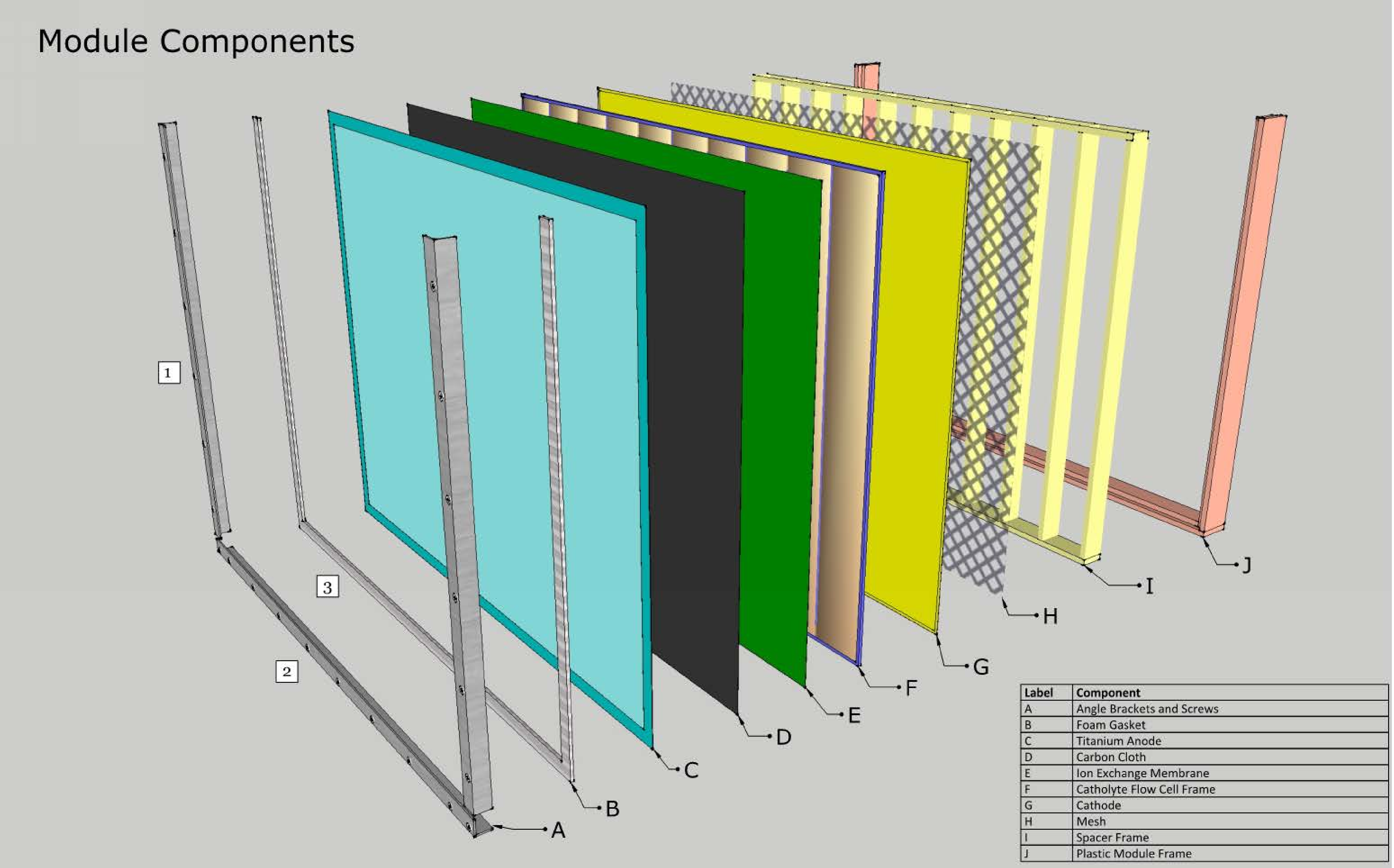

Label	Component
A	Angle Brackets and Screws
B	Foam Gasket
C	Titanium Anode
D	Carbon Cloth
E	Ion Exchange Membrane
F	Catholyte Flow Cell Frame
G	Cathode
H	Mesh
I	Spacer Frame
J	Plastic Module Frame

Figure 102. Expanded view of a single module showing the individual components.

The next series of figures show detailed views of the individual components of the module.

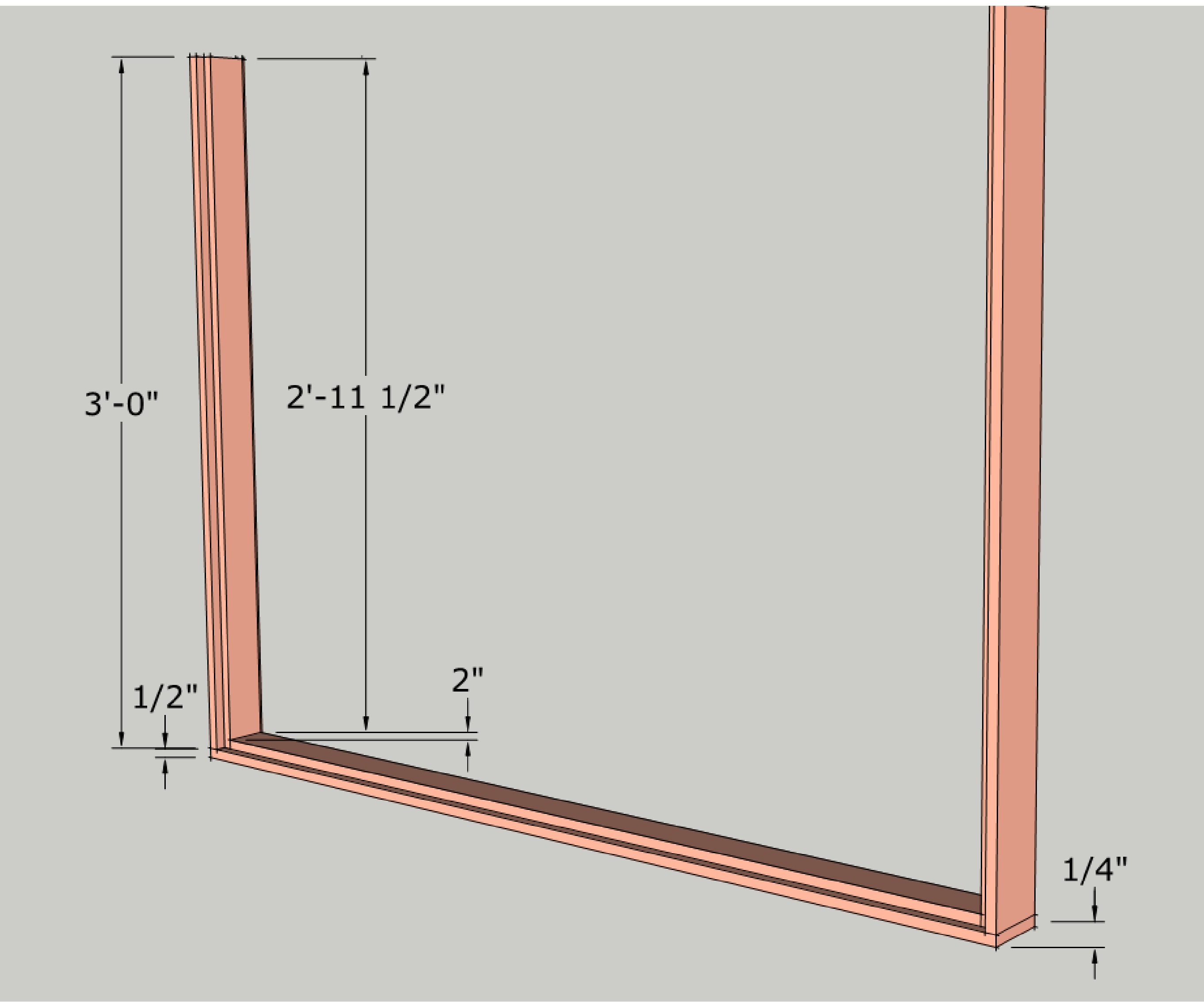

Figure 103. Plastic frame.

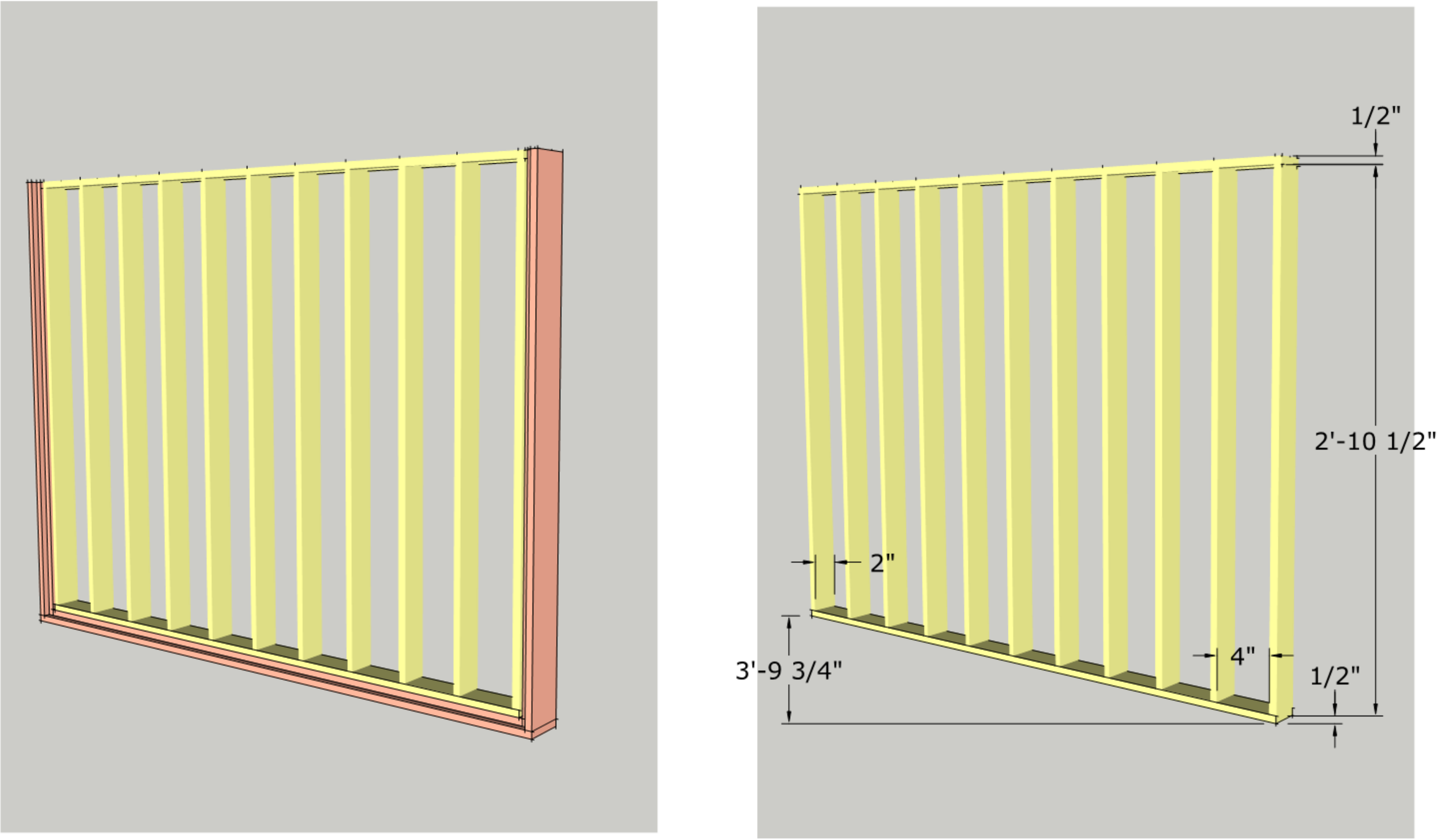

Figure 104. Plastic frame with spacer frame.

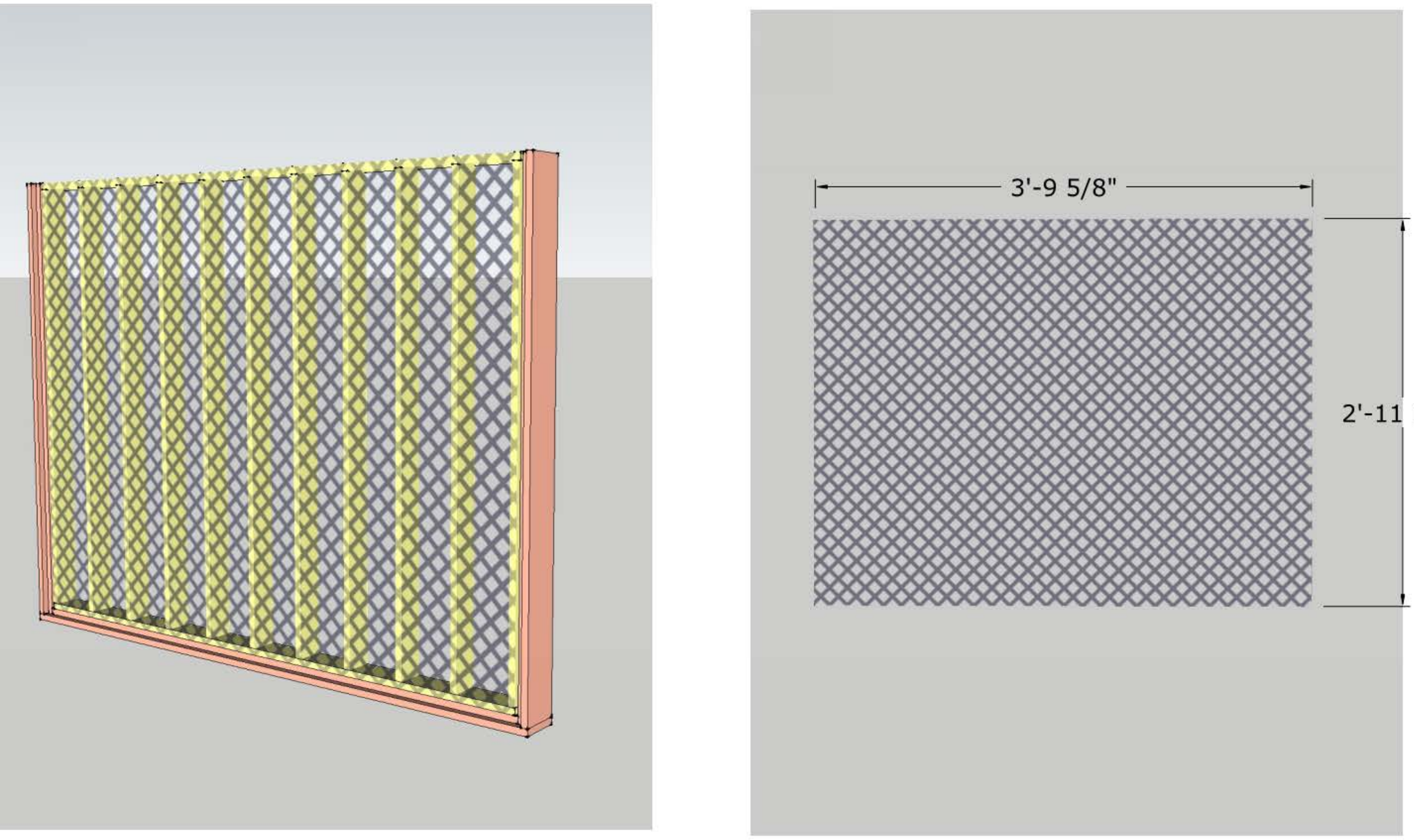

Figure 105. Plastic mesh.

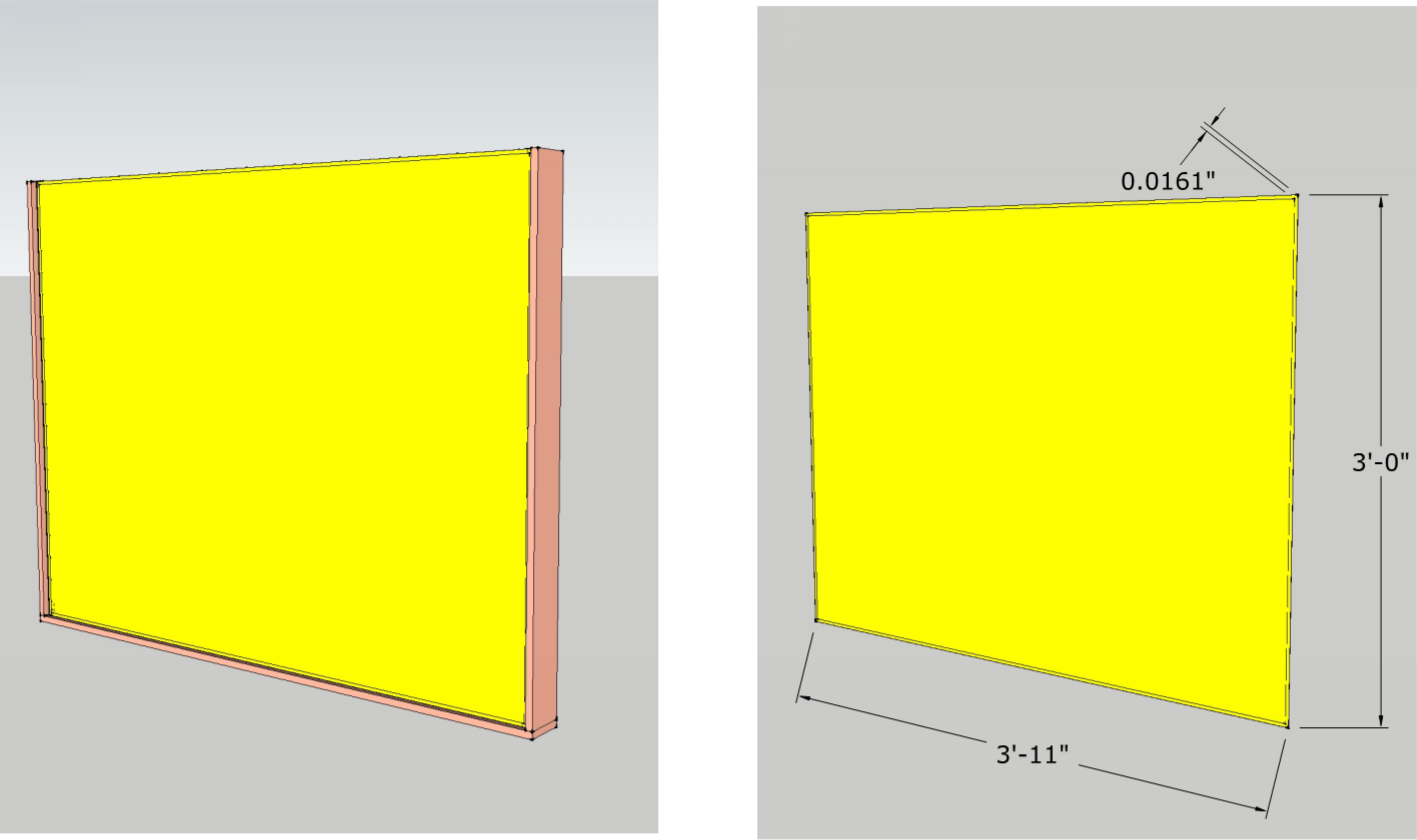

Figure 106. Cathode sheet

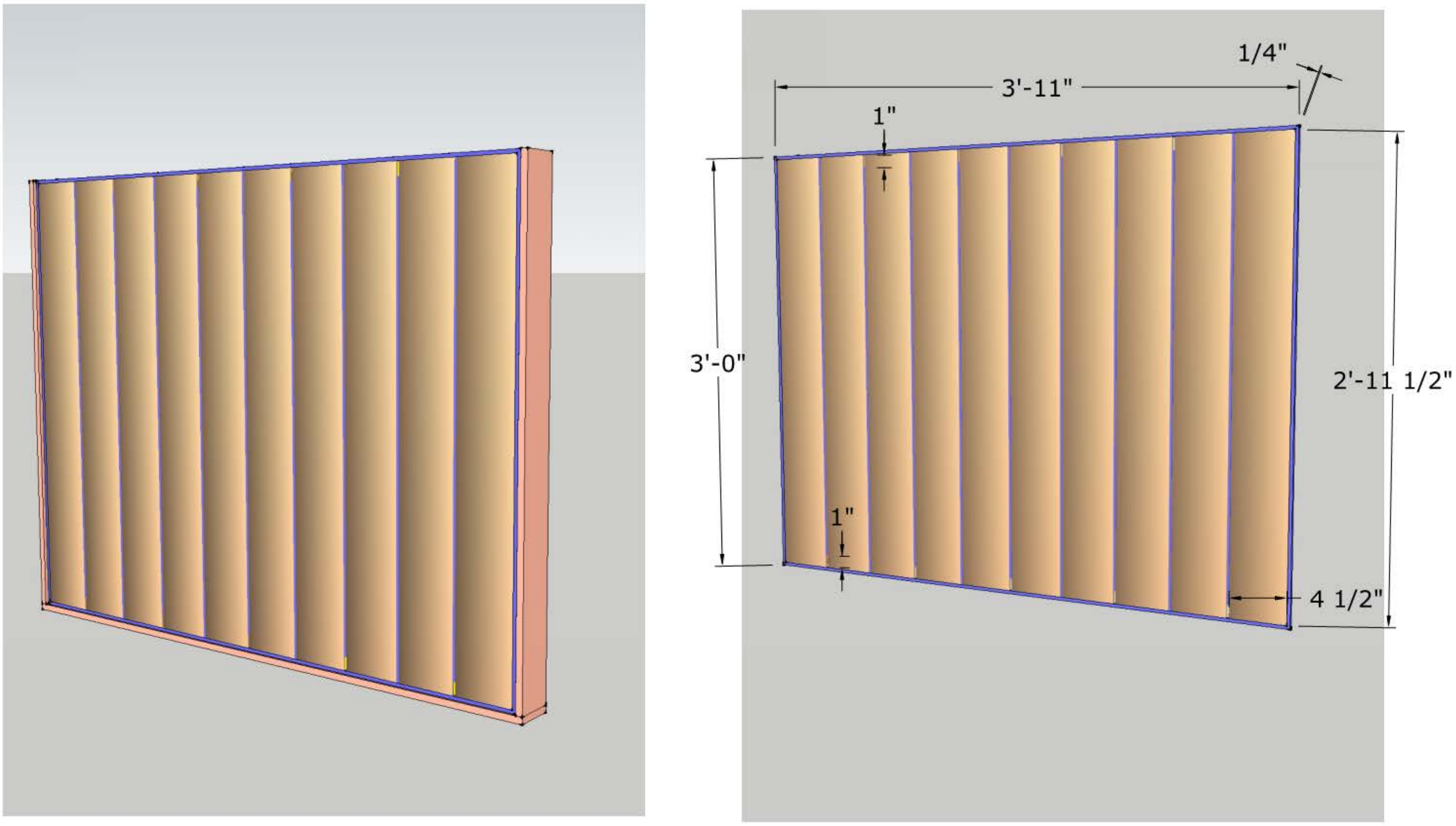

Figure 107. Catholyte frame. Catholyte flows through the geonet insets in a serpentine flow pattern.

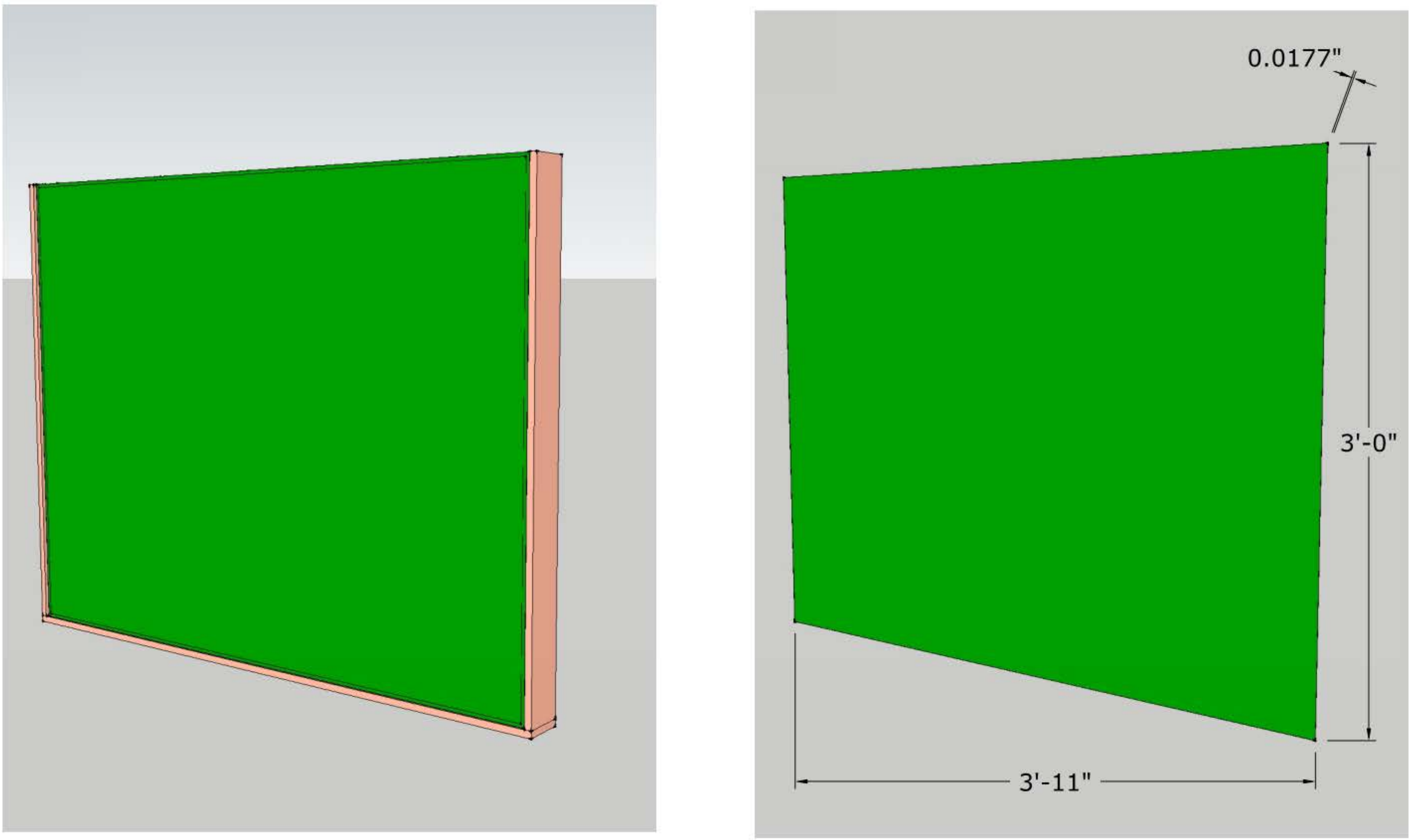

Figure 108. Ion exchange membrane.

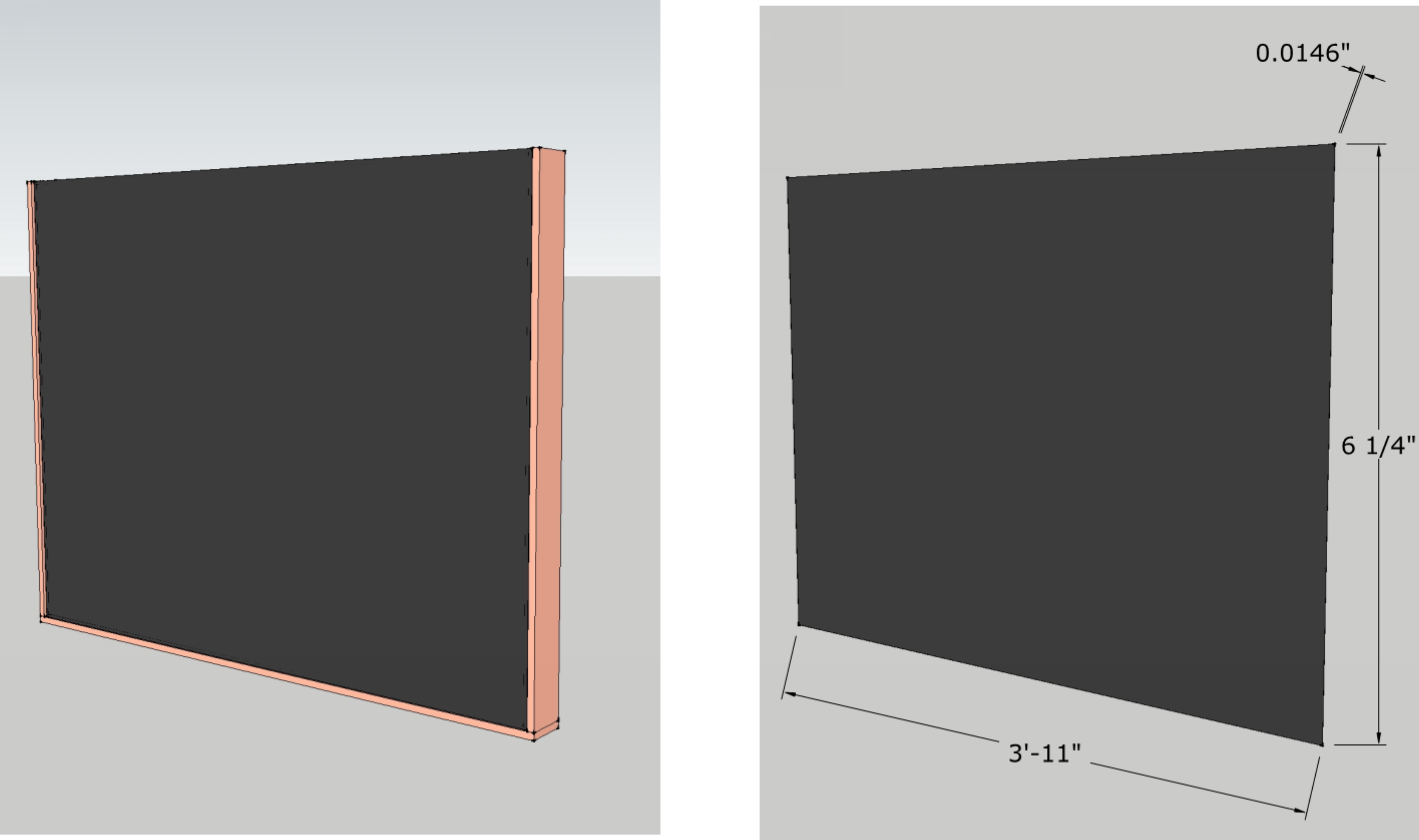

Figure 109. Carbon cloth.

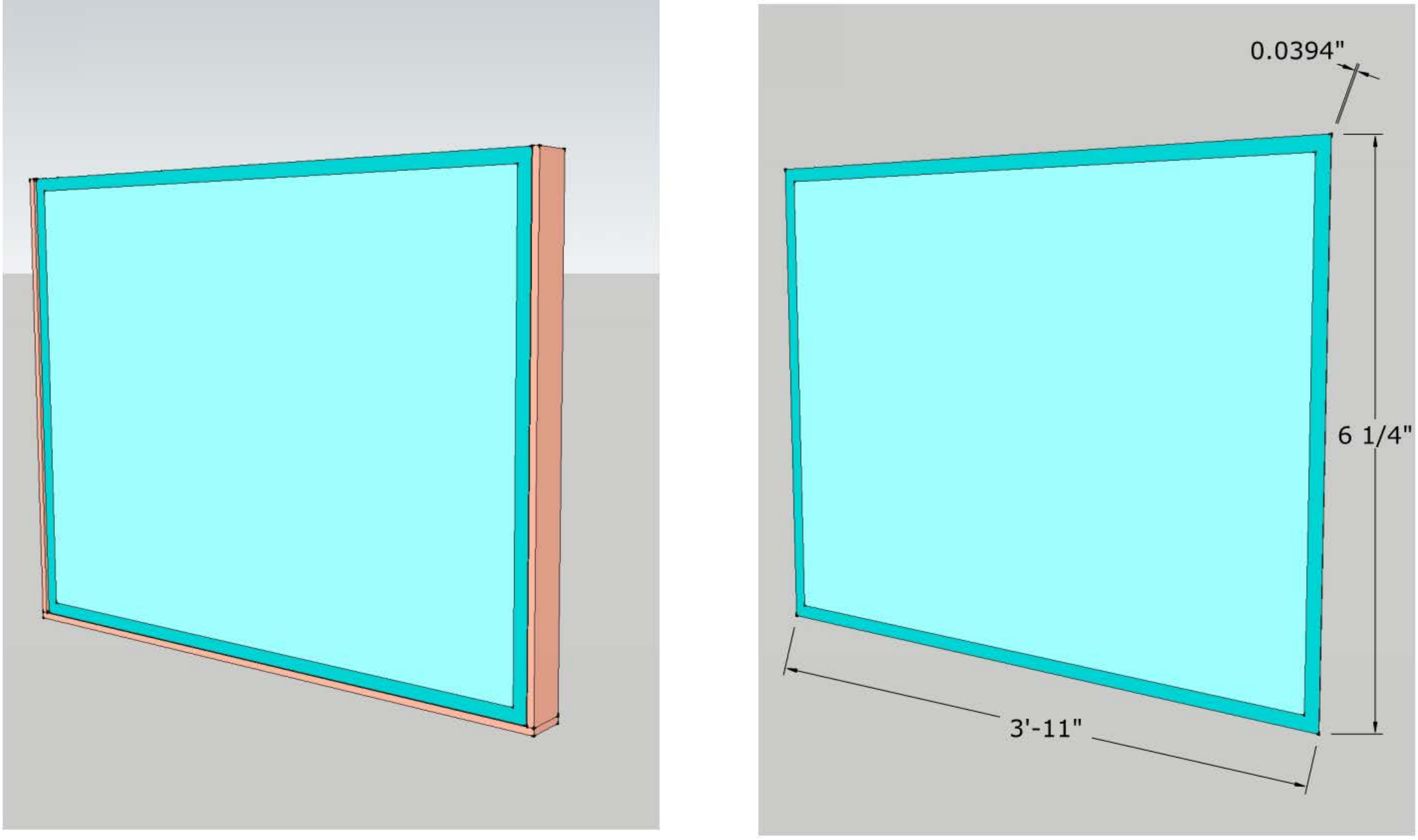

Figure 110. Titanium anode.

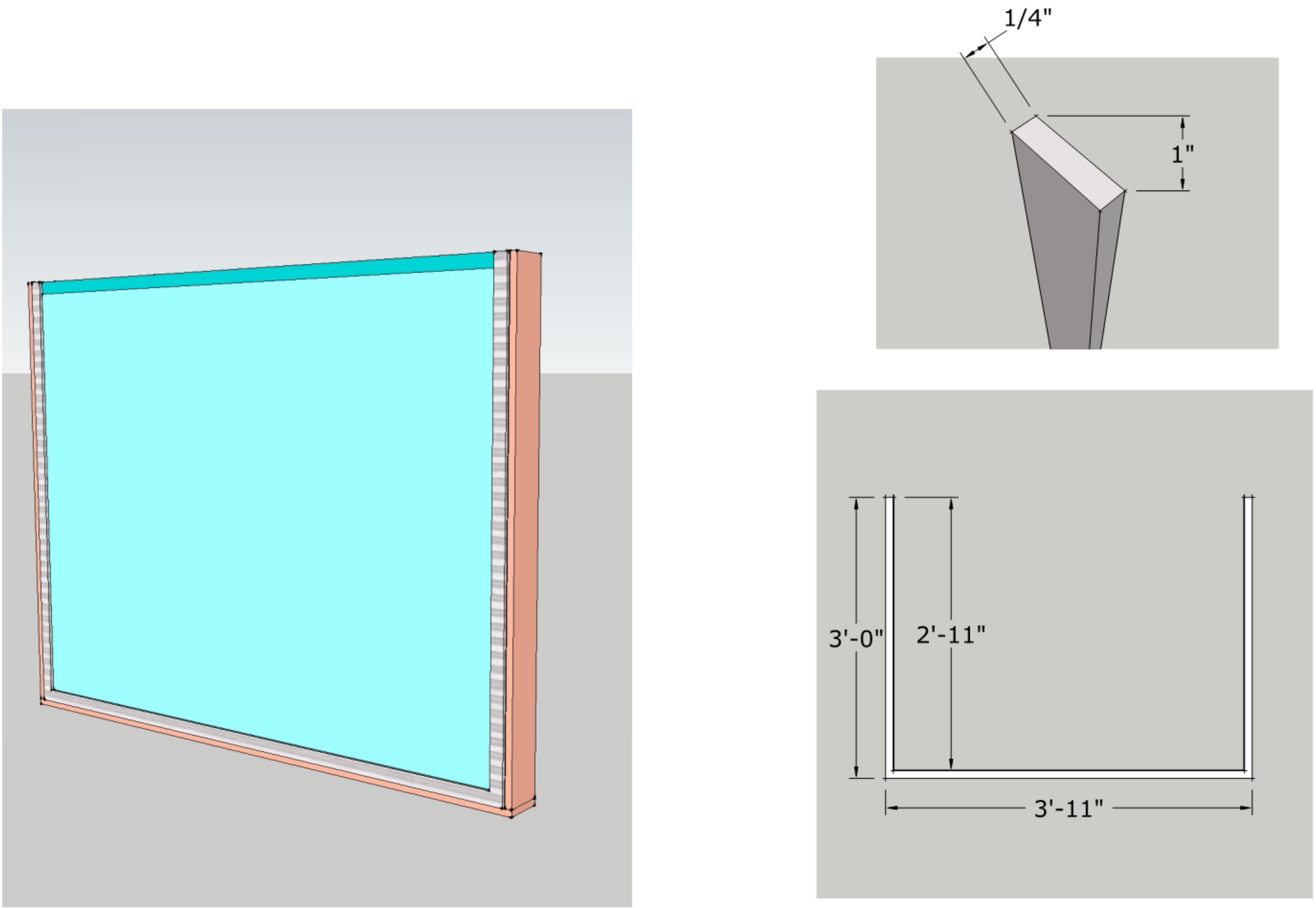

Figure 111. Foam gaskets.

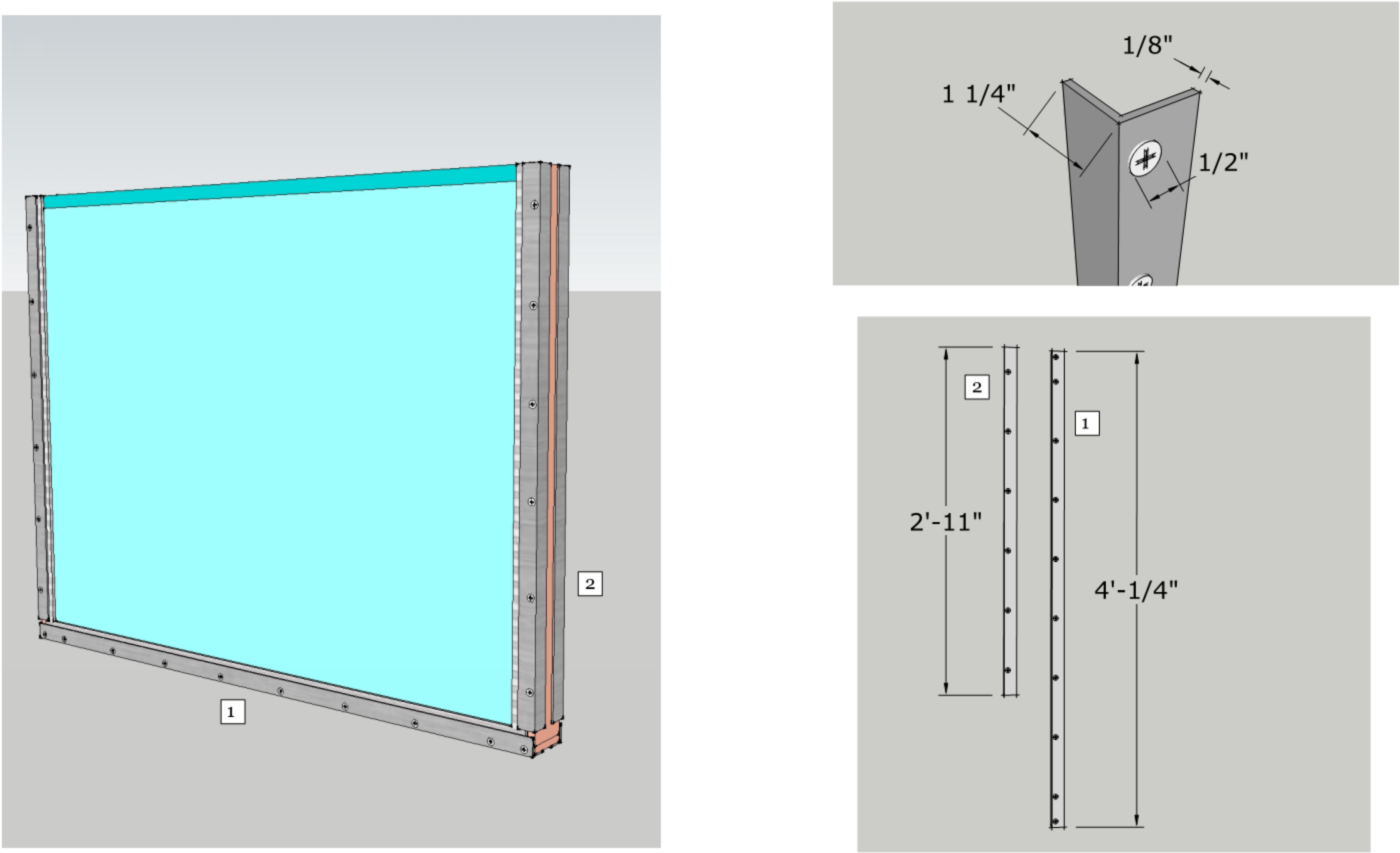

Figure 112. Angle brackets and screws.

Liquid gasket that is compatible with individual components is to be used to coat material edges and provide permeation resistance to a minimum of 6 feet water column upon compression of the electrode sandwich by the angle brackets and screws.

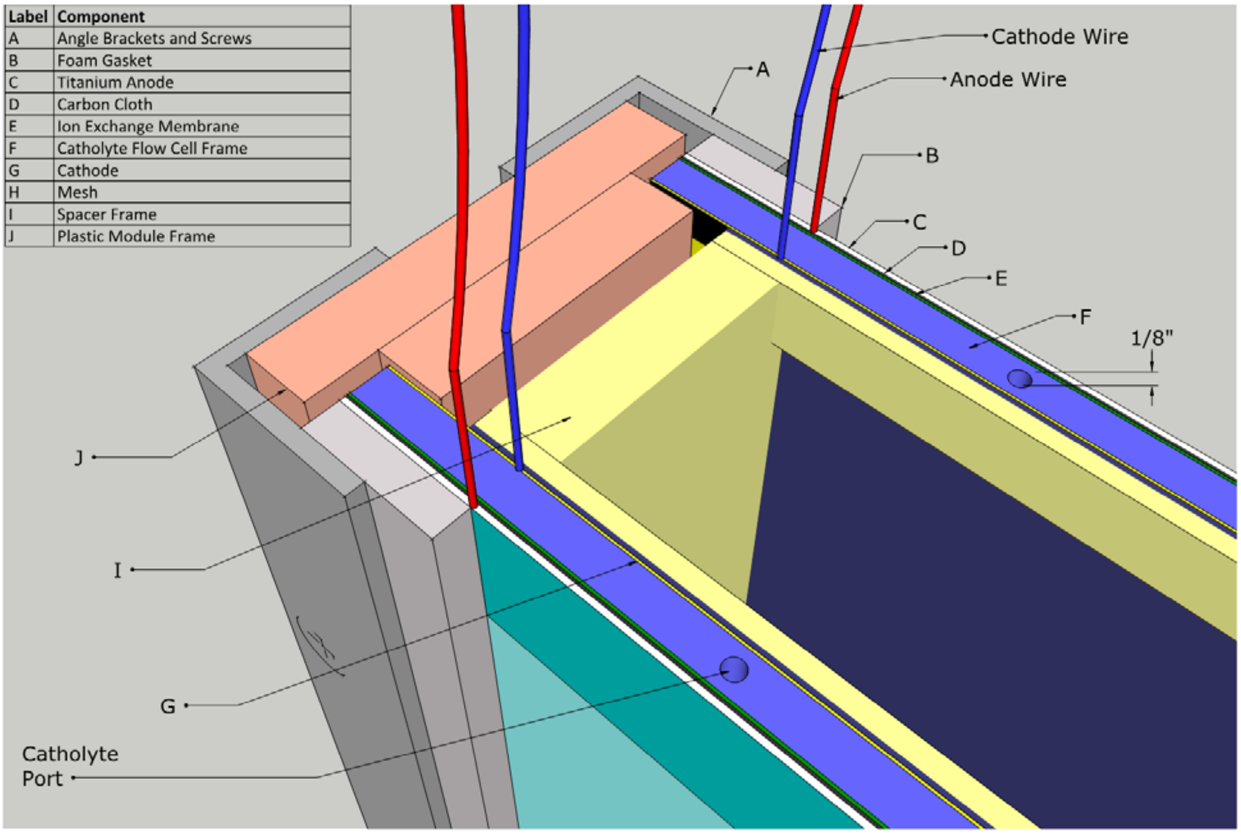

Figure 113. Isometric and cross-section detail views of the upper corner of an electrode module including the plastic frame, plastic spacer frame, plastic support mesh (Industrial Netting XN4821 polypropylene mesh; 0.1” x 0.1”; 0.031” thickness; 76% open area), specialized cathode (to be specified by others), plastic catholyte flow cell with inlet port, ion exchange membrane (Membranes International AMI-7001), carbon cloth (to be specified by others), expanded titanium mesh current collector (Stanford Materials or equivalent), neoprene closed-cell foam gasket (0.25” thickness), and aluminum angle securement bracket (6061 aluminum 90° angle stock; 0.125” thickness; 1.25” wide x 1.25” high). The mesh material emplaced in the spacer frame (GSE Hypernet Geonet 250 MIL; 0.25” thickness) is not shown.

Electrical engineering design. Each The most intricate aspect of the electrical engineering design is current and/or potential control of the electrodes. Additional design aspects include wiring and interconnection details to ensure impedance losses are negligible; power distribution to motors, instruments and control devices and other appurtenances; and design of enclosures and conduit to ensure compliance with the National Electrical Code. The focus of this section is on the current/potential control. Other aspects are easily addressed by a qualified design-build contractor.

The design current for each electrode module 9 A. There are two anode-cathode pairs in each electrode module thus the design current for each anode-cathode pair is 4.5 A. The design potential – measured across the anode and the reference electrode – is - 0.2 to - 0.5 V ± 0.05V. Two approaches can be taken: voltage control or current control. Each will be discussed below.

A low-cost potentiostat is required for practical voltage control. ASU has conducted a preliminary design of such as potentiostat illustrated in Figure 114. This potentiostat is theoretically capable of delivering 5A current.

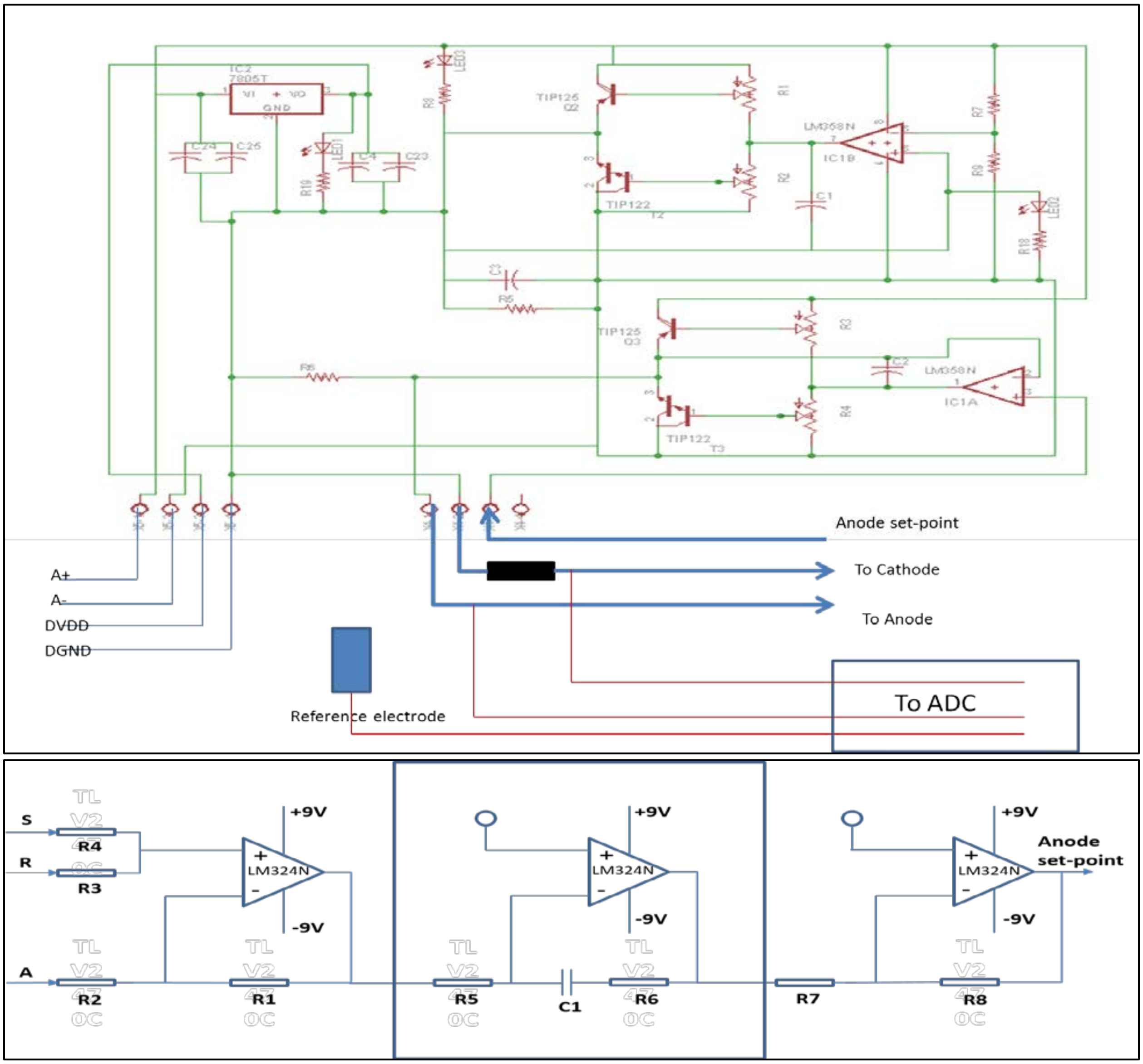

Figure 114. Potentiostat design. Top diagram: Bipolar junction transistors (Darlington pairs) used are TIP125 and TIP122 with a gain of -2000 to 3000 and a maximum current rating of 5A(max). The low cost potentiostat unit (Voltage divider + voltage follower + proportional-integral controller) requires 0-18V voltage source that can supply up to 5A current.; Bottom diagram: Op-amp circuit of PI controller, this is used to regulate anode(A)- reference(R) (A-R) voltage to match to a set-point.

Testing results of the above circuit using 1ohm resistor as load are presented in Figure 115. and illustrate good voltage control. A DC bias of about 0.08V exists because of the shifter circuits used in the measurement. Standard deviations in measurements are 0.0011V and 000826V for

1V tracking and for 0.5 V tracking respectively. The delivered current for these tests was measured through a 1-Ohm resistor.

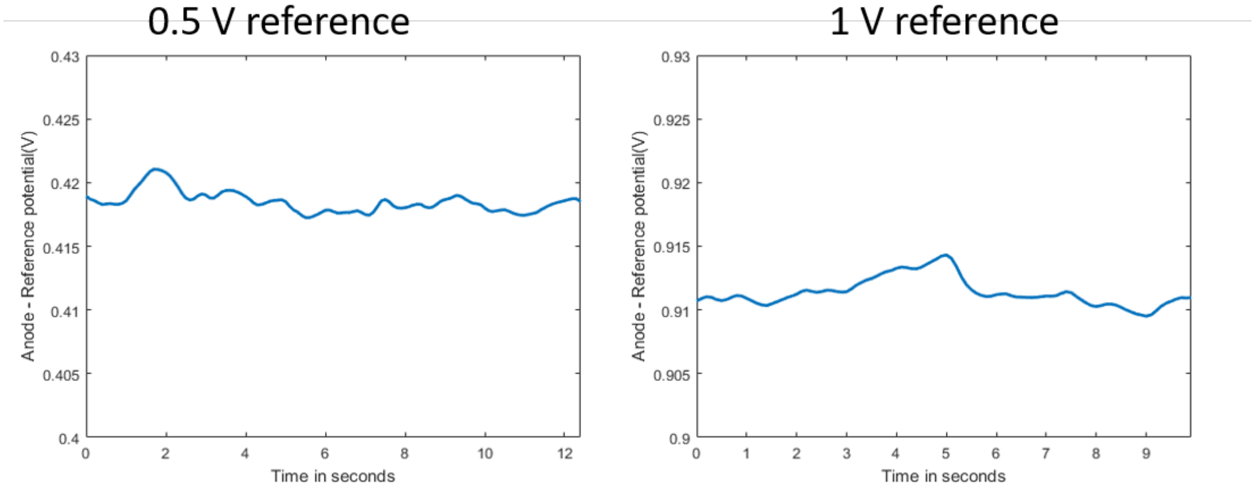

Figure 115. Test results of the potentiostat design. Set-point tracking results; There is a dc bias (~ 0.08V) because of shifter circuits (used in the measurement).

Current control. The objective of this circuit was to control potential. We can optimize a current related objective by continuously adjusting the set points to the potentiostat circuit. To control current, we would need to use the reactor model along the lines of the model predictive control paradigm (Rawlings and Mayne, 2009). An individual controller would be required for each anode-cathode pair totaling 36 controllers. The wiring schematic for a single electrode subreactor containing six electrode modules is illustrated in Figure 116.

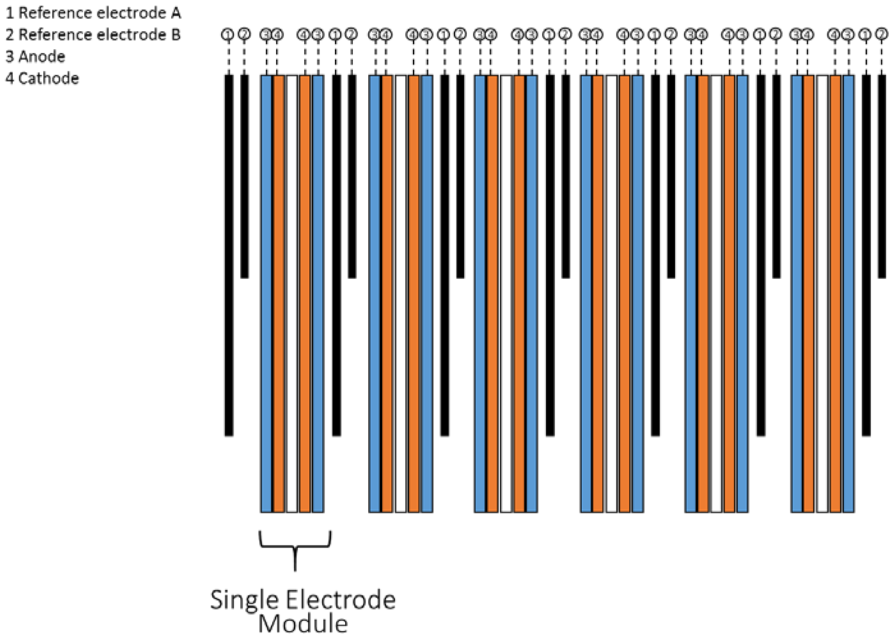

Figure 116. Wiring schematic for a single electrode module.

5.7.2 LCA Results and Discussion

Capital Costs. The results of each alternative's capital costs are summarized in Figure 117. Operations and maintenance costs were not directly analyzed as part of this assessment. A full life cycle cost analysis would provide a more holistic view of the cost of each scenario.

As expected, the highest capital cost per cubic meter treated water (functional unit) scenario is the MPPC, due to the increased cost of the MPPC itself. A savings in cost per cubic meter treated water is seen at the battalion scale for the MFC and MPPC scenarios; however, the cost is slightly higher at the battalion scale for CT because of the increase complexity in the scenario, as opposed to pit burning in the company scale.

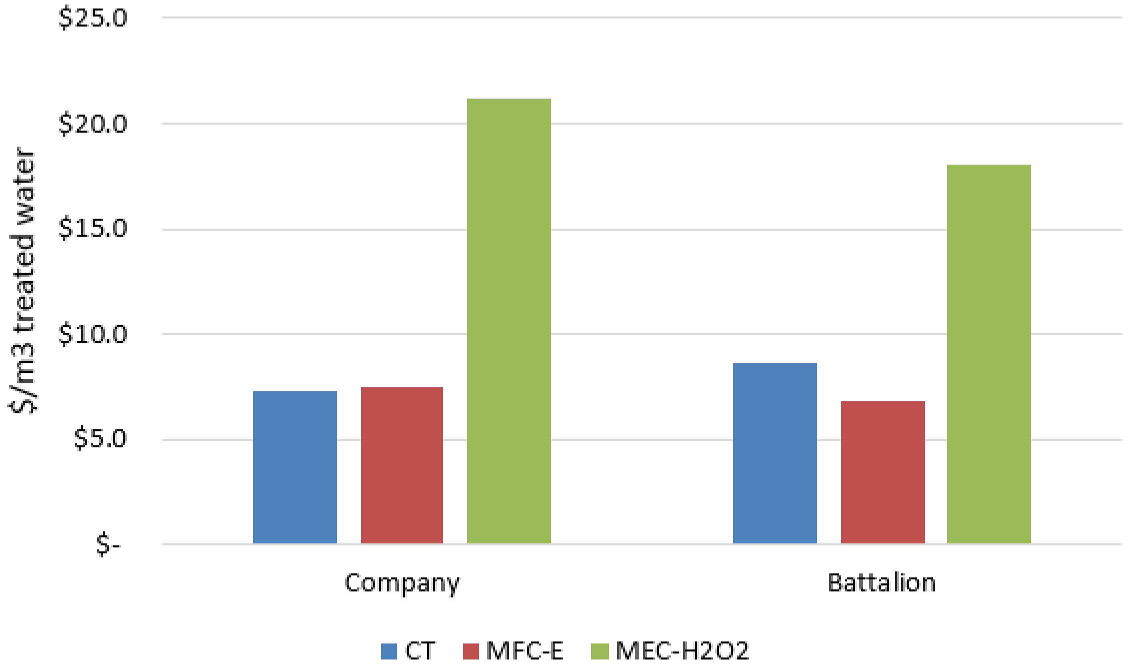

Figure 117. Summary of capital cost per cubic meter treated water for each WWT scenario and scale.

LCA. Endpoint results comparing all scales and WWT scenarios are illustrated in Figures 118 and 119. With regard to all endpoint categories, with the exception of soldier casualties, the CT scenario has the highest environmental impact at the company and battalion scales. This is mainly attributed to the positive environmental benefit of the electricity generation in the MFC-E scenarios and the H_2O_2 production in the MPPC scenarios. However; the positive environmental impacts from the H_2O_2 production outweigh those seen in the MFC-E scenario (electricity production), which makes this scenario have the lowest environmental impact of all three. At the midpoint level, the impacts to HH and the ecosystem are dominated by climate change categories at both the company and battalion scales, due in great part to the transportation requirements of goods to and from the FOB.

With regard to soldier casualties, all scenarios show a similar impact. The MFC and MPPC scenarios produce significantly less biomass, but as seen above in Table 23, the percent solids of the conventional sludge is assumed to be 10%, whereas the MPPC sludge is assumed be to 4% solids, giving a similar impact for sludge disposal.

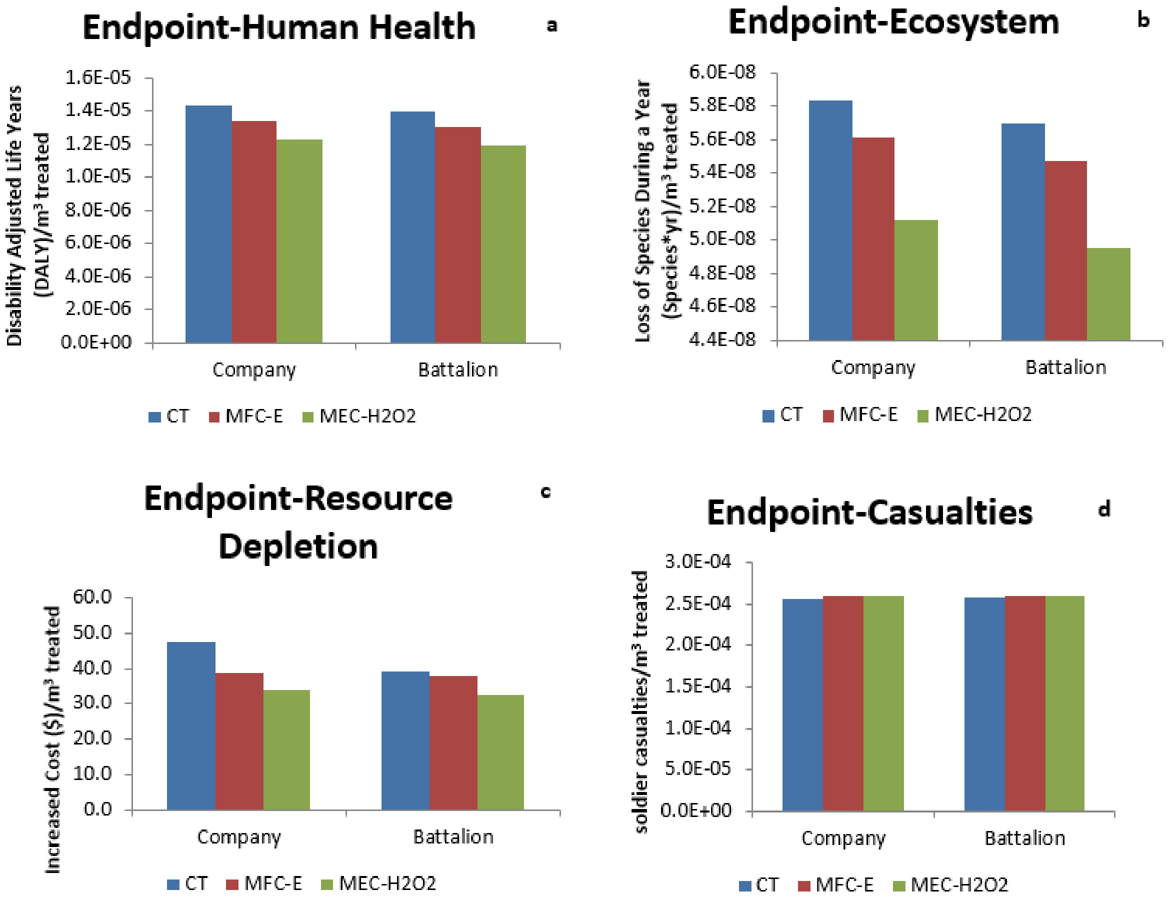

Figure 118. Endpoint LCA impact to human health (a) Endpoint LCA impact to the ecosystem (b) Endpoint LCA impact to resource depletion (c) Endpoint LCA impact to soldier casualties (d).

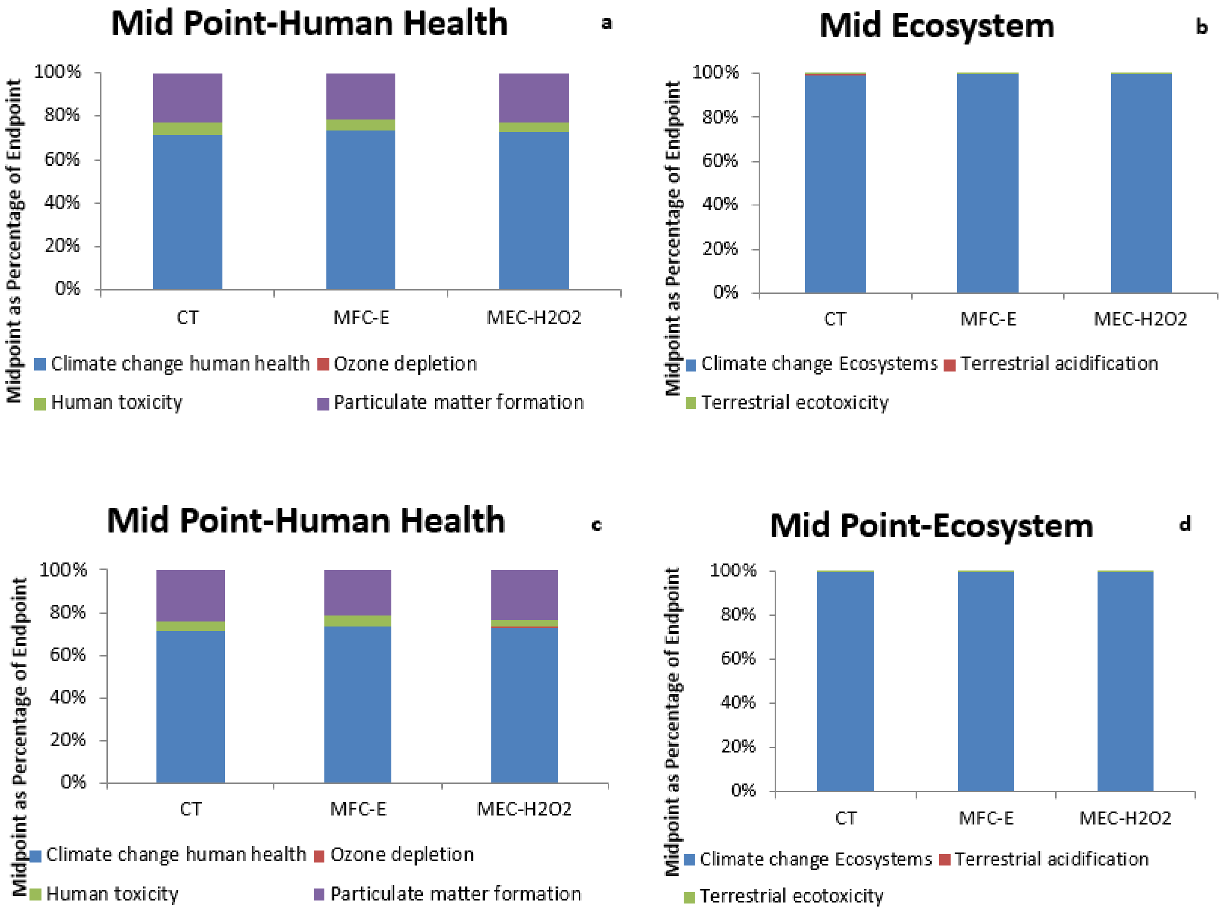

Figure 119. Midpoint LCA impacts to human health – company scale (a) Midpoint LCA impacts to human the ecosystem – company scale (b), Midpoint LCA impacts to human health – battalion scale (c) Midpoint LCA impacts to human the ecosystem – battalion scale (d).

Conventional Wastewater Treatment.

All environmental impacts are lower at the battalion scale when compared to the company scale. Midpoint impacts are dominated by impacts to climate change for both HH and the ecosystem. This is due to the contribution from transportation of goods to the FOBs, discussed in more detail below.

Across all scales, the impact from transportation, including frequent transport of water to the FOB for consumption and use by the soldiers, contributes the largest environmental impact. At the company scale, a higher environmental impact is attributed to sludge disposal, which consist primarily of pit burning using some form of fuel. These impacts are seen in use of fuel for the burning, which is included in the energy category seen in Figure 120, as opposed to environmental impact from sludge disposal to the landfill. Solids are periodically dredged and disposed of at a landfill in these scenarios at both the company and battalion scale; however, at the battalion scale, it was assumed that solids would only be disposed of once during the 1 year time frame of this assessment due to the nature of solids accumulation in the facultative and aerated lagoons. Similar patterns are seen in impacts to HH, ecosystem and resource impacts for all scales with a more significant impact to fossil fuel depletion, as seen in the company scale. To show of the percent contribution of each LCA category to the overall LCA impact, the breakdown of each LCA category for each scale is shown in Figure 120.

MFC with Electricity Production

Similar to CT, the battalion scale has a lower impact when compared to the company scale. The same patterns are seen at the midpoint due to the large contribution from transportation. At both scales, the benefits from the production of electricity is seen. As stated in the boundary conditions, impacts from effluent discharge were not included in this LCA. The impact from capital construction goods has a higher percent contribution at the smaller scale. This can be explained by economy of scale.

MEC with Hydrogen Peroxide Production

As was the case for CT, as well as the MEC for electricity production, the battalion scale has a lower overall environmental impact when compared to the company scale. Midpoint impacts are again dominated by climate change due to transportation, which is the case for all scenarios and scales. The negative impact of peroxide production is seen, which is included in the ‘chemicals’ category in Figure 120, and is significantly higher than the negative environmental impact of electricity generation in the MFC-E scenarios. The impact from capital goods has a higher contribution at the company scale than at the battalion due to economy of scale.

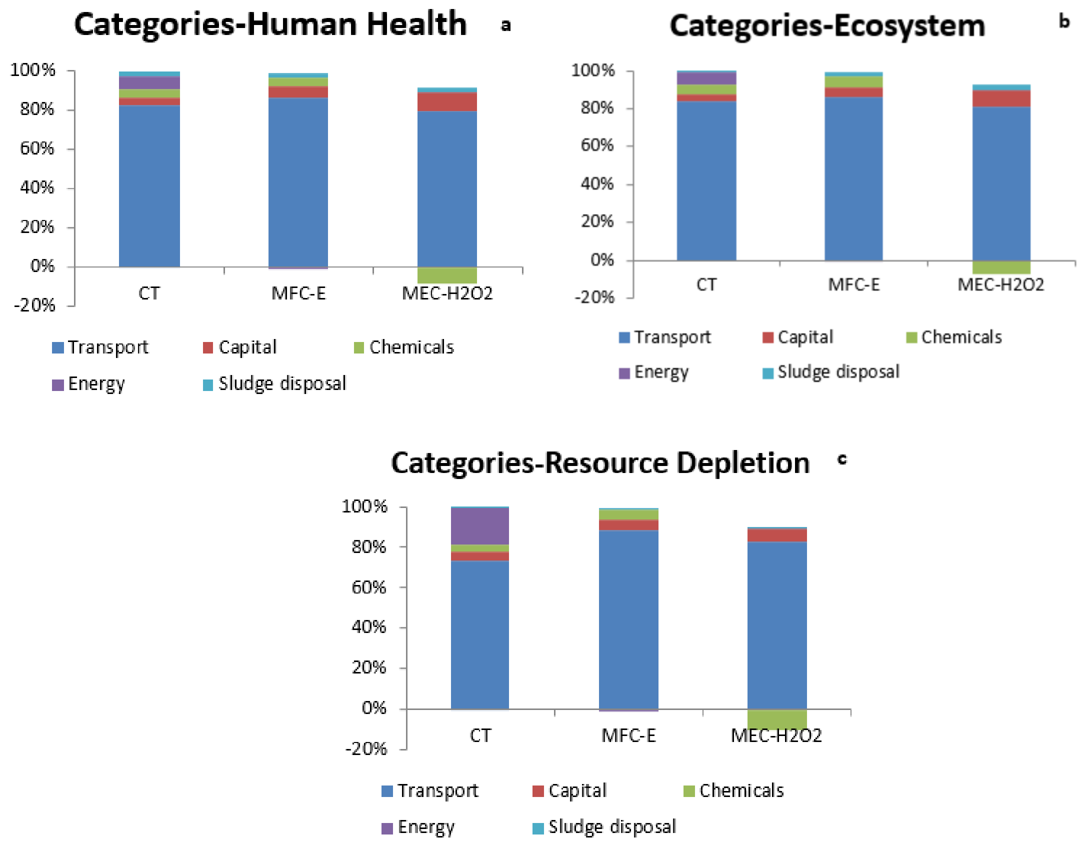

Figure 120. Human health LCA impacts by category – company scale (a) Ecosystem LCA impacts by category – company scale (b), Resource depletion LCA impacts by category – company scale (c).

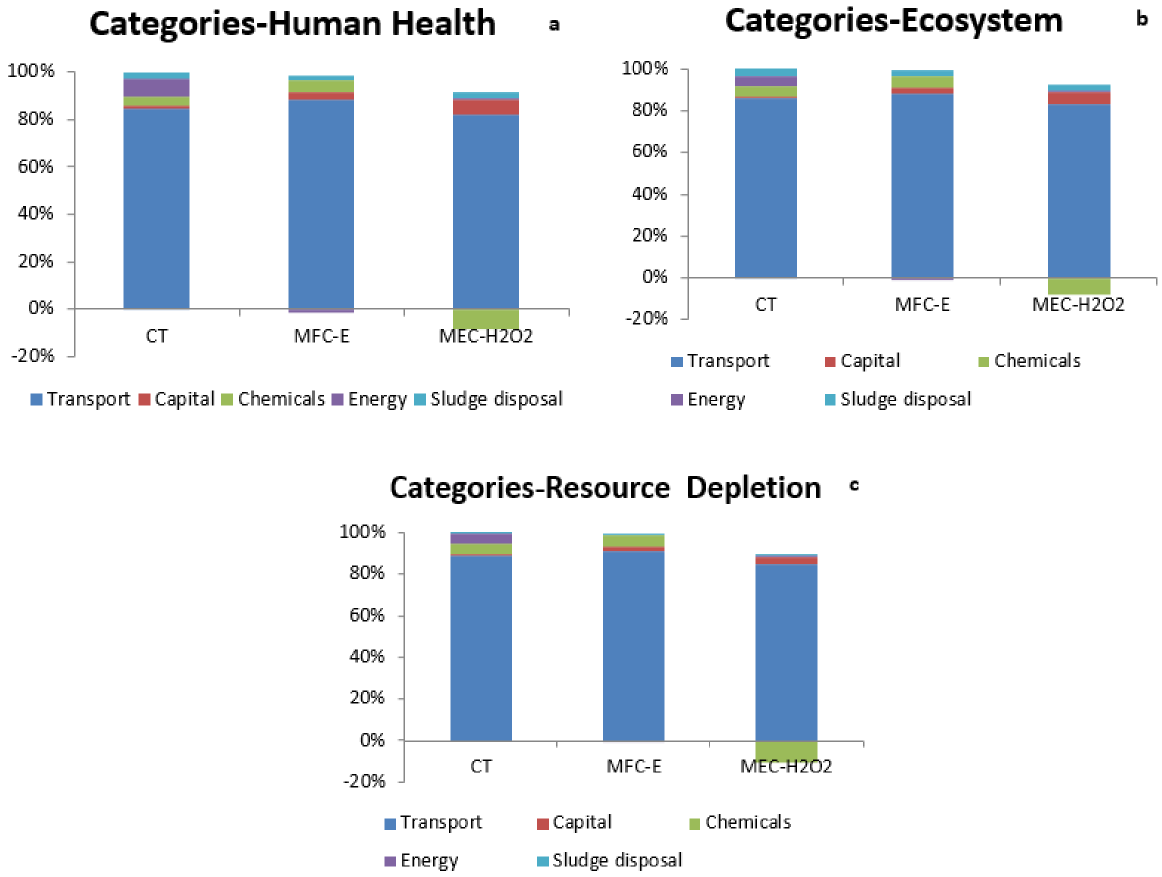

Figure 121. Human health LCA impacts by category – battalion scale (a) Ecosystem LCA impacts by category – battalion scale (b), Resource depletion LCA impacts by category – battalion scale (c).

Recommendations

This LCA provides the basis for future LCIA and cost work. At the beginning of this task, it was assumed that feasible treatment trains could also be assessed for FOBs at the brigade and division scales. Additionally, it was assumed that the treatment trains could also be modified to achieve adequate treatment for non-potable water to be reused at the FOBs. Through this initial assessment, it was determined that at these larger scales the amount of package units that would be required to treatment the increased flow would make the cost of these applications infeasible. Additionally, due to the volume of effluent, disinfection would be required at the larger scales, which is not comparable to the smaller scales in which the effluent volume would not require disinfection. At this point, the team decided not to include the larger FOB scales in the assessment. Additionally, an enhanced greywater treatment system would be required following the MEC and MFC scenarios. The team selected the Aquacell GX20A module for GW treatment (PHOENIX Process Equipment Co., Louisville, KY) for this application, but it was determined through discussions with vendor that this unit could not achieve the 30/30 effluent water quality standards. As such, GW treatment and subsequent nonportable water reuse at the FOBs was not included in this assessment. During future phases of work, research should be done on feasible treatment processes that could be included in the treatment trains for MFC and MPPC scenarios that are capable of achieving 30/30 effluent standards. Additional effort could be put into how larger scale plants would feasibly be built in remote FOB locations and how those would compare to smaller FOB installations. A significant reduction in environmental and social impacts could be seen from the application of water reuse at the FOB sites.

Cost results indicate that the MEC-H_2O_2 scenario has the highest cost per cubic meter treatment water. Additional studies could be done on how to minimize MEC costs so that this treatment alternative becomes more economically viable, when compared to conventional or MFC alternatives.

6. CONCLUSIONS AND IMPLICATIONS FOR FUTURE RESEARCH

Our research not only demonstrates the feasibility to produce hydrogen peroxide from blackwater using a microbial fuel cell, but it also shows that high rates and production efficiencies are possible. The microbial fuel cell efficiently treats the blackwater with or without the aid of the hydrogen peroxide produced. However, higher quality and rates are achieved through the aid of hydrogen peroxide. The development of this technology can change approaches at forward operating bases and at municipal wastewater treatment plants by having an in situ chemical production of a strong oxidant for treatment.

In Task 2, semi-continuous pre-fermentation of PS was evaluated as a means to avoid direct solids addition to the MPPC. A 3-day SRT (= HRT) pre-fermentation led to more VFA accumulation and less methane production. However, the overall recoveries from the sludge were low (Figure 34a), which led to experiments with direct addition of sludge into the MPPC. Through the direct sludge addition, HRT was a key parameter that we optimized. We show that MPPCs can operate at significantly lower HRTs when compared to anaerobic digesters. The maximum current density exceeded 2 A m^{-2} for the 6- and 9-day HRTs, and the CR was the highest with an 9-day HRT (34%). A VSS reduction of ~60% shows similar or better performance than anaerobic digestion. Also, we developed a non-steady-state mathematical model, MYAnode, which integrates the chemical and biological processes in the bulk liquid of the microbial fuel cell with substrate utilization and current production in the anode biofilm. MYAnode is able to predict similar behavior between methanogens and anode respiration, stressing the importance of pH and influent methanogens into the expected performance of the reactor. Based on these results, other studies focused largely on a 6-9 day HRT in MPPCs.

With anode processes optimized, a material characterization required to design MPPCs was performed. Vulcan carbon with a Nafion binder provided chemical stability in the presence of H_2O_2 while producing minimal activation overpotentials compared to tested catalysts. Stability tests with an anion-exchange-membrane (AEM) stability tests established AMI-7001 as the optimal membrane to resist H_2O_2 degradation and promote long-term MPPC performance due to its high structural integrity. These materials were used in Tasks 6 and 7 for the construction and optimization of MPPC prototypes. Our first MPPC produced H_2O_2 at a concentration as high as 3.8 g L^{-1} during continuous operation when fed with acetate as substrate. These concentrations are much higher than those needed for disinfection and micropollutant removal and with low power input (1.1 Wh g^{-1} H_2O_2). The MPPC's Ohmic overpotentials were small – 69 Ω cm^2 – and the cathode performed well using a simple NaCl catholyte with a 1- to 4-h HRT and no stabilizers. Thus, continuous H_2O_2 production in an MPPC is achievable if materials are optimized for compatibility with and production of H_2O_2.

Our optimized MPPC was also able to produce H_2O_2, with a maximum H_2O_2 concentration achieved ∼230 mg/L. The lower current densities and degradation within the cathode chamber explain the lower concentrations obtained. The MPPC achieved ∼30% Coulombic recovery for primary sludge in these studies. On the other hand, a single-chambered MPPC had only a Coulombic recovery of 19%, since the H_2O_2 aided in COD removal, which reached 49%, along with a 52% of VSS removal. The high rates of VSS destruction in the single-chamber MPPC at a 6-day HRT (5 gCOD/L/day or 2.7g VSS/L/day), along with a low fecal coliform concentration (1.2 x 10^5 MPN/gram dry solid), confirm that the MPPC is an excellent alternative for sludge stabilization, meeting the requirements of Class B biosolids.

In summary, the MPPC technology has proven to reliably obtain significant treatment and solids reduction from municipal primary sludge used as a surrogate for blackwater. Better and faster treatment is achieved if the H_2O_2 produced is delivered directly to the anode chamber, where sludge treatment occurs. cathodic H_2O_2 production efficiency was as high as 78%, although at lower H_2O_2 of 1.02 g/L, partly because of degradation H_2O_2 within the cathode at longer HRTs. Thus, our report compiles a comprehensive knowledge of optimum materials and design for an MPPC that achieves the major goals of the project: efficient blackwater treatment and efficient production of H_2O_2 at near energy-neutral conditions.

Based on our research results, we developed a pilot-scale design that takes into consideration the major hurdles regarding solids treatment, cathodic flow for H_2O_2 collection, and power management. The design closely resembles our laboratory prototypes, while using cheaper alternatives available at larger scale. Despite this, our LCA economic analysis shows a significantly higher capital cost in our MPPC treatment when compared to conventional treatment. While benefits of H_2O_2 production and lower energy consumption can offset capital costs, our future research should focus on finding lower-cost materials with similar performance to the ones used in our laboratory.

The cathodic HRT was the most crucial parameter affecting the effluent H_2O_2 concentration and its production efficiency. The MPPC design also plays an important role in the HRT and concentration. A smaller cathode chamber can reduce the HRT without affecting the effluent concentration, which depends on the cathode surface area and current density. Future studies should take our learnings to re-optimize the MPPC design to the specific current density achievable and desired H_2O_2 concentration desired.

Finally, we performed an initial effort to compare MPPCs and MFCs with conventional treatment for FOBs through LCA. This is a first effort that definitely requires a more extensive analysis in order to correctly determine the impacts of this new technology when compared to existing approaches.

7. LITERATURE CITED

Abbot J, Brown DG. 1990. Kinetics of Iron-catalyzed decomposition of hydrogen peroxide in alkaline solution. International Journal of Chemical Kinetics 22:963-974.

AEPI. 2009. Sustain the Mission project: Casualty Factors for Fuel and Water Resupply Convoys. Arlington, Army Environmental Policy Institute.

Al-Duwaish H, Naeem W. 2001. Nonlinear model predictive control of hammerstein and wiener models using genetic algorithms. IEEE International Conference on Control Applications.

Althaus H, Chudacoff M, Hischier R, Jungbluth N, Osses M, Primas A. 2007. Life cycle inventories of chemicals.

Alvarez H, Londono C, di Sciascio F, Carelli R. 2001. pH neutralization process as a benchmark for testing nonlinear controllers. Industrial & Engineering Chemistry Research. 40(11): 2467-2473.

American Water Works Association. 2005. Water Treatment Plan Design. New York: Mc-Graw-Hill.

An J, Lee H-S. 2013. Implication of endogenous decay current and quantification of soluble microbial products (SMP) in microbial electrolysis cells. Rsc Advances 3(33):14021-14028.

Angelidaki I, Alves M, Bolzonella D, Borzacconi L, Campos JL, Guwy AJ, Kalyuzhnyi S, Jenicek P, van Lier JB. 2009. Defining the biomethane potential (BMP) of solid organic wastes and energy crops: a proposed protocol for batch assays. Water Science and Technology 59(5):927-934.

Angosto JM, Fernandez-Lopez JA, Godinez C. 2015. Brewery and liquid manure wastewaters as potential feedstocks for microbial fuel cells: a performance study. Environmental Technology 36(1):68-78.

APHA. 2012. Standard Methods for the Examination of Water and Wastewater. Washington, D.C.

Aquacell Website. Greywater Systems;http://aquacell.com.au/services/systems/greywater/.

Aquino SF, Stuckey DC. 2008. Integrated model of the production of soluble microbial products (SMP) and extracellular polymeric substances (EPS) in anaerobic chemostats during transient conditions. Biochem Eng J 38:138-146.

Arends JBA, Van Denhouwe S, Verstraete W, Boon N, Rabaey K. 2014. Enhanced disinfection of wastewater by combining wetland treatment with bioelectrochemical H2O2 production. Bioresour Technol 155:352-358.

Åström KJ, Hägglund T. 2006. Advanced PID Control. ISA-The Instrumentation, Systems, and Automation Societ.

Atasoy E, Murat S, Baban A, Tiris M. 2007. Membrane bioreactor (MBR) for treatment of segregated household wastewater for reuse. Clean 35(5): 465-472.

Badalamenti JP, Torres CI, Krajmalnik-Brown R. 2013. Light-responsive current generation by phototrophically enriched anode biofilms dominated by green sulfur bacteria. Biotechnology and Bioengineering 110(4):1020-1027.

Bard AJ, Faulkner LR. 2001. Electrochemical Methods: Fundamentals and Applications.

Barth C, Powers T, Rickman J. 1992. Agricultural Waste Management Field Handbook, USDA.

Batstone D, Keller J, Angelidaki I, Kalyuzhnyi S, Pavlostathis S, Rozzi A, Sanders W, Siegrist H, Vavilin V. 2002. The IWA Anaerobic Digestion Model No 1 (ADM1). Water Science and Technology 45:65-73.

Benjamin MM. 2015. Water Chemistry. Long Grove, Ill.:Waveland Press, Inc.

Bhattacharya SK, Madura RL, Walling DA, Farrell JB. 1996. Volatile solids reduction in two-phase and conventional anaerobic sludge digestion. Water Research 30(5):1041-1048.

Boling JM, Seborg DE, Hespanha JP. Multi-model adaptive control of a simulated pH neutralization process. Control Engineering Practice 15(6):663-672.

Bolzonella D, Fatone F, Pavan P, Cecchi F. 2005. Anaerobic fermentation of organic municipal solid wastes for the production of soluble organic compounds. Industrial & Engineering Chemistry Research 44(10):3412-3418.

Bonakdarpour A, Lefevre M, Yang R, Jaouen F, Dahn T, Dodelet J, Dahn J. 2008. Impact of loading in RRDE experiments on Fe–N–C catalysts: two-or four-electron oxygen reduction? Electrochemical and Solid-State Letters 11:B105-B108.

Bond DR, Strycharz-Glaven SM, Tender LM, Torres CI. 2012. On Electron Transport through Geobacter Biofilms. ChemSusChem 5:1099-1105.

Brown RE, Jarvis KL, Hyland KJ. 1989. Protein measurement using bicinchoninic acid - elimination of interfering substances. Analytical Biochemistry 180(1):136-139.

Call D, Logan BE. 2008. Hydrogen production in a single chamber microbial electrolysis cell lacking a membrane. Environmental Science & Technology 42(9):3401-3406.

Campos-Martin JM, Blanco-Brieva G, Fierro JLG. 2006. Hydrogen Peroxide Synthesis: An Outlook beyond the Anthraquinone Process. Angewandte Chemie International Edition 45:6962-6984.

Cao Y, Pawlowski A. 2012. Sewage sludge-to-energy approaches based on anaerobic digestion and pyrolysis: Brief overview and energy efficiency assessment. Renewable & Sustainable Energy Reviews 16(3):1657-1665.

Caporaso JG, Bittinger K, Bushman FD, DeSantis TZ, Andersen GL, Knight R. 2010a. PyNAST: a flexible tool for aligning sequences to a template alignment. Bioinformatics 26(2):266-267.

Caporaso JG, Kuczynski J, Stombaugh J, Bittinger K, Bushman FD, Costello EK, Fierer N, Pena AG, Goodrich JK, Gordon JI and others. 2010b. QIIME allows analysis of high-throughput community sequencing data. Nature Methods 7(5):335-336.

Caporaso JG, Lauber CL, Walters WA, Berg-Lyons D, Huntley J, Fierer N, Owens SM, Betley J, Fraser L, Bauer M and others. 2012. Ultra-high-throughput microbial community analysis on the Illumina HiSeq and MiSeq platforms. Isme Journal 6(8):1621-1624.

CDM Smith. 2000. Cruise ship wastewater study.

Chen J-y, Li N, Zhao L. 2014. Three-dimensional electrode microbial fuel cell for hydrogen peroxide synthesis coupled to wastewater treatment. Journal of Power Sources 254:316-322.

Chen J-Y, Zhao L, Li N, Liu H. 2015. A microbial fuel cell with the three-dimensional electrode applied an external voltage for synthesis of hydrogen peroxide from organic matter. Journal of Power Sources 287:291-296.

Chen J. 2013. Recent Progress in Advanced Materials for Lithium Ion Batteries. Materials 6(1):156-183.

Cho SK, Shin HS, Kim DH. 2012. Waste activated sludge hydrolysis during ultrasonication: Two-step disintegration. Bioresource Technology 121:480-483.

Cokgor EU, Oktay S, Tas DO, Zengin GE, Orhon D. 2009. Influence of pH and temperature on soluble substrate generation with primary sludge fermentation. Bioresource Technology 100(1):380-386.

Cole JR, Wang Q, Cardenas E, Fish J, Chai B, Farris RJ, Kulam-Syed-Mohideen AS, McGarrell DM, Marsh T, Garrity GM and others. 2009. The Ribosomal Database Project: improved alignments and new tools for rRNA analysis. Nucleic Acids Research 37:D141-D145.

CONTECH. 2014. Wastewater Solutions. Contech Engineering Solutions LLC. USA: 1-4.

Couper AM, Pletcher D, Walsh FC. 1990. Electrode materials for electrosynthesis. Chemical Reviews 90(5):837-865.

de Graaff MS. 2010. Resource recovery from black water. Wageningen University.

DeSantis TZ, Hugenholtz P, Larsen N, Rojas M, Brodie EL, Keller K, Huber T, Dalevi D, Hu P, Andersen GL. 2006. Greengenes, a chimera-checked 16S rRNA gene database and workbench compatible with ARB. Applied and Environmental Microbiology 72(7):5069-5072.

Ditzig J, Liu H, Logan BE. 2007. Production of hydrogen from domestic wastewater using a bioelectrochemically assisted microbial reactor (BEAMR). International Journal of Hydrogen Energy 32(13):2296-2304.

Drogui P, Elmaleh S, Rumeau M, Bernard C, Rambaud A. 2001. Oxidising and disinfecting by hydrogen peroxide produced in a two-electrode cell. Water Res 35:3235-3241.

Edgar RC. 2010. Search and clustering orders of magnitude faster than BLAST. Bioinformatics 26(19):2460-2461.

Elbeshbishy E, Nakhla G, Hafez H. 2012. Biochemical methane potential (BMP) of food waste and primary sludge: Influence of inoculum pre-incubation and inoculum source. Bioresource Technology 110:18-25.

Elimitwalli T. 2006. Treatment of concentrated black-water and kitchen organic-wastes in accumulation systems. Tenth International Water Technology Conference, IWTC10 Alexandria, Egypt.

Eskicioglu C, Kennedy KJ, Droste RL. 2006. Characterization of soluble organic matter of waste activated sludge before and after thermal pretreatment. Water Research 40(20):3725-3736.

Estevez-Canales M, Kuzume A, Borjas Z, Füeg M, Lovley D, Wandlowski T, Esteve-Núñez A. 2015. A severe reduction in the cytochrome C content of Geobacter sulfurreducens eliminates its capacity for extracellular electron transfer. Environmental microbiology reports 7:219-226.

Eul W, Moeller A, Steiner N. 2001. Hydrogen peroxide. Kirk-Othmer encyclopedia of chemical technology

Ferreiro N, Soto M. 2003. Anaerobic hydrolysis of primary sludge: influence of sludge concentration and temperature. Water Science and Technology 47(12):239-246.

Foley JM, Rozendal RA, Hertle CK, Lant PA, Rabaey K. 2010. Life Cycle Assessment of High-Rate Anaerobic Treatment, Microbial Fuel Cells, and Microbial Electrolysis Cells. Environ Sci Technol 44:3629-3637.

Foller P, Bombard R. 1995. Processes for the production of mixtures of caustic soda and hydrogen peroxide via the reduction of oxygen. J Appl Electrochem 25:613-627.

Fornero JJ, Rosenbaum M, Angenent LT. 2010. Electric Power Generation from Municipal, Food, and Animal Wastewaters Using Microbial Fuel Cells. Electroanalysis 22(7-8):832-843.

Fornero JJ, Rosenbaum M, Cotta MA, Angenent LT. 2010. Carbon Dioxide Addition to Microbial Fuel Cell Cathodes Maintains Sustainable Catholyte pH and Improves Anolyte pH, Alkalinity, and Conductivity. Environmental Science & Technology 44(7):2728-2734.

Franks AE, Nevin KP, Jia H, Izallalen M, Woodard TL, Lovley DR. 2009. Novel strategy for three-dimensional real-time imaging of microbial fuel cell communities: monitoring the inhibitory effects of proton accumulation within the anode biofilm. Energy & Environmental Science 2:113-119.

Friedman ES, Rosenbaum MA, Lee AW, Lipson DA, Land BR, Angenent LT. 2012. A cost-effective and field-ready potentiostat that poises subsurface electrodes to monitor bacterial respiration. Biosensors and Bioelectronics 32(1):309-313.

Fu L, You S, Yang F, Gao M, Fang X, Zhang G. 2010. Synthesis of hydrogen peroxide in microbial fuel cell. Journal of Chemical Technology & Biotechnology 85:715-719.

Ge Z, Zhang F, Grimaud J, Hurst J, He Z. 2013. Long-term investigation of microbial fuel cells treating primary sludge or digested sludge. Bioresource Technology 136:509-514.

Gerges H, Wahlberg E, Block T. 1999. Evaluation of primary sedimentation tanks performance by integrating mathematical modeling with field testing. WEFTEC, Federation, W. E., Ed. WEF: New Orleans.

Ghosh S, Buoy K, Dressel L, Miller T, Wilcox G, Loos D. 1995. Pilot-scale and full-scale 2-phase anaerobic-digestion of municipal sludge. Water Environment Research 67(2):206-214.

Ghosh S. 1987. Improved sludge gasifcation by two-phase anaerobic digestion. J Environ Eng 113:1265–1284.

Ghyoot W, Verstraete W. 1997. Anaerobic digestion of primary sludge from chemical pre-precipitation. Water Science and Technology 36(6-7):357-365.

Gnoth S, Kuprijanov A, Simutis R, Lübbert A. 2009. Simple adaptive pH control using gain-scheduling methods. Applied Microbiology and Biotechnology 85: 955-964.

Goedkoop M, Heijungs R, Huijbregts M, De Schryver A, Struijs J, van Zelm R. 2008. A life cycle impact assessment method which comprises harmonised category indicators at the midpoint and the endpoint level. Netherlands, Ruimte En Milieu Ministerie can Volkshuivesting, Ruimtelijke Ordening en Milieubeheer.

Goor G, Glenneberg J, Jacobi S. 2000. Hydrogen Peroxide. Ullmann's Encyclopedia of Industrial Chemistry. Weinheim, Germany:Wiley-VCH. p 393-427.

Graf E, Penniston JT. 1980. Method for determination of hydrogen peroxide, with its application illustrated by glucose assay. Clin Chem 26:658-660.

Grassi E, Tsakalis KS. 2000. PID controller tuning by frequency loop-shaping: application to diffusion furnace temperature control. IEEE Transactions on Control Systems Technology 8(5):842-847.

Güler E. 2014. Anion exchange membrane design for reverse electrodialysis. Enschede: Universiteit Twente DOI: 10.3990/1.9789036535700.

Gustafsson TK, Waller KV. 1983. Dynamic modeling and reaction invariant control of pH. Chemical Engineering Science 38(3):389-398.

Harnisch F, Schroeder U. 2010. From MFC to MXC: chemical and biological cathodes and their potential for microbial bioelectrochemical systems. Chemical Society Reviews 39(11):4433-4448.

Hart PW, Rudie AW. 2014. Anthraquinone-A review of the rise and fall of a pulping catalyst. Tappi Journal 13:23-31.

Heidrich ES, Dolfing J, Scott K, Edwards SR, Jones C, Curtis TP. 2013. Production of hydrogen from domestic wastewater in a pilot-scale microbial electrolysis cell. Applied Microbiology and Biotechnology 97(15):6979-6989.

Henson MA, Seborg DE. 1994. Adaptive nonlinear control of a pH neutralization process. IEEE transactions on control systems technology 2(3): 169-182.

Henze M. 2000. Activated sludge models ASM1, ASM2, ASM2d and ASM3. IWA publishing.

Hoskins DL, Zhang X, Hickner MA, Logan BE. 2014. Spray-on polyvinyl alcohol separators and impact on power production in air-cathode microbial fuel cells with different solution conductivities. Bioresource Technology 172:156-161.

Hu H, Fan Y, Liu H. 2009. Hydrogen production in single-chamber tubular microbial electrolysis cells using non-precious-metal catalysts. International Journal of Hydrogen Energy 34(20):8535-8542.

Hu H, Fan Y, Liu H. 2010. Optimization of NiMo catalyst for hydrogen production in microbial electrolysis cells. International Journal of Hydrogen Energy 35(8):3227-3233.

Jayasinghe N, Franks A, Nevin KP, Mahadevan R. 2014. Metabolic modeling of spatial heterogeneity of biofilms in microbial fuel cells reveals substrate limitations in electrical current generation. Biotechnology Journal 9:1350-1361.

Jeremiasse AW, Hamelers HVM, Saakes M, Buisman CJN. 2010. Ni foam cathode enables high volumetric H(2) production in a microbial electrolysis cell. International Journal of Hydrogen Energy 35(23):12716-12723.

Jia J, Tang Y, Liu B, Wu D, Ren N, Xing D. 2013. Electricity generation from food wastes and microbial community structure in microbial fuel cells. Bioresource Technology 144:94-99.

Jones R, Parker W, Khan Z, Murthy S, Rupke M. 2008. Characterization of sludges for predicting anaerobic digester performance. Water Science and Technology 57(5):721-726.

Joshi R, Tsakalis K, MacArthur J, Dash S. 2014. Account for uncertainty with robust control design: Part 1. Chemical Engineering Progress 110(11):31-38.

Joshi R, Tsakalis K, MacArthur J, Dash S. 2014. Account for uncertainty with robust control design: Part 2. Chemical Engineering Progress 110(12):46-50.

Kato S, Hashimoto K, Watanabe K. 2013. Iron-oxide minerals affect extracellular electron-transfer paths of Geobacter spp. Microbes and Environments 28:141-148.

Ki D, Parameswaran P, Popat SC, Rittmann BE, Torres CI. 2015. Effects of pre-fermentation and pulsed-electric-field treatment of primary sludge in microbial electrochemical cells. Bioresour Technol 195:83-88.

Ki D, Parameswaran P, Rittmann BE, Torres CI. 2015. Effect of pulsed electric field (PEF) pretreatment on primary sludge for enhanced bioavailability and energy capture. Environmental Engineering Science 32(10): 831-837.

Ki D, Popat SC, Torres CI. 2016. Reduced overpotentials in microbial electrolysis cells through improved design, operation, and electrochemical characterization. Chem Eng J 287:181-188.

Ki D, Parameswaran P, Popat SC, Rittmann BE, Torres CI. 2017. Maximizing Coulombic recovery from primary sludge by changing retention time and pH in a flat-plate microbial electrolysis cell. Environmental Science: Water Research and Technology 3:333-339.

Ki D, Popat SC, Rittmann BE, Torres CI. 2017. H2O2 production in microbial electrochemical cells fed with primary sludge. Environ Sci Technol 51(11):6139–6145.

Kiely PD, Rader G, Regan JM, Logan BE. 2011. Long-term cathode performance and the microbial communities that develop in microbial fuel cells fed different fermentation endproducts. Bioresource Technology 102(1):361-366.

Kim J, Park C, Kim TH, Lee M, Kim S, Kim SW, Lee J. 2003. Effects of various pretreatments for enhanced anaerobic digestion with waste activated sludge. Journal of Bioscience and Bioengineering 95(3):271-275.

Kim KK, Jin L, Yang HC, Lee S-T. 2007. Halomonas gomseomensis sp nov, Halomonas janggokensis sp nov, Halomonas salaria sp nov and Halomonas denitrificans sp nov, moderately halophilic bacteria isolated from saline water. International Journal of Systematic and Evolutionary Microbiology 57:675-681.

Korth B, Rosa LF, Harnisch F, Picioreanu C. 2015. A framework for modeling electroactive microbial biofilms performing direct electron transfer. Bioelectrochemistry 106:194-206.

Krstajic NV, Gajic-Krstajic L, Lacnjevac U, Jovic BM, Mora S, Jovic VD. 2011. Non-noble metal composite cathodes for hydrogen evolution. Part I: The Ni-MoOx coatings electrodeposited from Watt's type bath containing MoO3 powder particles. International Journal of Hydrogen Energy 36(11):6441-6449.

Laspidou C, Rittmann B. 2002. Non-steady state modeling of extracellular polymeric substances, soluble microbial products, and active and inert biomass. Water Res 36:1983-1992.

Laspidou C, Rittmann B. 2002. A unified theory for extracellular polymeric substances, soluble microbial products, and active and inert biomass. Water Res 36:2711-2720.

Lee H-S, Parameswaran P, Kato-Marcus A, Torres CI, Rittmann BE. 2008. Evaluation of energy-conversion efficiencies in microbial fuel cells (MFCs) utilizing fermentable and non-fermentable substrates. Water Research 42(6-7):1501-1510.

Lee H-S, Torres CI, Parameswaran P, Rittmann BE. 2009. Fate of H-2 in an Upflow Single-Chamber Microbial Electrolysis Cell Using a Metal-Catalyst-Free Cathode. Environmental Science & Technology 43(20): 7971–7976.

Lee H-S, Torres CI, Rittmann BE. 2009. Effects of Substrate Diffusion and Anode Potential on Kinetic Parameters for Anode-Respiring Bacteria. Environmental Science & Technology 43(19): 7571–7577.

Lee H-S, Rittmann BE. 2010. Characterization of energy losses in an upflow single-chamber microbial electrolysis cell. International Journal of Hydrogen Energy 35(3):920-927.

Lee H-S, Vermaas WFJ, Rittmann BE. 2010. Biological hydrogen production: prospects and challenges. Trends in Biotechnology 28(5):262-271.

Lee HH, Park A, Oloman C. 2000. Stability of hydrogen peroxide in sodium carbonate solutions. TAPPI J 83:94-101.

Lee IS, Parameswaran P, Alder JM, Rittmann BE. 2010. Feasibility of Focused-Pulsed Treated Waste Activated Sludge as a Supplemental Electron Donor for Denitrification. Water Environment Research 82(12):2316-2324.

Lee IS, Rittmann BE. 2011. Effect of low solids retention time and focused pulsed pre-treatment on anaerobic digestion of waste activated sludge. Bioresource Technology 102(3):2542-2548.

Lerke T, Riggs S, Castle H. 2010. Demonstration of advanced oxidation treatment of shipboard blackwater and graywater. ESTCP report WP-200802.

Li N, An J, Zhou L, Li T, Li J, Feng C, Wang X. 2016. A novel carbon black graphite hybrid air-cathode for efficient hydrogen peroxide production in bioelectrochemical systems. J Power Sources 306:495-502.

Liu H, Logan BE. 2004. Electricity generation using an air-cathode single chamber microbial fuel cell in the presence and absence of a proton exchange membrane. Environmental Science & Technology 38(14):4040-4046.

Liu H, Ramnarayanan R, Logan BE. 2004. Production of electricity during wastewater treatment using a single chamber microbial fuel cell. Environmental Science & Technology 38(7):2281-2285.

Liu H, Cheng SA, Logan BE. 2005. Production of electricity from acetate or butyrate using a single-chamber microbial fuel cell. Environmental Science & Technology 39(2):658-662.

Liu J, Zhang F, He W, Yang L, Feng Y, Logan BE. 2014. A microbial fluidized electrode electrolysis cell (MFEEC) for enhanced hydrogen production. Journal of Power Sources 271:530-533.

Logan BE, Hamelers B, Rozendal RA, Schrorder U, Keller J, Freguia S, Aelterman P, Verstraete W, Rabaey K. 2006. Microbial fuel cells: Methodology and technology. Environmental Science & Technology 40(17):5181-5192.

Lusk BG, Khan QF, Parameswaran P, Hameed A, Ali N, Rittmann BE, Torres CI. 2015. Characterization of Electrical Current-Generation Capabilities from Thermophilic Bacterium Thermoanaerobacter pseudethanolicus Using Xylose, Glucose, Cellobiose, or Acetate with Fixed Anode Potentials. Environmental Science & Technology 49(24):14725-14731.

Lusk BG, Parameswaran P, Popat SC, Rittmann BE, Torres CI. 2016. The effect of pH and buffer concentration on anode biofilms of Thermincola ferriacetica. Bioelectrochemistry 112:47-52.

Lusk BG, Colin A, Parameswaran P, Rittmann BE, Torres CI. 2017. Simultaneous fermentation of cellulose and current production with an enriched mixed culture of thermophilic bacteria in a microbial electrolysis cell. Microb Biotechnol. doi: 10.1111/1751-7915.12733.

Mahmoud M, Parameswaran P, Torres CI, Rittmann BE. 2014. Fermentation pre-treatment of landfill leachate for enhanced electron recovery in a microbial electrolysis cell. Bioresource Technology 151:151-158.

Malvankar NS, Vargas M, Nevin KP, Franks AE, Leang C, Kim B-C, Inoue K, Mester T, Covalla SF, Johnson JP and others. 2011. Tunable metallic-like conductivity in microbial nanowire networks. Nature Nanotechnology 6(9):573-579.

Marcus AK, Torres CI, Rittmann BE. 2007. Conduction-based modeling of the biofilm anode of a microbial fuel cell. Biotechnol Bioeng 98:1171-1182.

Marcus AK, Torres CI, Rittmann BE. 2010. Evaluating the impacts of migration in the biofilm anode using the model PCBIOFILM. Electrochim Acta 55:6964-6972.

Marcus AK, Torres CI, Rittmann BE. 2011. Analysis of a microbial electrochemical cell using the proton condition in biofilm (PCBIOFILM) model. Bioresour Technol 102:253-262.

McAvoy TJ, Hsu E, Lowenthal S. 1972. Dynamics of pH in Controlled Stirred Tank Reactor. Industrial & Engineering Chemistry Process Design and Development 11(1):68-70.

McCarty PL, Smith DP. 1986. Anaerobic wastewater treatment. Environmental Science & Technology 20(12):1200-1206.

McCarty PL, Bae J, Kim J. 2011. Domestic Wastewater Treatment as a Net Energy Producer-Can This be Achieved? Environmental Science & Technology 45(17):7100-7106.

Metcalf & Eddy I. 2014. Wastewater Engineering: Treatment and Reuse.

Miceli JF, III, Parameswaran P, Kang D-W, Krajmalnik-Brown R, Torres CI. 2012. Enrichment and Analysis of Anode-Respiring Bacteria from Diverse Anaerobic Inocula. Environmental Science & Technology 46(18):10349-10355.

Miceli III JF, Garcia-Peña I, Parameswaran P, Torres CI, Krajmalnik-Brown R. 2014. Combining microbial cultures for efficient production of electricity from butyrate in a microbial electrochemical cell. Bioresour Technol 169:169-174.

Miron Y, Zeeman G, Van Lier JB, Lettinga G. 2000. The role of sludge retention time in the hydrolysis and acidification of lipids, carbohydrates and proteins during digestion of primary sludge in CSTR systems. Water Research 34(5):1705-1713.

Modin O, Fukushi K. 2012. Development and testing of bioelectrochemical reactors converting wastewater organics into hydrogen peroxide. Water Science and Technology 66:831-836.

Modin O, Fukushi K. 2013. Production of high concentrations of H2O2 in a bioelectrochemical reactor fed with real municipal wastewater. Environ Technol 34:2737-2742.

Nam J-Y, Logan BE. 2012. Optimization of catholyte concentration and anolyte pHs in two chamber microbial electrolysis cells. International Journal of Hydrogen Energy 37(24):18622-18628.

National Energy Technology Laboratory and U.S. Department of Energy. 2004. Fuel Cell Handbook. University Press of the Pacific.

Ni B, Zeng RJ, Fang F, Xie W, Sheng G, Yu H. 2010. Fractionating soluble microbial products in the activated sludge process. Water Res 44:2292-2302.

Nicoll W, Smith A. 1955. Stability of dilute alkaline solutions of hydrogen peroxide. Industrial & Engineering Chemistry 47:2548-2554.

Noblis. 2010. Sustainable Forward Operating Bases, Strategic Environmental research and Development Program (SERDP).

Noguera DR, Araki N, Rittmann BE. 1994. Soluble microbial products (SMP) in anaerobic chemostats. Biotechnol Bioeng 44:1040-1047.

Nopens I, Batstone DJ, Copp JB, Jeppsson U, Volcke E, Alex J, Vanrolleghem PA. 2009. An ASM/ADM model interface for dynamic plant-wide simulation. Water Res 43:1913-1923.

Oarga A. 2013. Blackwater treatment at tourist facilities. University of Nova Gorica Graduate School.

Oh SE, Logan BE. 2005. Hydrogen and electricity production from a food processing wastewater using fermentation and microbial fuel cell technologies. Water Research 39(19):4673-4682.

Otsuka K, Yamanaka I. 1990. One step synthesis of hydrogen peroxide through fuel cell reaction. Electrochim Acta 35:319-322.

Owen WF, Stuckey DC, Healy JB, Young LY, McCarty PL. 1979. Bioassay for monitoring biochemical methane potential and anaerobic toxicity. Water Research 13(6):485-492.

Palmquist H, Hanaeus J. 2005. Hazardous substances in separately collected grey- and black-water from ordinary Swedish households. Sci Total Environ 348: 151-163.

Pandiaraj M, Benjamin AR, Madasamy T, Vairamani K, Arya A, Sethy NK, Bhargava K, Karunakaran C. 2014. A cost-effective volume miniaturized and microcontroller based cytochrome c assay. Sensors and Actuators 220: 290-297.

Pant D, Van Bogaert G, Diels L, Vanbroekhoven K. 2010. A review of the substrates used in microbial fuel cells (MFCs) for sustainable energy production. Bioresource Technology 101(6):1533-1543.

Pant D, Singh A, Van Bogaert G, Gallego YA, Diels L, Vanbroekhoven K. 2011. An introduction to the life cycle assessment (LCA) of bioelectrochemical systems (BES) for sustainable energy and product generation: Relevance and key aspects. Renew Sust Energ Rev 15(2): 1305-1313.

Parameswaran P, Torres CI, Lee HS, Krajmalnik-Brown R, Rittmann BE. 2009. Syntrophic Interactions Among Anode Respiring Bacteria (ARB) and Non-ARB in a Biofilm Anode: Electron Balances. Biotechnology and Bioengineering 103(3):513-523.

Parameswaran P, Zhang H, Torres CI, Rittmann BE, Krajmalnik-Brown R. 2010. Microbial Community Structure in a Biofilm Anode Fed With a Fermentable Substrate: The Significance of Hydrogen Scavengers. Biotechnology and Bioengineering 105(1):69-78.

Parameswaran P, Torres CI, Lee H, Rittmann BE, Krajmalnik-Brown R. 2011. Hydrogen consumption in microbial electrochemical systems (MXCs): the role of homo-acetogenic bacteria. Bioresour Technol 102:263-271.

Parameswaran P, Torres CI, Dae-Wook Kang, Rittmann BE, Krajmalnik-Brown R. 2012. The role of homoacetogenic bacteria as efficient hydrogen scavengers in microbial electrochemical cells (MXCs). Water Science & Technology 65:1-6.

Park B, Ahn JH, Kim J, Hwang S. 2004. Use of microwave pretreatment for enhanced anaerobiosis of secondary sludge. Water Science and Technology 50(9):17-23.

Park S, Bae W, Chung J, Baek S. 2007. Empirical model of the pH dependence of the maximum specific nitrification rate. Process Biochemistry 42:1671-1676.

Paulus U, Schmidt T, Gasteiger H, Behm R. 2001. Oxygen reduction on a high-surface area Pt/Vulcan carbon catalyst: a thin-film rotating ring-disk electrode study. J Electroanal Chem 495:134-145.

Pavlostathis SG, Giraldogomez E. 1991. Kinetics of anaerobic treatment - a critical-review. Critical Reviews in Environmental Control 21(5-6):411-490.

Peymani E, Fatehi A, Bashivan P, Sedigh AK. 2008. An experimental comparison of adaptive controllers on a ph neutralization pilot plant. INDICON, INDIA.

Pham TH, Rabaey K, Aelterman P, Clauwaert P, De Schamphelaire L, Boon N, Verstraete W. 2006. Microbial fuel cells in relation to conventional anaerobic digestion technology. Engineering in Life Sciences 6(3):285-292.

Pilli S, Bhunia P, Yan S, LeBlanc RJ, Tyagi RD, Surampalli RY. 2011. Ultrasonic pretreatment of sludge: A review. Ultrasonics Sonochemistry 18(1):1-18.

Pinto RP, Srinivasan B, Manuel M-, Tartakovsky B. 2010. A two-population bio-electrochemical model of a microbial fuel cell. Bioresour Technol 101:5256-5265.

Pinto R, Srinivasan B, Escapa A, Tartakovsky B. 2011. Multi-population model of a microbial electrolysis cell. Environ Sci Technol 45:5039-5046.

Pirbadian S, El-Naggar MY. 2012. Multistep hopping and extracellular charge transfer in microbial redox chains. Physical Chemistry Chemical Physics 14(40):13802-13808.

Popat SC, Ki D, Rittmann BE, Torres CI. 2012. Importance of OH- Transport from Cathodes in Microbial Fuel Cells. ChemSusChem 5:1071-1079.

Popat SC, Ki D, Young MN, Rittmann BE, Torres CI. 2014. Buffer pKa and Transport Govern the Concentration Overpotential in Electrochemical Oxygen Reduction at Neutral pH. ChemElectroChem 1:1909-1915.

Popat SC, Torres CI. 2016. Critical transport rates that limit the performance of microbial electrochemistry technologies. Bioresour Technol 215:265-273.

Pratt S, Liew D, Batstone DJ, Werker AG, Morgan-Sagastume F, Lant PA. 2012. Inhibition by fatty acids during fermentation of pre-treated waste activated sludge. Journal of Biotechnology 159(1-2):38-43.

Qiang Z, Chang J, Huang C. 2002. Electrochemical generation of hydrogen peroxide from dissolved oxygen in acidic solutions. Water Res 36:85-94.

Rabaey K, Rozendal RA. 2010. Microbial electrosynthesis - revisiting the electrical route for microbial production. Nature Reviews Microbiology 8(10):706-716.

Rajala-Mustonen RL, Heinonen-Tanski H. 1995. Effect of advanced oxidation processes on inactivation of coliphages. Water Science and Technology 31:131-134.

Raposo F, Banks CJ, Siegert I, Heaven S, Borja R. 2006. Influence of inoculum to substrate ratio on the biochemical methane potential of maize in batch tests. Process Biochemistry 41(6):1444-1450.

Rawlings JB, Mayne DQ. 2009. Model Predictive Control: Theory and Design. Nob Hill Publishing, Madison, WI, ISBN 978-0-9759377-0-9.

Ren H, Torres CI, Parameswaran P, Rittmann BE, Chae J. 2014. Improved current and power density with a micro-scale microbial fuel cell due to a small characteristic length. Biosensors & Bioelectronics 61:587-592.

Rismani-Yazdi H, Carver SM, Christy AD, Yu Z, Bibby K, Peccia J, Tuovinen OH. 2013. Suppression of methanogenesis in cellulose-fed microbial fuel cells in relation to performance, metabolite formation, and microbial population. Bioresource Technology 129:281-288.

Ristow NE, Sotemann SW, Wentzel MC, Loewenthal RE, Ekama GA. 2006. The effects of hydraulic retention time and feed COD concentration on the rate of hydrolysis of primary sewage sludge under methanogenic conditions. Water Science and Technology 54(5):91-100.

Rittmann BE, McCarty PL. 2001. Environmental Biotechnology: Principles and Applications. New York: McGraw-Hill.

Rittmann BE, Krajmalnik-Brown R, Halden RU. 2008. Pre-genomic, genomic and postgenomic study of microbial communities involved in bioenergy. Nature Reviews Microbiology 6:604-612.

Rittmann BE, Lee HS, Zhang HS, Alder J, Banaszak JE, Lopez R. 2008. Full-scale application of focused-pulsed pre-treatment for improving biosolids digestion and conversion to methane. Water Science and Technology 58(10):1895-1901.

Rittmann BE, Torres CI, Marcus AK. 2008. Understanding the Distinguishing Features of a Microbial Fuel Cell as a Biomass-Based Renewable Energy Technology. Emerging Environmental Technologies:1-28.

Rivera DE, Morari M, Skogestad S. 1986. Internal model control: PID controller design. Industrial & Engineering Chemistry Process Design and Development 25(1): 252-265.

Rozendal RA, Hamelers HVM, Euverink GJW, Metz SJ, Buisman CJN. 2006. Principle and perspectives of hydrogen production through biocatalyzed electrolysis. International Journal of Hydrogen Energy 31(12):1632-1640.

Rozendal RA, Hamelers HVM, Rabaey K, Keller J, Buisman CJN. 2008. Towards practical implementation of bioelectrochemical wastewater treatment. Trends in Biotechnology 26(8):450-459.

Rozendal RA, Sleutels THJA, Hamelers HVM, Buisman CJN. 2008. Effect of the type of ion exchange membrane on performance, ion transport, and pH in biocatalyzed electrolysis of wastewater. Water Science and Technology 57(11):1757-1762.

Rozendal RA, Leone E, Keller J, Rabaey K. 2009. Efficient hydrogen peroxide generation from organic matter in a bioelectrochemical system. Electrochem Commun 11:1752-1755.

Rulkens W. 2008. Sewage sludge as a biomass resource for the production of energy: Overview and assessment of the various options. Energy & Fuels 22(1):9-15.

Salerno MB, Lee HS, Parameswaran P, Rittmann BE. 2009. Using a Pulsed Electric Field as a Pretreatment for Improved Biosolids Digestion and Methanogenesis. Water Environment Research 81(8):831-839.

Schleheck D, Weiss M, Pitluck S, Bruce D, Land ML, Han S, Saunders E, Tapia R, Detter C, Brettin T and others. 2011. Complete genome sequence of Parvibaculum lavamentivorans type strain (DS-1(T)). Standards in Genomic Sciences 5(3):298-310.

Sedaqatvand R, Esfahany MN, Behzad T, Mohseni M, Mardanpoura MM. 2013. Parameter estimation and characterization of a single-chamber microbial fuel cell for dairy wastewater treatment. Bioresource Technology 146:247–253.

Selembo PA, Merrill MD, Logan BE. 2010. Hydrogen production with nickel powder cathode catalysts in microbial electrolysis cells. International Journal of Hydrogen Energy 35(2):428-437.

Sheng J, Vannela R, Rittmann BE. 2011. Evaluation of Cell-Disruption Effects of Pulsed-Electric-Field Treatment of Synechocystis PCC 6803. Environmental Science & Technology 45(8):3795-3802.

Shi L, Dong H, Reguera G, Beyenal H, Lu A, Liu J. 2016. Extracellular electron transfer mechanisms between microorganisms and minerals. Nature Reviews Microbiology 14(10):651-662.

Sim J, An J, Elbeshbishy E, Ryu H, Lee H. 2015. Characterization and optimization of cathodic conditions for H2O2 synthesis in microbial electrochemical cells. Bioresour Technol 195:31-36.

Sleutels THJA, Hamelers HVM, Rozendal RA, Buisman CJN. 2009. Ion transport resistance in Microbial Electrolysis Cells with anion and cation exchange membranes. International Journal of Hydrogen Energy 34(9):3612-3620.

Sleutels THJA, Lodder R, Hamelers HVM, Buisman CJN. 2009. Improved performance of porous bio-anodes in microbial electrolysis cells by enhancing mass and charge transport. International Journal of Hydrogen Energy 34(24):9655-9661.

Sleutels THJA, Ter Heijne A, Buisman CJN, Hamelers HVM. 2013. Steady-state performance and chemical efficiency of Microbial Electrolysis Cells. International Journal of Hydrogen Energy 38(18):7201-7208.

Snoeyink VL, Jenkins D. 1980. Water Chemistry. New York:John Wiley & Sons, Inc.

Snyder S, Lei H, Wert E, Westerhoff P, Yoon Y. 2008. Removal of EDCs and Pharmaceuticals in Drinking Water. Water Environment Research Foundation.

Sorokin DY, Tourova TP, Mussmann M, Muyzer G. 2008. Dethiobacter alkaliphilus gen. nov sp nov., and Desulfurivibrio alkaliphilus gen. nov sp nov.: two novel representatives of reductive sulfur cycle from soda lakes. Extremophiles 12(3):431-439.

Sun D, Call DF, Kiely PD, Wang A, Logan BE. 2012. Syntrophic interactions improve power production in formic acid fed MFCs operated with set anode potentials or fixed resistances. Biotechnology and Bioengineering 109(2):405-414.

Tartakousky B, Mehta P, Santoyo G, Guiot SR. 2011. Maximizing hydrogen production in a microbial electrolysis cell by real-time optimization of applied voltage. International Journal of Hydrogen Energy 36(17):10557-10564.

Tchobanoglous G, Burton FL, Stensel HD. 2003. Wastewater engineering: Treatment and Reuse. Eddy M, editor. Boston: McGraw-Hill.

Torres CI. SERDP Project ER-2239: Wastewater Treatment Using Microbial Fuel Cells with Peroxide Production.

Torres CI, Kato Marcus A, Rittmann BE. 2007. Kinetics of consumption of fermentation products by anode-respiring bacteria. Applied Microbiology and Biotechnology 77(3): 689-697.

Torres CI, Marcus AK, Parameswaran P, Rittmann BE. 2008. Kinetic experiments for evaluating the Nernst− Monod model for anode-respiring bacteria (ARB) in a biofilm anode. Environ Sci Technol 42:6593-6597.

Torres CI, Kato Marcus A, Rittmann BE. 2008. Proton transport inside the biofilm limits electrical current generation by anode-respiring bacteria. Biotechnol Bioeng 100:872-881.

Torres CI, Lee HS, Rittmann BE. 2008. Carbonate Species as OH- Carriers for Decreasing the pH Gradient between Cathode and Anode in Biological Fuel Cells. Environmental Science & Technology 42(23):8773-8777.

Torres CI, Krajmalnik-Brown R, Parameswaran P, Marcus AK, Wanger G, Gorby YA, Rittmann BE. 2009. Selecting Anode-Respiring Bacteria Based on Anode Potential: Phylogenetic, Electrochemical, and Microscopic Characterization. Environmental Science & Technology 43(24): 9519-9524.

Torres CI, Marcus AK, Lee H, Parameswaran P, Krajmalnik-Brown R, Rittmann BE. 2010. A kinetic perspective on extracellular electron transfer by anode-respiring bacteria. FEMS Microbiol Rev 34:3-17.

Torres CI. 2014. On the importance of identifying, characterizing, and predicting fundamental phenomena towards microbial electrochemistry applications. Curr Opin Biotechnol 27:107-114.

Tsakalis KS, Dash S. 2007. Multivariable controller performance monitoring using robust stability conditions. Journal of Process Control 17(9): 702-714.

Tsakalis KS, Dash S. 2013. Approximate H infty loop shaping in pid parameter adaptation. International Journal of Adaptive Control and Signal Processing 27(1-2):1099-1115.

Ursua A, Gandia LM, Sanchis P. 2012. Hydrogen Production From Water Electrolysis: Current Status and Future Trends. Proceedings of the IEEE 100(2):410-426.

US EPA Handbook. 1984. Septage treatment and disposal. EPA-625/6-84-009.

US EPA. 2000. Guide to field storage of biosolids, EPA/832-B-00-007.

US EPA. 2003. Environmental Regulations and Technology: Control of Pathogens and Vector Attraction in Sewage Sludge, EPA/625-R-92-013.

VanBriesen J, Rittmann B. 1999. Modeling speciation effects on biodegradation in mixed metal/chelate systems. Biodegradation 10:315-330.

Veeken A, Kalyuzhnyi S, Scharff H, Hamelers B. 2000. Effect of pH and VFA on hydrolysis of organic solid waste. Journal of Environmental Engineering-Asce 126(12):1076-1081.

Vologni V, Kakarla R, Angelidaki I, Min B. 2013. Increased power generation from primary sludge by a submersible microbial fuel cell and optimum operational conditions. Bioprocess and Biosystems Engineering 36(5):635-642.

Vyas PV, Shah BG, Trivedi GS, Ray P, Adhikary SK, Rangarajan R. 2001. Characterization of heterogeneous anion-exchange membrane. Journal of Membrane Science 187(1-2):39-46.

Wang Y, Chen KS, Mishler J, Cho SC, Adroher XC. 2011. A review of polymer electrolyte membrane fuel cells: Technology, applications, and needs on fundamental research. Applied Energy 88(4):981-1007.

Wang Z, Lee T, Lim B, Choi C, Park J. 2014. Microbial community structures differentiated in a single-chamber air-cathode microbial fuel cell fueled with rice straw hydrolysate. Biotechnology for Biofuels 7.

Wendland C, Deegener S, Behrendt J, Toshev P, Otterpohl R. 2007. Anaerobic digestion of blackwater from vacuum toilets and kitchen refuse in a continuous stirred tank reactor (CSTR). Water Sci Technol 55 (7):187-194.

Wendland C. 2008. Anaerobic digestion of blackwater and kitchen refuse. Technical University of Hamburg-Harburg.

Xiao B, Han Y, Liu X, Liu J. 2014. Relationship of methane and electricity production in two-chamber microbial fuel cell using sewage sludge as substrate. International Journal of Hydrogen Energy 39(29):16419-16425.

Xie W, Ni B, Seviour T, Sheng G, Yu H. 2012. Characterization of autotrophic and heterotrophic soluble microbial product (SMP) fractions from activated sludge. Water Res 46:6210-6217.

Yamada N, Yaguchi T, Otsuka H, Sudoh M. 1999. Development of Trickle-Bed Electrolyzer for On-Site Electrochemical Production of Hydrogen Peroxide. J Electrochem Soc 146:2587-2591.

Yamanaka I, Onizawa T, Takenaka S, Otsuka K. 2003. Direct and Continuous Production of Hydrogen Peroxide with 93 % Selectivity Using a Fuel-Cell System. Angewandte Chemie International Edition 42:3653-3655.

Yang W, Zhou H, Cicek N. 2014. Treatment of organic micropollutants in water and wastewater by UV-based processes: a literature review. Crit Rev Environ Sci Technol 44:1443-1476.

Yoho RA, Popat SC, Torres CI. 2014. Dynamic Potential-Dependent Electron Transport Pathway Shifts in Anode Biofilms of Geobacter sulfurreducens. Chemsuschem 7(12):3413-3419.

Yoho RA, Popat SC, Rago L, Guisasola A, Torres CI. 2015. Anode Biofilms of Geoalkalibacter ferrihydriticus Exhibit Electrochemical Signatures of Multiple Electron Transport Pathways. Langmuir 31(45):12552-12559.

You SJ, Zhao QL, Jiang JQ, Zhang JN, Zhao SQ. 2006. Sustainable approach for leachate treatment: Electricity generation in microbial fuel cell. Journal of Environmental Science and Health Part a-Toxic/Hazardous Substances & Environmental Engineering 41(12):2721-2734.

Young MN, Marcus AK, Rittmann BE. 2013. A Combined Activated Sludge Anaerobic Digestion Model (CASADM) to understand the role of anaerobic sludge recycling in wastewater treatment plant performance. Bioresource Technology 136:196-204.

Young M, Ki D, Stadie M, Thompson J, Chowdhury N, Popat S, Rittmann B, Torres CI. 2016. Tailoring Microbial Fuel Cells for Production of Hydrogen Peroxide. Meeting Abstracts MA2016-01:1795-1795.

Young MN, Links MJ, Popat SC, Rittmann BE, Torres CI. 2016. Tailoring Microbial Electrochemical Cells for Production of Hydrogen Peroxide at High Concentrations and Efficiencies. ChemSusChem 9:3345-3352.

Young MN, Chowdhury N, Garver E, Evans PJ, Popat SC, Rittmann BE, Torres CI. 2017. Understanding the impact of operational conditions on performance of microbial peroxide producing cells. Journal of Power Source 356:448-458.

Yuan Y, Chen Q, Zhou S, Zhuang L, Hu P. 2012. Improved electricity production from sewage sludge under alkaline conditions in an insert-type air-cathode microbial fuel cell. Journal of Chemical Technology and Biotechnology 87(1):80-86.

Zhang F, Saito T, Cheng S, Hickner MA, Logan BE. 2010a. Microbial Fuel Cell Cathodes With Poly(dimethylsiloxane) Diffusion Layers Constructed around Stainless Steel Mesh Current Collectors. Environmental Science & Technology 44(4):1490-1495.

Zhang Y, Merrill MD, Logan BE. 2010b. The use and optimization of stainless steel mesh cathodes in microbial electrolysis cells. International Journal of Hydrogen Energy 35(21):12020-12028.

Zhuang L, Chen Q, Zhou S, Yuan Y, Yuan H. 2012. Methanogenesis Control using 2-Bromoethanesulfonate for Enhanced Power Recovery from Sewage Sludge in Air-cathode Microbial Fuel Cells. International Journal of Electrochemical Science 7(7):6512-6523.

APPENDIX A

Integrate results into MFC kinetic models (Task 2)

Application of the Proton Condition

A general form of the complexation reaction is defined in reference to the components:

$$\sum_{j=1}^{N_c} \nu_{ij} \hat{C}_j \leftrightarrow \widehat{P}_i$$

(Eqn. 1)

where ν_{ij} is the stoichiometric coefficient giving the number of moles of component j in complex i, $\hat{C}$ is the chemical formula for component j (listed in the first row of Table A.2), and $\widehat{P}$ is the chemical formula for complex i (listed in the first column of Table A.2), and N_c is the number of components in the system. For example, in row 1 of Table A.2 one mole of H^+ and one mole CH_3COO^- produce one mole of CH_3COOH, or the reaction $H^+ + CH_3COO^- \leftrightarrow CH_3COOH$. The following are the component species in MYAnode: H^+, CH_3COO^-, HPO_4^{2-}, HCO_3^-, NO_2^-, NH_4^+, NO_3^-, Na^+, and Cl^-.

Since the complexation reactions generally achieve thermodynamic equilibrium very rapidly, the concentration of complexes and components satisfy the law of mass action:

$$p_i = \beta_i^c \prod_{j=1}^{N_c} \upsilon_{ij} c_j$$

(Eqn. 2)

where p_i is the concentration of complex i (M/L^3), c_j is the concentration of component j (M/L^3), and β_i^c is formation constant of complex i adjusted for the solution's ionic strength (thus, the c coefficient). The units of β_i^c vary depending upon the reaction stoichiometry. Several textbooks, including Snoeyink and Jenkins (1980) and Benjamin (2015), discuss correcting formation constants for ionic strength.

The law of mass conservation requires that the total aqueous concentration of component j must equal the sum of component j and all complexes i in the system for all components in the system, or

$$C_j = c_j + \sum_{i=1}^{N_p} \upsilon_{ij} p_i \qquad j = 1, \dots, N_c$$

(Eqn. 3)

where C_j is the total analytical concentration of component j and N_p is the total number of complexes associated with component j. For example, the mass conservation equation for bicarbonate is

$$C_{HCO_3^-} = p_{H_2CO_3} + c_{HCO_3^-} + p_{CO_3^{2-}}$$

(Eqn. 4)

The value of C_j is always a positive value.

The PC has a key advantage in biological systems in that the tracking of protons integrates well with oxidation-reduction reactions, which produce and consume H^+ ions. Variations in H^+ can be used to determine changes in pH. (Eqn. 3) is expanded to include protons

$$C_{H^+} = c_{H^+} + \sum_{i=1}^{N_p} \upsilon_{iH^+} p_i$$

(Eqn. 5)

where C_{H^+} is the total analytical concentration of H^+ defined in reference to the component species and $c_{H^+}$is the concentration of uncomplexed H^+ which is represented by the solution pH. Since $\upsilon_{iH^+}p_i$ represents the amount of protons in reference to the component species i, C_{H^+} can be a positive or negative value. Since electrochemical reactions result in electrical charge taking different paths in the anode and cathode chambers, the PC is useful in the anode biofilms for estimating ionic current production at the anode and ionic migration (i.e., the impacts of ion transport due to an electric field) calculations.

Since the total analytical concentration is sufficient for calculating the concentrations of all components and complexes, I follow the precedent of previous works and use the total aqueous concentrations of the components as the primary dependent variables for pH and transport, while treating the complexes as secondary variables and calculating their values for biological reactions as needed (Steefel and McQuarrie 1996; Parkhurst and Appelo 1999; Van Briesen and Rittmann 1999). Chemical complexation reactions are generally much faster than biological reactions; thus, they are treated as instantaneous values rather than time dependent variables.

Table A.1. Acid-base reactions and pK_a information

Reaction	**pK_a [a]**
$CH_3COOH \leftrightarrow CH_3COO^- + H^+$	4.76
$H_2CO_3 \leftrightarrow HCO_3^- + H^+$	6.35
$HCO_3^- \leftrightarrow CO_3^{2-} + H^+$	10.33
$H_3PO_4 \leftrightarrow H_2PO_4^- + H^+$	2.14
$H_2PO_4^- \leftrightarrow HPO_4^{2-} + H^+$	6.77
$HPO_4^{2-} \leftrightarrow PO_4^{3-} + H^+$	11.57
$NH_4^+ \leftrightarrow NH_3 + H^+$	9.25
$HNO_2 \leftrightarrow NO_2^- + H^+$	4.50 [b]
$H_2O \leftrightarrow H^+ + OH^-$	14.00

[a] From Snoeyink and Jenkins (1980) unless otherwise stated

[b] From da Silva et al. (2006)

Table A.2. The tableau method illustrating the relationship between components and complexes for reaction and transport as described for the proton condition. Blank cells are equal to zero.

Complexes	**Components**									**Charge**	**D (cm^2/d)[a]**
	H^+	CH_3COO^-	HPO_4^{2-}	HCO_3^-	NO_2^-	NH_4^+	NO_3^-	Na^+	Cl^-		
CH_3COOH	1	1								0	1.05
H_3PO_4	2		1							0	1.00[b]
$H_2PO_4^-$	1		1							-1	0.83
PO_4^{3-}	-1		1							-3	0.71
H_2CO_3	1			1						0	1.66
CO_3^{2-}	-1			1						-2	0.80
HNO_2	1				1					0	1.00[b]
NH_3	-1					1				0	1.00[b]
Charge	+1	-1	-2	-1	-1	+1	-1	+1	-1		
D (cm^2/d)[a]	N/A	0.94	0.66	1.02	1.65	1.69	1.64	1.15	1.76		

[a] From Haynes et al. (2011)

[b] Value not available -- assumed value

Biofilm kinetics modeling

The maximum specific growth rate in the biofilm ($\hat{q}X_f$; M/L^3-t) was adjusted using Nernst-Monod kinetics (Marcus et al. 2007; Torres et al. 2008a):

$$\hat{q}X_f \text{ at } E = \hat{q}X_f \frac{1}{1 + \exp(-\frac{F}{RT}(E - E_{KA}))}$$

(Eqn. 6**)**

where F is Faraday's constant (96485 C/mol), R is the idea gas constant (8.314 J/mol K), T is temperature (K), and E_{KA} (V) is the potential at which half of the maximum specific growth rate is achieved.

Within an ARB biofilm, two phenomena dictate the transport of ions: mass transport via diffusion and migration due to the induced electric field. The total flux of an ion, J_{ion} (M/L^2-t), within the system is described as

$$J_{ion,k} = J_{diff,k} + J_{mig,k}$$

(Eqn. 7)

where k is the ion (component or complex), J_{diff} is the diffusion flux (M/L^2-t), and J_{mig} is the migration flux (M/L^2-t). Diffusive flux of components j and complexes i through the biofilm is described by Fick's law

$$-J_{diff,j} = D_j \frac{\partial c_j}{\partial x} + \sum_{i=1}^{Nx} \left(D_i \frac{\partial p_i}{\partial x} \right)$$

(Eqn. 8)

where J_j is the total flux of component j (M/L^2-t), D is the diffusion coefficient (L^2/t), x is the spatial coordinate (L), and N_x is the number of complexes. Since there can be large variations, I assign independent diffusivities for each complex and component. Derived in Marcus et al. (2010), migration of ions is due to changes in the electrostatic potential through the biofilm and is described as

$$J_{mig,k} = z_k c_k D_k E^*$$

(Eqn. 9)

where z is the charge of ion k, c is the concentration (M/L^3), and E^* is the apparent electric field (1/L). E* can be calculated from

$$E^* = \frac{F}{RT} E$$

(Eqn. 10)

where E is the electric field (V/L), F is Faraday's constant (96485 C/mol), R is the ideal gas constant (8.314 CV/K-mol), and T is temperature (K).

Supplemental Figures

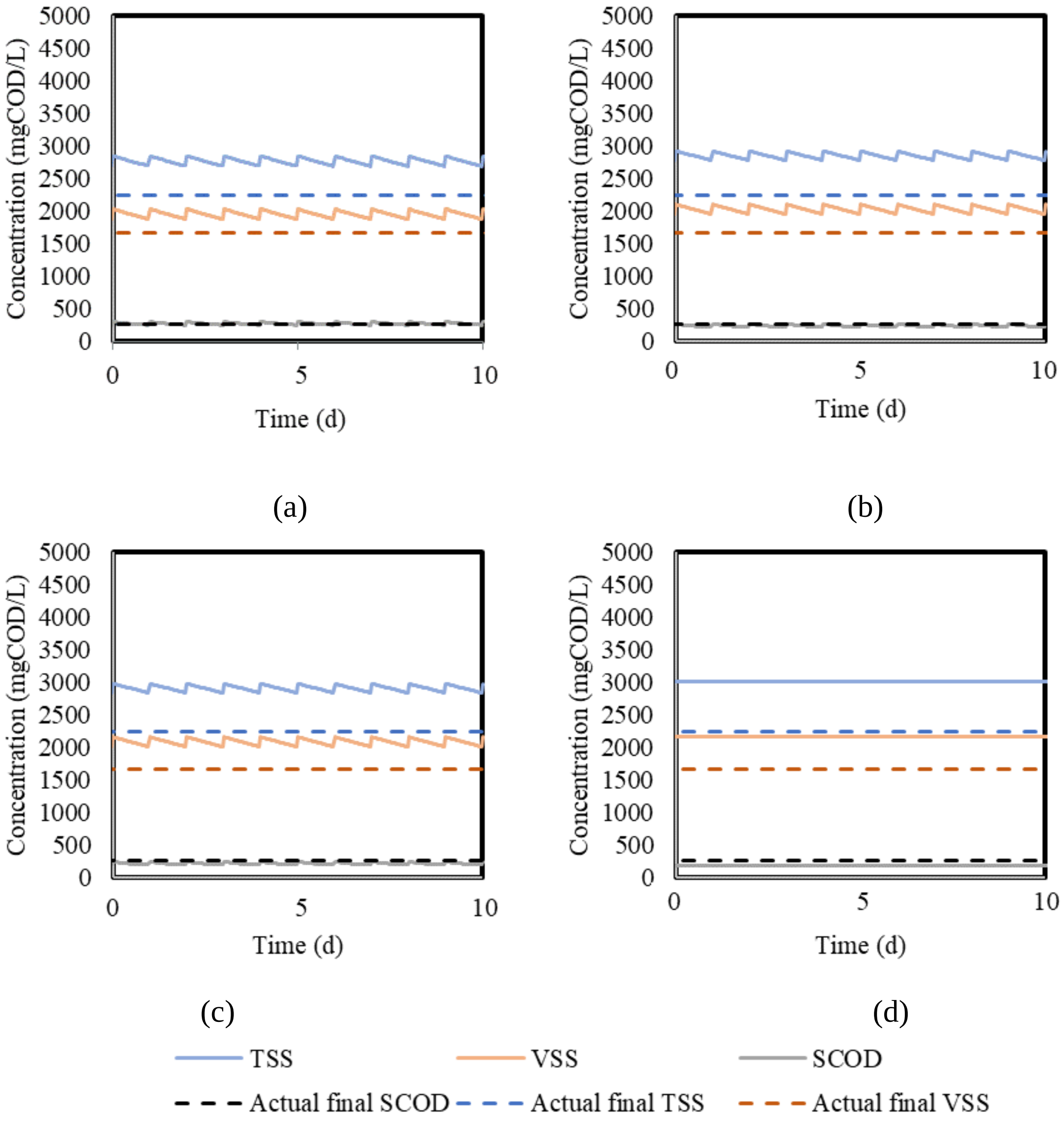

(a) (b)

(c) (d)

Appendix A Figure A1. Effluent TSS, VSS, and SCOD concentrations at a 12-day HRT for hydrolysis rate 0.12/d and: (a) X_m = 1 mgVSS/L, (b) X_m = 10 mgVSS/L, (c) X_m = 25 mgVSS/L, and (d) X_m = 100 mgVSS/L. Effluent TSS, VSS, and SCOD concentrations at a 12-day HRT for hydrolysis rate 0.25/d and: (e) X_m = 1 mgVSS/L, (f) X_m = 10 mgVSS/L, (g) X_m = 25 mgVSS/L, and (h) X_m = 100 mgVSS/L.

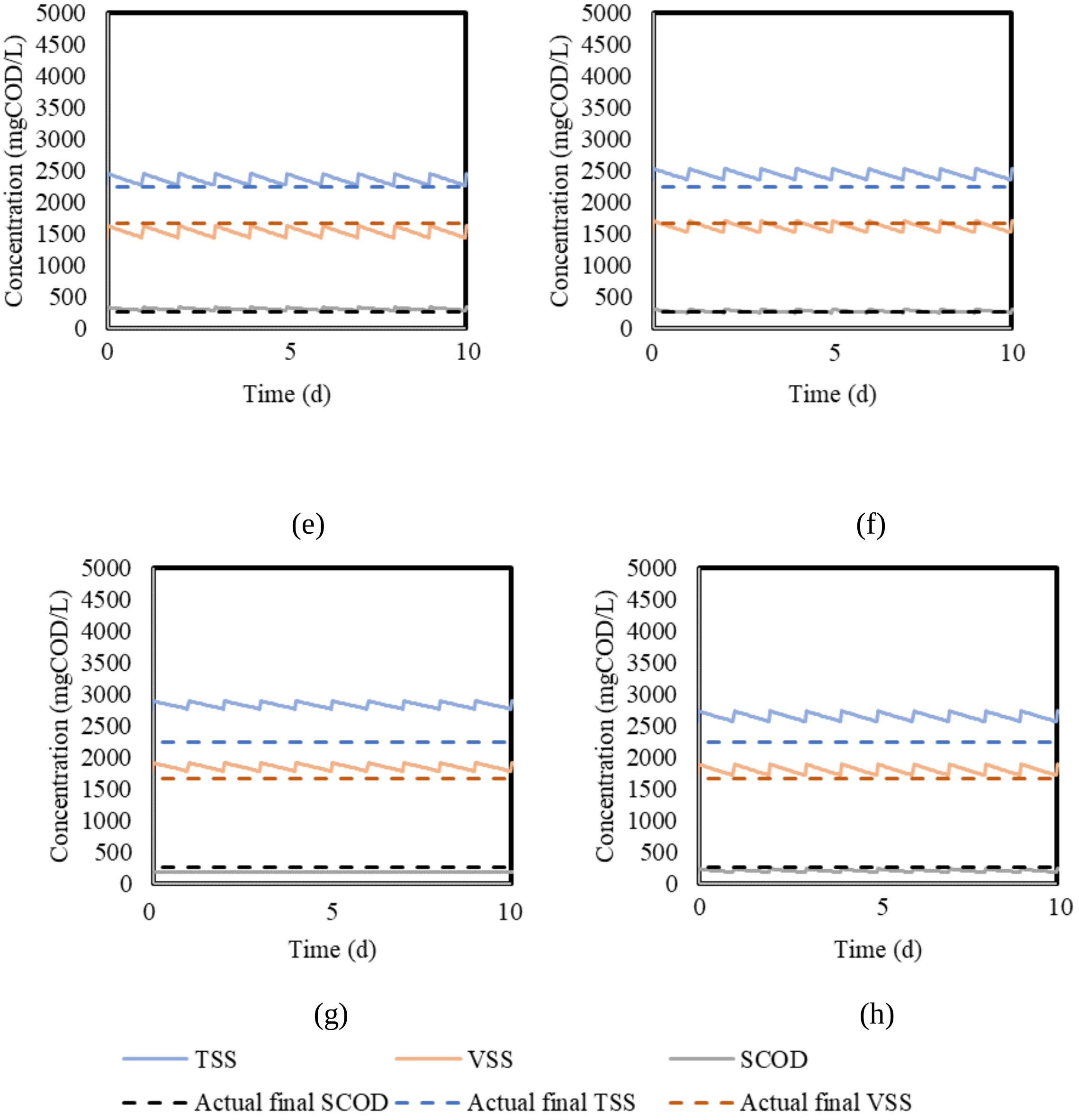

Appendix A Figure A1 continued. Effluent TSS, VSS, and SCOD concentrations at a 12-day HRT for hydrolysis rate 0.12/d and: (a) X_m = 1 mgVSS/L, (b) X_m = 10 mgVSS/L, (c) X_m = 25 mgVSS/L, and (d) X_m = 100 mgVSS/L. Effluent TSS, VSS, and SCOD concentrations at a 12-day HRT for hydrolysis rate 0.25/d and: (e) X_m = 1 mgVSS/L, (f) X_m = 10 mgVSS/L, (g) X_m = 25 mgVSS/L, and (h) X_m = 100 mgVSS/L.

Appendix B

Engineering Design Calculations

ESTCP ASU MXC Design

1.0 Purpose/Objective

Design fluidized bed reactor for black water stabilization and H2O2 production

2.0 Procedure

Calculate reactor size/ dimensions required to keep blackwater solids suspended via upflow fluidization. Consider solids hydrolysis rates, desired volatile solids destruction, and optimal residence time. Use assumptions and data from ASU to develop design.

3.0 References/Data Sources

ASU laboratory data demonstrating:

1) Settling velocity is 0.53 cm/min
2) First order hydrolysis rate constant of 0.1/d
3) Optimal residence time is 7 days

4.0 Assumptions

Primary sludge settling velocity based on results from ASU.

$$v_{reactor} := 0.53 \frac{cm}{min}$$

Assume influent VSS is 10,000 mg/L

$$VSS_{in} := 10000 \frac{mg}{L}$$

EPA 503B rule for Class B biosolids requires 38% volatile solids destruction for vector reduction. ASU has been able to get 50% VSD.

ASU has determined rate constants for hydrolysis of about 0.1/d

$$k := \frac{0.1}{day}$$

Assume fluidized bed reactor operates as a plug flow reactor and apply first-order kinetics

5.0 Calculations

For a plug flow reactor where dC/dτ = -kC where τ is space time or V/Q.

Assume pilot system has a flow rate of 144 gal/day (0.1 gpm) and a full-scale system is for a battalion with 3150 gal/d. Just calculate pilot system for now.

$$Q_{in} := 144 \frac{gal}{day}$$

Fix HRT based on ASU data

$$\tau := 7day$$

$$V_{reactor} := Q_{in} \cdot \tau = 1008\,gal$$

This is the wetted reactor volume. It does not include volume of anode/cathode modules and return-flow downcomers (see below).

Solving plug flow equation:

$$VSS_{out} := VSS_{in} \cdot \exp(-k\,\tau) = 4965.853 \cdot \frac{mg}{L}$$

Calculate volatile solids destruction.

$$VSD := \frac{(VSS_{in} - VSS_{out})}{VSS_{in}} = 50.3415 \cdot \%$$

This is similar to what ASU has been getting and is greater than 38% so OK.

Now calculate reactor dimensions to get fluidization. The reactor dimensions will be a function of the reactor flow rate which is defined as the recycle ratio times the influent flow rate. Assume the recycle ratio is 10.

$$Recycle := 10$$

$$Q_{reactor} := Q_{in} \cdot Recycle = 1\,gpm$$

Calculate recycle flow rate

$$Q_{recycle} := Q_{reactor} - Q_{in} = 0.9\,gpm$$

ESTCP ASU MXC Design

Now calculate the total reactor area (i.e., cross-sectional area for flow). First we need to define the reactor dimensions as shown below. There will be multiple subreactors (sub) where flow is upward. X, Y, and Z are defined in the figures. The white spacers inbetween the subreactors are downcomers to allow flow to go from one subreactor to the next while maintaining upward flow.

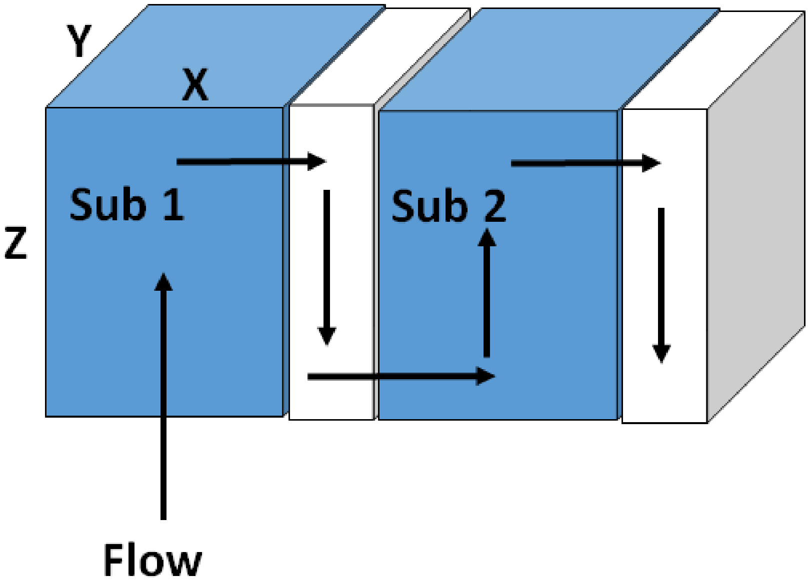

The cross sectional area to flow is the XY cross section in the above figure.

$$A_{sub} := \frac{Q_{reactor}}{v_{reactor}} = 7.6879\,ft^2$$

Calculate the total reactor length (i.e., length with respect to fluid flow) based on required reactor volume. This is the Z direction multiplied by the number of modules

$$L_{reactor.flow.path} := \frac{V_{reactor}}{A_{sub}} = 17.5276\,ft$$

Assume we have multiple subreactors in series rather than one very tall reactor. Assume each module is 3 ft tall (wetted height).

$$L_{z.wetted} := 3ft$$

Now calculate number of subreactors in series

$$N_{sub} := \text{round}\left[\left(\frac{L_{reactor.flow.path}}{L_{z.wetted}}\right), 0\right] = 6$$

ESTCP ASU MXC Design

The sketch below illustrates the concept with 6 subreactors. The downcomers and the recycle stream are also shown.

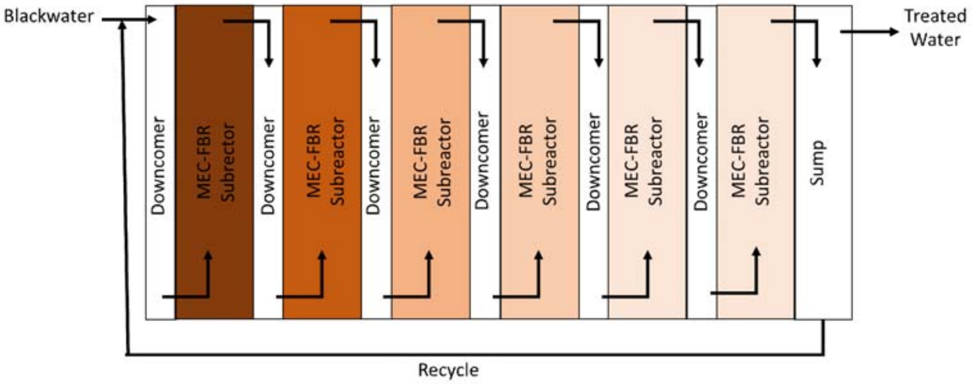

The following sketch illustrates a single subreactor along with adjacent downcomers and electrode modules. The water flow path is also shown.

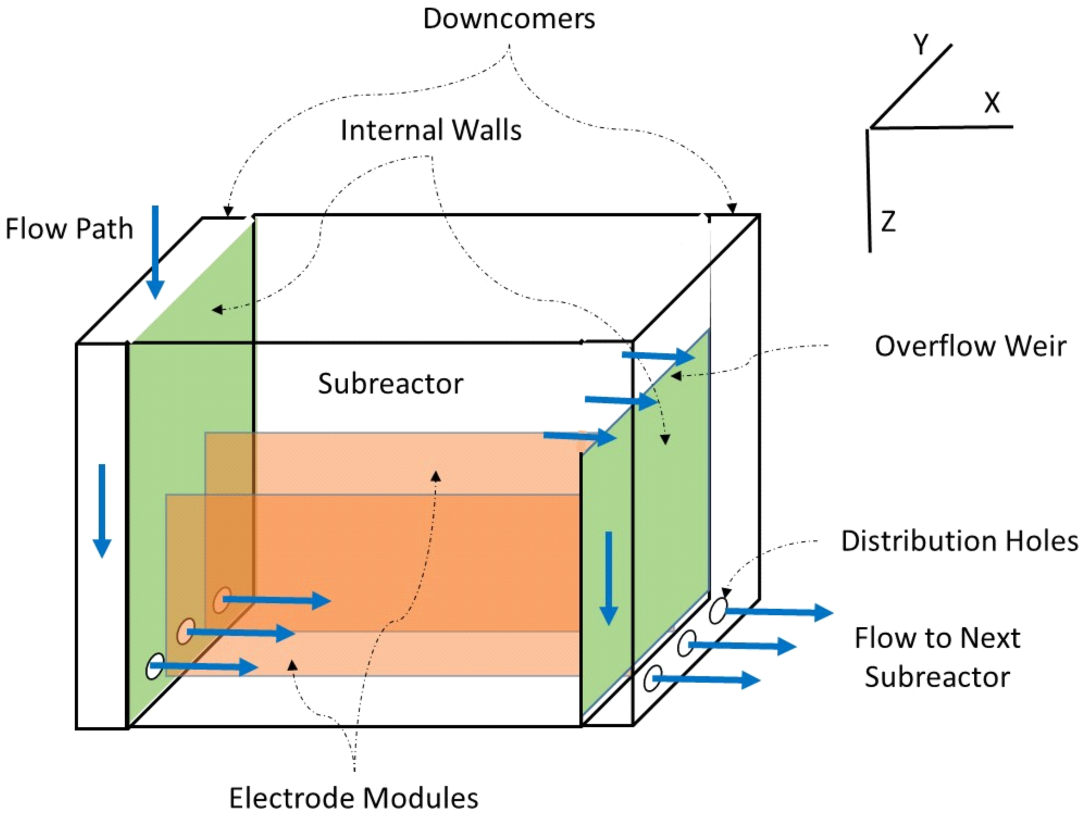

Now calculate the wetted subreactor dimensions. Assume the X dimension (Lx) is 4 ft for the pilot. Calculate the Y dimension for water flow (additional width will be calculated for the electrode modules later.

$L_{x.sub} := 4ft$

$$L_{y.sub.flow} := \frac{A_{sub}}{L_{x.sub}} = 23.0637 \bullet in$$

Now calculate the anode/cathode module requirements.

First calculate the area of a single module. Define the area as one side of the module.

$A_{module.side} := L_{z.wetted} \bullet L_{x.sub} = 12\,ft^2$

The area of both sides of the module is:

$A_{module} := 2 \bullet A_{module.side} = 24\,ft^2$

Calculate the number of modules by determining the total current for COD reduction in combination with the current density.

First convert TSS to COD. Assume 1.6 g COD per g TSS

$$COD_{removed} := VSD \bullet VSS_{in} \bullet 1.6 = 8054.6351 \bullet \frac{mg}{L}$$

Calculate COD removal mass rate

$$R_{COD} := COD_{removed} \bullet Q_{in} = 3.049 \bullet \frac{gm}{min}$$

Calculate electron flow via COD reduction to hydrogen peroxide (2 e-/mol)

$F := 96485.3329 \frac{C}{mol}$ Faraday constant

Assume conversion efficiency from COD to current

$\eta_{COD.current} := 50\%$

$$I_{COD} := R_{COD} \bullet \left(\frac{mol}{32gm}\right) \bullet \left(4\frac{mol}{mol}\right) \bullet F \bullet \eta_{COD.current} = 306.4426\,A$$

ESTCP ASU MXC Design

Assume rate limiting current density of anode/cathode

$$I_{density} := 4\frac{A}{m^2}$$

Calculate total anode/cathode area for reactor

$$A_{modules} := \frac{I_{COD}}{I_{density}} = 824.6301\,ft^2$$

Calculate total number of modules required in overall reactor

$$N_{modules} := round\left[\left(\frac{A_{modules}}{A_{module}}\right), 0\right] = 34$$

Calculate the current per module

$$I_{module} := \frac{I_{COD}}{N_{modules}} = 9.013\,A$$

Calculate number of modules per subreactor

$$N_{modules.per.subreactor} := round\left[\left(\frac{N_{modules}}{N_{sub}}\right), 0\right] = 6$$

The number of modules per subreactor (6) times the number of subreactors (6) is greater than the number of modules calculated above (35) because of rounding. So recalculate the number of total modules using the rounded values.

$$N_{modules} := N_{modules.per.subreactor} \cdot N_{sub} = 36$$

Each module design is shown below:

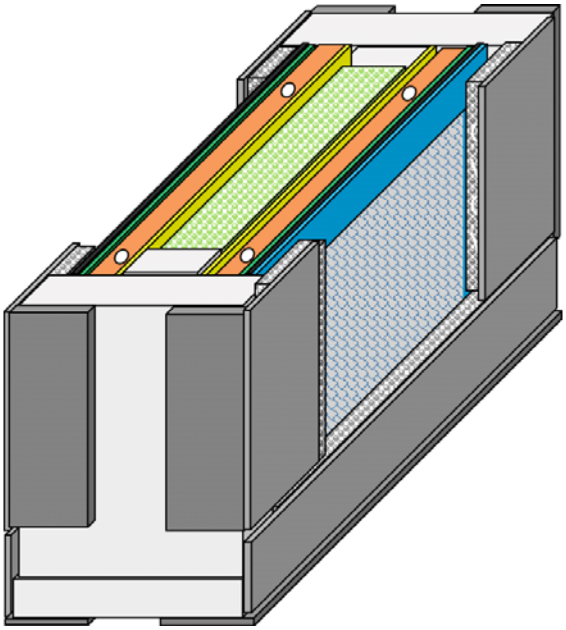

Now calculate the module thickness

$\text{Thickness}_{\text{spacer}} := 2.0\text{in}$

$\text{Thickness}_{\text{anode}} := 0.37\text{mm}$

$\text{Thickness}_{\text{cathode}} := 1\text{mm}$ assumed

$\text{Thickness}_{\text{ix.membrane}} := 0.45\text{mm}$ Assume Membranes International AMI-7001

$\text{Thickness}_{\text{geonet}} := 0.25\text{in}$ Assume 250 mil GSE Hypernet Geonet

$\text{Thickness}_{\text{titanium.mesh}} := 1\text{mm}$

$\text{Thickness}_{\text{angle.bracket}} := 0.125\text{in}$ McMaster Carr 8982K4 or K11

$\text{Thickness}_{\text{foam}} := 0.25\text{in}$ McMaster Carr 93375K16

Only 50% of the foam thickness will be on the frame

$\text{Thickness}_{\text{foam.on.frame}} := 0.5 \cdot \text{Thickness}_{\text{foam}} = 0.125 \cdot \text{in}$

$$L_{\text{y.module}} := \text{Thickness}_{\text{spacer}} + 2 \cdot \left(\begin{array}{l} \text{Thickness}_{\text{anode}} + \text{Thickness}_{\text{ix.membrane}} \cdots \\ + \text{Thickness}_{\text{geonet}} + \text{Thickness}_{\text{titanium.mesh}} \cdots \\ + \text{Thickness}_{\text{angle.bracket}} + \text{Thickness}_{\text{cathode}} \cdots \\ + \text{Thickness}_{\text{foam.on.frame}} \end{array} \right) = 3.222 \cdot \text{in}$$

Thickness of plastic frame is thickness above minus the angle bracket

$Thickness_{plastic.frame} := L_{y.module} - 2 \bullet Thickness_{angle.bracket} = 2.972 \bullet in$

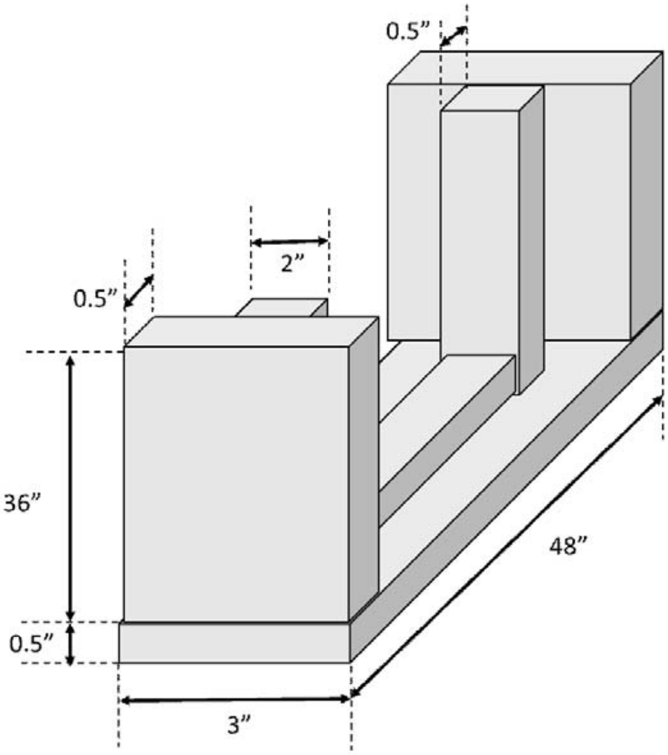

Calculate spacing between modules and between module and reactor wall (y direction) for flow. Note the spacing between modules is twice the spacing between the module and the reactor wall. This is because the former is exposed to 2 anodes and the later only to 1 anode. First calculate the number of inter-module spaces in each subreactor:

$N_{intermodule.spaces} := N_{modules.per.subreactor} - 1 = 5$

Now calculate the y dimension between a module and the wall.

$$L_{y.flow.wall} := \frac{\left(L_{y.sub.flow}\right)}{\left(2 + 2 \bullet N_{intermodule.spaces}\right)} = 1.922 \bullet in$$

Needs to have enough space for solids flow.

The spacing between modules is established as twice this value because the water will be exposed to twice the anode area and theoretically twice the wastewater flow can be treated.

$L_{y.flow.between.modules} := 2 \bullet L_{y.flow.wall} = 3.8439 \bullet in$

ESTCP ASU MXC Design

Calculate surface area to volume ratio and compare to ASU lab value of 40 m2/m3.

$$A_V := \frac{A_{modules}}{V_{reactor}} = 20.0778 \bullet \frac{1}{m}$$

Now calculate total subreactor width (Ly.sub) including wetted dimension and module.

$$L_{y.sub} := L_{y.sub.flow} + N_{modules.per.subreactor} \bullet L_{y.module} = 3.533\,ft$$

Assume downcomer Lx is 6 inches

$$L_{x.downcomer} := 6in$$

Calculate velocity

$$v_{downcomer} := \frac{Q_{in}}{\left(L_{y.sub} \bullet L_{x.downcomer}\right)} = 0.0001\,\frac{ft}{s}$$

Will not cause headloss

Total reactor length in the X direction including downcomers and the sump (assumed to be 1 ft) is:

$$L_{reactor} := N_{sub} \bullet \left(L_{x.sub} + L_{x.downcomer}\right) + 1ft = 28\,ft$$

From the figure above, the geonet is the place where the catholyte is and H2O2 is produced. Calculate the liquid volume of the geonet compartment in a single module.

$$Thickness_{geonet} = 0.25 \bullet in$$

$$Void_{geonet} := 80\%$$

Assumed

There are 2 geonets per module, so calculate the catholyte volume in each module

$$V_{catholyte.module} := L_{x.sub} \bullet L_{z.wetted} \bullet Thickness_{geonet} \bullet 2 \bullet Void_{geonet} = 2.9922\,gal$$

Assume catholyte hydraulic residence time in each module

$$t_{module} := 1hr$$

Assume catholyte flows to each module in parallel

Calculate catholyte flow rate in each module and for the entire reactor

$$Q_{catholyte.module} := \frac{V_{catholyte.module}}{t_{module}} = 188.779 \bullet \frac{mL}{min}$$

$$Q_{catholyte.reactor} := Q_{catholyte.module} \bullet N_{modules} = 6796.0432 \bullet \frac{mL}{min}$$

Calculate catholyte velocity in geonet. Assume a serpentine flow (i.e., up and down) through geonet sections that are isolated with baffles.

Assume the width of each geonet section is 4.4375 inches.

$$W_{geonet.section} := 4.4063in$$

Specify slop between geonet section edge and frame edge

$$Slop_{geonet} := \frac{1in}{32} = 0.0313 \bullet in$$

Space between baffles:

$$space_{between.baffles} := W_{geonet.section} + 2 \bullet Slop_{geonet} = 4.4688 \bullet in$$

The entire width of the geonet frame is the width of the electrode module frame minus the electrode module frame thickness.

$$Thickness_{frame} := 0.5in$$

$$W_{geonet.frame.available} := L_{x.sub} - 2 \bullet Thickness_{frame} = 47 \bullet in$$

Specify baffle thickness

$$Thickness_{baffle} := 0.125in$$

$$N_{baffles} := 9$$

$$N_{geonet.sections} := 10$$

$$W_{geonet.frame} := N_{baffles} \bullet Thickness_{baffle} + N_{geonet.sections} \bullet space_{between.baffles} \cdots + 2 \bullet Thickness_{frame} = 46.813 \bullet in$$

Calculate liquid velocity in geonet

$$Velocity_{geonet} := \frac{L_{z.wetted} \bullet N_{geonet.sections}}{t_{module} \bullet Void_{geonet}} = 0.0104 \bullet \frac{ft}{s}$$ Too low to cause head loss

Now calculate H2O2 production rate and concentration. First calculate mass of H2O2 produced per unit mass of COD destroyed.

$FW_{O2} := 32\,\frac{gm}{mol}$ $Stoich_{elec.H2O} := 4\,\frac{mol}{mol}$ $\eta_{COD.current} = 0.5$

$FW_{H2O2} := 34\,\frac{gm}{mol}$ $Stoich_{elec.H2O2} := 2\,\frac{mol}{mol}$ $\eta_{current.H2O2} := 0.8$

$$M_{H2O2.COD} := \frac{Stoich_{elec.H2O} \cdot \eta_{COD.current} \cdot \eta_{current.H2O2} \cdot FW_{H2O2}}{FW_{O2} \cdot Stoich_{elec.H2O2}} = 0.85 \cdot \frac{gm}{gm}$$

Now calculate rate of H2O2 production

$$R_{H2O2} := R_{COD} \cdot M_{H2O2.COD} = 2.5917 \cdot \frac{gm}{min}$$

Now calculate H2O2 concentration

$$C_{H2O2} := \frac{R_{H2O2}}{Q_{catholyte.reactor}} = 381.3483 \cdot \frac{mg}{L}$$

< 1/4 of what has been observed.

Design of inlet distribution system. Use orifice equation from Perry. Beta is 0 because of infinite expansion.

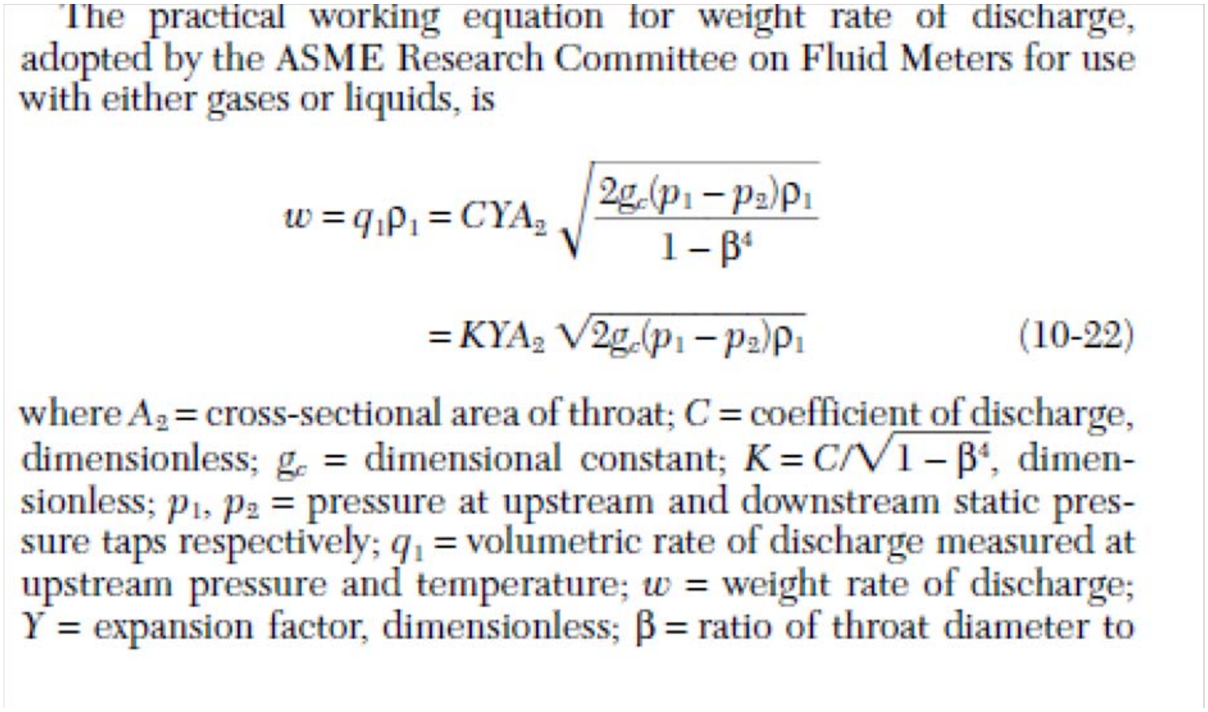

The practical working equation for weight rate of discharge, adopted by the ASME Research Committee on Fluid Meters for use with either gases or liquids, is

$$w = q_1\rho_1 = CYA_2\sqrt{\frac{2g_c(p_1 - p_2)\rho_1}{1-\beta^4}}$$

$$= KYA_2\sqrt{2g_c(p_1 - p_2)\rho_1} \qquad (10\text{-}22)$$

where A_2 = cross-sectional area of throat; C = coefficient of discharge, dimensionless; g_c = dimensional constant; $K = C/\sqrt{1-\beta^4}$, dimensionless; p_1, p_2 = pressure at upstream and downstream static pressure taps respectively; q_1 = volumetric rate of discharge measured at upstream pressure and temperature; w = weight rate of discharge; Y = expansion factor, dimensionless; β = ratio of throat diameter to

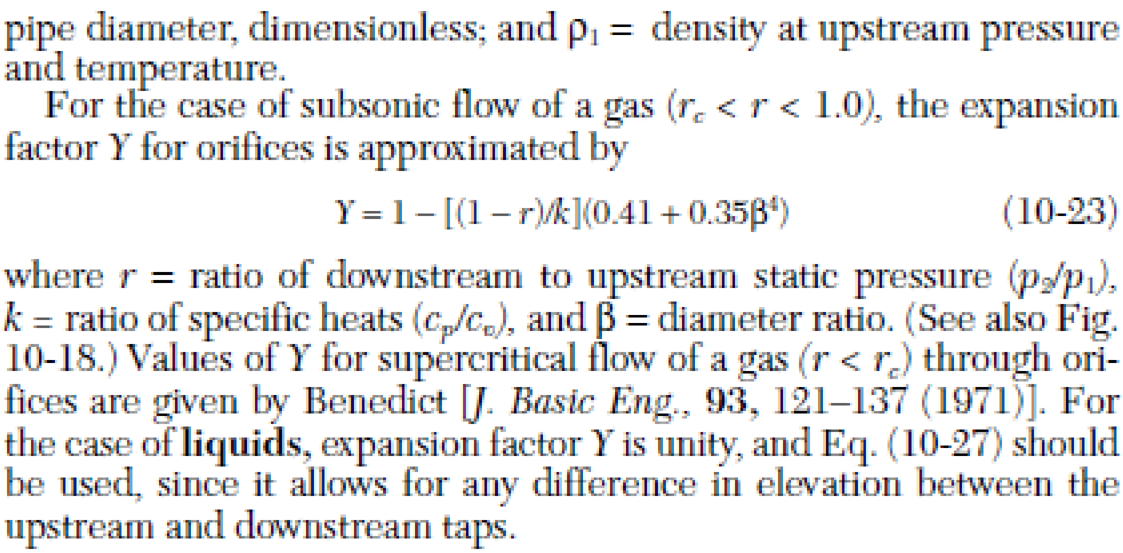

pipe diameter, dimensionless; and ρ_1 = density at upstream pressure and temperature.

For the case of subsonic flow of a gas ($r_c < r < 1.0$), the expansion factor Y for orifices is approximated by

$$Y = 1 - [(1-r)/k](0.41 + 0.35\beta^4) \qquad (10\text{-}23)$$

where r = ratio of downstream to upstream static pressure (p_2/p_1), k = ratio of specific heats (c_p/c_v), and β = diameter ratio. (See also Fig. 10-18.) Values of Y for supercritical flow of a gas ($r < r_c$) through orifices are given by Benedict [*J. Basic Eng.*, **93**, 121–137 (1971)]. For the case of **liquids**, expansion factor Y is unity, and Eq. (10-27) should be used, since it allows for any difference in elevation between the upstream and downstream taps.

$Q_{reactor} = 1\,\text{gpm}$

$D_{orifice} := 0.25\text{in}$

Make actual holes 0.75 inches to allow for 10 gpm flow. Use grommets to reduce size to 0.25 in for 1 gpm flow

$$A_{orifice} := \pi\left(\frac{D_{orifice}}{2}\right)^2 = 0.0003\,\text{ft}^2$$

ESTCP ASU MXC Design

Assume on orifice for each intermodule space and also between the end modules and the subreactor walls.

$N_{orifice} := N_{intermodule.spaces} + 2 = 7$ Note the previous drawing shows only 3 orifices.

$v_{orifice} := \frac{Q_{reactor}}{N_{orifice} \cdot A_{orifice}} = 0.9337 \frac{ft}{s}$ This velocity will help to move particles in the x direction.

$C := 0.62$ This is a typical value for the orifice coefficient

$\rho := 8.34 \frac{lb}{gal}$

$P_{loss.orifice} := \left(\frac{v_{orifice}}{C}\right)^2 \cdot \frac{\rho}{2} = 0.0153 \cdot \frac{lbf}{in^2}$ Note gc is not needed because Mathcad does internal unit correction.

Calculate pressure loss in inches of water

$$P_{loss.orifice.in.wc} := P_{loss.orifice} \cdot \frac{(34ft)}{\left(14.7 \frac{lbf}{in^2}\right)} = 0.4238 \cdot in$$

Pressure losses will be incurred for each subreactor entrance. Calculate the total head loss for the subreactors. Assume loss in downcomer and over weirs at subreactor exits are negligible.

$P_{loss.total} := P_{loss.orifice.in.wc} \cdot N_{sub} = 2.5429 \cdot in$

Need to include a safety factor for unaccounted losses and for orifice fouling. Assume 1 in loss for each subreactor for a total loss of 6 in. So make reactor height 1 ft greater than wetted height.

$L_z := L_{z.wetted} + 1ft = 4\,ft$

ESTCP ASU MXC Design

Design Summary

Reactor components

Number of subreactors $N_{sub} = 6$

Number of downcomers is equal to the number of subreactors

1 sump at end

Reactor operating conditions

Wastewater flow rate $Q_{in} = 0.1\,gpm$

Recycle flow rate $Q_{recycle} = 0.9\,gpm$

Reactor flow rate $Q_{reactor} = 1\,gpm$

Hydraulic residence time based on wastewater influent flow rate $\tau = 7 \cdot day$

Catholyte flow rate in each module $Q_{catholyte.module} = 188.779 \cdot \frac{mL}{min}$

Total catholyte flow rate $Q_{catholyte.reactor} = 1.7953\,gpm$

Reactor dimensions

Subreactor width $L_{y.sub} = 3.533\,ft$

Subreactor length $L_{x.sub} = 4\,ft$

Subreactor height $L_z = 4\,ft$

Downcomer length $L_{x.downcomer} = 6 \cdot in$

Total reactor length $L_{reactor} = 28\,ft$

Number of electrode modules $N_{modules} = 36$

Number of electrode modules per subreactor $N_{modules.per.subreactor} = 6$

Electrode module length $L_{x.sub} = 4\,ft$

Electrode module height $L_{z.wetted} = 3\,ft$

Electrode module width $L_{y.module} = 3.222 \cdot in$

Current in each module $I_{module} = 9.013\,A$

Appendix C
Process Flow Diagrams

1- Conventional Treatment (Company - CT)

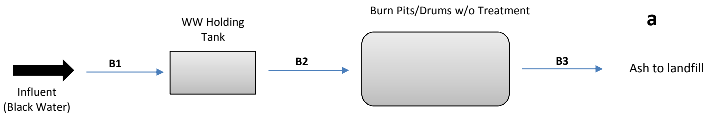

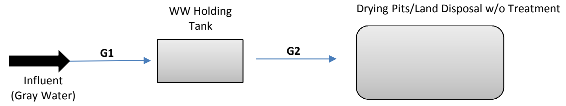

Table 1- Influent Criteria- Combined Gray/Black

Check	Design Parameter	Value	Units	Reference
	Black Water Flow	0.000788	mgd	Company
	Black Water COD	8,350	mg/L	
	Black Water TSS	4,600	mg/L	
	Ash Production	30%		EPA Biosolids Technology Fact Sheet, 1992: Approximately 65-75% of solids are combustable
	Gray Water Flow	0.00446	mgd	Company
	Gray Water COD	285	mg/L	
	Gray Water TSS	215	mg/L	Assumed Gray Water TSS concentration (average) based on literature survey

Table 2- Working Mass Balance Table

Check	Node	Description	Flow (mgd)	BOD_5 (mg/L)	COD (mg/L)	COD Load (lb/d)	TSS (mg/L)	TSS (lb/d)	Notes
	B1	Black Water Influent	0.000788	4175	8,350	55	4,600	30	
	B2	Black Water Effluent	0.000788	4175	8,350	55	4,600	30	Assumed no removal
	B3	Ash to Landfill	-	-	-	-	-	9	Assume 70% destruction. EPA Biosolids Technology Fact Sheet, 1992: Approximately 65-75% of solids are combustable
	G1	Gray Water Influent	0.004463	142.5	285	11	215	8	
	G2	Gray Water Effluent	0.004463	142.5	285	11	215	8	Assumes no removal

1- Conventional Treatment (Battalion - CT)

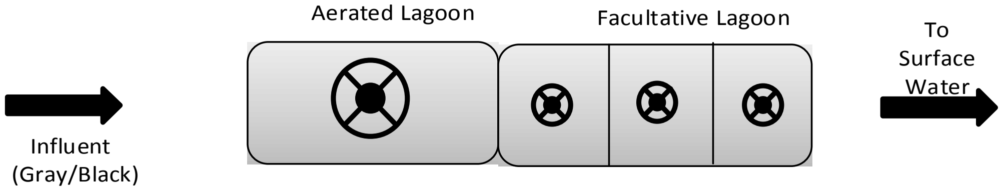

Design Parameter	Value	Units	Reference/Notes
Flow Rate	0.021	mgd	Gray and Black Water
Influent TSS	875	mg/L	
Effluent TSS	90	mg/L	Effluent can be <30 mg/L to > 150 mg/L - EPA Facultative Lagoon Fact Sheet
Effluent TSS Loading Rate	16	lb/day	
Total Solids Influent Loading	55,935	lb/year	
VS Loading Rate	39,155	lb/year	Assume VSS/TSS = 0.7
FS Loading Rate	16,781	lb/year	Assume FSS/TSS = 0.3
Total Solids Undegraded	32,442	lb/year	Assume 60% VSS destruction
Cell Yield	10%		Assumed for aerobic/facultative
Cell Yield	1402	lb/year	For growth on COD
Total Solids Accumulation in Lagoon	28,092	lb/year	Undegraded solids plus cell yield minus discharged solids
Sludge Wasting	14	dry tons/year	
Sludge concentration	10%		Assumed
Sludge Volume	33,683	gallons/year	assume 10% solids and density of 8.34 lb/gal
Facultative Pond Sizing			
HRT	3	days	Wastewater Engineering, Metcalf&Eddy, 4th Ed, pp. 840-854
Volume	0.097	mg	include volume for HRT and annual solids accumulation
	12,926	ft3	
Depth	10	ft	
Area	1,293	ft^2	

Dual Powered Lagoon - COD Removal

Design Parameter	Value	Units	Reference/Notes
CODin - Aerated Lagoon	1500	mg/L	
k rate constant	-0.5	day^-1	Wastewater Engineering, Metcalf&Eddy, 4th Ed, pp. 840-854
HRT	3	days	Wastewater Engineering, Metcalf&Eddy, 4th Ed, pp. 840-854
CODout - Aerated Lagoon	335	mg/L	
CODout Loading - Aerated Lagoon	58.62	lb/d	
COD Removal Efficiency	77.69	% removed	
CODin - Facultative	335	mg/L	
k rate constant	-0.2	day^-1	Assumed to be 20% of aerated lagoon rate constant
HRT	3	days	Wastewater Engineering, Metcalf&Eddy, 4th Ed, pp. 840-854
CODout- Facultative	184	mg/L	
BOD5 out - Facultative	91.8	mg/L	Assumed to be 50% of COD
COD Effluent Loading Rate- Facultative	32.17	lb/d	

Mass Loading Rates Summary

COD In	263	lb/d	
CODout - Aerated Lagoon	59	lb/d	After three days (SRT = HRT)
CODout- Facultative	32	lb/d	After three days (SRT = HRT)
COD Removed (6 days retention)	231	lbs	After six days
COD Removed per day	38	lb/day	

2- MEC with Electricty Generation (Company - MEC-E)

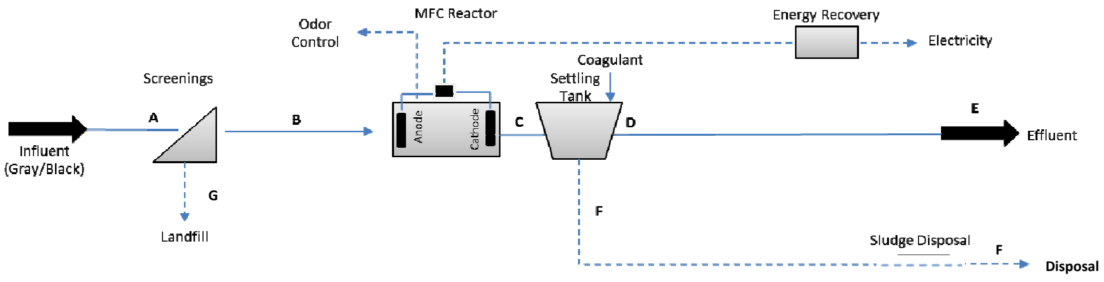

Table 1- Performance Criteria- Combined Gray/Black

Design Parameter	Value	Units	Reference
Influent Flow	0.00525	mgd	Battalion
MFC Influent COD	1,500	mg/L	Combined Gray/Black Water- Assumed BOD is 50% of COD
Assumed % COD Removal	80%		Penn State University research study
Assumed Rate Constant (k)	4.0	1/day	Penn State University research study
Calculated MFC Effluent COD	300	mg/L	
Calculated HRT	10	hrs	Based on 1st Order Kinetics Ct=Co*e^(-kt)
MFC Influent TSS	875	mg/L	Combined Gray/Black Water
Influent VSS/TSS	70%		Assumed
MFC influent VSS	613	mg/L	
MFC VSS Removal	60%		Assumed
MFC VSS Removed	368	mg/L	
MFC Yield	5%	TSS lb/lb COD removed	Assumed for anaerobic
MFC Yield	60	mg/L VSS	VSS contributed by growth on COD
MFC FSS effluent	263	mg/L	
MFC VSS effluent	305	mg/L	Undegraded VSS plus cell yield
MFC TSS effluent	568	mg/L	
Clarifier COD Removal %	0.45		M&E 4th ed. P. 405, figure 5-46 primary settler
Clarifier TSS Removal %	0.60		M&E 4th ed. P. 405, figure 5-46 primary settler
Clarifier COD effluent	165	mg/L	
Clarifier TSS effluent	227	mg/L	
Clarifier Sludge	4.0%		Typical Gravity Thickening Performance per Wastewater Engineering, Metcalf&Eddy, 4th Ed, Pg. 1489
Clarifier sludge removal	45	gal/day	

Table 2- Working Mass Balance Table

Node	Description	Flow (mgd)	BOD (mg/L)	COD (mg/L)	COD Load (lb/d)	TSS (mg/L)	TSS (lb/d)
A	Screenings Influent	0.005250	750	1,500	66	875	38
B	MFC Influent	0.005250	750	1,500	66	875	38
C	MFC Effluent	0.005250	150	300	13	568	25
D	Clarifer Effluent	0.005205	83	165	7	227	10
E	Plant Effluent	0.005205	83	165	7	227	10
F	Sludge Withdrawal	0.000045				40,000	15
G	Screenings	Assumed to be negligible					

2- MEC with Electricty Generation (Battalion - MEC-E)

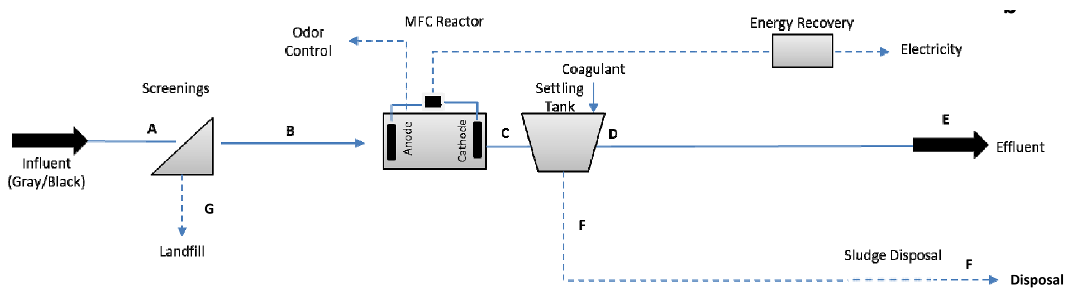

Table 1- Performance Criteria- Combined Gray/Black

Design Parameter	Value	Units	Reference
Influent Flow	0.02100	mgd	Battalion
MFC Influent COD	1,500	mg/L	Combined Gray/Black Water- Assumed BOD is 50% of COD
Assumed % COD Removal	80%		Penn State University research study
Assumed Rate Constant (k)	4.0	1/day	Penn State University research study
Calculated MFC Effluent COD	300	mg/L	
Calculated HRT	10	hrs	Based on 1st Order Kinetics Ct=Co*e^(-kt)
MFC Influent TSS	875	mg/L	Combined Gray/Black Water
Influent VSS/TSS	70%		Assumed
MFC influent VSS	613	mg/L	
MFC VSS Removal	60%		Assumed
MFC VSS Removed	368	mg/L	
MFC Yield	5%	TSS lb/lb COD removed	Assumed for anaerobic
MFC Yield	60	mg/L VSS	VSS contributed by growth on COD
MFC FSS effluent	263	mg/L	
MFC VSS effluent	305	mg/L	Undegraded VSS plus cell yield
MFC TSS effluent	568	mg/L	
Clarifier COD Removal %	0.45		M&E 4th ed. P. 405, figure 5-46 primary settler
Clarifier TSS Removal %	0.60		M&E 4th ed. P. 405, figure 5-46 primary settler
Clarifier COD effluent	165	mg/L	
Clarifier TSS effluent	227	mg/L	
Clarifier Sludge	4.0%		Typical Gravity Thickening Performance per Wastewater Engineering, Metcalf&Eddy, 4th Ed, Pg. 1489
Clarifier sludge removal	180	gal/day	

Table 2- Working Mass Balance Table

Node	Description	Flow (mgd)	BOD (mg/L)	COD (mg/L)	COD Load (lb/d)	TSS (mg/L)	TSS (lb/d)
A	Screenings Influent	0.021000	750	1,500	263	875	153
B	MFC Influent	0.021000	750	1,500	263	875	153
C	MFC Effluent	0.021000	150	300	53	568	99
D	Clarifer Effluent	0.020820	83	165	29	227	39
E	Plant Effluent	0.020820	83	165	29	227	39
F	Sludge Withdrawal	0.000180				40,000	60
G	Screenings	Assumed to be negligible					

3- MFC with H2O2 Production (Company-MFC-H2O2)

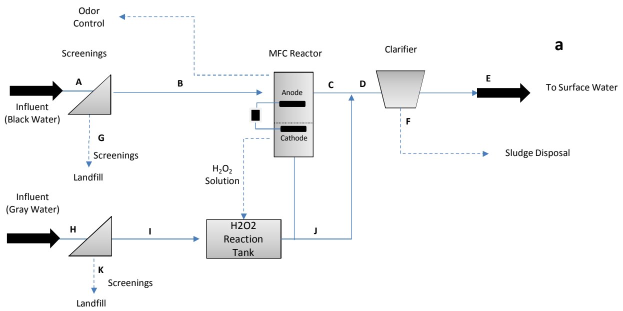

Table 1- Performance Criteria- Black Water Treatment in MFC

Check	Design Parameter	Value	Units	Reference
	Influent Flow	0.000788	mgd	Company Blackwater
	MFC Influent COD	8,350	mg/L	Black Water Only - Assume BOD is 50% of COD
	COD Removal	80%		Assumed to be equal to Penn State study
	Assumed Rate Constant (k)	0.19	1/day	Arizona State University research study
	Calculated MFC Effluent COD	1670	mg/L	
	Calculated HRT	8.5	days	Based on 1st Order Kinetics Ct=Co*e^(-kt)
	MFC Influent TSS	4,600	mg/L	
	Influent VSS/TSS	70%		Assumed
	MFC Influent VSS	3,220	mg/L	
	MFC VSS Removal	60%		Assumed
	MFC Yield	5%	TSS lb/lb COD removed	Assumed for anaerobic
	MFC Yield	334	mg/L	
	MFC FSS effluent	1,380	mg/L	
	MFC VSS effluent	1,622	mg/L	
	MFC TSS effluent	3,002	mg/L	
	Gray Water Flow	0.004463	mgd	
	Gray Water Influent COD	285	mg/L	
	Gray Water Influent TSS	215	mg/L	Assumed Gray Water TSS concentration (average) based on literature survey
	Gray Water COD Load	11	lb/day	
	O2 Load from H2O2	18	lb/day	
	COD removal efficiency	90%		Assumed based on relative H2O2 and COD load
	H2O2 reaction tank effluent COD	29	mg/L	
	H2O2 reaction tank effluent TSS	215	mg/L	Assumed to have no net removal
	Clarifier influent Flow	0.005251	mgd	
	Clarifier influent COD	275	mg/L	
	Clarifier influent TSS	633	mg/L	
	Clarifier COD Removal %	45%		Wastewater Engineering, Metcalf&Eddy, 4th Ed, P. 405, Figure 5-46
	Clarifier TSS Removal %	60%		Wastewater Engineering, Metcalf&Eddy, 4th Ed, P. 405, Figure 5-46
	Clarifier effluent COD	151	mg/L	
	Clarifier effluent TSS	253	mg/L	
	Clarifier Sludge	4.0%		Wastewater Engineering, Metcalf&Eddy, 4th Ed, Pg. 1489

Table 2- Working Mass Balance Table

Check	Node	Description	Flow (mgd)	BOD (mg/L)	COD (mg/L)	COD Load (lb/d)	TSS (mg/L)	TSS (lb/d)
	A	Screenings Influent	0.000788	4,175	8,350	55	4,600	30
	B	MFC Influent	0.000788	4,175	8,350	55	4,600	30
	C	MFC Anode Eff	0.000788	835	1,670	11	3,002	20
	D	Clarifier Influent	0.005251	137	275	12	633	28
	E	Clarifier Eff	0.005200	76	151	7	253	11
	F	Sludge Withdrawal	0.000050				40,000	17
	G, K	Screenings	Assumed to be negligible					
	H	Gray Water Influent	0.004463	143	285	11	215	8
	I	Influent to H2O2 treatment	0.004463	143	285	11	215	8
	J	H2O2 treatment effluent	0.004463	14	29	1.1	215	8

Table 3 - Hydrogen Peroxide Production

Design Parameter	Value	Units
CODin	55	lb/d
CODout	11	lb/d
Δ COD	44	lb/d
H2O2:COD	0.85	lb/lb
H2O2 Mass Loading	37	lb/d
O2 Mass Loading	17.5	lb/d
Transfer Efficiency	1.0	
Available O2	17.5	lb/d
Annual O2 Available	6,405	lbs/year
Annual H2O2 Available	13,611	lbs/year

Note:
Assume 0.5 mole O2/mole H2O2
Assume O2 is available for direct COD oxidation at in H2O2 reaction tank

3- MFC with H2O2 Production (Battalion MFC-H2O2)

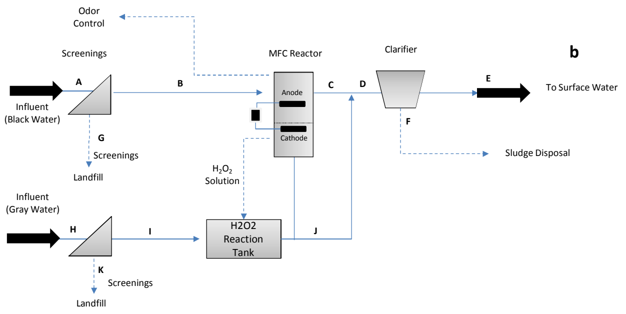

Table 1- Performance Criteria- Black Water Treatment in MFC

Check	Design Parameter	Value	Units	Reference
	Influent Flow	0.003150	mgd	Company Blackwater
	MFC Influent COD	8,350	mg/L	Black Water Only - Assume BOD is 50% of COD
	COD Removal	80%		Assumed to be equal to Penn State study
	Assumed Rate Constant (k)	0.19	1/day	Arizona State University research study
	Calculated MFC Effluent COD	1670	mg/L	
	Calculated HRT	8.5	days	Based on 1st Order Kinetics Ct=Co*e^(-kt)
	MFC Influent TSS	4,600	mg/L	
	Influent VSS/TSS	70%		Assumed
	MFC Influent VSS	3,220	mg/L	
	MFC VSS Removal	60%		Assumed
	MFC Yield	5%	TSS lb/lb COD removed	Assumed for anaerobic
	MFC Yield	334	mg/L	
	MFC FSS effluent	1,380	mg/L	
	MFC VSS effluent	1,622	mg/L	
	MFC TSS effluent	3,002	mg/L	
	Gray Water Flow	0.017850	mgd	
	Gray Water Influent COD	285	mg/L	
	Gray Water Influent TSS	215	mg/L	Assumed Gray Water TSS concentration (average) based on literature survey
	Gray Water COD Load	42	lb/day	
	O2 Load from H2O2	70	lb/day	
	COD removal efficiency	90%		Assumed based on relative H2O2 and COD load
	H2O2 reaction tank effluent COD	29	mg/L	
	H2O2 reaction tank effluent TSS	215	mg/L	Assumed to have no net removal
	Clarifier influent Flow	0.021000	mgd	
	Clarifier influent COD	275	mg/L	
	Clarifier influent TSS	633	mg/L	
	Clarifier COD Removal %	45%		Wastewater Engineering, Metcalf&Eddy, 4th Ed, P. 405, Figure 5-46
	Clarifier TSS Removal %	60%		Wastewater Engineering, Metcalf&Eddy, 4th Ed, P. 405, Figure 5-46
	Clarifier effluent COD	151	mg/L	
	Clarifier effluent TSS	253	mg/L	
	Clarifier Sludge	4.0%		Wastewater Engineering, Metcalf&Eddy, 4th Ed, Pg. 1489

Table 2- Working Mass Balance Table

Check	Node	Description	Flow (mgd)	BOD (mg/L)	COD (mg/L)	COD Load (lb/d)	TSS (mg/L)	TSS (lb/d)
	A	Screenings Influent	0.003150	4,175	8,350	219	4,600	121
	B	MFC Influent	0.003150	4,175	8,350	219	4,600	121
	C	MFC Anode Eff	0.003150	835	1,670	44	3,002	79
	D	Clarifier Influent	0.021000	137	275	48	633	111
	E	Clarifier Eff	0.020799	76	151	26	253	44
	F	Sludge Withdrawal	0.000201				40,000	67
	G, K	Screenings	Assumed to be negligible					
	H	Gray Water Influent	0.017850	143	285	42	215	32
	I	Influent to H2O2 treatment	0.017850	143	285	42	215	32
	J	H2O2 treatment effluent	0.017850	14	29	4.2	215	32

Table 3 - Hydrogen Peroxide Production

Design Parameter	Value	Units
CODin	219	lb/d
CODout	44	lb/d
Δ COD	175	lb/d
H2O2:COD	0.85	lb/lb
H2O2 Mass Loading	149	lb/d
O2 Mass Loading	70.2	lb/d
Transfer Efficiency	1.0	
Available O2	70.2	lb/d
Annual O2 Available	25,622	lbs/year
Annual H2O2 Available	54,446	lbs/year

Note:
Assume 0.5 mole O2/mole H2O2
Assume O2 is available for direct COD oxidation at in H2O2 reaction tank

Appendix D
Design Criteria and Cost Summary

Basis of Design and Cost Summary

Alt	Scale	Waste Stream	Major Process Unit	Dimensions (varies)	Standard Volume (gal)	Standard Cost ($)	Module Unit Weight (tons)	Module Unit Power (hp)	Energy Production (kWh/m^3)	Flow Rate (gpd)	HRT (days)	Calculated Min. Volume (gal)	Unit Scale (1 = full size)	Scaled Module Volume (gal)	Scaled Module Cost ($)	Weekly Run Time (hr)	Duty Modules (qty)	Spare Modules (qty)	Total Scaled Modules (qty)	Total Scaled Weight (tons)	Total Scaled Capital Costs ($)	Total Scaled Annual Usage (kW-hr/yr)	Energy Recovery (kWh/yr)	Gallons of Diesel
1	Company	Black	WW Holding Tank - Poly Tank or Equal	Round Poly Tank 8-ft D x 24-ft L	8,000	$ 20,000	1.5	0.5	-	788	7	5,516	1	8,000	$ 20,000	1	0.7	0	1.0	1.5	$ 20,000	13	-	
1	Company	Gray	WW Holding Tank - Poly Tank or Equal	Round Poly Tank 8-ft D x 30-ft L	18,000	$ 25,000	2.5	0.5	-	4,463	2	8,926	0.5	9,000	$ 12,500	7	1.0	0	1.0	1.3	$ 25,000	68	-	
																		Total:	**2.0**	**2.8**	**$ 45,000**	**81.1**	**-**	**2**
1	Battalion	Combined	Dual Lagoon	1 x Aerobic Pond 30-ft L x 30-ft W x 10-ft D 1 x Falcutative Pond 30-ft L x 30-ft W x 10-ft D	-	$ 250,000	-	5	-	-	-	-	1	-	$ 250,000	168	1.0	0	1.0	-	$ 250,000	32,760	-	
																		Total:	**-**	**-**	**$ 250,000**	**32,760**	**-**	**814**
2	Company	Combined	Headworks	Conex Module	18,000	$ 100,000	6.5	0.5	-	5,250	0.34	1,785	0.1	1,800	$ 100,000	56	1.0	0	1.0	0.7	$ 10,000	108		
			MFC	Conex Module	18,000	$ 136,000	6.5	1	0.24	5,250	0.40	2,112	0.2	3,600	$ 136,000	14	0.6	0	1.0	1.3	$ 27,200	64	1,748	
			Settling Tank	Conex Module	18,000	$ 150,000	6.5	0.5	-	5,250	0.34	1,785	0.1	1,800	$ 150,000	168	1.0	0	1.0	0.7	$ 15,000	325		
			Solids Disposal	Round Poly Tank 8-ft D x 24-ft L	8,000	$ 20,000	1.5	0.1	-	45	7	315	0.1	800	$ 20,000	0.5	1.0	0	1.0	0.2	$ 2,000	0.20		
																		Total:	**4.0**	**2.8**	**$ 54,200**	**497**	**1,748**	**-31**
2	Battalion	Combined	Headworks	Conex Module	18,000	$ 100,000	6.5	0.5	-	21,000	0.34	7,140	0.5	9,000	$ 100,000	56	0.8	0	1.0	3.3	$ 50,000	433		
			MFC	Conex Module	18,000	$ 136,000	6.5	1	0.24	21,000	0.40	8,450	0.5	9,000	$ 136,000	14	0.9	0	1.0	3.3	$ 68,000	256	6,990	
			Settling Tank	Conex Module	18,000	$ 150,000	6.5	0.5	-	21,000	0.34	7,140	0.5	9,000	$ 150,000	168	0.8	0	1.0	3.3	$ 75,000	1,299		
			Solids Disposal	Round Poly Tank 8-ft D x 30-ft L	12,000	$ 25,000	2.5	0.2	-	180	7	1,258	0.1	1,200	$ 25,000	0.5	1.0	0	1.0	0.3	$ 2,500	0.39		
																		Total:	**4.0**	**10.0**	**$ 195,500**	**1,989**	**6,990**	**-124**
3	Company	Gray	GW Holding	Round Poly Tank 8-ft D x 30-ft L	12,000	$ 25,000	2.5	0.5	-	4,463	0.5	2,232	0.2	2,400	$ 25,000	56	0.9	0	1.0	0.5	$ 5,000	203	-	
3	Company	Black	Headworks	Conex Module	18,000	$ 100,000	6.5	0.5	-	788	0.34	268	0.1	1,800	$ 100,000	56	0.15	0	1.0	0.7	$ 10,000	16	-	
			MFC	Conex Module	18,000	$ 300,000	6.5	1	-	788	8.5	6,675	0.4	7,200	$ 300,000	14	0.9	0	1.0	2.6	$ 120,000	202	-	
			Settling Tank	Conex Module	18,000	$ 150,000	6.5	0.5	-	788	0.34	268	0.1	1,800	$ 150,000	168	0.1	0	1.0	0.7	$ 15,000	49	-	
			Solids Disposal	Round Poly Tank 8-ft D x 24-ft L	8,000	$ 20,000	1.5	0.1	-	50	7	351	0.1	800	$ 20,000	0.5	1.0	0	1.0	0.2	$ 2,000	0.2	-	
																		Total:	**5.0**	**4.6**	**$ 152,000**	**471**	**-**	**12**
3	Battalion	Gray	GW Holding	Round Poly Tank 8-ft D x 30-ft L	12,000	$ 25,000	2.5	0.5	-	17,850	0.34	6,069	0.5	6,000	$ 25,000	56	1.0	0	2.0	2.5	$ 25,000	552	-	
3	Battalion	Black	Headworks	Conex Module	18,000	$ 100,000	6.5	0.5	-	3,150	0.5	1,575	0.1	1,800	$ 100,000	56	0.9	0	1.0	0.7	$ 10,000	96	-	
			MFC	Conex Module	18,000	$ 300,000	6.5	1.0	-	3,150	8.5	26,683	1.5	27,000	$ 300,000	14	1.0	0	1.0	9.8	$ 450,000	809	-	
			Settling Tank	Conex Module	18,000	$ 150,000	6.5	0.5	-	3,150	0.34	1,071	0.1	1,800	$ 150,000	168	0.6	0	2.0	1.3	$ 30,000	195	-	
			Solids Disposal	Round Poly Tank 8-ft D x 24-ft L	12,000	$ 25,000	1.5	0.2	-	201	7	1,405	0.2	2,400	$ 25,000	0.5	1.0	0	1.0	0.3	$ 5,000	0.8	-	
																		Total:	**7.0**	**14.5**	**$ 520,000**	**1,653**	**-**	**41**

Appendix E
Life Cycle Assessment Results

23-Aug-17

End Point Totals

	Convention w/o reuse	MXC elec w/o reuse	MXC h2o2 w/o reuse		Convention w/o reuse	MXC elec w/o reuse	MXC h2o2 w/o reuse		Convention w/o reuse	MXC elec w/o reuse	MXC h2o2 w/o reuse		Convention w/o reuse	MXC elec w/o reuse	MXC h2o2 w/o reuse
		Human Health				**Ecosystem**				**Resource Depletion**				**Casualties**	
	CT	MEC-E	MEC-H2O2		CT	MEC-E	MEC-H2O2		CT	MEC-E	MEC-H2O2		CT	MEC-E	MEC-H2O2
Company	1.42994E-05	1.33838E-05	1.23178E-05	Company	5.83234E-08	5.61058E-08	5.11709E-08	Company	47.5189559	38.7213564	33.759647	Company	0.0002567	0.00026	0.000261
Battalion	1.3932E-05	1.2377E-05	1.18751E-05	Battalion	5.69842E-08	5.29696E-08	4.94967E-08	Battalion	39.329909	36.4493658	32.5207644	Battalion	0.0002576	0.00026	0.00026

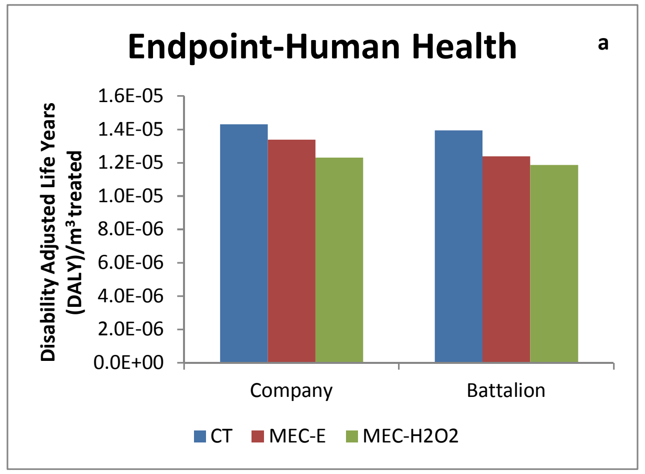

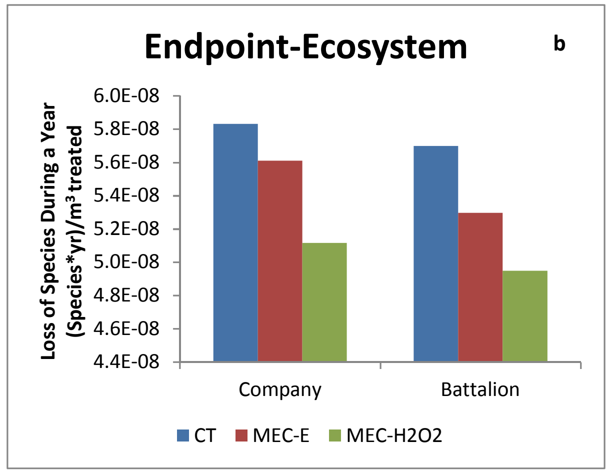

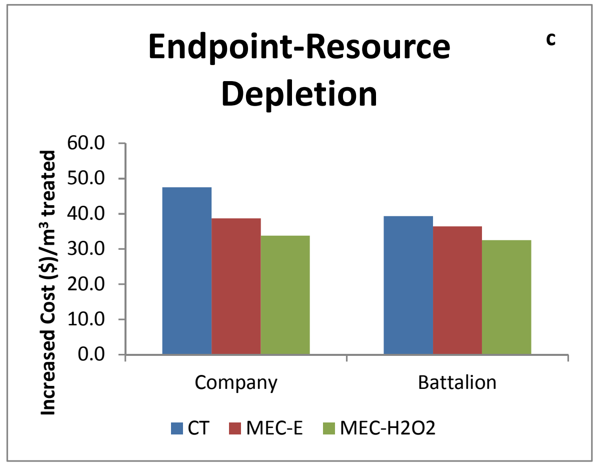

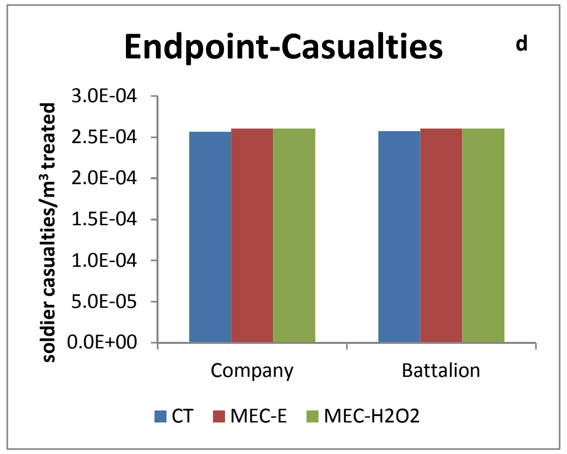

Mid Points

	Convention w/o reuse	MXC elec w/o reuse	MXC h2o2 w/o reuse		Convention w/o reuse	MXC elec w/o reuse	MXC h2o2 w/o reuse
Company							
		Human Health				**Ecosystem**	
Mid Point	CT	MEC-E	MEC-H2O2		CT	MEC-E	MEC-H2O2
Climate change human health	1.02E-05	9.85135E-06	8.98238E-06	Climate change Ecosystems	5.79556E-08	5.57985E-08	5.08782E-08
Ozone depletion	2.57E-09	6.62481E-09	1.60158E-08	Terrestrial acidification	1.92658E-10	1.59244E-10	1.51194E-10
Human toxicity	8.27E-07	6.29436E-07	4.61722E-07	Terrestrial ecotoxicity	1.7515E-10	1.48069E-10	1.41486E-10
Particulate matter formation	3.24E-06	2.89634E-06	2.85771E-06				

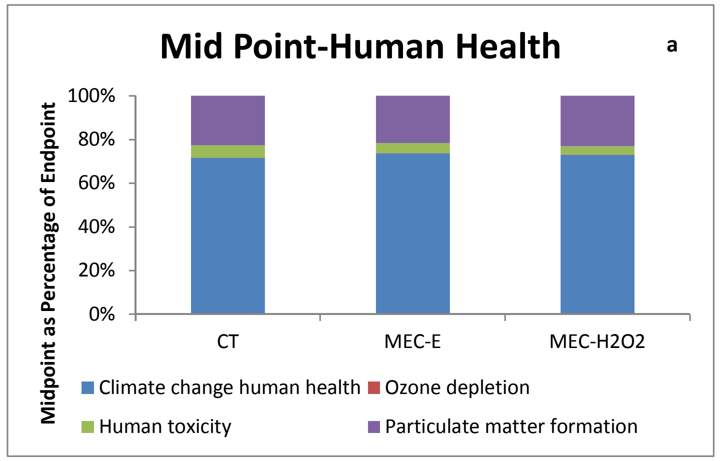

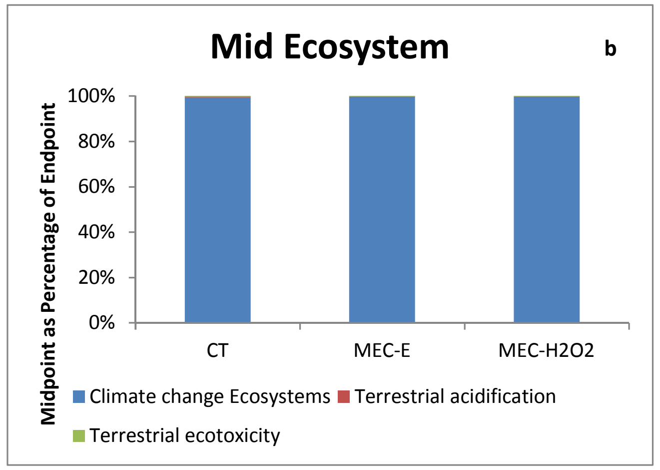

Battalion

	Human Health				Ecosystem		
Mid Point	CT	MEC-E	MEC-H2O2		CT	MEC-E	MEC-H2O2
Climate change human health	1.00E-05	9.30156E-06	8.68797E-06	Climate change Ecosystems	5.67E-08	5.26846E-08	4.92109E-08
Ozone depletion	2.16E-09	6.54445E-09	1.60047E-08	Terrestrial acidification	1.79E-10	1.41527E-10	1.47687E-10
Human toxicity	5.36E-07	5.93367E-07	3.945E-07	Terrestrial ecotoxicity	1.47E-10	1.43465E-10	1.38194E-10
Particulate matter formation	3.39E-06	2.47553E-06	2.77659E-06				

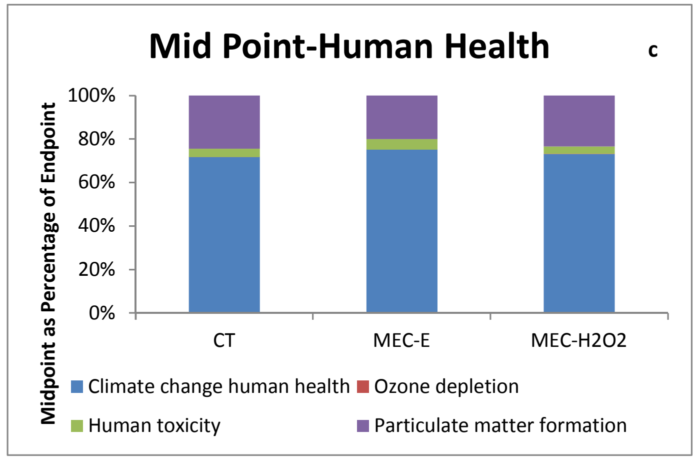

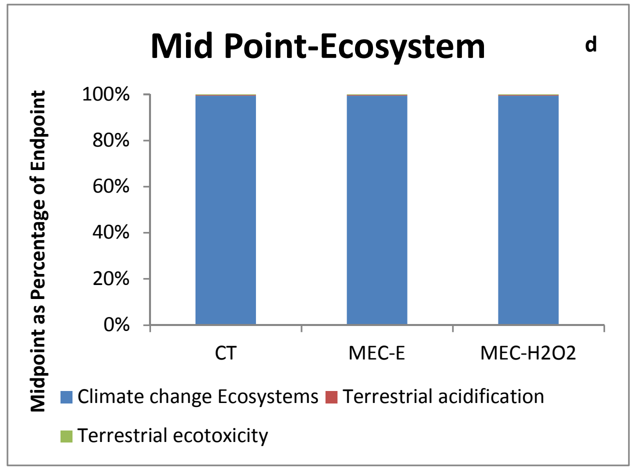

Categories

Company

	Human Health				Ecosystem				Fossil Depletion		
	CT	MEC-E	MEC-H2O2		CT	MEC-E	MEC-H2O2		CT	MEC-E	MEC-H2O2
Transport	1.18148E-05	1.18271E-05	1.1834E-05	Transport	4.88836E-08	4.89343E-08	4.89628E-08	Transport	34.9121827	34.9483404	34.9687071
Capital	5.85256E-07	7.91894E-07	1.34445E-06	Capital	2.19406E-09	3.01231E-09	5.02619E-09	Capital	2.06953142	1.94086345	2.79388563
Chemicals	5.6788E-07	6.37889E-07	-1.243E-06	Chemicals	2.99544E-09	3.19871E-09	-4.5362E-09	Chemicals	1.87651739	1.99960894	-4.2639447
Energy	1.02865E-06	-1.6146E-07	6.06834E-08	Energy	3.69951E-09	-4.3332E-10	1.62862E-10	Energy	8.52124656	-0.3002374	0.11284196
Sludge disposal	3.02749E-07	2.88357E-07	3.21748E-07	Sludge disposal	5.50818E-10	1.39383E-09	1.55523E-09	Sludge disposal	0.1394778	0.13278105	0.14815698

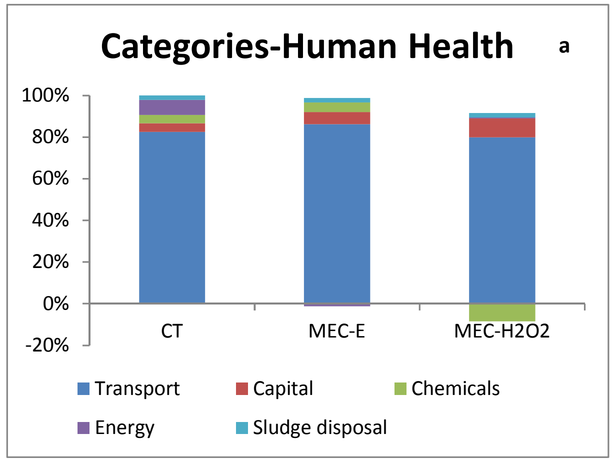

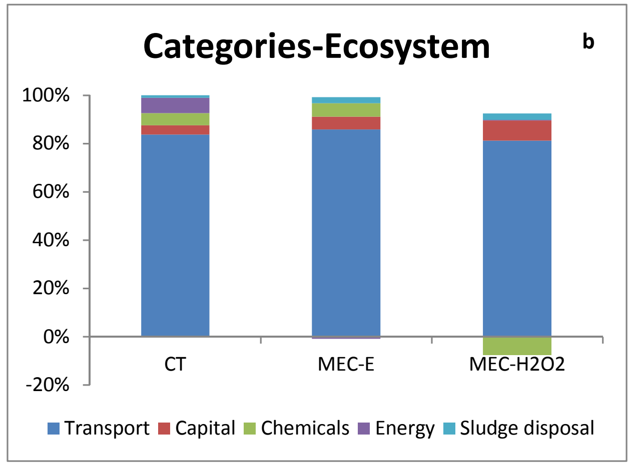

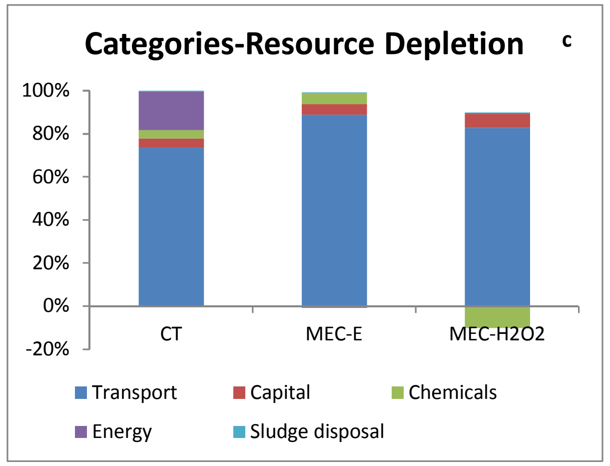

Battalion

	Human Health				Ecosystem				Fossil Depletion		
	CT	MEC-E	MEC-H2O2		CT	MEC-E	MEC-H2O2		CT	MEC-E	MEC-H2O2
Transport	1.18201E-05	1.18238E-05	1.18304E-05	Transport	4.89055E-08	4.89208E-08	4.8948E-08	Transport	34.9278097	34.938739	34.9581537
Capital	1.14429E-07	4.40143E-07	8.46615E-07	Capital	4.50907E-10	1.63875E-09	3.22751E-09	Capital	0.38491678	0.89042518	1.47523199
Chemicals	5.6788E-07	6.37889E-07	-1.2553E-06	Chemicals	2.99544E-09	3.19871E-09	-4.5873E-09	Chemicals	1.87651739	1.99960894	-4.3055591
Energy	1.05956E-06	-8.1321E-07	1.31637E-07	Energy	2.84363E-09	-2.1825E-09	3.53286E-10	Energy	1.97026277	-1.5121884	0.24478081
Sludge disposal	3.70058E-07	2.88357E-07	3.21748E-07	Sludge disposal	1.78875E-09	1.39383E-09	1.55523E-09	Sludge disposal	0.17040235	0.13278105	0.14815698

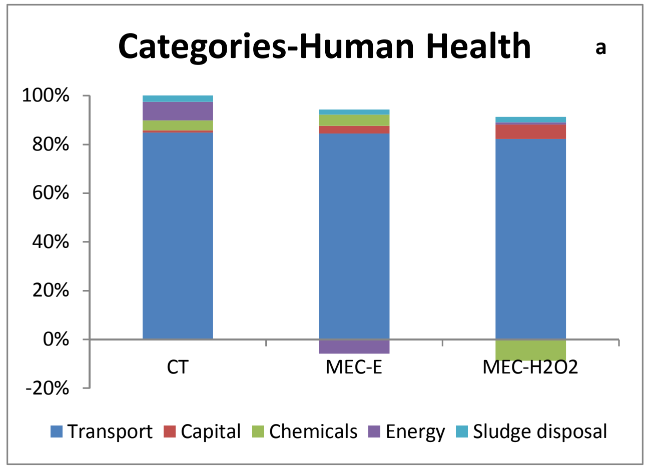

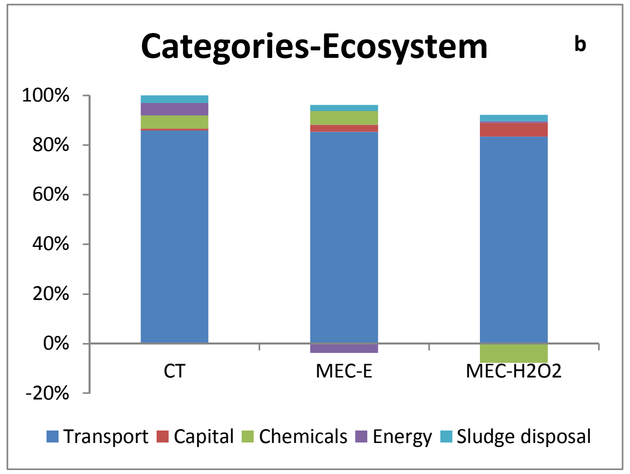

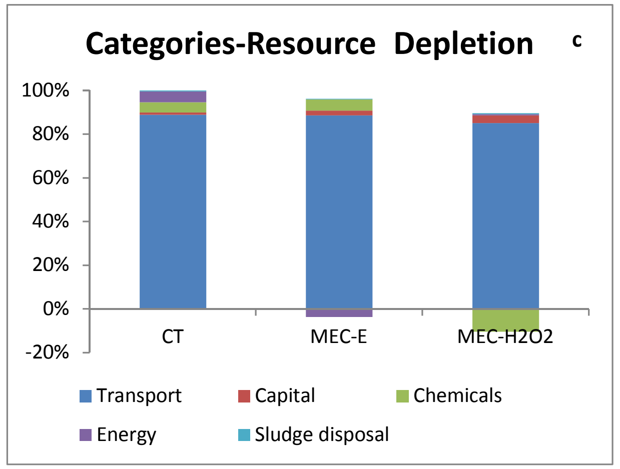

APPENDIX F

List of Scientific/Technical Publications

1. Articles in peer-reviewed journals

In print:

Ki D, Parameswaran P, Popat SC, Rittmann BE, Torres CI. 2017. Maximizing Coulombic recovery from primary sludge by changing retention time and pH in a flat-plate microbial electrolysis cell. Environmental Science: Water Research and Technology 3:333-339.

Young MN, Chowdhury N, Garver E, Evans PJ, Popat SC, Rittmann BE, Torres CI. 2017. Understanding the impact of operational conditions on performance of microbial peroxide producing cells. Journal of Power Source 356:448-458.

Ki D, Popat SC, Rittmann BE, Torres CI. 2017. H_2O_2 production in microbial electrochemical cells fed with primary sludge. Environmental Science and Technology 51(11):6139–6145.

S.C. Popat, C.I. Torres. Critical transport rates that limit the performance of microbial electrochemistry technologies. Bioresource Technology, 2016, 215, 265-273.45.

Young MN, Links MJ, Popat SC, Rittmann BE, Torres CI. 2016. Tailoring Microbial Electrochemical Cells for Production of Hydrogen Peroxide at High Concentrations and Efficiencies. ChemSusChem 9:3345-3352.

Ki D, Popat SC, Torres CI. 2016. Reduced overpotentials in microbial electrolysis cells through improved design, operation, and electrochemical characterization. Chemical Engineering Journal 287:181-188.

Ki D, Parameswaran P, Popat SC, Rittmann BE, Torres CI. 2015. Effects of pre-fermentation and pulsed-electric-field treatment of primary sludge in microbial electrochemical cells. Bioresource Technology 195:83-88.

Ki D, Parameswaran P, Rittmann BE, Torres CI. 2015. Effect of pulsed electric field (PEF) pretreatment on primary sludge for enhanced bioavailability and energy capture. Environmental Engineering Science 32(10): 831-837.

S. C. Popat, D. Ki, M. N. Young, B. E. Rittmann, C. I. Torres. Buffer pKa and transport govern concentration overpotential in electrochemical oxygen reduction at neutral pH. ChemElectroChem, 2014, 1, 1909-1915.

Joshi R, Tsakalis K, MacArthur J, Dash S. 2014. Account for uncertainty with robust control design: Part 1. Chemical Engineering Progress 110(11):31-38.

Joshi R, Tsakalis K, MacArthur J, Dash S. 2014. Account for uncertainty with robust control design: Part 2. Chemical Engineering Progress 110(12):46-50.

C. I. Torres. On the importance of identifying, characterizing, and predicting fundamental phenomena towards microbial electrochemistry applications. Current Opinion in Biotechnology, 2014, 27, 107-114.

To be submitted soon:

Ki D, Kupferer R, Torres CI. *In situ* stabilization of primary sludge in a single-chamber microbial H_2O_2 producing cell (sMPPC).

Young MY, Ki D, Torres, CI, Marcus AK, Rittmann BE. Understanding the impact of primary sludge on MEC performance using MYAnode.

2. Technical reports

Young MN. 2014. A Life Cycle Assessment of Alternative Wastewater Treatment Processes at Forward Operation Bases (FOBs). Arizona State University Repository. ASU-SSEBE-CESEM-2014-CPR-008.

3. Conference or symposium proceedings scientifically recognized and referenced

Young MN, Ki D, Stadie M, Thompson J, Chowdhury N, Popat SC, Rittmann BE, Torres CI. Tailoring Microbial Fuel Cells for Production of Hydrogen Peroxide. The Electrochemical Society Abstract MA2016-01:1795.

Ki D, Popat SC, Torres CI. On Design, Operation, and Characterization of Microbial Electrochemical Cells with Reduced Overpotentials. The Electrochemical Society Abstract MA2016-01:1797.

Young MN, Popat SC, Rittmann BE, Torres CI. Continuous hydrogen peroxide production in microbial electrochemical cells. Proceedings of the Water Environment Federation, Water Energy 2015(2):1-5.

Bogosh M, Richards P, Evans PJ, Nguyen T, Guven E, Young MN, Torres CI, Logan B. Life Cycle Environmental Assessment Comparison of Microbial Electrochemical Cells and Conventional Technologies for Wastewater Treatment at Forward Operating Bases. Proceedings of the Water Environment Federation, Water Energy 2015(2):1-8.

4. Conference or symposium abstracts

Shafique MA, Joshi R, Tsakalis K. Control Relevant System Identification Using Multiple Short Data Sets. IEEE Conference on Control Technology and Applications, August 2017.

Ki D, Popat SC, Kupferer R, Rittmann BE, Torres CI. Microbial hydrogen peroxide producing cells (MPPCs) fed with primary sludge. AEESP, June 2017.

Ki D, Young MN, Kupferer III R, Chowdhury N, Thompson J, Rittmann BE, Popat SC, Torres CI. Optimization of microbial hydrogen peroxide producing cells (MPPCs) for wastewater applications. KAUST Research Conference, Thuwal, Saudi Arabia, March 2017.

Ki D, Popat SC, Rittmann BE, Torres CI. Hydrogen peroxide production in a flat-plate microbial electrochemical cell semi-continuously fed with primary sludge. NA-ISMET, October 2016.

Ki D, Parameswaran P, Popat SC, Rittmann BE, Torres CI. Maximizing Coulombic recovery from primary sludge by changing retention time and pH in a flat-plate microbial electrolysis cell. AP-ISMET, August 2016.

Young MN, Chowdhudy N, Popat SC, Rittmann BE, Torres CI. Continuous Hydrogen Peroxide Production in Microbial Electrochemical Cells. International Water Association Leading Edge Technologies Conference, June 2016.

Young MN, Chowdhudy N, Popat SC, Rittmann BE, Torres CI. Hydrogen Peroxide Production using Microbial Electrochemical Cells. Arizona Water Association Annual Conference, May 2016.

Ki D, Parameswaran P, Popat SC, Rittmann BE, Torres CI. Maximizing Coulombic recovery from primary sludge by changing retention time and pH in a flat-plate microbial electrolysis cell. FUSION 2016-A Biodesign Institute Event, March 2016.

Young MN, Popat SC, Rittmann BE, Torres CI. Continuous Hydrogen Peroxide Production in Microbial Electrochemical Cells. FUSION 2016-A Biodesign Institute Event, March 2016.

Torres CI. Ionic transport in microbial fuel cells and its importance in design optimization. Congreso Nacional de Biotecnología, Guadalajara, México, Jun 2015.

Ki D, Popat SC, Torres CI. Towards microbial electrochemical cell design and operation with low overpotentials. The 5th International Meeting of the International Society of Microbial Electrochemistry and Technologies, October 2015.

Ki D, Parameswaran P, Popat SC, Rittmann BE, Torres CI. Enhancing Coulombic recovery from primary sludge in microbial electrochemical cells. The 5th International Meeting of the International Society of Microbial Electrochemistry and Technologies, October 2015.

Young MN, Popat SC, Rittmann BE, Torres CI. Continuous hydrogen peroxide production in microbial electrochemical cells. The 5th International Meeting of the International Society of Microbial Electrochemistry and Technologies, October 2015.

M. Young, S.C. Popat, B.E. Rittmann, C.I. Torres. "Continuous hydrogen peroxide production in microbial electrochemical cells." WEF Water and Energy 2015. June 2015.

Ki D, Parameswaran P, Popat SC, Rittmann BE, Torres CI. Energy recovery from primary sludge using microbial electrochemical cells (MXCs). AEESP, June 2015.

Ki D, Parameswaran P, Popat SC, Rittmann BE, Torres CI. Energy recovery from primary sludge using microbial electrochemical cells (MXCs). Arizona Water Association Annual Conference, May 2015.

Popat SC, Parameswaran P, Torres CI. Electron and ionic transport in microbial anode respiration and their importance in microbial electrochemical cell applications. Platform presentation at 226th Electrochemical Society Meeting, Cancun, Mexico, Oct 2014.

Ki D, Popat SC, Parameswaran P, Rittmann BE, Evans PJ, Torres CI. Kinetic study of microbial hydrolysis and anode respiration in microbial electrochemical cells (MXCs) fed with primary sludge. NA-ISMET, May 2014.

Torres CI. The importance of ionic transport in designing large-scale microbial electrochemical cells. Environmental Science and Engineering Division Seminar Series at KAUST, Thuwal, Saudi Arabia, Aug 2014.

Ki D, Prameswaran P, Torres CI. Kinetic study of microbial hydrolysis of primary sludge for microbial electrochemical cells. Arizona Water Association Annual Conference, May 2013.

Popat SC, Ki D, Rittmann BE, Torres CI. Overcoming ionic transport limitations in microbial electrochemical cells. European ISMET Conference, Ghent, Belgium, Sep 2012.

Popat SC, Ki D, Rittmann BE, Torres CI. Cathodic transport limitations in microbial electrochemical cells. 1st Microbial Fuel Cell Symposium at GIST, Gwangju, Korea, Jun 2012.

Popat SC, Ki D, Rittmann BE, Torres CI. On cathodic potential losses in microbial fuel cells. Platform Presentation at North American ISMET Meeting, Ithaca NY, Oct 2012.